Mechanical Modelling and Imaging of Human Tendons



Isabelle Scott

St John's College

University of Oxford

A thesis submitted for the degree of
Doctor of Philosophy

Hilary 2022

Preface

This thesis describes a body of research completed at the Mathematical Institute at the University of Oxford between May 2018 and May 2022. The thesis was completed under the supervision of Professor Sarah Waters and Professor Derek Moulton, and with external supervision from Associate Professor Peter Malliaras from Monash University, Australia. I am grateful for the funding provided by the Engineering and Physical Sciences Research Council and the Australian Musculoskeletal Imaging Group which allowed me to carry out this research. I am also grateful to Imaging at Olympic Park in Melbourne for providing us access to their data.

No part of my thesis has already been submitted for any degree or other qualification at the University of Oxford or any other institution. This thesis is my own work and includes no elements which are the outcome of work done through collaboration except where explicitly stated in text. All ultrasound images analysed in Chapter 4 were masked and analysed by myself, although the images were collected by an experienced ultrasonographer as part of another study. All required ethics approvals were obtained.

Acknowledgements

To my supervisors Sarah Waters and Derek Moulton: you have provided me with constant support, knowledge and guidance. You have shown a strong interest in my welfare and offered great support when I was navigating the more difficult periods of my studies. I have been challenged to be better in all areas of my academic work. I have learnt an immense amount and am incredibly grateful. To learn from two people who have achieved such success in their fields has been an incredible privilege. Thank you to my external supervisor Peter Malliaras, who has ensured my work is clinically relevant and has been a great source of positivity. I am also grateful to Anurag Arnab for bringing additional imaging expertise to this work.

A special thank you to the women in my family who have not only supported me through my doctoral studies, but inspired me by their own intelligence, strength and successes. My late grandmother Carol, who was one of very few women in her time to become a doctor. My mother Linda, who has taught me resilience and to be confident in voicing my opinions and taking on new opportunities. Finally, my sister Laura, who's work ethic and writing skills have always set such a high standard for me to aim.

Thank you to my father Bill, who has been one of my biggest supports and worn his Oxford beanie with pride. There were countless times in which you relieved my stress in some small or large way. My parents have always been immensely supportive of my academic pursuits and my time at Oxford would not have been possible if not for the opportunities they have provided.

Lastly, thank you to my friends Melis, Rose, Tom and Floren for the encouragement, laughs and runs during my time in Oxford.

Abstract

Tendons are fibrous connective tissues which are saturated with fluid. Cells within the tendon control the production and organisation of tendon constituents in response to local mechanical signals. Tendinopathy is a painful condition characterised by collagen disruption, accumulation of proteoglycans (protein-sugar complexes), and altered cell behaviour. Exercise is both a key aetiological factor for tendinopathy and a means for rehabilitation. High-frequency high-magnitude forms of loading can be detrimental to tendon structure and cause pain, especially when performed with small rest intervals between loading bouts. In contrast, low-frequency high-magnitude forms of loading have been demonstrated to reduce pain in tendinopathy and increase tendon stiffness. Evidence suggests that the disruption to tendon structure seen in tendinopathy is due to a maladaptive cellular response to loading. However, to date there is no clear understanding of how the spatially heterogeneous mechanical environment within the tendon subject to load, and the resulting changes in tendon material properties coordinated by cellular processes, contributes to damage or rehabilitation. Evidence to date suggests that tensile strains promote type I collagen synthesis and cause an increase in tendon stiffness, while high fluid flux or shear may lead to a reduction in collagen content and increase in proteoglycans, leading to a reduction in the stiffness and increase in permeability.

In this thesis, we aim to combine physical models of tendon deformation with imaging techniques to identify why high- and low-frequency loading regimes have differential effects on tendon stiffness and permeability. Using a poroelastic adaptation model for tendon we investigate how the local mechanical environment contributes to beneficial rehabilitative and maladaptive changes in tendon material properties in response to loading. The spatial distribution of tendinopathic changes predicted by the adaptation model are then contrasted

with imaging results generated by a machine learning approach which identifies tendinopathic regions, providing mechanistic insight into why damage occurs in certain regions.

We first derive a poroelastic model for tendon to identify differences in the local mechanical environment when the tendon is subject to cyclic tensile high- and low-frequency loading. The results are used to infer which local mechanical stimuli promote a maladaptive response by the cells and which promote an adaptive response. Increases in proteoglycans and reductions in collagen content have been posited to cause a reduction in the permeability and stiffness, respectively. Hence, we also investigate how localised reductions in permeability and stiffness alter the local mechanical environment, to identify whether changes in collagen and proteoglycan content amplify or reduce the mechanical stimuli that occur with high- and low-frequency loading.

We proceed by combining the poroelastic tendon model with a set of phenomenological rules prescribing the changes in tendon stiffness and permeability, which serve as surrogates for changes in type I collagen and proteoglycans, in response to local mechanical stimuli occurring during loading. The phenomenological component is time-dependent, allowing us to incorporate the effects of recovery time between loading bouts. A series of loading bouts are simulated and stiffness and permeability changes predicted by the model are contrasted with the global stiffness measurements and qualitative changes in the proteoglycans observed clinically.

To complement the preceding work, we develop an automated means for the texture-based segmentation of ultrasound images of the tendon. We utilise a hidden Gaussian Markov random field (HGMRF) model to automatically segment a dataset of tendinopathic and healthy ultrasound images of the Achilles tendon. The algorithm provides a means to identify and quantify disruption to healthy collagen architecture on imaging, allowing us to gain greater insight into the spatial pattern of changes that occur in tendinopathy.

Using the poroelastic model we show that high fluid fluxes occur with high-frequency loading while the axial strain remains comparable between different loading frequencies. A set of phenomenological rules in which reductions in the permeability and stiffness occur in response to high fluid flux, and increases in stiffness occur in response to axial strain, are able to predict clinically observed material property changes seen with high- and low-frequency loading scenarios. The model predicts tendinopathic changes to occur near the transverse tendon border due to high fluid flux, which is consistent with the location of damage predicted by the HGMRF-based segmentation approach.

Contents

1 Introduction **1**

1.1 Motivation 1

1.2 The Healthy Tendon 4

1.2.1 Anatomy and Physiology 4

1.2.2 Mechanotransduction with Loading 5

1.3 Tendinopathy 7

1.3.1 Aetiology and Rehabilitation 7

1.3.2 Pathophysiology 11

1.3.3 Changes in Material Properties with Tendinopathy 14

1.4 Mechanical Behaviour of Tendons 16

1.5 Poroelasticity and Modelling in Biology 18

1.6 Mathematical Modelling of the Tendon 21

1.7 Imaging in Tendinopathy 25

1.8 Machine Learning Methods for Medical Image Segmentation 28

1.9 Hypothesis and Objectives 33

1.10 Key Contributions 35

1.11 Thesis Structure 36

2 A Poroelastic Model for Tendon **38**

2.1 Synopsis 38

2.2 Chapter Outline 39

2.3 Literature Review 40
2.3.1 Fluid Models of Tendons 40
2.3.2 Poroelastic Small Strain Models 44
2.4 Small Strain Poroelastic Theory 48
2.4.1 Nomenclature 49
2.4.2 Solid and Fluid Phases 50
2.4.3 Kinematics 51
2.4.4 Conservation Equations 52
2.4.5 Constitutive Law for the Flow through a Porous Medium 53
2.4.6 Linear Flow Equation 54
2.4.7 Constitutive Law for the Solid Skeleton 55
2.5 Problem Description 57
2.6 Model Setup 60
2.6.1 Scaling 63
2.6.2 Dimensionless Governing Equations 64
2.7 One-Dimensional Model 65
2.7.1 Homogeneous Tendon Subject to Cyclic Loading 66
2.7.2 Numerical Solution 70
2.7.3 One-Dimensional Model Results 71
2.7.4 One-Dimensional Model Discussion 78
2.7.5 Conclusions from One-Dimensional Model 82
2.8 Two-Dimensional Model 83
2.8.1 Dimensionless Two-Dimensional System 84
2.8.2 Numerical Scheme 86
2.8.3 Two-Dimensional Model Results 86

2.8.4 Summary of Parameter Changes on Mechanical Environment 96
2.8.5 Discussion 97
2.8.6 Conclusions and Future Work 102
2.A Further Mathematical Background 105
2.A.1 Hooke's Law and Plane Stress Reductions 105
2.A.2 Small Strain Theory and Lagrangian and Eulerian Descriptions . . . 108
2.B Details of Numerical Solution 109
2.C Details of Numerical Solution 109
2.C.1 Numerical Procedure for One-Dimensional Model 109
2.C.2 Numerical Procedure for Two-Dimensional Model 111
2.4 Additional Results 118
2.4.1 Sensitivity to Transverse to Axial Permeability Ratio 118
2.4.2 Sensitivity to Location of Damage 119

3 A Load-Driven Adaptation Model for Tendon 121

3.1 Synopsis 121
3.2 Introduction 122
3.3 Chapter Outline 123
3.4 Literature Review 124
3.4.1 Previous Damage and Adaptation Models 124
3.4.2 Effect of Local Mechanical Stimulation on Proteoglycan and Collagen Content 128
3.4.3 Effect of Micro-Structural Changes on Material Properties 132
3.4.4 Loading Scenarios 133
3.5 Aims of Model 134
3.6 Model Setup 136

3.7 Model Implementation . . . 145
3.7.1 Pseudocode . . . 145
3.7.2 Loading Interventions . . . 146
3.7.3 Parameter Values . . . 147
3.7.4 Metrics . . . 148
3.8 Results . . . 149
3.8.1 Parameter Sensitivity . . . 149
3.8.2 Changes in Stiffness Following a Single Loading Bout . . . 150
3.8.3 Rehabilitative Loading . . . 154
3.8.4 Damage-Inducing Loading . . . 157
3.8.5 In-Season Loading Regimes . . . 163
3.9 Discussion . . . 168
3.10 Conclusion and Limitations . . . 172
3.A Adaptation Model Parameterisation . . . 174
3.A.1 Parameter Values . . . 174
3.A.2 Parameter Sensitivity . . . 174
3.B Additional Results . . . 178
3.B.1 Changes in Stiffness at Transverse Boundary Following a Single Loading Bout . . . 178
3.B.2 Changes in Stiffness Following a Single Loading Bout . . . 178
3.B.3 Long-Time Behaviour . . . 179
3.B.4 Model-Based Prescription of Loading . . . 180

4 Tendon Image Segmentation 182

4.1 Synopsis . . . 182
4.2 Introduction . . . 183

4.2.1 Literature Review 184
4.3 Key Mathematical Concepts 191
4.3.1 Notation 191
4.3.2 Hidden Gaussian Markov Random Fields 193
4.3.3 Extension of the Expectation-Maximisation Algorithm to Hidden Gaussian Markov Random Fields 196
4.3.4 Grey-Level-Co-Occurrence-Matrix 201
4.3.5 Textons 203
4.3.6 Decision Trees 205
4.4 Image Collection and Pre-Processing 205
4.5 Algorithm for Texture-Based Segmentation of Tendon Images 206
4.6 Code Validation 210
4.6.1 Hyperparameter Optimisation and Variable Selection 211
4.7 Segmentation Results 212
4.7.1 Texture Features and Initial K-Means Clustering 213
4.7.2 GLCM-Based HMRF-EM Segmentation 218
4.8 Discussion 224
4.9 Conclusions and Limitations 227
4.A Key Mathematical Concepts 228
4.A.1 Fundamental Statistical Principles 228
4.A.2 Convolution Filters 229
4.A.3 K-Means Clustering 230
4.A.4 Stochastic Modelling of Image Textures 232
4.B Additional Results 234

5 Summary and Future Work **241**

5.1 Summary of Thesis 241

5.2 Future Work 243

5.2.1 Parameter Accuracy and Sensitivity for Mechanical Modelling of Tendon 243

5.2.2 Three-Dimensional Heterogeneous Anisotropic Model for Tendon . . . 244

5.2.3 Investigating the Osmotic Effect of Proteoglycans 245

5.2.4 Constitutive Relationships for the Mechanical and Adaptation Models of Tendon 246

5.2.5 Correlating Image Segmentation Results with Severity and Local Material Property Measurements 247

5.3 Concluding Remarks 248

CHAPTER 1

Introduction

1.1 Motivation

Tendons are fibrous connective tissues within the human body that connect muscles to bone. Tendons are key in enabling human movement to occur, allowing force transmission from the muscular system to the skeleton (Figure 1.1) (Kannus 2000). Tendinopathy is a condition characterised by pain, changes in tendon cell activity, fluid accumulation and collagen degeneration within the tendon (Maffulli et al. 2004). It is a common musculoskeletal condition associated with high rates of recurrence and restriction of daily activities. The condition is usually a result of overload and/or compression of the tendon from surrounding structures. In the case of energy storing tendons, such as the Achilles or patellar, overuse is frequently associated with high strain rate activities such as running and jumping. For positional tendons, such as those encompassing the rotator cuff surrounding the shoulder joint, overuse is also associated with repetitive use of the tendon. However, in contrast to energy-storing tendons, the relationship between loading rate and injury risk is less clear (Maffulli et al. 2003).

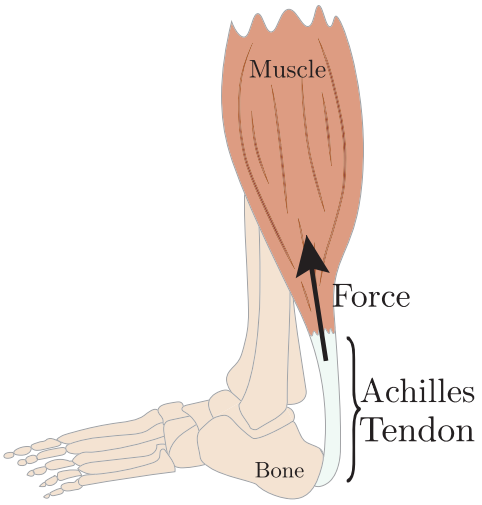


Figure 1.1: Diagram of the Achilles tendon. The Achilles tendon originates from the triceps surae (calf) muscle complex and inserts into the calcaneus (heel) bone.

Despite reasonable knowledge on the aetiology of tendinopathy, the exact pathological mechanism and sequence of microscopic events leading to tendinopathy are still unknown, limiting our ability to design more effective medical therapies and physical rehabilitation regimes. Evidence suggests that cells play an important role in tendinopathic changes due to physiological loading (Magnusson et al. 2010). Tendon cells are subject to a variety of local stresses and strains associated with the activities of daily living. In response to these local mechanical stimuli, tendon cells modulate the tendon constituents, which in turn alters the material properties of the tendon, to cope with these loads (Bohm et al. 2015). Whilst the exact pathological process of tendinopathy is unknown, evidence suggests it may occur as a maladaptive response to loading: the adaptive process in which tendon cells modify the tendon in response to load is overactive or distorted (Cook et al. 2016). There is insufficient research to fully understand the role of mechanotransduction in tendinopathy (Chatterjee et al. 2021). It is unclear which local intratendon mechanical stimuli promote tendinopathic changes; how these mechanical stimuli relate to features of the applied load such as the loading rate, magnitude, and recovery period between; and how these local mechanical stimuli stimulate the tendon cells to modify the material properties of the tendon.

Mathematical modelling provides a means of investigating the interplay between extrinsic loading factors, the intrinsic mechanical environment within the tendon, and changes in the tendon constituents and material properties in response to load. Rather than investigate the mechanical environment in tendon that occurs with loading, a large proportion of the previous modelling work on tendon has focussed on phenomenological modelling of the microscopic components (often incorporated into a multiscale model) to investigate the role of different microscopic components of tendon and predict observed mechanical behaviour. The macroscopic models that have focused on predicting the mechanical environment with loading and identifying key individual mechanical cell stresses that precipitate injury or maladapta-

tion have utilised finite element modelling software packages[1] (Lavagnino et al. 2008, Wren et al. 2000). However, these models were not paired with more recent research which has implicated specific loading rates and magnitudes in the development of tendinopathy. Modelling work has the potential to address our need in further understanding the microscale mechanical environment with loading and related changes in local tendon structure (Maganaris et al. 2017). However, to complement such research, it is important to have a clinical tool to accurately assess the spatial pattern of changes in tendon constituents in response to loading. The current approaches to tendon imaging analysis are limited in their capacity to detect micro-structural changes which correlate with pain, prognosis, or response to rehabilitation (Khan et al. 2003, Paavola et al. 1998, Docking et al. 2019b, Ark et al. 2018).

In this thesis we utilise mathematical modelling to explore the interplay between extrinsic loading factors, the mechanical environment within the tendon, and material properties, and how interactions between these factors impact tendinopathy development and resolution. Such a potentially complex and nuanced relationship between multiple variables would be difficult to analyse in a wet lab or clinical setting, and, to our knowledge, has not been explored in previous modelling work. We use the model to predict the most likely sites of tendinopathic changes and gain mechanistic insight into why these changes occur. We complement this model by investigating the use of machine learning techniques for tendon imaging, to provide a more precise means of investigating the spatial pattern of changes in material properties that occurs in tendinopathy. The imaging results can then be paired with insight gained from the adaptation model to provide mechanistic insight as to why certain regions within the tendon are most likely to exhibit damage.

[1]The finite element method solves for the governing equations numerically by dividing the domain into a fine mesh and approximating the system of equations by a set of simpler equations that can be solved algebraically.

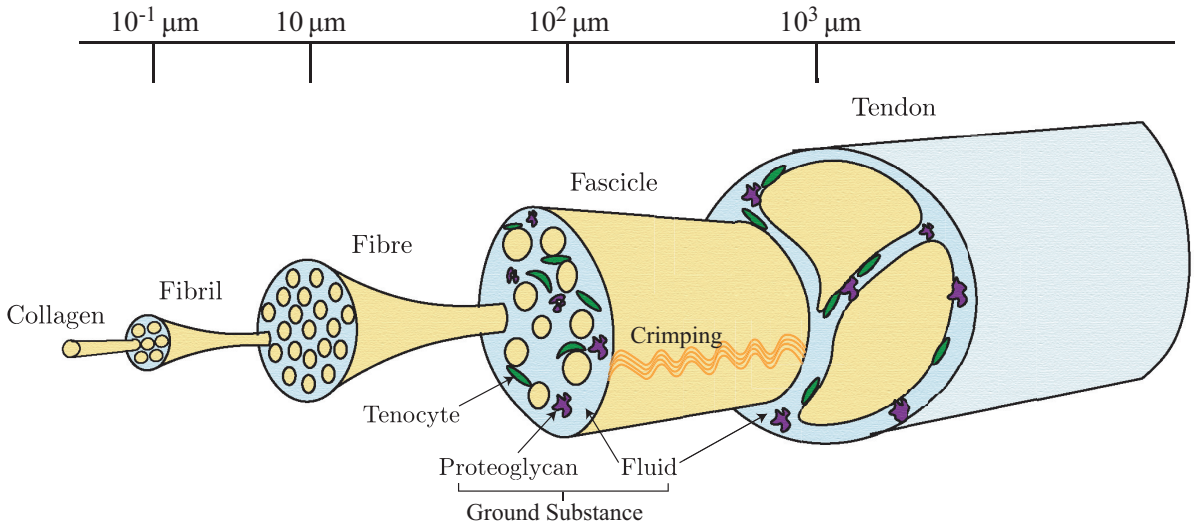


Figure 1.2: Hierarchical structure of tendons. Type I collagen is the predominant solid constituent forming a network of fibres aligned axially along the tendon. Cells lie along fibres, whilst a proteoglycan-water matrix termed 'ground substance' fills the gaps between. Note: Adapted from Carrillo et al. 2021. "Mathematical modelling of collagen fibres rearrangement during the tendon healing process". *Kinetic and Related Models* 12 (2):283. Used under CC BY 4.0.

1.2 The Healthy Tendon

1.2.1 Anatomy and Physiology

Tendons have their origin (proximal attachment) at the muscle and insertion (distal attachment) at the bone. At this insertional end, many tendons wrap tightly around the bone. Forces generated within the muscle lead to tendon strains and subsequent movement of the skeleton (Jull et al. 2015). Tendons are composed of a hierarchical collagen structure, cells, and surrounding fluid (Figure 1.2). Collagen, predominantly type I, is the basic building block for fibres, which intertwine in bundles to form fascicles. Fascicles run parallel to each other, longitudinally along the tendon. Collagen fibres have a crimped pattern, which is stretched at the initial application of an applied load. The arrangement and mechanical properties of type I collagen are thought to give the tendon its macroscopic tensile properties (Screen 2009). Tendon cells, termed tenocytes, lie along both fibres and fascicles, and are responsible for the synthesis and degradation of tendon components (Benjamin et al. 2008). Tendons are

approximately 70% water by weight. Associated with this water is an abundance of proteins and glycosaminoglycans, termed 'ground substance'. Glycosaminoglycans (GAGs) are large unbranched polysaccharides, usually attached to protein molecules (jointly termed proteoglycans in this case), which bind and organise water molecules (Tresoldi et al. 2013). Whilst the role of proteoglycans in tendons is not fully understood, there is evidence that they reduce the permeability of the tissues and bind water due to their highly negative charge (Jurvelin et al. 1988, Tavakoli Nia et al. 2015). It has been proposed that this causes a retainment of fluid, thereby cushioning the cells and protecting them from compression by solid components of the tendon (Cook et al. 2012, Grigg et al. 2009). This hypothesis is supported by the high presence of proteoglycans in cartilage and around tendon insertions, corresponding to areas subject to high compressive stresses from adjacent bone (Grad et al. 2011, Docking et al. 2013, Cook et al. 2012).

1.2.2 Mechanotransduction with Loading

Mechanotransduction is the process by which cells sense a local mechanical stimulus and produce a biochemical response. Mechanical cues are sensed by proteins at the cell membrane surface and are relayed to the cell nucleus. The cell then produces chemical signals or alters gene expression in response (Lavagnino et al. 2015). Tendon cells are exposed to tensile and potentially compressive strains due to deformation of the collagen fibres and fascicles to which they are attached, as well as to fluid shear and pressure changes induced by movement of the surrounding fluid (Thompson et al. 2017). It is well established that tendon cells are mechanosensitive; *in vitro* animal experiments have shown that fluid shear stress, hydrostatic pressure, and tensile strain are all drivers for tendon cell mechanotransduction (Archambault et al. 2002, Lavagnino et al. 2008, Shim et al. 2006). As a result, tendons are constantly being remodelled in response to macroscopic loading (Figure 1.3). The microscopic mechanical stimuli due to loading are highly dependent on the tendon structure at the time of loading, which is, in turn, dependent both on the prior loading history of the tendon, as well as

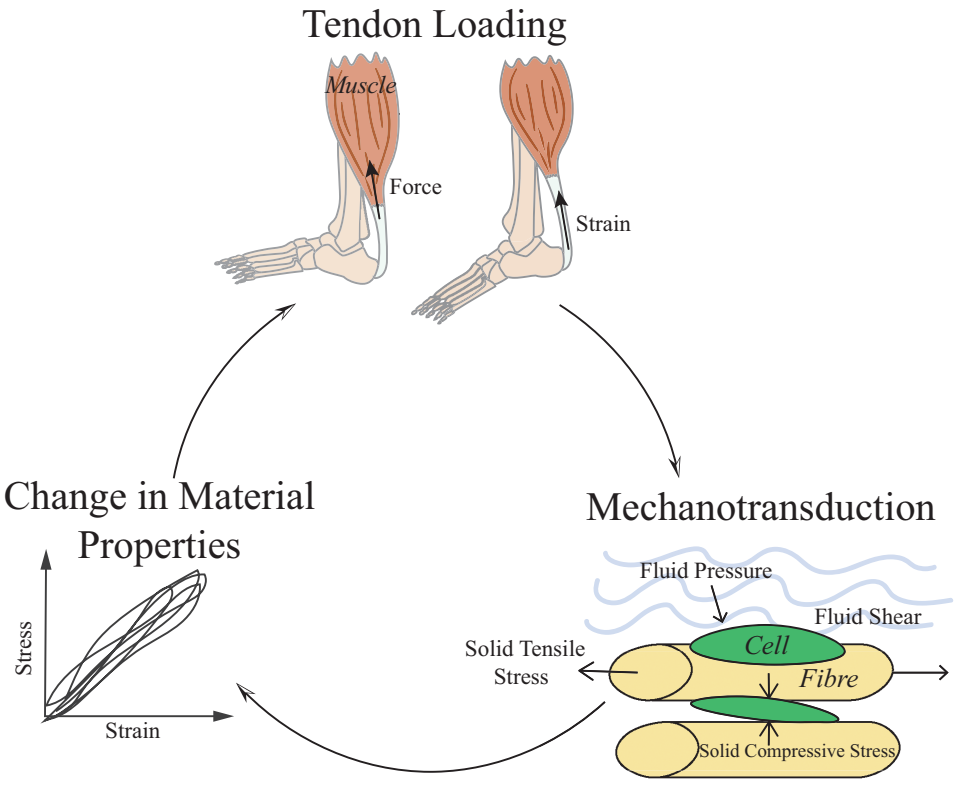


Figure 1.3: Schematic of tendon mechanotransduction with loading. Tendons are subject to tensile and compressive forces with loading, leading to microstructural fluid and solid induced stresses at the cell level. Cells are responsive to both fluid and solid induced stress, altering their synthesis and degradation of tendon constituents in response to these stresses. Alteration of the tendon constituents leads to local changes in material properties which further modulates microstructural stresses with subsequent loading.

personal factors such as age, sex or whether any chronic diseases are present (Lavagnino et al. 2015). In response to loading, tendon cells can both synthesise (Miller et al. 2005) and degrade collagen (Langberg et al. 1999b). A larger tendon diameter has been found in healthy tendons of athletes, compared to non-athletes, suggesting an increase in type I collagen content as a beneficial adaptive response to large tensile loads (Kulig et al. 2013). Increases in non-collagenous components of the tendon also occur, with larger proteoglycans more predominant in areas within the tendon subject to higher external compression (Docking et al. 2013).

Mechanotransduction not only affects the synthesis and degradation of tendon constituents

by tenocytes in response to the classical tensile loads that the tendon experiences, but also affects the differentiation of mesenchymal stem cells into tenocytes and the maintenance of the tenocyte's phenotype[2] (Lavagnino et al. 2015). Mesenchymal stem cells can differentiate to form resident cells in bone, cartilage, nerve, muscle, or tendon, amongst other tissues. The mechanical stimuli that direct mesenchymal stem cell differentiation are influenced by the material properties of the cell's surrounding tissue and the applied load to that tissue (Steward et al. 2015). Hence, mesenchymal cells take on a phenotype which is specific to their environment and enables them to produce constituents that allow the tissue to tolerate applied loads. For example, compression has been shown to upregulate genes associated with cartilage cells. Cartilage is a tissue which is exposed to high compressive loads due to its location within joints (Haudenschild et al. 2009). However, this response to loading is not fixed once differentiation occurs; the phenotype of mesenchymal cells is dynamic. As such, tenocytes, which usually reside in tissue exposed to predominantly tensile forces (Lavagnino et al. 2015), are able to take on a phenotype resembling cartilage cells, when the tissue is exposed to extrinsic compressive forces. This change in cell phenotype can then lead to a subsequent, and potentially maladaptive, change in the tendon constituents (Cook et al. 2012).

1.3 Tendinopathy

1.3.1 Aetiology and Rehabilitation

Exercise is both a key aetiological factor in the development of tendinopathy and a means for rehabilitation. Tendinopathy is a condition that is common in populations who engage in activities which expose the tendon to high strain rates (Malliaras et al. 2017, Maffulli et al. 2003). Tendinopathy is not only a disease occurring in athletes. Advanced age and

[2]The combination of cellular processes that occur through certain gene and protein expression and characterise the cell as a classic tendon cell.

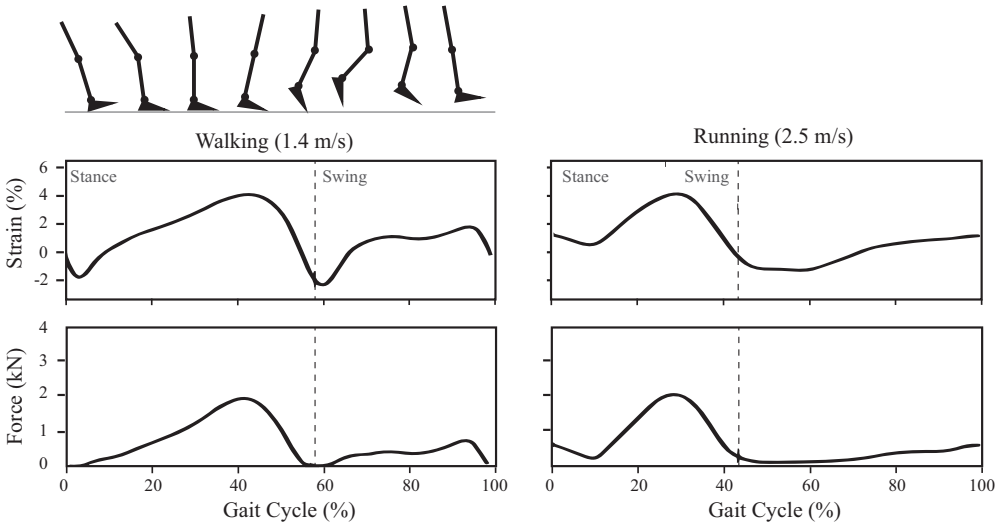


Figure 1.4: Achilles tendon strain and force during walking (1.4 m/s) and slow running (2.5 m/s). The x-axis is normalised to the gait cycle which is depicted visually on the right. Dashed vertical line separates stance (foot in contact with ground) and swing (foot in air) phase. Note: Adapted from M. Kharazi et al. 2021. "Quantifying mechanical loading and elastic strain energy of the human Achilles tendon during walking and running". *Scientific Reports* 11 (1): 1–13. Used under CC BY 4.0.

diseases such as diabetes result in changes which predispose patients to injury at even lower loads (lower loading duration or strain rates). Consequently, subgroups of the population may develop tendinopathy with normal activities of daily living, such as walking (Abate et al. 2016). Rehabilitative exercises that cause large tendon strains (around 4-5%) but at a slow rate, have shown to reduce pain and increase tendon stiffness (Bohm et al. 2014).

Common examples of *damage-inducing loading* for energy storing tendons, such as the patellar and Achilles tendons, include running, jumping, and walking for elderly populations (Malliaras et al. 2013, Malliaras et al. 2017). Figure 1.4 depicts the global strain and force curves for the Achilles tendon during walking and running (Kharazi et al. 2021). These are cyclic forms of loading and, omitting the swing phase where the foot is not in contact with the ground and minimal forcing occurs, can be approximated by a sine wave (Lee et al. 2019, Elvin et al. 2009). It is during the early stance phase when tendon elongation takes place that evidence suggests damage and rehabilitation mechanisms occur. Specifically, poor muscle strength controlling tendon elongation and adaptive movement strategies to minimise tendon

elongation during the stance phase have both been associated with patients presenting with tendinopathy (Bisseling et al. 2008, Wyndow et al. 2010). Rehabilitation training involving only tendon elongation (only a positive tensile load is applied) has proven to have similar benefits to rehabilitation involving lengthening and shortening of the tendon (cyclic applied tensile load) (Jonsson et al. 2005).

Walking occurs at a frequency of around 1-2 Hz, whilst slow jogging occurs at around 2.5 Hz (Rowlands et al. 2007). Throughout this text we use the term *loading frequency* to refer to the number of loading cycles per second within an individual loading bout, rather than the number of individual loading bouts within a given period of time. We use the term *fast loading* to refer to cyclic forms of loads with a frequency of at least 1 Hz. The time between loading bouts is also an important contributor to the development of tendinopathy, with shorter recovery intervals between loading bouts increasing injury risk (Mead et al. 2018).

In contrast to fast cyclic loading, which can be provocative for tendons, slow-heavy (the associated muscle is working at $\geq$70% capacity) tendon loading has been identified as one of the most effective rehabilitation tools for tendinopathy. Similar to damage-inducing forms of loading, *rehabilitative loading* often takes a cyclic form, such as calf raises or leg extensions. Heavy slow resistance training (HSRT) is a popular rehabilitation regime that, when applied over 14 weeks, has been shown to reduce pain in both patellar and Achilles tendinopathy (Malliaras et al. 2013), as well as increase the Young's modulus of the tendon (Arampatzis et al. 2007, Bohm et al. 2015). A schematic of this loading regime, using the Achilles tendon as an example, is given in Figure 1.5. Heavy slow resistance training involves using heavy weights to impose a high resistance for the muscle-tendon unit to work against. Usually 3-4 sets of 6-8 repetitions are carried out, at a resistance of at least 70% of the maximum possible for the subject if they were to perform only one repetition. We refer to this as a % maximum voluntary contraction (MVC). The rate of loading is much slower for HSRT than walking or running; each repetition is performed over six seconds (0.17 Hz) (Beyer et al. 2015).

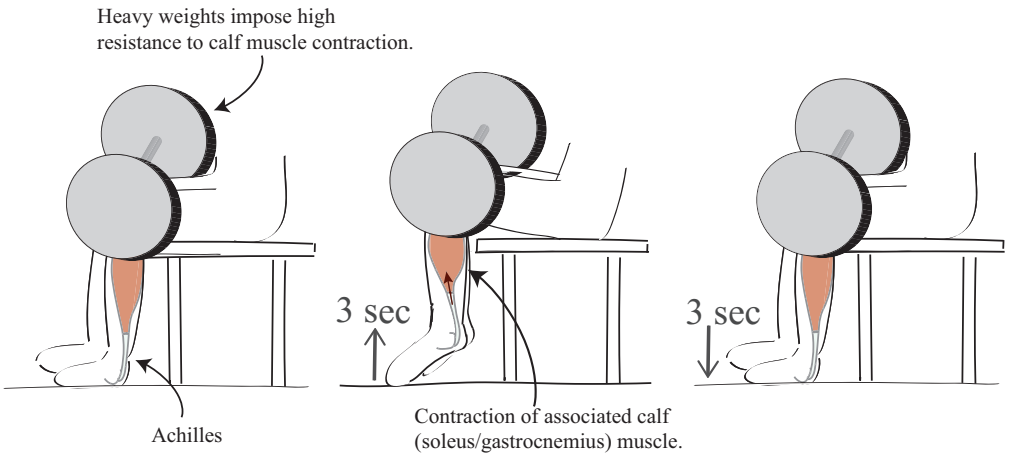


Figure 1.5: An schematic of heavy slow resistance training for the Achilles tendon. A heavy resistance is applied for the gastrocnemius and soleus - the associated muscles of the Achilles tendon - to work against. Contraction of this associated muscle group causes a small global strain of the Achilles tendon.

Whilst forces of around 2500 N are experienced by the Achilles tendon with running (Farris et al. 2012a), similar forces have been observed during rehabilitation regimes, which impose slow loading of the tendon (Rees et al. 2008, Bohm et al. 2014). Both types of loading produce strains greater than 3.5 % (Bohm et al. 2015). In fact, it has been demonstrated that rehabilitation regimes need to use sufficiently heavy weights for a reduction in pain or increase in stiffness to take place, indicating that the axial/longitudinal tensile strain may be an important positive stimulus for the tendon (Bohm et al. 2015, Arampatzis et al. 2007). The key difference between rehabilitative loading, such as HSRT, and damage-inducing loading appears to be the strain rate of loading, or equivalently, since these are usually cyclic forms of load, the loading frequency. This is supported by Bohm et al. (2014) who had participants engage in slow and fast cyclic Achilles tendon loading, of the same magnitude, over a period of 14 weeks. They found an increase in tendon stiffness at the slower loading rate. Herein we use the terms *rehabilitative loading* and HSRT synonymously. However, we note that other rehabilitation regimes that impose slow high magnitude loads to the tendon are also available (Clifford et al. 2020).

A rapid increase in training load, such as over a period of several weeks, is also a contribut-

ing factor to the development of tendinopathy. An increase in training load entails a sudden reduction in the recovery time between loading bouts, an increase in the loading frequency[3] or a substantial increase in the volume (duration and number of bouts) of high-frequency loading from a low baseline level (Malliaras et al. 2017). In order to return to pre-injury levels of activity following rehabilitation, a gradual increase in the loading frequency with each loading bout is required (Mascaró et al. 2018). The development of tendinopathy has a stronger relationship to the relative increase in loading frequency for a patient than the absolute frequency undertaken during loading, which suggests that the tendon gradually develops a tolerance - through modification of the material properties - to higher loading frequencies. Exactly how this tolerance occurs is still debated, but one popular theory is that there is an increase in collagen content with a subsequent enhancement in tensile stiffness (Malliaras et al. 2013).

1.3.2 Pathophysiology

Several theories have been proposed regarding the pathophysiology of tendon disease. It has been suggested that the primary pathological process falls into one of three categories: a maladaptive cellular response, an inflammatory response, or a collagen tearing event (Cook et al. 2009, Cook et al. 2016). Multiple changes in cell behaviour, suggestive of a maladaptive response, are evident in tendinopathy, including cellular proliferation and change of shape, as well as altered collagen and proteoglycan production (Docking et al. 2019a, Cook et al. 2009, Burssens et al. 2013). Whether inflammation is present in tendinopathy remains controversial, in part because of the varying definitions of an inflammatory response. There is, however, general agreement that the dominant acute inflammatory cell type typically seen in acute inflammation is absent. Chronic inflammatory markers have been found to occur in tendinopathy, though these changes still appear to be linked to changes in res-

[3]For example, engaging in hopping can be provocative for the Achilles tendon if the patient has no prior history of engaging in this exercise.

ident tenocyte behaviour in which the tenocytes secrete proinflammatory cytokines (Dean et al. 2016). Collagen tearing as the initiating event has been proven unlikely; *in vivo* studies have shown collagen fibres cannot tear without substantial alterations in the surrounding ground substance (Screen et al. 2005). Collectively, there is stronger evidence to suggest that tendinopathy occurs through a maladaptive cellular response to loading, and that inflammation and collagen tearing (at a later stage) may occur but are more likely secondary to a maladaptive cellular response (Cook et al. 2009, Cook et al. 2016).

Many of the changes seen in tendinopathy represent cartilagenous changes, including cell rounding and an increase in the cellular deposition of the large proteoglycans, biglycan and aggrecan. This modifies the tendon structure to share similarities with cartilage in human joints, a tissue with a high tolerance to external compressive loads (Burssens et al. 2013). This has prompted several authors (Cook et al. 2012, Docking et al. 2013, Burssens et al. 2013) to suggest that the maladaptive changes seen in tendinopathy are in response to external compression with loading. This is supported by the fact that many tendinopathies arise near the tendon insertion, where the tendon experiences compression from adjacent bone during loading (Cook et al. 2012). However, since extrinsic compression would be expected to cause both solid deformation and fluid movement, it is still unclear which local intratendon mechanical stimulus plays the predominant mechanotransductive role in extrinsic compression-related changes, or whether the changes result from the interplay between several mechanical stimuli. Whilst it is obvious that extrinsic compression is likely to result in local compressive solid strains, the mechanical environment may be altered in other ways. For example, Buschmann et al. (1999) showed that extrinsic compression of cartilage resulted in regions of high fluid shear and that aggrecan was predominantly deposited in these regions. Furthermore, several tendinopathies also arise more centrally along the long axis of the tendon, away from any obvious sources of external compression. It has been suggested that in these cases, compressive transverse strains may occur due to axial tensile loading, leading to a reduction in pore space and subsequent compression of the cells within the solid matrix.

Several authors (Cook et al. 2012, Grigg et al. 2009) have suggested this as an explanation for the aggrecan deposition seen in these midportion cases, proposing that the molecule would serve to reduce permeability and hence maintain a fluid 'cushion' around the cells.

Whilst the theory of tendinopathy occurring as a cartilagenous response to load explains the proteoglycan deposition and cell rounding characteristic of tendinopathy, the changes in collagen seen in tendinopathy are not fully representative of a cartilagenous response. In healthy cartilage, type II collagen is the dominant collagen, an important constituent providing compressive stiffness (Korhonen et al. 2003). In contrast, in tendinopathic regions much of the type I collagen usually seen in healthy tendons is replaced with type III collagen and only modest increases in type II collagen have been detected (Gigante et al. 2004, Mos et al. 2009, Burssens et al. 2013). This is problematic since type III collagen is a weaker collagen and generally associated with a poorly organised collagen matrix when present as the dominant collagen constituent (Nielsen et al. 2016). Cook et al. (2009) suggests that short recovery timeframes between loading bouts may cause a disruption to collagen synthesis, favouring type III collagen synthesis and leading to a net decrease in type I collagen (Magnusson et al. 2010). This could explain the higher presence of collagen III, which is laid down more quickly than type I and often acts as an interim collagen while connective tissue remodelling takes place (Hirose et al. 2004, Voleti et al. 2012, Gay et al. 1978). The importance of adequate recovery time between loading bouts is supported by clinical work (Malliaras et al. 2015), however whether this is because of a disruption to collagen synthesis has not been fully proven. Short recovery times may also lead to an imbalance between collagen and proteoglycan deposition. The rate of proteoglycan synthesis in tendons is unknown but an increased net synthesis has been shown to occur within 24 hours following loading in cartilage (Schätti et al. 2013, De Croos et al. 2006), which is much faster than the net synthesis of collagen I seen in tendons following loading (Magnusson et al. 2010).

Excess fluid accumulation is another characteristic feature of tendinopathy, leading to

swelling of the tendon which is visible on imaging. Fluid accumulation is presumed to occur as a result of the increased proteoglycan deposition and disruption to the collagen architecture due to a loss of type I collagen content (Parkinson et al. 2011). For simplicity, we do not explicitly address the contribution of proteoglycans as water-binding molecules or tendon swelling in our modelling work here, however, we note that these are important characteristics of tendinopathy that should be incorporated in future modelling work.

Substantial advances have been made in understanding the microstructural changes that occur in tendinopathy (Cook et al. 2016). However, more research is needed to understand exactly why a reduction in type I collagen and an increase in proteoglycans occurs in tendinopathy, and how these changes either contribute to or mitigate progression of the disease. This is especially the case in midportion tendinopathy, where there is no obvious source of external compression. Whilst it could be the case that the inappropriate deposition of proteoglycans in tendon leads to pain and a reduced load tolerance in some way, the interruption of collagen synthesis could also be implicated. Furthermore, it could be that the combination of these two factors is especially detrimental to tendon structure.

1.3.3 Changes in Material Properties with Tendinopathy

Given that collagen and proteoglycans constitute the bulk of the tendon's solid skeleton (Screen 2009), the disruption to the collagen content and increase in proteoglycans seen in tendinopathy (Tom et al. 2009, Magnusson et al. 2010) are likely to produce changes in the material properties. However, since it is difficult to measure material properties *in vivo*, several material properties are unreported or their reported values are conflicting (Firminger et al. 2021, Safa et al. 2020).

Given the tensile role tendons play in the body, there has been strong interest in the role of stiffness changes or changes in the Young's modulus in tendinopathy. The tendon stiffness measures the average axial force-elongation ratio whilst the Young's modulus measures the

axial stress-strain ratio (Bohm et al. 2014). Macroscopically there are multiple means for measuring the stiffness and Young's modulus in tendons but the accuracy of many of these methods is questionable. This is especially the case *in vivo*, where a range of factors may influence the results, such as operator dependence, the direction of stiffness measured (tendons are anisotropic), whether active or passive stiffness was assessed (whether the associated muscle was in a contracted state), and whether tendon preconditioning was employed. Overall there is moderate *in vivo* evidence suggesting that there is a reduction in axial stiffness with tendinopathy (Arya et al. 2010, Obst et al. 2018). Aside from variability in measurement procedures, another reason that some studies have not detected a reduction in stiffness is that, despite tendinopathy resulting in only localised tendon changes, with surrounding tendon demonstrating healthy structure (Maffulli et al. 2003), stiffness measurements are usually taken globally (Obst et al. 2018).

Whilst there is at least some general agreement regarding stiffness changes in tendinopathy, a vast range of values have been reported for the tendon permeability and Poisson's ratios of healthy tendons (Safa et al. 2020, Gatt et al. 2015, Han et al. 2000). A large variation in Poisson's ratio for healthy animal tendons is reported in the literature, ranging from negative values to those exceeding the isotropic limit. We discuss this issue in further detail in Chapter 2 when reviewing previous mathematical models of the tendon, as these unusual values have motivated a proportion of previous modelling work. To our knowledge, there are no studies investigating changes in either the permeability or Poisson's ratio with tendinopathy. However, authors have assumed that there is a reduction in the permeability due to the accumulation of proteoglycans (Wren et al. 2000, Thorpe et al. 2016a), which have been shown to alter permeability in other tissues (Jurvelin et al. 1988, Tavakoli Nia et al. 2015). Estimates as to what degree aggrecan reduces the permeability in tendon is unknown. In contrast, it is more difficult to infer whether the Poisson's ratio would be expected to change with tendinopathy, especially given that the Poisson's ratio for healthy tendons is debated (Firminger et al. 2021).

1.4 Mechanical Behaviour of Tendons

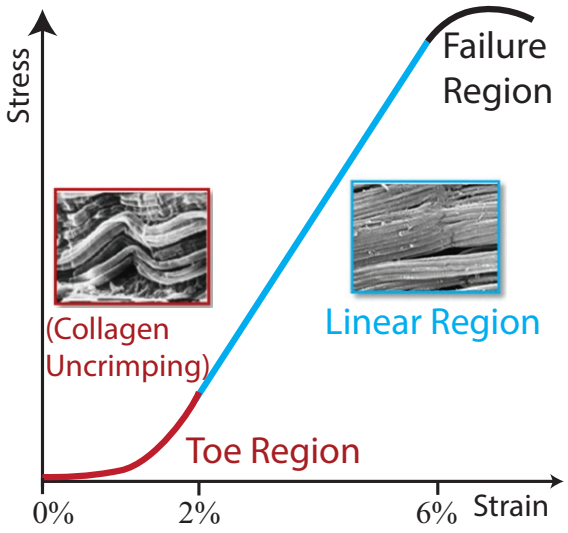


Figure 1.6: Stress-strain curve for tendon. A non-linear region occurs at the start of loading, followed by a linear region for strains >2%. Note: Adapted from B. Freedman et al. 2018. "Dynamic loading and tendon healing affect multiscale tendon properties and ECM stress transmission". *Scientific reports* 8 (1): 1–13. Used under CC BY 4.0.

Tendons are complex hierarchical structures, in which the exact contribution of many of the microscopic constituents, such as proteoglycans, to the mechanical behaviour of tendons is largely unknown (Parkinson et al. 2011). The three key components usually considered when modelling the tendon mathematically are water, proteoglycans and collagen fibres (Fang et al. 2016). The stress-strain curve (Figure 1.6) is approximately linear for tendon subject to physiological loading, termed *curvilinear*: there is a small slightly curved "toe" region at $< 2\%$ global strain, which is explained by the uncrimping of the collagen fibres, and a linear region for physiological global strains ($< 6\%$) beyond this (Maganaris et al. 2004, Freedman et al. 2018).

Tendons have been modelled as both poroelastic and poroviscoelastic structures (Wang et al. 2012, Khayyeri et al. 2015, Wren et al. 2000). In poroviscoelastic structures, both poroelastic and viscoelastic mechanisms for relaxation[4] occur, and often over different timescales (Oftadeh et al. 2018). Poroelastic relaxation, in which the solid phase takes an increasingly larger portion of the applied stress, involves equalisation of the pressure through fluid redistribution. As such, the timescale for poroelastic relaxation to occur is dependent on the length scale over which fluid redistribution occurs. Viscoelastic effects that may influence the

[4]The tissue gradually requires less force to maintain the same elongation over time.

mechanical behaviour of tendon include: the material being stiffer for faster loading rates; an increase in strain with additional cycles of loading, termed *viscoelastic (dynamic) creep*; and a difference in the stress-strain curve for loading and unloading of the material during each cycle, termed *hysteresis* (De Zee et al. 2000). These effects involve the rearrangement of the tendons subcomponents and can occur at multiple scales: the rearrangement of collagen molecules, fibrils, and fibres all occur, with the rearrangement of fibres through inter-fibre sliding occurring most rapidly over a period of 10 seconds (Gupta et al. 2010). Whether these viscoelastic effects occur is dependent on how quickly a load is applied (the loading frequency). Accounting for these effects adds complexity to the model through the introduction of a strain rate dependent component (Peltonen et al. 2013, De Zee et al. 2000), Detournay et al. 1993). Hence, whether a poroelastic or poroviscoelastic model is appropriate for tendon depends on which mechanical behaviour the model aims to capture and the loading scenarios of interest.

Collectively, evidence suggests that the viscoelastic effects of tendons are less relevant for simulating and contrasting rehabilitative and damage-inducing loading. Firstly, several authors have demonstrated the absence of significant rate-dependent stiffening of the tendon for physiological loading rates equal to or faster than the rates implemented for rehabilitative loading (0.17 Hz) (Peltonen et al. 2013, Rosario et al. 2020, Kubo et al. 2002). Secondly, no significant dynamic creep was observed for 30 minutes of running (Farris et al. 2012b) or when running was simulated by applying a cyclic force to *ex vivo* animal tendons (De Zee et al. 2000). Whilst dynamic creep has not been specifically investigated for rehabilitative regimes, Hawkins et al. (2009) demonstrated that, when slow moderate (0.75 Hz, 25% MVC) loads are applied, dynamic creep is limited to the first five minutes of loading, with the stress-strain behaviour remaining steady thereafter. Thirdly, several studies have demonstrated that the hysteresis in energy storing tendons, measured as the difference in the area under the

strain curve for loading and unloading, appears to be small ($< 10\%$)[5] (Peltonen et al. 2013, De Zee et al. 2000).

1.5 Poroelasticity and Modelling in Biology

Poroelasticity describes the reversible deformation of aggregates composed of both solid and fluid phases. The term *solid* is used to refer to the porous solid skeleton while the term *fluid* refers to the infiltrating fluid within these pore spaces. Poroelastic modelling is a subject of immense interest in the field of biology due to the abundance of tissues, such as bone, cartilage, brain, lung, and tumours, which can be considered as poroelastic or poroviscoelastic structures. Most poroelastic biological tissues exhibit three increasing characteristic length scales: the size of a single cell, the diameter of individual collagen fibres, and the size of the overall tissue.

Mixture theory is a commonly used approach to modelling poroelastic biological materials where the smaller characteristic length scales are ignored and the domain is viewed as a superposition of interacting continuous constituents. A set of governing equations is used to describe the behaviour of each constituent of the mixture (each constituent must obey the individual equations of motion) and coupling terms are introduced to model the interaction between constituents (Mow et al. 1980, Ateshian et al. 2012). The final governing equations are then derived through spatial averaging procedures, based on the assumption that the mean motion results from the cumulative motion of the constituents (Ateshian et al. 2012).

Biot's theory is another macroscale approach to poroelastic modelling in which the domain is viewed as a superposition of interacting continuous constituents. In 1941 Maurice Anthony

[5]Several in vivo ultrasound studies have reported hysteresis values above 10% (Maganaris et al. 2000, Maganaris et al. 2002). However, because of the limitations of ultrasound in capturing such time dependent effects, several authors have suggested that these values represent overestimates (Lichtwark et al. 2013, Finni et al. 2013).

Biot (Biot 1941) derived a set of phenomenological laws relating the strain of a linearly elastic porous material to the applied stress and pore pressure. In contrast to mixture theory, in which the governing equations are derived through a strict averaging procedure, Biot's work represents an approximation of the governing macroscale equations (Kapellos et al. 2010, Guo et al. 2020). However, given certain assumptions, Biot's governing equations can be derived through a mixture theory-based approach, and hence Biot's theory can be considered as a special case of mixture theory (Bowen 1982). Despite being a phenomenological-based approach, Biot's theory represents a widely used and straightforward continuum theory approach in which the constitutive relationships involve well-defined and measurable quantities at the macroscale (Guo et al. 2020).

Using Biot theory, the poroelastic media is modelled as a continuum and we consider the two (solid and fluid) phases as volume fractions of the poroelastic material. We assume that both phases are fully connected and the fluid is Newtonian. The behaviour of the solid and fluid is coupled, with solid deformation impacting fluid movement, and fluid pressure providing a reciprocal stress for solid deformation to occur. The strength of fluid-to-solid and solid-to-fluid coupling can vary, depending on the material properties, rate of applied stress, and boundary conditions imposed (Detournay et al. 1993). The key kinematic quantities are the solid displacement relative to a reference configuration and the fluid movement relative to the solid. The related solid strain and variation in fluid content then serve as conjugate quantities for the stress and pore pressure, that is, the product of these two variables has the dimension of energy. For example, the mechanical work required to achieve an incremental change in pore volume is given by the incremental change in pore volume multiplied by the pore pressure (Carcione 2007). Time dependence is introduced into the formulation by using Darcy's law to describe the relationship between the fluid flux and pressure gradient. The full set of conservation and constitutive equations which are derived from Biot theory are presented in Chapter 2.

A key component of Biot theory concerns the behaviour of the poroelastic material in the drained and undrained states. The undrained behaviour characterises the material when fluid is consider to be trapped in the material such that there is zero flow relative to the solid skeleton. In contrast, the drained response characterises the material behaviour when fluid is freely able to move throughout the material and the pressure has sufficient time to equilibrate, such that the pore pressure is zero everywhere. These two scenarios are considered as limiting behaviours of the material and can often be replicated experimentally to investigate poroelastic phenomena.

Alternative theories to these single-scale poroelastic modelling approaches have also been presented but have not shown any distinct advantage over Biot or Mixture theory (Detournay et al. 1993). Approaches using homogenisation methods or multiscale (bottom-up) descriptions of the material, to consider the contribution of the smaller scale components to the overall poroelastic behaviour, are also commonly used for poroelastic modelling of biological tissues (Kapellos et al. 2010).

Understanding the fluid-structure interactions in biological tissues allows us to gain insight into how the architecture of the tissue and cell function are effected by macroscopic mechanical loading of the tissue, and how nutrients and wastes are transported (in this work we are primarily interested in former). Cartilage is a fibrous tissue within joints which is commonly modelled using poroelastic theory to interrogate the mechanical environment to which resident cells are exposed. Extrinsic compression from bone means that superficial layers of cartilage have a different mechanical environment to that of the middle layers. Modelling work has been used to support the hypothesis that intermittent hydrostatic pressures help maintain cartilage, while local solid shear and tensile stresses promote hardening of the cartilage contributing to osteoarthritis (Carter et al. 2003). Bone is a mechanically stiffer tissue than both cartilage and tendon but can still be modelled using poroelastic theory (Thomopoulos et al. 2010, Cowin 1999). *In vitro* evidence strongly supports that bone cells are

responsive to fluid shear stress (Wittkowske et al. 2016). Poroelastic modelling investigating the contribution of fluid movement within bone has contributed to substantial advances in our understanding of bone remodelling (Metzger et al. 2015). Poroelastic modelling has also been effectively paired with *in vitro* experimental work on musculoskeletal cells to ensure that the cells are exposed to a mechanical environment that is representative of *in vivo* (Burova et al. 2019). Other tissues are also commonly modelled using poroelastic theory, such as brain and lung. In these two cases, multiple fluid phases may be considered to model the vascular fluids separately to the cerebrospinal fluid which surrounds the brain or gases within the lung (Hirsch 2018). Overall, because fluid is abundant within the human body, poroelastic theory has a plethora of applications in the field of biology (Hirsch 2018, Kapellos et al. 2010).

1.6 Mathematical Modelling of the Tendon

Evidence clearly suggests that extrinsic loading factors - including the magnitude, rate and time frame between loading bouts - affect the tendon's response to loading. However, how exactly the tendon's response to loading relates to the changes in the constituents and material properties that are seen in tendinopathy remains unclear (Cook et al. 2012). To understand how the changes in tendon constituents which occur with tendinopathy relate to loading frequency, it is essential to understand how changes in the material properties, occurring as a result of these changes in tendon constituents, influence the intratendon mechanical environment with different loading frequencies and how this in turn leads to further changes in the constituents and material properties. Mathematical modelling paired with knowledge of the effect of different extrinsic loading factors on rehabilitation and damage is a potential, and currently unexplored, avenue to further investigate this area. In this section we give a brief outline of the previous mathematical modelling work on tendon but note that further details are given in Chapter 2 and 3. Current approaches to whole tendon modelling can be largely grouped into two categories: hierarchical multiscale models and tissue level models. Multiscales models of the tendon predict the macroscopic behaviour through a set of

phenomenological rules at the microscale, with the behaviour of subcomponents contributing to the global mechanical behaviour. Tissue level models do not explicitly incorporate these microscale complexities. Instead, tissue level models are informed directly by macroscopic measurements of the material properties and observations of tendon mechanical behaviour.

Multiscale models are often used to interrogate the role of different tendon constituents at the microscopic scale. By contrasting model predictions of the macroscopic tendon behaviour with *ex vivo* measurements, researchers are able to investigate the plausibility of phenomenological assumptions at the microscale (Maceri et al. 2012,Ahmadzadeh et al. 2013, Wu et al. 2018). For example, shear-lag models are based on the assumption that glycosaminoglycan chains serve as springs linking collagen fibres, and have been used to investigate whether GAG chains impact the overall tensile behaviour of the tendon. This shear-lag component was able to predict the non-linear behaviour of the tendon occurring over the toe region of the stress-strain curve (Ahmadzadeh et al. 2013, Wu et al. 2018). Stochastic phenomenological models have been used which assume that fibre-recruitment is strain dependent, with authors also able to predict a non-linear toe region occurring at the macroscale through this mechanism (Raz et al. 2009). Viscoelastic effects within tendons have been captured using Maxwell configurations, which consist of a spring and dashpot, to represent the fibres (Khayyeri et al. 2015). A hyperelastic description of the tendon fibres has also been introduced to describe the curvilinear behaviour and predict the "toe" region of the stress strain curve (Shearer 2015). Hyperelastic descriptions use a strain energy potential, a relation between the imposed strain and the amount of energy in a unit volume of material, to prescribe the material behaviour (Rodrıguez et al. 2006). Because many of these models have focussed on predicting the initial non-linear macroscopic behaviour of tendons, there is less insight gained from these models when considering larger physiological strains (>2%) that occur with exercise such as rehabilitative loading or running (Arampatzis et al. 2007, Kharazi et al. 2021).

Several authors have assumed that viscoelastic effects explain the rate dependence of the tendon's response to loading (Malliaras et al. 2013). However, the mechanical environment within poroelastic structures is also influenced by the loading rate and hence could explain a difference in the local mechanical environment to which the cells are exposed with difference frequencies of loading. Finite element modelling at the tissue level has been used by several authors to model the tendon as a poroelastic structure (Lavagnino et al. 2008, Atkinson et al. 1997, Wren et al. 2000). Lavagnino et al. (2008) demonstrated that higher strain rates result in high levels of fluid shear stress. They explicitly modelled cells within the tendon, and, through a 'top-down' approach, predicted shear stress at the cell membrane. However, loading rates in their work were kept below those that are damage-inducing (Rowlands et al. 2007). To our knowledge, only commercially available software packages have been employed for finite element modelling of the tendon and less information was provided regarding the intricacies of the model setup. There is a wealth of literature in the field of porelasticity, outside of finite element modelling, which has been applied to modelling cartilage and bone (Armstrong et al. 1984, Kameo et al. 2008), as well as non-biological structures such as soil, but the approach has not been applied to tendon to the same degree. The effects of loading rate and local changes in the material properties have both been explored in cartilage and bone (Kameo et al. 2008, Wang et al. 2001, Kameo et al. 2016). Because of the simplicity of the setup, Kameo et al. (2008) and Kameo et al. (2016) obtained analytical solutions for the transient and steady state pressure when a cyclic load was applied, while Wang et al. (2001) utilised a finite difference scheme. The authors were able to use these models to investigate how heterogeneity in the permeability and stiffness affected the local mechanical environment. However, it is difficult to draw inferences from these studies in the setting of the tensile tendon, where similar analyses have not been carried out.

Accurate poroelastic and poroviscoelastic modelling of the tendon requires knowledge of material parameters such as the Poisson's ratio and permeability. One of the key challenges in producing accurate predictive models of tendon behaviour is the variability in parameter

values reported experimentally. Whilst this makes it difficult to draw strong inferences from modelling work, several researchers have also been motivated by this gap in knowledge, as modelling work can also be used to test the implications of various experimental results, for example, to the tendons macroscopic behaviour or to how damage can occur. It can also be used to examine the experimental setup and challenge experimental findings. Carniel et al. (2019) used a tissue level finite element model to demonstrate that the Poisson's ratio measurements are sensitive to the experimental setup, explaining the variability in reported values.

Several multiscale and tissue level models have been used to investigate how damage occurs in tendons. Older modelling work has investigated tendinopathy as a micro-tearing event (Hurschler et al. 1997), although, as noted previously, recent evidence does not support the role of microtearing as the initiating factor (Screen et al. 2005). Shear-lag models have been utilised to investigate the effects of GAG depletion, however, since there is an increase of GAGs with tendinopathy, this work is not strongly relevant clinically. To our knowledge, Wren et al. (2000) is the only author thus far who has used a poroelastic damage (or maladaptation) model in keeping with the theory of tendinopathy occurring as a maladaptive response to loading. They used finite element modelling to predict the local mechanical environment that occurs at the tendon insertion, where extrinsic compression from bone can occur. They used this to build an adaptation model which simulated a series of loading bouts over days and predicted permeability changes in response to hydrostatic pressure. However, they did not incorporate changes in tendon stiffness. Their model predicted high pressures to occur at the tendon insertion and hence a reduction in permeability due to loading occurred. To our knowledge, there is no adaptation or damage model for tendon that has incorporated the time-dependence of constituent or material property changes in response to loading. This is despite these changes occurring over a semi-acute (days) time frame rather than immediately following a loading bout, and hence influencing the recovery time needed before subsequent loading should be commenced (Magnusson et al. 2010). This

time-dependent component is essential to incorporate to predict differences in the material property changes between different loading regimes, as recovery times may vary between regimes.

Over the last decade substantial advances in our understanding of which forms of loading contribute to tendinopathy development and which forms of loading serve as a rehabilitative loading tool have been made. Since previous modelling work has not been coupled with our knowledge of damage-inducing and rehabilitative loading, there is great scope for modelling work to assist in our understanding of how these forms of loading affect the mechanical environment within the tendon. Mathematical modelling is an inexpensive and accessible tool which can be coupled with clinical and experimental results, as well as guide future clinical and experimental studies. This thesis derives a poroelastic model for tendon and couples this with a set of time-dependent phenomenological rules which govern the material property changes in response to loading. We use this modelling framework to simulate rehabilitative and damage-inducing forms of loading, addressing a key gap in previous work.

1.7 Imaging in Tendinopathy

Whilst mathematical modelling can be used to predict the local mechanical environment in tendon which occurs with loading and infer potential structural changes, there is a need for a tool to evaluate the spatial pattern of structural changes *in vivo* to couple with such modelling work. Ultrasound (US) imaging is fast, cheap, and readily accessible in the clinic (Grassi et al. 2000). Ultrasound devices use a transducer to emit sound waves into the tissue of interest. These sound waves are reflected by the tissue, depending on the density, uniformity, and orientation of the tissue, and are picked up as *echoes* by a transducer. Sound waves travel easily through uniform dense substances such as water and hence there is minimal reflection of the sound waves. These substances will appear dark on ultrasound (*hypoechoic*), while substances that strongly reflect sound waves will appear light (*echogenic*) (Chan et

al. 2011). Images of the tendon can be taken as longitudinal slices, aligned with the long axis of the tendon (Figure 1.7), or transverse slices, orthogonal to the long axis of the tendon. A barrier to measuring structural changes *in vivo* is the limited ability of current ultrasound analysis methods to detect and quantify micro-structural features that correlate with pain or changes in material properties in response to rehabilitation (Ark et al. 2018, Drew et al. 2014). For these reasons US is limited as a prognostic tool (Khan et al. 2003, Paavola et al. 1998). Several authors have suggested pain and structural changes may simply lack a strong correlation (Docking et al. 2015). However, US images are noisy, the modality is highly operator-dependent, and image analyses are done subjectively (Brattain et al. 2018). Hence, investigation of objective and quantitative tools for tendon image analysis is warranted before conclusions regarding the correlation between structural changes and pain are made. MRI offers an alternative to ultrasound that has a lower operator dependence. However, MRI is expensive and less accessible, and ultrasound provides tendon images with a higher spatial resolution (Cook 2019, Docking et al. 2015).

Tendinopathic lesions are visually identifiable on US by changes to the normal greyscale texture. In a healthy tendon image, consistent with uniform collagen alignment, there is a

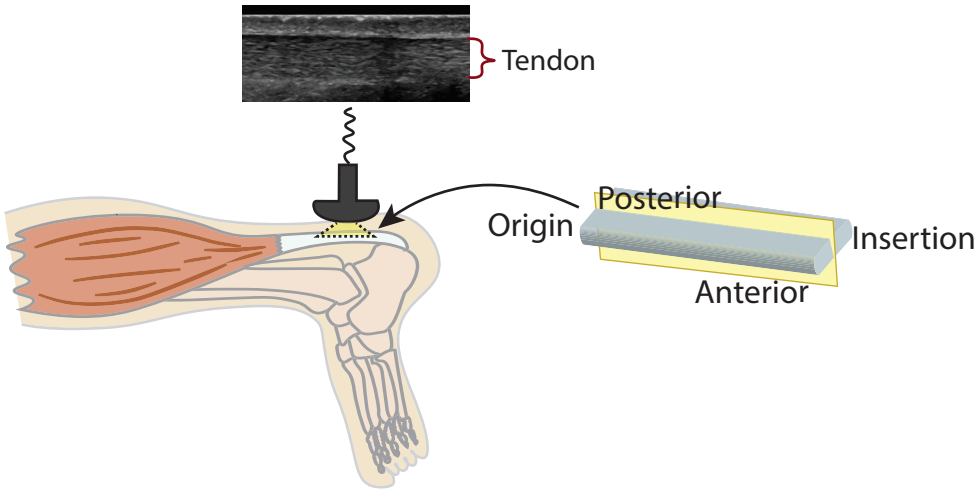


Figure 1.7: Ultrasound imaging of the Achilles tendon. The transducer is placed on the posterior aspect of the lower limb. The image is taken as a longitudinal section of the Achilles, running parallel to the fibres and fascicles.

homogeneous pattern of parallel echogenic lines, interspersed with dark hypoechoic spaces (Figure 1.8a). For the tendinopathic tendon, the tendon displays thickening and a disruption to the uniform pattern of parallel collagen fibres, in which there is a reduction in the number of visible echogenic lines and increased hypoechoic spacing between them (Figure 1.8b) (Hodgson et al. 2012). The degree of thickening, in isolation, does not directly correlate to

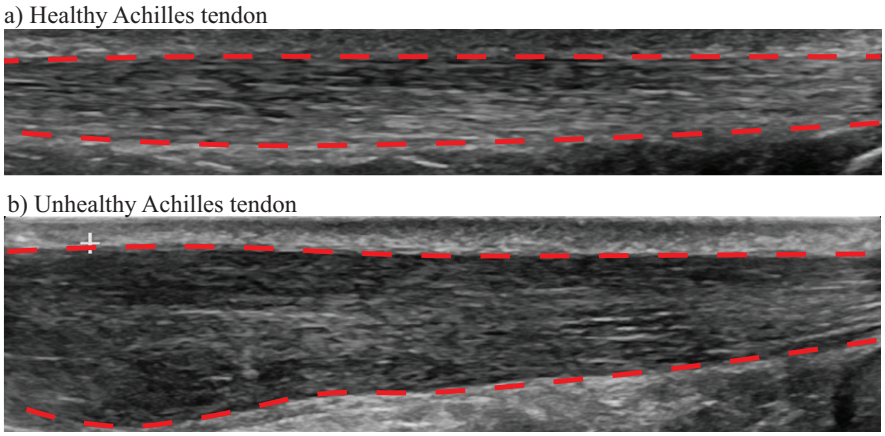


Figure 1.8: Longitudinal greyscale ultrasound images of an Achilles tendon (tissue between red dashed lines). (a) Healthy image displaying uniform pattern of light grey lines. (b) Unhealthy image displaying thickening of the tendon, loss of homogeneous structure, and increasing spacing between collagen fibres.

tendinopathy severity (Docking et al. 2015, Hirschmüller et al. 2012) and hence the disruption to the normal greyscale texture must be evaluated. In symptomatic individuals, radiologists are able to reliably detect deviations from healthy tissue texture on US (Warden et al. 2007), however, quantifying and determining the significance of these changes poses a challenge (Docking et al. 2019b). The clinical interpretation of tendon images, in consideration of a diagnosis of tendinopathy, can be considered as a visual texture-based segmentation of the tendon image generated by the radiologist. A wide variety of machine learning approaches have been investigated to provide objective texture-based segmentations of medical images (Sharma et al. 2010) and could provide a quantifiable adjunct for radiology reporting.

1.8 Machine Learning Methods for Medical Image Segmentation

Relative to the abundance of machine learning approaches available for medical image segmentation, few have been trialled for tendons. Machine learning is a branch of artificial intelligence which utilises algorithms that enable the machine to assimilate data and draw conclusions from, or form its own predictive rules based on, that data. In this way, the machine is said to *learn* from the data. Machine learning can be used for both image classification and segmentation. Classification involves labelling at the image level, for example classifying a set of tendon images into *healthy* and *tendinopathic*. Segmentation of an image involves labelling the image at the pixel level to divide the image into some set of chosen subgroups, for example, segmenting the tendon image into *healthy* and *tendinopathic*, regions. Segmentation of images through machine learning can be based on a range of different attributes such as colour, grey-level intensity, or texture (Kumar et al. 2012). The Random House dictionary of the English language refers to *texture* as the description of the appearance of an object characterised "by the size, shape, density, arrangement, proportion of its elementary parts" (Urdang 1968). We focus on texture-based segmentation in this work, as we expect changes in texture to correlate with microstructural tendinopathic changes.

The level of *supervision*, in the context of machine learning, refers to what level of insight the data provides to the machine learning algorithm. Different levels of supervision can be used for machine learning, depending on data availability. Fully supervised learning requires a dataset of input-output pairs in order for the machine to form a set of predictive rules that allow it to predict the output for new input data. Unsupervised learning is undertaken when no output data is available, and instead we want the machine to detect new patterns in the data (clustering methods usually fall into this category) (Jordan et al. 2015). Weakly supervised learning is utilised when the output data is imprecise compared to the desired output

predictions required of the machine (Zhou 2018). In the context of segmenting tendinopathic and healthy tendons, fully supervised learning would require a set of manually segmented (labelled at the pixel level) gold standard/ground truth tendon images. Weakly supervised learning would entail the machine learning to segment tendon images from a dataset of labelled *healthy* and *tendinopathic* images but without a ground truth segmentation of the images (labelled at the image level only). Unsupervised learning would involve the machine learning to segment the images in the absence of any ground truth segmentation or labelling of the images. If we aim to provide an adjunct which builds on the current reliability of ultrasound, the segmentation should be unsupervised or weakly supervised, allowing us to identify patterns in the dataset which are undetectable by human analysis.

The most common machine learning approaches to texture recognition can be broadly separated into three categories: filtering approaches, statistical approaches and structural approaches. Filtering theory is a well established means of extracting texture information that is based on accepted neurophysiological principles. In 1989 Silverman et al. (1989) demonstrated that the human visual cortex[6] filters incoming information detected by the human eye, with different neurons tuned to different spatial frequencies and orientations. From this work, filtering theory developed, suggesting that this human visual process can be reproduced computationally by convolution of an image with a bank (set) of linear filters (a single filter is displayed in Figure 1.9) and then applying a set of further non linear operations (Zhu et al. 1998, Jain et al. 1991). This mathematical operation generates a vector of new data points assigned to each pixel, with the dimensions equal to the number of filters

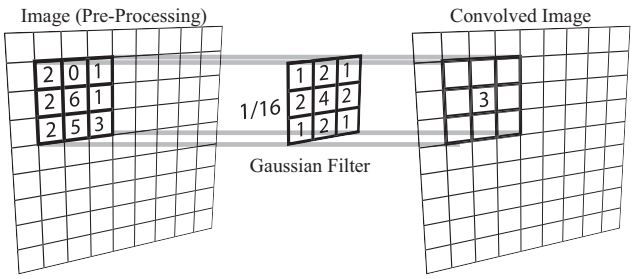


Figure 1.9: Convolution of an image with a 3-by-3 Gaussian filter. The value at the pixel given in the convolved image is calculated by $(1/16)\cdot(1\cdot 2+2\cdot 0+1\cdot 1+2\cdot 2+4\cdot 6+2\cdot 1+1\cdot 2+2\cdot 5+1\cdot 3)$.

[6]The part of the brain responsible for visual processing.

applied. Statistical theories for texture modelling suggest that textures are generated by some underlying stochastic process. Texture models are then usually defined by a joint probability distribution of some chosen texture features, with the model parameters serving to characterise unique textures. Structural approaches to modelling assume that textures are formed by a set of primitive features which occur in a repeated or regular pattern. Rather than utilise filtering, stochastic, and structural approaches in isolation, advances in texture modelling have come from utilising a combination of these approaches (Kumar et al. 2020). We now provide several examples of these approaches which have been applied to medical image segmentation.

The grey-level co-occurrence matrix (GLCM) is an older statistical approach to texture analysis and has been used as a feature extraction method to coarsely segment tendon images (Schneebeli et al. 2017, Nadeau et al. 2016, Benrabha et al. 2017). The GLCM provides a description of the spatial relationship of pixels with similar intensities and can be used to gain information such as the homogeneity of grey-levels. To our knowledge, the GLCM has only been used for image classification purposes (Nadeau et al. 2016) or for coarse detection of a region of interest (a square window over a large section of the image was identified) (Benrabha et al. 2017). While the GLCM has not been used to derive a full segmentation of the tendon image to detect tendinopathic regions, the GLCM has been used to successfully differentiate between healthy and tendinopathic tendons when applied at the image level (Lalumiere et al. 2020), suggesting this feature extraction method should be trialled for full segmentation. GLCM features have also been shown to have a high correlation with collagen morphology in blood vessels on microscopy (Mostaço-Guidolin et al. 2011), and hence the GLCM may have promise in detecting collagen disruption in tendon.

Stochastic model-based approaches are another statistical approach to texture segmentation that have made progress over the last decade. Stochastic model-based approaches have not been used for tendon images, except in edge detection (Chen et al. 2011, Chuang et

al. 2014). Model-based approaches consider the entire image and its associated segmentation as statistical realisations. A popular approach to stochastic segmentation is to consider pixel intensities as realisations of a Gaussian mixture distribution, a population formed from sub-populations of Gaussians, and the associated pixel segmentation labels are realisations from a multinomial distribution (Ilea et al. 2011). Markov random fields are a popular means to incorporate additional structural information into statistical models and have been coupled with Gaussian mixture modelling frameworks to successfully to segment brain and breast images (Azmi et al. 2011, Zhang et al. 2000). Whilst pure Gaussian mixture modelling approaches assume adjacent pixel class labels are independent, Markov random fields consider the entire image (pixel intensities and corresponding labels) as an interconnected network of dependent random variables. Mathematically, incorporating a Markov random field approach encourages adjacent pixels to be assigned the same class label (Rue et al. 2005).

Wavelet and curvelet methods, which use filter banks termed *wavelet filter banks* and *curvelet filter banks* respectively, are filtering based approaches that have been used to automate the segmentation of tendon tears on ultrasound (Fernández et al. 2002, Kim et al. 1998, Gupta et al. 2014). The difficulty of filter-based approaches lies in the optimal choice of the filter bank and filter size. There are a multitude of filter types available which are able to extract different spatial information and there is no one optimal choice for texture analysis (Bhosle et al. 2013). Advances have been made in the image analysis of other organs by combining filtering approaches with statistical descriptors to account for the randomness inherent in texture (Varma et al. 2005). *Texton*-based methods use clustering methods to define a set of exemplar filter bank responses/vectors. After applying a set of filters to the image and generating a filter bank response for each pixel, clustering is performed to identify the exemplar set of responses (the cluster centres - termed *textons*) and all pixels are then reassigned the closest exemplar filter bank response. A statistical component can then be incorporated by utilising a frequency histogram of textons in some small window around each pixel (Varma et al. 2005). This approach essentially uses filters to extract the repeating

subunits that comprise a texture and then utilises a histogram to model the texture by capturing how often these subunits repeat. As such, it can also be considered as incorporating a structural approach to texture analysis.

Deep learning has recently gained popularity in tendon image analysis. Deep learning methods, in the form of convolution neural networks, can be considered as another filter-based approach to image analysis which removes the problem of having to choose the correct filters (as the algorithm chooses the optimal set of filters). Convolution neural networks use a bank of filters and then apply a set of non-linear operations. They are able to extract a range of features from the image, such as pixel intensity, texture features, or edges. Such classically black box methods are usually used for image classification and usually require full supervision (a set of input-output data for training the model) (Jahanifar et al. 2020, Sezer et al. 2019). Deep learning methods have been used for tendon image segmentation in a fully supervised manner (Alzyadat et al. 2020). However, convolution neural networks are likely to become increasingly relevant, as models trained on only image-level labelled data can be coupled with emerging methods where post-hoc analysis is used to determine the regions within the image that most greatly affected the algorithms image-level classification assignment (Wyburd et al. 2021). That is, there are weakly supervised methods that allow us to determine which region of the tendon that the machine deemed as tendinopathic. However, the reliability of such methods is not yet optimal (Jung et al. 2021). Additionally, other key limitations of CNN methods include the large size of the data set required and the lack of control over how the machine carries out classification.

There is no one-size-fits-all approach for the texture analysis of medical images, as the imaging modalities and machine learning algorithms themselves have their own set of limitations. In the setting of weak or unsupervised approaches, there is benefit to exploring multiple approaches, as results can then be validated by comparison between approaches. Given the small number of machine learning approaches trialled for tendon image analysis, compared

to the number available, further investigation into this area is justified. To our knowledge, there are no studies which have investigated weakly supervised machine learning techniques to fully segment (labelling each pixel) the tendon into tendinopathic and healthy regions. This would allow us to both detect patterns or features of tendinopathic images, which may be missed by the radiologist, as well as rapidly quantify the proportion of the tendon which is deemed tendinopathic. This thesis will trial the use of both the GLCM and textons, pairing these methods with a stochastic representation of the images in terms of a Markov random field - due to the success of Markov random field approaches in other areas of medical image segmentation in the setting of noisy ultrasound images (Azmi et al. 2011, Zhang et al. 2000). We are motivated to use the GLCM due to the previous success of this approach in detecting collagen disruption in other tissues and in differentiating between tendinopathic and healthy tendons at the image level (Lalumiere et al. 2020, Mostaço-Guidolin et al. 2011). Furthermore, the GLCM output has a high level of interpretability, which is further outlined in Chapter 4. In contrast, because textons-based approaches provide a higher-dimensional output, they are less readily interpretable but may serve to capture additional texture information compared to the GLCM. Textons have also been widely used in medical image segmentation and shown success in this field (Morgado et al. 2013, Acharya et al. 2019), including when integrated with a Markov random field model (Petroudi et al. 2006).

1.9 Hypothesis and Objectives

This thesis seeks to use mathematical modelling to investigate how the intratendon mechanical environment which occurs with loading contributes to the structural changes seen in midportion tendinopathy. We investigate midportion tendinopathy, as little is known about how damage occurs in the absence of extrinsic compression. We hypothesise that large intratendon fluid induced stresses occur with high loading frequencies, disrupting tendon homoeostasis and leading to a reduction in permeability, due to increased proteoglycan deposition. We expect that if multiple loading bouts are also completed within a small time

period, that the effect will be compounded by a reduction in tendon stiffness, due to a loss of type I collagen. Conversely, we expect solid tensile strains to remain comparable between low and high loading frequencies, acting beneficially by stimulating cell synthesis of type I collagen. We expect this to lead to an increase in tendon stiffness for low-frequency loading but expect that, for high-frequency loading, competing effects from large fluid induced stresses will lead to a net loss of type I collagen and reduction in stiffness. We hypothesise that regions within the midportion that exhibit high fluid fluxes subject to high-frequency loading will correspond to regions which exhibit greater damage on imaging.

In order to investigate the above hypotheses, we develop a robust modelling framework which has several objectives. We first aim to develop and use a poroelastic model of tendon, governed by small strain theory, to determine how the mechanical environment of the tendon varies with different loading frequencies. We use a one- and two-dimensional setup and consider a system of partial differential equations which models flow through a linearly elastic porous material. We solve the system numerically using a finite difference scheme, as well as obtain a steady-state analytical solution for the one-dimensional case to further investigate the behaviour of the system. In the latter case, to further investigate the effect of high loading frequencies, we consider the limit as the loading frequency tends to infinity and obtain a solution for a boundary layer near the point of applied load. To mimic tendinopathic damage, we impose a local reduction in stiffness and/or permeability within the midportion and investigate local effects of these changes on the mechanical environment.

Following this, we seek to investigate changes in stiffness and permeability in response to mechanical stimuli occurring with loading. To do this, we build on the poroelastic model to derive a long term adaptation model in which we model both positive and maladaptive changes in the material properties in response to mechanical stimulation with loading. We consider the stiffness and permeability as a surrogate for type I collagen and proteoglycan content respectively, and implement a set of time-dependent phenomenological rules

that govern material property changes within the tendon in response to loading induced mechanical stimulation. We simulate a series of loading bouts over 14 weeks and contrast the adaptation model predictions with clinical knowledge regarding the tendon's response to damage-inducing and rehabilitative loading over this time frame.

Thirdly, to determine the spatial pattern of changes in tendinopathy, we develop a machine learning approach for tendon segmentation, using weakly supervised learning on *healthy* and *tendinopathic* labelled tendon images. We aim to contrast the findings from this analysis with results from previous chapters, using the poroelastic and adaptation models to provide mechanistic insight as to why damage occurs in certain regions within the midportion.

1.10 Key Contributions

This thesis makes several novel contributions in terms of mathematical approaches to understanding tendon disease. Firstly, we utilise a poroelastic model to predict the mechanical environment of the tendon, specifically contrasting the environment for damage-inducing and rehabilitative forms of loading which has not been accounted for in previous poroelastic modelling work of tendon. We also account for localised changes in the material properties at the midportion of the tendon, which has not been accounted for in previous poroelastic models of tendon. Secondly, we build an adaptation model which incorporates changes in both the stiffness and permeability, serving as surrogates for changes in the type I collagen content and proteoglycans respectively, in response to loading. Both tensile strain and fluid flux are drivers for these changes. This is in contrast to previous work which has only modelled fluid pressure driven changes in the permeability (also as a surrogate for proteoglycan content) (Wren et al. 2000). We use the adaptation model to simulate damage-inducing and rehabilitation loading regimes over a period of 14 weeks, and investigate the effect of recovery time between loading. Finally, using the grey-level co-occurrence matrix, textons and Markov random field theory, we implement a machine learning approach for image analysis which we

apply to tendons for the first time.

1.11 Thesis Structure

In Chapter 2 we develop a poroelastic model to investigate how loading frequency affects the intratendon mechanical environment that occurs with exercise. Specifically, we investigate how the loading frequency affects tendon strains, fluid flux, and pressure, since tendon cells are known to respond to these stimuli. We also evaluate the impact of a localised reduction in tendon stiffness or permeability on the mechanical environment occurring with low- and high-frequency loading. We use this model to infer which mechanical stimuli may be implicated in tendon disease and rehabilitation, and how local material property changes could modulate these stimuli.

In Chapter 3 we develop an adaptation model to investigate how positive and maladaptive changes occur over time with loading. We couple the poroelastic model developed in Chapter 2 with phenomenological modelling of material property changes in response to loading. We evaluate the effect of recovery time between loading and the competing effects of changes in stiffness and permeability on the mechanical environment. Informed by previous experimental work, we prescribe two different sets of phenomenological rules for changes in the tendon stiffness and permeability, in response to local mechanical stimuli that have occurred during a loading bout. We contrast the results for the two sets of phenomenological rules for semi-acute (days) material property changes in response to loading, and use the model predictions to support and challenge previous assumptions regarding material property changes in response to load.

Motivated by a need to further understand the spatial pattern of damage in tendinopathy, in Chapter 4 we utilise machine learning techniques to analyse ultrasound imaging data of the Achilles tendon. Tendinopathic changes in structure are analysed through a texture-based image segmentation approach. We trial two algorithms, utilising a model-based statistical

approach, paired with either texture features derived from the grey-level co-occurrence matrix (GLCM) or from convolving the image with a set of linear filters (texton-based approach). The results provide us with a data set constituting two-dimensional maps of changes in tendon structure for tendinopathic tendons. We contrast these results which with the spatial pattern of structural changes predicted our adaptation model in Chapter 3.

CHAPTER 2

A Poroelastic Model for Tendon

2.1 Synopsis

In this chapter we develop a small strain poroelastic model for energy storing tendons under load. The poroelastic model is used to characterise differences in the local mechanical environment when the tendon is subject to slow *rehabilitative* or fast *damage-inducing* physiological loading regimes. We also determine how a local reduction in the permeability or stiffness of the tendon alters the local mechanical environment when subject to these loading regimes. We are motivated by the observation that rehabilitation regimes involving low-frequency high-magnitude tensile cyclic loading of the tendon, for example, strength training involving slow contractions of the associated muscle against high resistance, reduce pain in tendinopathy. In contrast, high-frequency high-magnitude tensile cyclic loading, a common feature of sporting activities such as running and jumping which are aetiological factors for Achilles and Patellar tendinopathy, cause maladaptive changes in the tendon constituents and associated pain (Malliaras et al. 2013, Malliaras et al. 2017). Experimental evidence suggests that these maladaptive changes in the tendon constituents lead to a local reduction in the stiffness and permeability of the tendon (Arya et al. 2010, Cook et al. 2012). By using a poroelastic model of the tendon to characterise the mechanical environment within tendons subject to rehabilitative or damage-inducing loading regimes, we infer which local mechanical stimuli may be responsible for maladaptation and which may promote positive adaptation.

Furthermore, we investigate how localised reductions in the stiffness and permeability modulate the mechanical environment that occurs with rehabilitative or damage-inducing loading, and hence whether tendinopathic changes reinforce or mitigate the tendon's response to these forms of load. Our findings show that the fluid flux is higher for high-frequency loading, when compared with low-frequency loading, suggesting high shear stress as a potential cause for maladaptation. The tensile axial strain is found to remain comparable between low and high loading frequencies, indicating that the axial strain, when considered in isolation, is less likely to be a key determinant in the response of tendons to different loading frequencies. However, the results suggest that a high tensile axial strain to flux ratio may explain the positive adaptive response seen with low-frequency loading. A local reduction in the permeability reduces the flux, indicating this change may be a protective mechanotransduction response to the cells sensing high fluid shear. The model predictions are sensitive to parameter values within the ranges reported experimentally, indicating that further experimental work is required to generate more reliable parameter estimates and hence caution should be taken when drawing conclusive qualitative inferences from tendon modelling at this stage. For a subset of values for the Poisson's ratio and degree of anisotropy in the permeability, we predict larger compressive transverse strains to occur with high loading frequencies, suggesting this as an alternate mechanism for damage.

2.2 Chapter Outline

We start by reviewing existing modelling approaches for the tendon, as well as models of similar porous biological structures such as cartilage and bone. We also present the small strain poroelastic theory that we adopt in our modelling approach. We then outline the mathematical model for tendon subject to periodic tensile loading. The tendon is modelled as a long and thin poroelastic material; at one end the tendon is attached to muscle and a tensile force is applied, whilst at the other end the tendon is fixed to bone. A one-dimensional reduction is first used to gain basic insight into the relationship between loading frequency,

material properties, and the local mechanical environment within poroelastic structures. Next we develop and analyse a two-dimensional poroelastic model of the tendon. We focus on midportion (in terms of the axial/longitudinal dimension) tendinopathy, since this is a common site of damage and it is less clear how a reduction in stiffness or permeability would affect the mechanical environment within this tensile region, than at the tendon insertion, where extrinsic compression is known to also occur (Cook et al. 2012). We evaluate the effect of the loading frequency, and localised reductions in the stiffness and permeability, on the mechanical environment at the tendon midportion. Due to uncertainty regarding the values of the Poisson's ratio of tendons reported in the literature, as well as the degree of anisotropy in the permeability, we also investigate the sensitivity of our results to changes in these parameters.

2.3 Literature Review

2.3.1 Fluid Models of Tendons

Both poroelastic and poroviscoelastic modelling have been used to further enhance our understanding of tendon biomechanics and disease. The majority of these models were developed utilising finite element software (Lavagnino et al. 2008, Butler et al. 1997, Ahmadzadeh et al. 2013), in contrast to the analytic and finite difference methods employed here. Several authors (Reese et al. 2010, Ahmadzadeh et al. 2013, Lavagnino et al. 2008) have developed their models in keeping with *ex vivo* experimental results which suggest that the Poisson's ratio[1] of tendon exceeds the isotropic limit of 0.5 (Han et al. 2000, Hannafin et al. 1994). A Poisson's ratio which exceeds this isotropic limit[2] suggests a loss of volume and hence fluid must be expelled with tension of the tendon, behaviour which has obviously drawn interest

[1]The negative of the ratio of transverse-to-axial strain.
[2]This is physically possible but requires the material to be anisotropic, with greater compressive strains occurring in the transverse dimension relative to the axial tensile strain.

from these authors.

Butler et al. (1997) utilised a finite element package to model interstitial fluid flow in tendons. They modelled the tendon as an axisymmetric cylinder. Fluid flow was assumed to follow Darcy's law and they parametrically explored the effect of global permeability on shear rate and fluid pressure. A set displacement was applied at both the axial and radial boundaries, based on experimental work on rat ligaments (which have similar properties to tendon). A longitudinal symmetry condition was imposed and both the fluid and solid phases were assumed to be incompressible. They showed that a reduction in radial to axial permeability ratio resulted in a notable increase in the pressure and shear rate. However, as noted by the authors, their assumption of zero fluid flux across the radial boundary may have led to errors in their results. The epitendon, connective tissue which encases the transverse boundary of the tendon, is continuous with the interior and encases smaller structures (fascicles) within the tendon as well (Kaya et al. 2019). Hence, it may be more appropriate to set the radial permeability at the radial boundary to that of the interior, rather than imposing a zero flux condition. Another limitation was that the displacement at both boundaries was prescribed based on experimental results on a single rat ligament. As such, the external flux was indirectly prescribed, as it should be directly proportional to the prescribed volume change. Since the fluid flux and permeability are related, this may have affected the ability of the model to accurately capture fluid trends related to changes in permeability.

Lavagnino et al. (2008) utilised a finite element modelling package to develop a multi-scale model for tendons under load. In contrast to Butler et al. (1997), they assumed a uniform constant permeability throughout the tendon, and investigated how shear stress and matrix-induced deformation are transferred to the cell. Similar to Butler et al. (1997), they prescribed an axial displacement, however no results were directly conveyed about the transverse displacement. Presumably, since their global matrix was prescribed having a large

Poisson's ratio of greater than 0.5, a relatively large transverse deformation occurred. In contrast to several authors, they did not build a mechanistic explanation for this large Poisson's ratio into their model. They paired their multiscale modelling with experimental work, utilising their model to predict appropriate local stress and strains in keeping with physiologic loading, which they then applied to cells *in vitro*. They demonstrated that peak shear stress increased with increasing strain rate and magnitude, having the strong potential to modulate cellular collagen production. However, a key limitation of their work is that the global strain rates applied in their work were slower than those which are seen to cause damage (Bohm et al. 2015).

Ahmadzadeh et al. (2013) combined finite element and shear-lag modelling approaches in order to develop a poroelastic model for tendons that predicts an effective[3] Poisson's ratio of the mixture which exceeds the isotropic limit. Shear lag models consist of a series of collagen fibres with glycosaminoglycan chains (GAG) serving as interfibrillar linkers between adjacent fibres. These GAG chains act as small springs between the fibres, providing a force that encourages fibres to remain in parallel with loading. The tendon was modelled as a poroelastic extracellular matrix with fibres and linking GAG structures embedded. Whilst the fibres and matrix were assumed to have a Poisson's ratio of 0.3, the shear-lag component introduced a fluid expulsion mechanism which allows for the macroscopic Poisson's ratio of the mixture to exceed 0.5. Shear-lag models suggest that, because of the role of GAGs as interfibrillar linkers, GAG depletion would serve to reduce tendon stiffness (Ahmadzadeh et al. 2013). However, despite there being a known increase in GAG content in tendinopathy (Parkinson et al. 2011), there is moderate evidence that tendinopathy results in a reduction rather than increase in tendon stiffness (Arya et al. 2010). Furthermore, there is reasonable evidence that GAG depletion does not alter tendon stiffness (Fessel et al. 2011).

[3]Constant value which is only valid for the range and type of strains evoked. For example, it may differ between tension and compression.

A larger range of values for the Poisson's ratio have been recorded experimentally (Han et al. 2000, Hannafin et al. 1994, Gatt et al. 2015). At the extremes, Reese et al. (2010) presents a model that predicts the Poisson's ratio greatly exceeding 0.5 due to volume loss. In contrast, the experimental work of Gatt et al. (2015) suggests that the Poisson's ratio is slightly negative, making the tendon auxetic (expands laterally with axial tension). A potential issue with the previous modelling work (Ahmadzadeh et al. 2013, Reese et al. 2010, Khayyeri et al. 2016, Lavagnino et al. 2008) which has been developed in keeping with large Poisson's ratios reported in previous *ex vivo* experimental work (Han et al. 2000, Hannafin et al. 1994), is that the the validity of these experimental studies has been brought into question (Carniel et al. 2019, Firminger et al. 2021). Firminger et al. (2021) reproduced the experimental set ups of Han et al. (2000) and Hannafin et al. (1994), and demonstrated that the Poisson's ratio is sensitive to the clamping technique used to fix the tendon explants and the direction the transverse strain measurement is taken. Recent *in vivo* measurements have shown that healthy tendons remain isovolumetric immediately following loading (Merza et al. 2021), which contradicts the suggestion that a fluid expulsion mechanism is present.

Several hyperelastic biphasic models have also been used to model the human tendon (Khayyeri et al. 2016, Khayyeri et al. 2015, Bajuri et al. 2016). In these structural constitutive models, the global tendon response is governed by the behaviour of its individual components. For example, Khayyeri et al. (2015) modelled the solid matrix as a set of Maxwell elements and hyperelastic springs. Such models are useful in investigating the collagen structure at the microscale, and how these components influence macroscopic tendon mechanics. The introduction of Maxwell elements also allows for the incorporation of viscoelastic behaviour. However, these type of models also introduce additional parameters that are difficult to validate experimentally. Given that tendons generally exhibit small strains, and operate primarily in the linearly elastic regime when larger forces are applied (Sensini et al. 2018), it is unclear whether this additional complexity is needed.

Despite the abundance of poroelastic models developed for tendons, further work is needed in order to advance our understanding of how tendinopathy develops and progresses in relation to loading. Much of the previous modelling work has either utilised a finite element modelling package to model global tendon behaviour or has incorporated constitutive equations at the microscale to explore the collagen mechanics at this level. These models certainly play a role in our understanding of collagen mechanics, however, there is room for simpler models with fewer constitutive relations to further our understanding of the effects of poroelasticity with physiological loading. Whilst many of these models have utilised in vitro and *ex vivo* results to pair with or guide their modelling, results from clinical tendon research, where we have made great strides in recent years, have not been incorporated to the same degree. Since much of the previous poroelastic modelling work has not been coupled with current knowledge of the impact of different loading frequencies on tendons in the clinical setting, it is still unclear which intratendon mechanical stresses are implicated in the maladaptation which occurs with high loading frequencies. Furthermore, to our knowledge, no one has yet utilised a poroelastic model to investigate the potential effects of the localised material property changes that have been proposed to occur with midportion tendinopathy. If we are to advance our understanding of tendon disease through poroelastic modelling, our approach must be appropriately guided by both clinical and laboratory findings. This gap in pairing modelling work with clinical research is something we address here.

2.3.2 Poroelastic Small Strain Models

Whilst the approach we choose to take here is quite different from that of the previous modelling work on tendons, there are several models of other porous structures that motivate and offer a comparison to our work here. Work in cartilage modelling is extensive and there has been a strong interest in rate-dependent poroelastic effects, as well as the impact of heterogeneity in the material properties on the mechanical environment. Models of bone and more general models derived from Biot's theory of poroelasticity have also been useful in

formulating our approach.

Armstrong et al. (1984) explored a model for the unconstrained compression of cartilage. Two plates applied an axial load to a poroelastic cylinder with fluid allowed to leave radially. The plates were assumed to be impermeable and frictionless, and the axial strain was assumed to be independent of the axial coordinate. Thus the key problem was reduced to one in only the radial direction which they could solve analytically for an applied ramped load. They investigated how the fluid pressure and stress-strain behaviour varied with the rate of ramped loading. The response in their model consisted of three phases: an initial response, a transient response and a steady-state response. They demonstrated that the behaviour for unconfined and confined compression is quite distinct, with unconfined compression allowing for an instantaneous deformation of the matrix, leading to a subsequent recoil of the matrix and fluid exudation in the following transient phase. The transient state was controlled by the interstitial fluid flow, with the length of this phase controlled by the classic poroelastic timescale, which is in turn dependent on the aggregate modulus, length scale and permeability. When the ramped loading was performed slowly, the interstitial fluid pressure contributed little to the load support. Conversely, when the ramped loading was performed at a very rapid rate then the material behaved similar to a single phased elastic material. They showed that in the equilibrium response, since the load is entirely carried by the solid skeleton, the deformation is largely dependent on the aggregate modulus of the solid.

A very similar set up to that of Armstrong et al. (1984) was used by Kameo et al. (2008), who imposed cyclic squeezing of a poroelastic structure and similarly solved for flow and pressure changes in the perpendicular direction to loading. The material was assumed to be isotropic with a plane strain condition imposed and they investigated both the effect of the Poisson's ratio and loading rate in their model. Whilst much of their work was focused on the initial transient state which occurs at the start of cyclic loading, they also provide

solutions for the steady state (long time solution). When the drained Poisson's ratio was approximately equal to the undrained Poisson's ratio, indicating that the interstitial fluid pressure had minimal impact on solid deformation (i.e. weak fluid to solid coupling), lower magnitudes of pressure changes were observed across the material. With higher loading frequencies they demonstrated that sharp gradients in the pressure were observed close to the outer boundary and the phase shift between the pressure and forcing was greater.

Wang et al. (2001) utilised a biphasic one-dimensional model to explore the effects of imposing a depth-dependent aggregate modulus in cartilage. They suggested that a localised reduction in the aggregate modulus could potentially allow for finite strains to occur, and hence used a non-linear constitutive law which has been developed for compressed hydrated elastic tissues. It was shown that the importance of considering such heterogeneity in the aggregate modulus is dependent on what one aims to extract from the model. For example, in the case of predicting local cell stresses, the heterogeneity had a substantial impact. However, when taking surface to surface measurements of deformation, there was little difference between the homogeneous and heterogeneous case. Depth dependent variations in the material properties were also implemented in the work of Kafka (2002). Rather than directly incorporate heterogeneity into their macroscopic description, the effect of constituents at the mesoscale was considered in relatively high detail. In some ways this parallels some of the previous work on tendons, in which several constitutive equations at the microscale are considered in order to predict macroscopic behaviour.

Similar to cartilage and tendon, mechanotransduction, specifically involving fluid induced shear stress, is an important phenomenon that occurs in bone (Owan et al. 1997). Motivated by findings that even healthy bone tissue exhibits spatial variations in the permeability (Turner et al. 1999), Kameo et al. (2016) used a poroelastic model to investigate the effects of such spatial variation on fluid flow through bone. The model was composed of several layers, with each layer exhibiting a different permeability. An axial cyclic stress, with a

dimensionless frequency (scaled on the classical poroelastic timescale) of either $\tilde{\omega} = 10$ or $\tilde{\omega} = 100$, was imposed by two rigid impermeable plates. Similar to much of the prior work on cartilage, a symmetry condition was imposed and zero shear stress assumed throughout the poroelastic slab, reducing the fluid flow problem to one in the tangential direction to loading. A one-dimensional diffusion equation for the pressure in each layer was derived and continuity of the pressure and flux was imposed at the boundaries of each layer. They were able to then solve this problem analytically by means of a Laplace transform. Their results demonstrated that both the loading frequency and heterogeneity in the permeability had an effect on the spatial profile of the flux.

As part of their work comparing the effects of linear and large-deformation poroelasticity, MacMinn et al. (2016) gives a comprehensive description of the small strain poroelastic response. They modelled a general poroelastic material subject to a prescribed displacement or stress, work which is directly relevant to our problem and hence we seek to extend and further explore here. They provided a one-dimensional example of the classic consolidation problem, assuming that the stiffness is homogeneous and permeability deformation-dependent. In contrast to this work, we shall account for a spatially varying stiffness and permeability here, enabling us to model localised changes in material properties with damage. We also apply a cyclic loading regime, which can be solved analytically for long time, and evaluate the effect of loading frequency.

Whilst these models are derived from similar theory and use a similar set up to that which we intend to use here, there are key differences which prohibit direct extensions of their work to tendons. Firstly, in all cartilage models the load was applied at the bony interface, requiring that the fluid must flow perpendicular to the direction of load. As such, plane or homogeneous strain conditions were assumed in the direction perpendicular to load and the models focused on the flow behaviour perpendicular to loading. In the case of tendons, however, we expect the muscular insertion at which the load is applied to be relatively perme-

able. Furthermore, in keeping with the physical setting, previous work in cartilage modelling has imposed compressive loading. As tendons are, in contrast to cartilage, primarily tensile structures, we shall apply a tensile loading regime here. Finally, much of the work in cartilage has simulated either static loading or slow cyclic loading, where as our area of interest is primarily in the difference between slow and fast cyclic loading.

2.4 Small Strain Poroelastic Theory

The load magnitudes that tendons are subjected to with physiological loading are generally small, with strains of around 4-5% occurring for high-magnitude forms of tendon loading (Arampatzis et al. 2007, Bohm et al. 2015). Both *ex vivo* and *in vivo* experiments show that the stress-strain curve for tendons is approximately linear when forces consistent with physiological loading, such as running and jumping or rehabilitation exercises, are applied[4] (Maganaris et al. 2004, Seynnes et al. 2015). Additionally, the Young's modulus, a linear material parameter, is frequently used to characterise tendon stiffness (McKee et al. 2011, Arampatzis et al. 2007), suggesting that it is generally accepted that small-strain linear poroelastic theory is applicable to tendons.

When a force is applied to a poroelastic structure, not only does solid deformation affect fluid movement, but interstitial fluid pressures affect solid deformation. Poroelastic theory describes this fluid structure interaction between the solid and fluid components of a poroelastic material. We now introduce the reader to classic poroelastic theory originating from Biot's work in 1941 (Biot 1941). Much of this theory is also outlined in MacMinn et al. (2016), and we follow their approach to derive a linear flow equation relating the porosity and pressure, although in contrast to MacMinn et al. we account for a heterogeneous stiffness

[4] *Ex vivo*: Physiological loading is mimicked by imposing similar forces to *ex vivo* specimens. The force-length relationship is then recorded. *In vivo*: Ultrasound and force plate measurements capture the displacement and force respectively.

to describe the solid behaviour. We introduce the reader to theory pertinent to our model development here, and refer the interested reader to the *Fundamentals of Poroelasticity* by Detournay and Cheng (Detournay et al. 1993) for a more in depth explanation of poroelastic theory.

2.4.1 Nomenclature

For reference, the variable and parameter definitions used throughout this chapter are given in Table 2.1.

Table 2.1: Variable and parameter values for poroelastic model of tendon subject to tensile loading.

Variable	Definition	Parameter	Definition
$\boldsymbol{x}$=(x,y,z)	Spatial coordinates	L_0	Reference length
t	Time	W_0	Reference width
$\boldsymbol{u}$	Solid displacement	$\phi_{f,0}$	Initial porosity
$\boldsymbol{v}_s$	Solid velocity	$\boldsymbol{k}$	Permeability tensor
$\boldsymbol{v}_f$	Fluid velocity	μ	Fluid viscosity
ϕ_f	Porosity/fluid volume fraction	M	Oedometric modulus
ϕ_s	Solid volume fraction	Λ	Lamé's first parameter
$\hat{\phi}_f$	Normalised porosity	E	Young's modulus
p	Pressure	ν	Poisson's ratio
$\boldsymbol{\sigma}$	Total stress	$\boldsymbol{F}^*$	Applied force
$\boldsymbol{\sigma}'$	Effective stress	ω	Forcing frequency
$\hat{\boldsymbol{F}}$	Deformation gradient tensor	ρ_s, ρ_f	Solid/fluid density
J	Jacobian	ρ	Total density

2.4.2 Solid and Fluid Phases

We consider two phases: a porous compressible solid skeleton saturated with a single fluid. Denoting $\boldsymbol{x}$ as the Eulerian spatial coordinate and t as time, the volume of the solid or fluid phase per unit mixture volume, at a given spatial point and time, are denoted by $\phi_s = \phi_s(\boldsymbol{x}, t)$ and $\phi_f = \phi_f(\boldsymbol{x}, t)$ respectively. Since the tendon is assumed to be fully saturated, the fluid volume fraction ϕ_f is synonymous with porosity. The fully saturated assumption implies

$$\phi_s + \phi_f = 1. \tag{2.1}$$

We assume that the initial porosity is uniform, and denote this as the reference porosity $\phi_{f,0} = \phi_f(t = 0)$. For later use in relating the porosity and deformation, we define the normalised porosity (MacMinn et al. 2016)

$$\hat{\phi}_f = \frac{\phi_f - \phi_{f,0}}{1 - \phi_{f,0}}, \tag{2.2}$$

which represents the ratio of the change in fluid volume, or equivalently the pore space, relative to the initial solid volume fraction. When $\phi_f = \phi_{f,0}$, the normalised porosity is equal to zero and if the solid volume fraction then increases, corresponding to a decrease in the porosity ϕ_f, $\hat{\phi}_f$ takes a negative value. For simplicity, we assume the solid grains and fluid are individually incompressible so that ρ_s and ρ_f are constant. We use the term *solid grains* here to represent the constituents of the solid skeleton. We define the total density to be $\rho(\boldsymbol{x}, t) = \phi_s(\boldsymbol{x}, t)\rho_s + \phi_f(\boldsymbol{x}, t)\rho_f$.

2.4.3 Kinematics

We denote the solid displacement by $\boldsymbol{u}$, and the solid and fluid velocities by $\boldsymbol{v}_s$ and $\boldsymbol{v}_f$ respectively. The solid velocity is given by the material derivative of the solid displacement

$$\boldsymbol{v}_s = \frac{D\boldsymbol{u}}{Dt} = \frac{\partial \boldsymbol{u}}{\partial t} + \boldsymbol{v}_s \cdot \nabla \boldsymbol{u}, \tag{2.3}$$

where ∇ is the Eulerian gradient operator. The Jacobian provides a measure of local volume change[5] of the compressible solid skeleton, and is given by

$$J(\boldsymbol{x}, t) = \det(\hat{\boldsymbol{F}}), \quad \text{where} \quad \hat{\boldsymbol{F}} = (I - \nabla \boldsymbol{u})^{-1}. \tag{2.4}$$

Here $\hat{\boldsymbol{F}}$ is the deformation gradient tensor for the solid. Since the fluid and solid grains are individually incompressible, solid deformation occurs only through changes in the porosity, via fluid leaving or entering the mixture. As a result, since $1-\phi_{f,0}$ and $1-\phi_f(\boldsymbol{x}, t)$ represent the initial and current solid volume fractions, respectively, the porosity is directly related to the local volume change through the relationship

$$J = \frac{1 - \phi_{f,0}}{1 - \phi_f(\boldsymbol{x}, t)}. \tag{2.5}$$

[5]Given an initial configuration $\boldsymbol{X}$ and current configuration $\boldsymbol{x}$, such that the displacement $\boldsymbol{u} = \boldsymbol{x} - \boldsymbol{X}$, the term $(I - \nabla \boldsymbol{u})^{-1} = d\boldsymbol{x}/d\boldsymbol{X}$. The determinant of this matrix gives the volume of a parallelepiped formed by the column vectors - which is the volume change occurring as a result of deformation from the initial to current configuration.

2.4.4 Conservation Equations

Assuming there is no change of phase between the solid and fluid, conservation of mass is expressed in terms of the continuity equation for each phase as

$$\frac{\partial \phi_s}{\partial t} + \nabla \cdot (\phi_s \boldsymbol{v}_s) = 0, \quad \frac{\partial \phi_f}{\partial t} + \nabla \cdot (\phi_f \boldsymbol{v}_f) = 0. \tag{2.6}$$

For completeness we have included both continuity of the solid and fluid. However, we note that the relationship between the Jacobian and the solid deformation given in (2.5) implies that conservation of mass for the solid is satisfied.

We write the total stress $\boldsymbol{\sigma}$ in terms of the stress components supported by the solid and fluid

$$\boldsymbol{\sigma} = \phi_s \boldsymbol{\sigma}_s + \phi_f \boldsymbol{\sigma}_f. \tag{2.7}$$

For a fluid, the shear component of the stress is negligible relative to the volumetric component such that

$$\boldsymbol{\sigma}_f = -p\boldsymbol{I}. \tag{2.8}$$

In the setting of incompressible solid grains and a compressible solid skeleton, the fluid pressure leads to an isotropic reactive stress in the solid skeleton $-\phi_s p\boldsymbol{I}$ which does not contribute to deformation (MacMinn et al. 2016). Subtracting this component from the solid stress leads to

$$\phi_s \boldsymbol{\sigma}_s = \boldsymbol{\sigma}' - \phi_s p\boldsymbol{I}, \tag{2.9}$$

where $\boldsymbol{\sigma}'$ is known as the Terzaghi effective stress, the force per unit total area supported by

deformation of the solid skeleton (MacMinn et al. 2016). Using Equations (2.7) and (2.9), the total stress is given by

$$\boldsymbol{\sigma} = \boldsymbol{\sigma}' - p\boldsymbol{I}. \tag{2.10}$$

In the absence of body forces and neglecting inertia, mechanical equilibrium requires

$$\nabla \cdot \boldsymbol{\sigma} = \nabla \cdot \boldsymbol{\sigma}' - \nabla p = \mathbf{0}. \tag{2.11}$$

2.4.5 Constitutive Law for the Flow through a Porous Medium

We assume that the flow through the porous matrix is governed by the generalised Darcy's law (Biot 1955)

$$\phi_f(\boldsymbol{v}_f - \boldsymbol{v}_s) = \frac{-\boldsymbol{k}}{\mu}\nabla p, \tag{2.12}$$

where μ denotes the dynamic viscosity. The tensor $\boldsymbol{k}$ represents the symmetric permeability tensor. Assuming that the coordinate system is aligned with the principal axes of the permeability tensor, then, for a Cartesian coordinate system, $\boldsymbol{k}$ is given by the diagonal tensor (Cao et al. 2019)

$$\boldsymbol{k} = \begin{bmatrix} k_x & 0 & 0 \\ 0 & k_y & 0 \\ 0 & 0 & k_z \end{bmatrix}. \tag{2.13}$$

We consider k_x, k_y and k_z to be constants, except when we account for heterogeneity in the permeability, when they will be functions of the spatial coordinate, $\boldsymbol{x}$. Care must be taken when using values for the permeability derived from experimental work, as experiments often

measure $\boldsymbol{k}/\mu$, which is termed the hydraulic permeability and represents the ease with which the fluid can move throughout the pore structure. Whilst the hydraulic permeability $\boldsymbol{k}/\mu$ depends on viscosity, the permeability $\boldsymbol{k}$ is an intrinsic property of the porous material, depending on factors such as pore size and tortuosity.

2.4.6 Linear Flow Equation

We now utilise the derivation given by MacMinn et al. (2016) to obtain a linear flow equation relating the porosity and pressure in a small strain regime. Combining Equations (2.6) and (2.12) gives the nonlinear flow equation for the fluid

$$\frac{\partial \phi_f}{\partial t} + \nabla \cdot \left(\phi_f \boldsymbol{v}_s - \frac{\boldsymbol{k}}{\mu} \nabla p \right) = 0. \tag{2.14}$$

Equation (2.14) can be written in terms of the normalised porosity (2.2) as

$$\frac{\partial \hat{\phi}_f}{\partial t} + \nabla \cdot \left(\hat{\phi}_f \boldsymbol{v}_s - \frac{\boldsymbol{k}}{\mu} \nabla p \right) = 0. \tag{2.15}$$

Using (2.4)-(2.5), the normalised porosity can be given in terms of the solid strain

$$\begin{aligned} \hat{\phi}_f = \frac{\phi_f - \phi_{f,0}}{1 - \phi_{f,0}} &= 1 - \frac{1}{J} = 1 - \det(I - \nabla \boldsymbol{u}) \\ &\approx \nabla \cdot \boldsymbol{u}, \end{aligned} \tag{2.16}$$

where we have used the small strain assumption $\|\nabla \boldsymbol{u}\| \sim \epsilon \ll 1$ where $\|\cdot\|$ is the Euclidean norm and ϵ will be formally defined in terms of the driving force in Section 2.6.2. Equations (2.3) and (2.16) then imply that both $\hat{\phi}_f \ll 1$ and $\|\nabla \boldsymbol{v}_s\| \ll 1$. As such, the term $\nabla \cdot (\hat{\phi}_f \boldsymbol{v}_s)$ in (2.15) is quadratic in ϵ. Neglecting terms $\mathcal{O}(\epsilon^2)$ gives

$$\frac{\partial \hat{\phi}_f}{\partial t} - \nabla \cdot \left(\frac{\boldsymbol{k}}{\mu} \nabla p \right) = 0. \tag{2.17}$$

We proceed using the normalised porosity, dropping the hat for notational convenience.

2.4.7 Constitutive Law for the Solid Skeleton

For a nonlinear elastic material the stress-strain relation is often given in the form (Ogden 1997)

$$\boldsymbol{\sigma}' = f(\frac{1}{J}, \boldsymbol{e}), \tag{2.18}$$

where $\boldsymbol{e}$ is the Eulerian finite strain tensor. The small strain assumption $\|\nabla \boldsymbol{u}\| \ll 1$ allows us to linearise the Eulerian finite strain tensor

$$\boldsymbol{e} = \frac{1}{2}\Big(\nabla \boldsymbol{u} + (\nabla \boldsymbol{u})^T - \nabla \boldsymbol{u}(\nabla \boldsymbol{u})^T\Big) \approx \frac{1}{2}\Big(\nabla \boldsymbol{u} + (\nabla \boldsymbol{u})^T\Big), \tag{2.19}$$

where

$$\boldsymbol{\varepsilon} = \frac{1}{2}\Big(\nabla \boldsymbol{u} + (\nabla \boldsymbol{u})^T\Big) \tag{2.20}$$

denotes the infinitesimal strain tensor used in small strain theory. Similarly,

$$\frac{1}{J} = \det(I - \nabla \boldsymbol{u}) \approx 1 - \nabla \cdot \boldsymbol{u}. \tag{2.21}$$

As a result, many elasticity laws for finite deformations reduce to the classic linear elasticity law when quadratic terms in ϵ are ignored (MacMinn et al. 2016).

We assume the material is isotropic, and use Hooke's law, the classic linear constitutive relationship, to link the stress and strain for the solid skeleton:

$$\boldsymbol{\sigma}' = \Lambda tr(\boldsymbol{\varepsilon}) I + (M - \Lambda)\boldsymbol{\varepsilon}. \tag{2.22}$$

Here M denotes the oedometric modulus and Λ denotes Lamé's first parameter. The oedometric modulus is defined as the ratio of axial stress to axial strain when expansion in the transverse direction is prevented (Sawicki et al. 1998). In three dimensions the material parameters M and Λ can also be expressed in terms of the Young's modulus E and Poisson's ratio ν for the solid skeleton:

$$M = \frac{E(1-\nu)}{(1+\nu)(1-2\nu)}, \quad \Lambda = \frac{E\nu}{(1+\nu)(1-2\nu)}. \tag{2.23}$$

The Young's modulus for an elastic material is measured by calculating the slope of the linear portion of the stress-strain curve, in which the stress and strain are both taken along the axis of the applied load. The Poisson's ratio is given by the negative of the ratio of transverse strain to axial strain when a force is applied axially (for a three-dimensional structure the Poisson's ratio is measured separately for the two transverse dimensions). If a tensile applied force is accompanied by a contraction of the material then the Poisson's ratio will be positive.

For a poroelastic material there are two situations in which the material parameters are often measured: undrained or drained. In the drained case, the pore pressure is allowed to completely equilibrate, whilst in the undrained case, fluid pressures can develop within the material but fluid is prevented from leaving the mixture. The drained Poisson's ratio is always less than or equal to the undrained ratio (Detournay et al. 1993), and for incompressible fluid and solid grains is equal to 0.5. Since we are modelling the mechanical behaviour of the solid skeleton, we utilise the drained[6] Poisson's ratio to express the elastic behaviour of the solid here (Equation (2.23)), and since the solid skeleton is compressible this can be less than 0.5. In Appendix 2.A.1 we discuss the interpretation of the Young's modulus, Poisson's ratio, odeometric modulus and Lamé's first parameter in further detail.

[6]The 'drained' Poisson's ratio is often used synonymously with the 'dry' Poisson's ratio as both describe behaviour of the solid skeleton when pore pressures have no mechanical effect on the deformation (Steeb et al. 2019).

When considering a dimensional reduction, it is important to check whether assumptions regarding the third dimension lead to a modification of (2.23). In the case of a plane strain assumption, the relations given in (2.23) are preserved. We give further details of when this is not the case in Appendix 2.A.1. We note that in the one-dimensional case, Λ does not feature in (2.23) and hence only M is needed to describe the solid behaviour.

2.5 Problem Description

We predict and contrast the mechanical environment of tendons during *rehabilitative* and *damage-inducing* loading scenarios as described in Section 1.3.1. The parameters introduced here are based on prior *in vivo* and *ex vivo* measurements and are given in Table 2.2. Tendons are long and thin fibrous structures which are saturated with fluid (Jull et al. 2015). Ultrasound measurements are used to measure geometric parameters of the tendon (Kurihara et al. 2012, Maffulli et al. 1987, Yoo et al. 2007, Szaro et al. 2021). The resting length L_0 is generally an order of magnitude larger than the tendon thickness W_{x0} and width W_{y0}, with the exact ratio varying between tendon types. The cross section of the tendon is obround[7] (Figure 2.1). At one end, the tendon is attached to muscle and at the other end it is fixed to bone. These are termed the 'origin' and 'insertion' respectively. The cross section of tendon is surrounded by a thin layer of synovial fluid at viscosity μ (Grassi et al. 2000). Because muscles contain a large proportion of fluid (Granger et al. 1984) and muscle fibres transition into tendon fibres, we assume that fluid can move freely between the muscle and tendon. Only the transverse hydraulic permeability (k_x/μ or k_y/μ) has been measured within tendons, however there is evidence to suggest that the axial permeability (k_z/μ) may be greater than the transverse permeability (Federico et al. 2008). As such, we utilise the upper bound on the reported transverse permeability values (Lavagnino et al. 2008) as a reference value k_0/μ for the hydraulic permeability.

[7]A shape consisting of two semicircles connected by parallel lines.

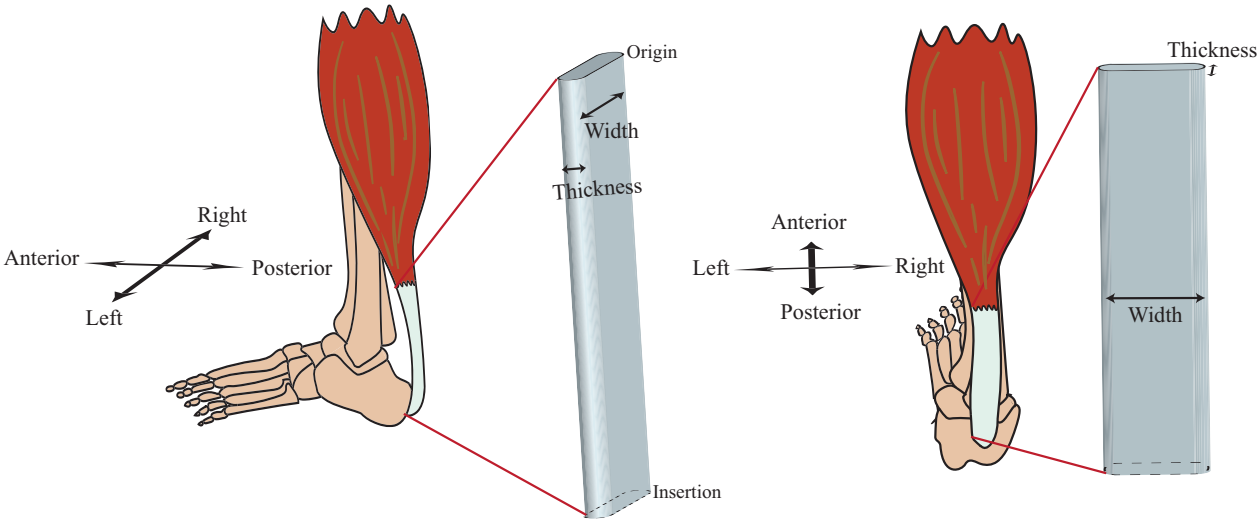


Figure 2.1: Schematic of the Achilles tendon taken in posterolateral (left) and posterior (right) view. The thickness is taken anterior to posterior and the width is taken in the frontal plane (left to right). The tendon is a long and thin obround poroelastic structure with its origin at the muscle and insertion at the bone.

Consistent with previous modelling work (Lavagnino et al. 2008), we assume the transverse boundaries and the origin of the tendon are surrounded by a bath of fluid at some constant unknown pressure. We assume that this constant pressure P_A is equal between the origin and transverse boundaries, suggesting that the fluid pressure within the muscle is equal to the pressure of fluid surrounding the tendon's transverse boundary. This is a simplifying assumption, as the pressure surrounding the tendon and within the muscle are unknown. Given muscle fibres are continuous with fibres of the tendon (the solid skeleton is continuous) (Thorpe et al. 2016b), we assume the volume fractions of fluid and solid are equal at the origin and that fluid can flow freely between the muscle and tendon. At the insertional end, since the density of bone is much greater than that of tendon (Schlesinger et al. 2020), we assume the bone represents a solid impermeable boundary to which the tendon is fixed. This can be interpreted as the tendon being attached to a fixed stationary plate. We assume that the axial strains occurring at the muscular origin are uniform, as if the tendon is attached to a fixed plate at the origin. We assume that the tendon can move freely at the transverse boundaries, as there is no source of compression or tensile stress (aside from potentially a small region near the origin - away from the midportion - where the tendon neighbours bone,

which we ignore for simplicity).

Damage-inducing and rehabilitative loading are approximated by a sinusoidal axial tensile force, applied at the muscular origin. The applied force causes a small time-dependent change in the tendon length from L_0 to $L(t)$. The frequency of this force ω varies between damage-inducing and rehabilitative loading but the magnitude is similar, and results in global strains of $4-5\%$ (Farris et al. 2012a, Rees et al. 2008, Bohm et al. 2014). The Young's modulus E and the Poisson's ratio ν describe the behaviour of the solid skeleton of the tendon. We do not account for directional dependence in these parameters. We choose values of the Poisson's ratio remaining within the isotropic limit ($\nu \leq 0.5$), following the lower end of the reference range reported and used in previous work (Thorpe et al. 2014, Lavagnino et al. 2008, Gatt et al. 2015). To represent damage, we impose a continuous localised reduction in the permeability and/or Young's modulus. For simplicity, and due to the lack of knowledge regarding changes in the Poisson's ratio with tendinopathy, we assume that the Poisson's ratio is homogeneous. Equation (2.23) implies that M and Λ are then linearly related through $\nu/(1-\nu)$[8].

[8]In the case of a linear isotropic material, the aggregate modulus is often used synonymously with the oedometric modulus as defined in (2.23) (Armstrong et al. 1984). As such, spatial variations in the parameter $M = M(\boldsymbol{x})$, or $E = E(\boldsymbol{x})$ when ν is held fixed, correspond to variations in the aggregate modulus as defined in previous work on cartilage (Wang et al. 2001).

Table 2.2: Parameter Values for Achilles Tendon (Lavagnino et al. 2008, Thorpe et al. 2014, Kurihara et al. 2012, Maffulli et al. 1987, Yoo et al. 2007, Szaro et al. 2021, Gatt et al. 2015).

Parameter		Value [Ref]	Parameter		Value [Ref]
Length (m)	L_0	$0.03 - 0.2$ [K,Y]	Hydraulic Permeability $(m^4/N \cdot s)$	k_0/μ	$5.5e^{-15} - 3.98e^{-14}$ [L]
Thickness (m)	W_{x0}	0.003 − 0.011 [M,Y,S]	Young's Modulus (GPa)	E	$0.9 - 1.1$ [K]
Width (m)	W_{y0}	0.014−0.031 [M,S]	Poisson's Ratio	ν	-0.1−0.49 [L,T,G]

2.6 Model Setup

We now develop a mathematical description of the human tendon subject to periodic loading (Figure 2.2). We utilise a Cartesian coordinate system $\boldsymbol{x} = (x, y, z)$ in which the long axis of the tendon is aligned with the z-axis ($\boldsymbol{e}_3$), while, in the transverse dimensions, the thickness and width are aligned with the x and y-axes ($\boldsymbol{e}_1$ and $\boldsymbol{e}_2$), respectively. We denote the tendon boundary by $\partial\Omega$ and explicitly refer to the transverse, muscular/original and fixed insertional boundaries by $\partial\Omega_t$, $\partial\Omega_m$ and $\partial\Omega_b$, respectively. We model the tendon as a poroelastic structure, subject to axial loads which induce small strains only, and use the small strain poroelastic theory (including variable definitions) outlined in Section 2.4. The solid displacement $\boldsymbol{u} = (u, v, w)$ represents the displacement of the porous tendon skeleton. We define $\boldsymbol{u}^{\perp} = (u, v)$ to represent displacements in the transverse dimensions.

The governing equations relating the displacement $\boldsymbol{u}$, normalised porosity ϕ_f and pressure p are given by

$$\phi_f = \nabla \cdot \boldsymbol{u} \tag{2.24}$$

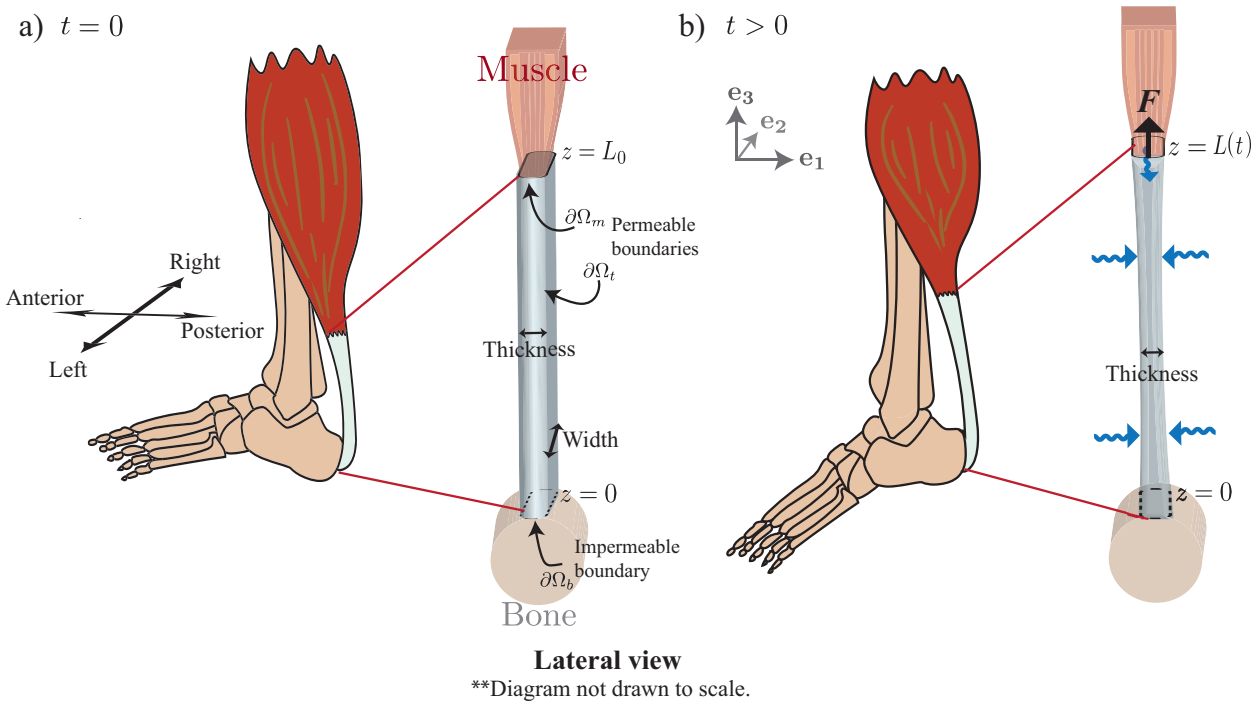


Figure 2.2: Model setup. A depiction of the Achilles tendon is given, however this setup is relevant to tendons in general. The tendon is attached to muscle at the original end and bone at the insertional end. The tendon is surrounded by a bath of fluid, with all boundaries permeable except at the insertion. An axial tensile force is applied at the muscular end, resulting in a concurrent transverse contraction of the tendon. The diagram has exaggerated the displacement for illustrative purposes and is not drawn to scale.

and

$$\frac{\partial \phi_f}{\partial t} - \nabla \cdot \left(\frac{\boldsymbol{k}}{\mu} \nabla p \right) = 0. \tag{2.25}$$

In terms of the strain, (2.22) can be written as

$$\boldsymbol{\sigma}' = \Lambda tr\left(\nabla \boldsymbol{u} + (\nabla \boldsymbol{u})^T\right) I + (M - \Lambda)\left(\nabla \boldsymbol{u} + (\nabla \boldsymbol{u})^T\right). \tag{2.26}$$

A positive normal strain component ($\nabla \boldsymbol{u}_{ii} > 0$) represents tension of the tendon in this direction ($\boldsymbol{e}_i$) whilst a negative normal strain represents compression. Combining Equations

(2.11) and (2.26), mechanical equilibrium relates the pressure and strain

$$\nabla p = \nabla \cdot \left(\Lambda \left(\nabla \cdot \boldsymbol{u} \right) I + \frac{M - \Lambda}{2} \left(\nabla \boldsymbol{u} + (\nabla \boldsymbol{u})^T \right) \right), \tag{2.27}$$

where $M = M(\boldsymbol{x})$ and $\Lambda = \Lambda(\boldsymbol{x})$.

At the origin we assume continuity of fluid pressure, zero transverse displacement, and that the axial load is taken by the solid skeleton

$$p = P_A, \quad \boldsymbol{u}^{\perp} = \boldsymbol{0}, \quad \iint_{\Omega_m} \boldsymbol{\sigma}' \cdot \boldsymbol{n} \, d\Omega_m = F^*(t) \boldsymbol{e}_z \ \text{ on } \partial\Omega_m, \tag{2.28}$$

where $F^*(t) = A - A\cos(\omega t)$. We use the convention that a tensile applied force is positive. The amplitude of the force A is chosen to produce strains consistent with damage-inducing and rehabilitative forms of loading whilst the frequency ω is varied to distinguish between these two forms of loading.

The insertional end is assumed to be impermeable to fluid and we assume zero displacement

$$\boldsymbol{v}_f \cdot \boldsymbol{e}_z = \boldsymbol{u} = \boldsymbol{0} \ \text{ on } \partial\Omega_b. \tag{2.29}$$

By definition of the normalised porosity (2.2):

$$\phi_f = 0 \ \text{ at } t = 0. \tag{2.30}$$

We refrain from prescribing boundary conditions at the transverse boundary until presenting one- and two-dimensional formulations of the problem.

2.6.1 Scaling

Letting tildes denote a dimensionless quantity, we non-dimensionalise as follows

$$\boldsymbol{x} = L_0\tilde{\boldsymbol{x}}, \qquad \boldsymbol{u} = L_0\tilde{\boldsymbol{u}}, \qquad \boldsymbol{k} = k_0\tilde{\boldsymbol{k}}, \qquad p = M_0\tilde{p} + P_A,$$

$$t = \frac{\mu L_0^2}{k_0 M_0}\tilde{t}, \qquad \omega = \frac{k_0 M_0}{\mu L_0^2}\tilde{\omega}, \qquad M = M_0\tilde{M}, \qquad \Lambda = \frac{\nu M_0}{1-\nu}\tilde{M},$$

$$\boldsymbol{\sigma}' = M_0\tilde{\boldsymbol{\sigma}}', \qquad \phi_f = \phi_f.$$

Here the permeability tensor and oedometric modulus, $\boldsymbol{k} = \boldsymbol{k}(\boldsymbol{x})$ and $M = M(\boldsymbol{x})$, are non-dimensionalised by k_0 and M_0, a scalar reference permeability and oedometric modulus. The parameter $\Lambda = \Lambda(\boldsymbol{x})$ is also scaled by M_0. The permeability k_0 is taken directly from Table 2.2, whilst the reference oedometric modulus M_0 is calculated using Equation (2.23) with reference values from Table 2.2 for the Young's modulus and Poisson's ratio.

We let $t_c = \mu L_0^2/(k_0 M_0)$, which represents the classical poroelastic timescale: the timescale over which migration of the fluid occurs. The variable $\tilde{\omega} = t_c\omega$ then represents the ratio of the classical poroelastic timescale to the loading timescale (ω^{-1}). Using reference values (Table 2.2) of 1 GPa for the Young's modulus, 3cm for the tendon length, a Poisson's ratio of 0.33 and a hydraulic permeability of 3.98 $e^{-14}m^4/N \cdot s$, the timescale t_c is approximately 14 seconds. In this case, for rehabilitative loading (HSRT) in which the dimensional loading frequency is at most 0.17 Hz (Beyer et al. 2015), then $\tilde{\omega} \leq 2$. Walking and jogging would then occur over ranges closer to $\tilde{\omega} \approx 10 - 20$ (Rowlands et al. 2007).

The small strain assumption allows us to solve the system on the undeformed domain $\partial\Omega(t = 0)$ (Appendix 2.A.2). We now proceed by dropping the tildes for notational convenience.

2.6.2 Dimensionless Governing Equations

The dimensionless governing equations are given by

$$\phi_f = \nabla \cdot \boldsymbol{u} \tag{2.31a}$$

$$\nabla p = \nabla \cdot \left(\Lambda \left(\nabla \cdot \boldsymbol{u} \right) I + \frac{M - \Lambda}{2} \left(\nabla \boldsymbol{u} + (\nabla \boldsymbol{u})^T \right) \right), \tag{2.31b}$$

with associated axial boundary and initial conditions

$$p = P_A, \;\; \boldsymbol{u}^{\perp} = \boldsymbol{0}, \;\; \iint_{\Omega_m} \boldsymbol{\sigma}' \cdot \boldsymbol{n} \, d\Omega_m = \left(\frac{A}{M_0 L_0^2} - \frac{A}{M_0 L_0^2} \cos(\omega t) \right) \boldsymbol{e}_z \;\; \text{on } \partial\Omega_m, \tag{2.32a}$$

$$\boldsymbol{v}_f \cdot \boldsymbol{e}_z = \boldsymbol{u} = \boldsymbol{0} \;\; \text{on } \partial\Omega_b, \tag{2.32b}$$

$$\phi_f = 0 \;\; \text{at } t = 0. \tag{2.32c}$$

We recall that we have left prescription of the transverse boundary conditions for latter sections, when presenting one- and two-dimensional formulations of the problem.

We let $\epsilon := A/(M_0 L_0^2)$, denoting the magnitude of the dimensionless applied force. Consistent with the linear small strain regime that has been applied, the magnitude of the dimensionless applied force $\epsilon \ll 1$. Considering an expansion in ϵ:

$$\boldsymbol{u} = \boldsymbol{u}_0 + \epsilon \boldsymbol{u}_1 + \epsilon^2 \boldsymbol{u}_2 + ..., \tag{2.33}$$

$$p = p_0 + \epsilon p_1 + \epsilon^2 p_2 + ..., \tag{2.34}$$

$$\boldsymbol{\sigma}' = \boldsymbol{\sigma}'_0 + \epsilon \boldsymbol{\sigma}'_1 + \epsilon^2 \boldsymbol{\sigma}'_2 + ..., \tag{2.35}$$

it is easy to see from the forcing condition given in Equation (2.32a) that the problem at leading order in ϵ is trivial, as there is no force driving the system. Hence, we proceed to

solve for the problem at first order in ϵ. We note that results are plotted for the first order solutions $\boldsymbol{u}_1$, p_1 and $\boldsymbol{\sigma}'_1$, as opposed to $\epsilon\boldsymbol{u}_1$, ϵp_1 and $\epsilon\boldsymbol{\sigma}'_1$.

2.7 One-Dimensional Model

We first consider a one-dimensional reduction in which we restrict the displacement $\boldsymbol{u} = w(z,t)\boldsymbol{e}_3$ and fluid flow to occur only along the length of the tendon. Using (2.31), the dimensionless governing equations are given by

$$\phi_f = \frac{\partial w}{\partial z}, \tag{2.36a}$$

$$\frac{\partial \phi_f}{\partial t} = \frac{\partial}{\partial z}\left(k\frac{\partial p}{\partial z}\right), \tag{2.36b}$$

$$\frac{\partial p}{\partial z} = \frac{\partial}{\partial z}\Big(M\frac{\partial w}{\partial z}\Big), \tag{2.36c}$$

where we have denoted the dimensionless axial permeability $k_z(z)$ by k. Using (2.32a) and (2.32b), the associated dimensionless boundary conditions are given by

$$\frac{\partial p}{\partial z} = w = 0 \qquad \text{at } z = 0, \tag{2.37a}$$

$$M\frac{\partial w}{\partial z} = \frac{A^*}{|\Omega_m|}\left(1-\cos(\omega t)\right), \quad p = 0 \ \text{ at } z = 1, \tag{2.37b}$$

where $|\Omega_m|$ denotes the area of the muscular origin $\Omega_{m,0}$ scaled by L_0^2. By scaling over the area, the forcing condition (2.28) has reduced to a pointwise stress condition (2.37b), in which we denote the stress (RHS) by σ^*. For all simulations, the magnitude of the cyclic tensile stress applied to the boundary (Equation (2.40b)) is kept constant with $A^*/|\Omega_M| = 10/3$, and we explore the behaviour of the system for varying ω.

The initial condition (2.32c), together with (2.36a) and the zero displacement boundary

condition (2.37a), imply

$$w = 0 \ \text{ at } t = 0. \tag{2.38}$$

We convert (2.36) to a single equation for the displacement by eliminating ϕ_f and p

$$\frac{\partial^2 w}{\partial t \partial z} = \frac{\partial}{\partial z}\left(k\frac{\partial}{\partial z}\left(M\frac{\partial w}{\partial z}\right)\right). \tag{2.39}$$

Using (2.36c), together with the boundary condition (2.37a), we can derive a second condition for the displacement at the insertion. Equation (2.39) is then solved subject to the boundary and initial conditions

$$\frac{\partial}{\partial z}\left(M\frac{\partial w}{\partial z}\right) = w = 0 \qquad \text{at } z = 0, \tag{2.40a}$$

$$M\frac{\partial w}{\partial z} = \frac{A^*}{|\Omega_m|}\left(1 - \cos(\omega t)\right) \quad \text{at } z = 1, \tag{2.40b}$$

$$w = 0 \qquad \text{at } t = 0. \tag{2.40c}$$

Using (2.36c), the flux, given by $-k(\partial p/\partial z)$, can readily be calculated from the displacement. To recover the pressure from the displacement, we integrate (2.36c) with respect to z to obtain

$$p(z,t) = M\frac{\partial w}{\partial z} - M\frac{\partial w}{\partial z}_{|z=1}. \tag{2.41}$$

2.7.1 Homogeneous Tendon Subject to Cyclic Loading

We now consider homogeneous stiffness and permeability of the tendon ($M = k = 1$) and we apply a cyclic stress. We determine the long-time periodic solution for the displacement, pressure and flux. In this case, the boundary conditions remain as per (2.40), but the initial

condition (2.38) is not required. Motivated by the cyclic loading

$$\sigma^* = \frac{A^*}{|\Omega_m|}\left(1-\cos(\omega t)\right) = \frac{A^*}{|\Omega_m|} - \frac{A^*}{2|\Omega_m|}(e^{i\omega t}+e^{-i\omega t}), \tag{2.42}$$

we assume a solution of the form

$$w(z,t) = \frac{A^*}{|\Omega_m|}z + Z(z)e^{i\omega t} + \bar{Z}(z)e^{-i\omega t}, \tag{2.43}$$

where $Z(z)$ and $\bar{Z}(z)$ are complex conjugates, and the term $(A^*/|\Omega_m|)z$ is chosen to satisfy the steady component of the applied stress (2.42). Substituting (2.43) into (2.39), and applying the boundary conditions (2.40), we find

$$Z' i\omega e^{i\omega t} + \bar{Z}' i\omega e^{-i\omega t} = Z''' e^{i\omega t} - \bar{Z}''' e^{-i\omega t}, \tag{2.44}$$

where

$$Z(0) = \bar{Z}(0) = 0, \quad Z''(0) = \bar{Z}''(0) = 0, \quad Z'(1) = \bar{Z}'(1) = \frac{A^*}{2\,|\Omega_m|}. \tag{2.45}$$

Solving $Z' i\omega = Z'''$ and using this solution to obtain $\bar{Z}$, we find

$$\begin{aligned} w(z,t) = \frac{A^*}{|\Omega_m|}z - \left(\frac{A^*}{2\sqrt{\frac{\omega}{2}}|\Omega_m|}\right) \times \\ \left(\frac{e^{\sqrt{\omega/2}\,(z+1)}\Big(\sin(\theta_{-+})+\cos(\theta_{-+})\Big) + e^{-\sqrt{\omega/2}\,(z-1)}\Big(\sin(\theta_{+-})-\cos(\theta_{+-})\Big)}{2\cos(2\sqrt{\frac{\omega}{2}}) + e^{2\sqrt{\omega/2}} + e^{-2\sqrt{\omega/2}}}\right. \\ \left. + \frac{e^{\sqrt{\omega/2}\,(z-1)}\Big(\sin(\theta_{++})+\cos(\theta_{++})\Big) + e^{-\sqrt{\omega/2}\,(z+1)}\Big(\sin(\theta_{--})-\cos(\theta_{--})\Big)}{2\cos(2\sqrt{\frac{\omega}{2}}) + e^{2\sqrt{\omega/2}} + e^{-2\sqrt{\omega/2}}}\right), \end{aligned} \tag{2.46}$$

where

$$\theta_{++} = \sqrt{\frac{\omega}{2}}(z+1) + \omega t, \quad \theta_{--} = \sqrt{\frac{\omega}{2}}(z-1) - \omega t,$$

$$\theta_{-+} = \sqrt{\frac{\omega}{2}}(z-1) + \omega t, \quad \theta_{+-} = \sqrt{\frac{\omega}{2}}(z+1) - \omega t.$$

Taking the spatial derivative of (2.46) we can then obtain the long time solution for the strain

$$\frac{\partial w}{\partial z} = \frac{A^*}{|\Omega_m|} - \frac{A^*}{|\Omega_m|}\left(\frac{e^{\sqrt{\omega/2}\,(z+1)}\cos(\theta_{-+}) + e^{-\sqrt{\omega/2}\,(z-1)}\cos(\theta_{+-})}{2\cos(2\sqrt{\frac{\omega}{2}}) + e^{2\sqrt{\omega/2}} + e^{-2\sqrt{\omega/2}}}\right.$$

$$\left. + \frac{e^{\sqrt{\omega/2}\,(z-1)}\cos(\theta_{++}) + e^{-\sqrt{\omega/2}\,(z+1)}\cos(\theta_{--})}{2\cos(2\sqrt{\frac{\omega}{2}}) + e^{2\sqrt{\omega/2}} + e^{-2\sqrt{\omega/2}}}\right). \tag{2.47}$$

At the muscular boundary the strain is given by

$$\frac{\partial w}{\partial z}(z=1,t) = \frac{A^*}{|\Omega_m|} - \frac{A^*}{|\Omega_m|}\cos(\omega t), \tag{2.48}$$

which, regardless of the frequency ω, takes a maximum of $2A^*/|\Omega_m|$. To understand how the strain (2.47) varies with increasing frequency for $z < 1$, we take the limit as $\omega \to \infty$. In this case, considering the fraction in the second line of (2.47), the second term in the denominator $\exp(2\sqrt{\omega/2})$ dominates and the fraction tends to zero. As such, away from the boundary $z = 1$, we find

$$\lim_{\omega\to\infty} \frac{\partial w}{\partial z} = \frac{A^*}{|\Omega_m|}. \tag{2.49}$$

To evaluate the behaviour near the boundary at $z = 1$ when $\omega \to \infty$, we consider (2.47) in a small boundary region of width $1/\sqrt{\omega/2}$ near $z = 1$. We introduce the new variable Z via

$z-1=Z/\sqrt{\omega/2}$ $(-\infty<Z\leq 0)$. The strain is then given by

$$\frac{\partial w}{\partial Z}=\frac{A^*}{\sqrt{\omega/2}|\Omega_m|}- \tag{2.50}$$

$$\frac{A^*}{\sqrt{\omega/2}|\Omega_m|}\left(\frac{e^{\sqrt{\omega/2}\,(Z+2)}\cos(\theta_{-+})+e^{-Z}\cos(\theta_{+-})+e^{Z}\cos(\theta_{++})+e^{-\sqrt{\omega/2}\,(Z+2)}\cos(\theta_{--})}{2\cos(2\sqrt{\frac{\omega}{2}})+e^{2\sqrt{\omega/2}}+e^{-2\sqrt{\omega/2}}}\right),$$

where

$$\theta_{++}=Z+2\sqrt{\frac{\omega}{2}}+\omega t,\quad \theta_{--}=Z-\omega t,$$

$$\theta_{-+}=Z+\omega t,\qquad\qquad \theta_{+-}=Z+2\sqrt{\frac{\omega}{2}}-\omega t.$$

Again the term $\exp(2\sqrt{\omega/2})$ dominates as $\omega\to\infty$. After transforming back to our original coordinates, we find

$$\lim_{\omega\to\infty}\frac{\partial w}{\partial z}=\frac{A^*}{|\Omega_m|}-\frac{A^*}{|\Omega_m|}e^{\sqrt{\omega/2}\,(z-1)}\cos\left(\sqrt{\omega/2}\,(z-1)+\omega t\right). \tag{2.51}$$

Hence, as the frequency of loading increases, the strain at the outer boundary remains periodic whilst, over the interior, except close to $z=1$, the deformation approaches a constant value which is independent of time.

Using the long-time solution for the strain (2.47), in combination with (2.41) and (2.36c), we obtain the long-time solutions for the pressure and flux (Appendix 2.B) respectively. In a similar manner to above, for the pressure and flux away from the boundary $z=1$, the limits in the frequency are given by

$$\lim_{\omega\to\infty}p=-\frac{A^*}{|\Omega_m|,}\qquad\lim_{\omega\to\infty}-\frac{\partial p}{\partial z}=0, \tag{2.52}$$

while over the boundary region $z \to 1$ when $\omega \to \infty$, the pressure and flux are given by

$$\lim_{\omega\to\infty} p = \frac{A^*}{|\Omega_m|}\cos(\omega t) - \frac{A^*}{|\Omega_m|}e^{\sqrt{\omega/2}\,(z-1)}\cos\left(\sqrt{\omega/2}\,(z-1)+\omega t\right), \tag{2.53}$$

$$\lim_{\omega\to\infty} -\frac{\partial p}{\partial z} = -\frac{A^*\sqrt{\omega/2}}{|\Omega_m|}e^{\sqrt{\omega/2}\,(z-1)}\left(\cos\left(\sqrt{\omega/2}\,(z-1)+\omega t\right) - \sin\left(\sqrt{\omega/2}\,(z-1)+\omega t\right)\right). \tag{2.54}$$

At the boundary $z = 1$, the flux continues to increase with increasing frequency. In the subsequent section we plot the full long-time solutions for the strain, pressure and flux given by Equations (2.47), (2.41) and (2.75) (Appendix 2.B). We contrast these with the analytical solutions obtained for the limit $\omega \to \infty$ ((2.49) and (2.51)-(2.54)).

2.7.2 Numerical Solution

To obtain the transient solution and solutions when we account of heterogeneity in the stiffness or permeability, we solve the system numerically by using a finite difference scheme to discretise the spatial derivatives. Finite difference method are a fast and computationally inexpensive tool that is widely used in solving ordinary differential equations that do not have an exact analytical solution. Finite difference methods are especially useful in the setting where the model is to be run multiple times and iteratively, which becomes relevant in Chapter 3 when we simulate a series of loading bouts (though utilising a two-dimensional model). Applying the finite difference method gives us a system of time dependent ODEs for the displacement w at each spatial point. We solve this time dependent system using *MATLAB*'s stiff ODE solver *ODE15s*. To test the numerical results, the numerical long-time solution was validated against the analytical long-time solution. We also tested a range of different grid sizes to ensure spatial convergence of the numerical results and that the accuracy was as expected for a second-order finite difference scheme. Full details for the numerical procedure implemented are given in Appendix 2.C.1.

2.7.3 One-Dimensional Model Results

2.7.3.1 Homogeneous Stiffness and Permeability

We first consider the case in which the stiffness and permeability are assumed to be homogeneous. For homogeneous stiffness $M = 1$, the dimensionless stress and strain are equal. This stress magnitude was found to produce global strains of around 4-5% (results not shown), consistent with physiological tendon strains under load (Arampatzis et al. 2010). We consider $\omega = 1$ and $\omega = 10 - 20$, corresponding to rehabilitative and damage-inducing loading. We also utilise the one-dimensional model, including our analytic solution, to investigate the poroelastic behaviour at larger values of ω to aid in our understanding of the material's behaviour.

Figure 2.3a depicts the numerical (solid lines) and long-time analytic solutions (dashed lines) for the displacement for $\omega = 10$. The displacement is plotted at different spatial points z within the tendon. The numerical solution depicts a transient ($t \lesssim 1.5$) and periodic ($t \gtrsim 1.5$) state; a constant amplitude cyclic displacement is observed at each point within the tendon for $t \gtrsim 1.5$. There is a lack of agreement between the analytical and numerical solutions for this transient state $t \lesssim 1.5$, however, there is exact agreement between the analytical and periodic numerical solution. The corresponding pressure, given in Figure 2.3b, follows a similar cyclic profile, albeit with a phase shift in which the pressure troughs occur ahead of the peak tensile displacements. There is also a phase shift in which, closer to the outer boundary $z = 1$, the pressures peak earlier relative to pressure profiles toward the insertional end. Figure 2.3c displays the corresponding flux profile in which the flux peaks just ahead of the pressure. A negative flux corresponds to fluid flowing into the tendon. Fluid is seen to flow into the tendon as the displacement increases. Since, relative to the resting state, only tensile forces are applied to the tendon, the cumulative flux (solid grey line) is negative throughout the applied loading time.

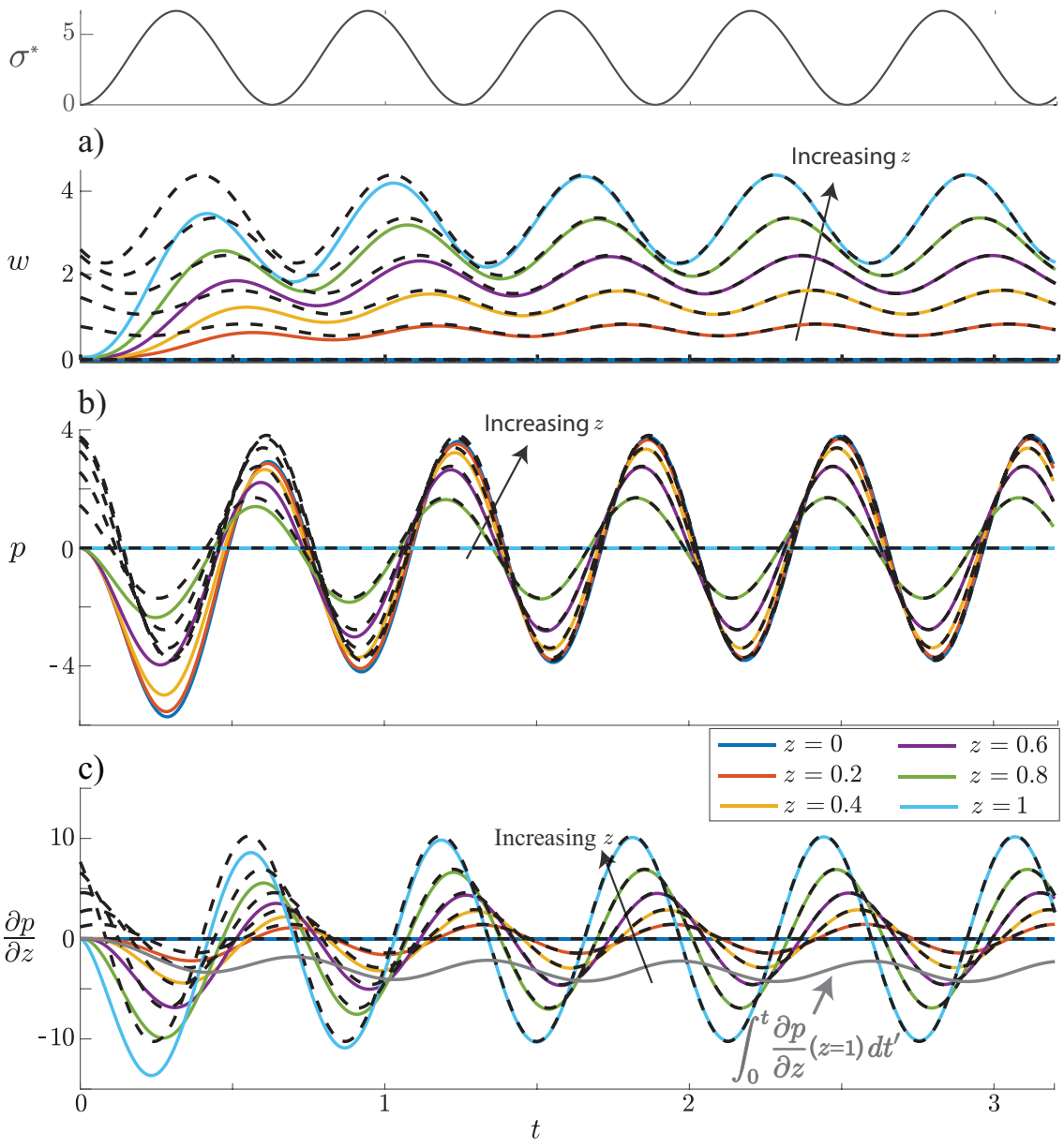


Figure 2.3: (a) Comparison of numeric (solid) and analytic (dashed lines) results for the dimensionless displacement at different spatial locations within the material. The permeability and stiffness are homogeneous $M = k = 1$, and the applied cyclic stress σ^* has a frequency of $\omega = 10$. (b) Corresponding pressure profile demonstrating a phase lag in the propagation of pressure across the material. (c) Corresponding flux profile with cumulative flux given by solid grey line.

In Figure 2.4 we convey how the strain, pressure and flux profiles vary with the frequency of loading. We use the metric

$$\frac{\partial w}{\partial z}^{\max}(z) = \max_t \frac{\partial w}{\partial z}(z,t) \tag{2.55}$$

to evaluate how the maximum strains reached during the loading cycle vary with the frequency of loading and position. In (2.55) we have maximised over time for each spatial point individually, as the time at which the maximum values for these variables occurs will show spatial dependence, as can be observed by the phase shift in the pressure in Figure 2.3b. Equivalent metrics $p^{\max}$ and $|\partial p/\partial z|^{\max}$ are used for the dimensionless pressure and flux. In Figure 2.4a,c,e we plot how this metric varies with loading frequency, where line colours correspond to different spatial points within the tendon. Figure 2.4b,d,e displays the spatial profiles of the strain, pressure and flux at the time point $t = 3\pi/\omega$ of maximum applied stress σ^*. A dotted red line shows the asymptotic solution on the interior $z < 1$ (outer solution) as $\omega \to \infty$. A solid red line shows the inner solution for the boundary layer and is displayed for $\omega = 50$ and $\omega = 100$. The strain, pressure and flux all vary sharply over the boundary region, scaling with $\sqrt{\omega/2}$. The inner solution (Equations (2.51), (2.53), (2.54)) is in agreement with the full solutions (black dashed and dotted lines for $\omega = 50$ and $\omega = 100$ respectively) for the strain, pressure and flux (Equations (2.47), (2.52)). Figure 2.4a,b shows that, as the frequency increases, larger solid strains occur in the neighbourhood of the origin $z = 1$, with a reduction of the maximum strain in the neighbourhood of the insertional boundary $z = 0$. Consistent with this result, a trend toward the asymptotic limit (Equation (2.49)) for the strain with increasing frequency is visible in Figure 2.4a,b, in which the strain at the outer boundary is approximately two-folds larger than the interior.

In Figures 2.4c,d the equivalent pressure profiles are shown. In Figure 2.4d it is evident that the pressure profile (which is negative in the case of tension) shows similar trends to the strain, though shifted by a constant. This must hold by construction, since, in the case of

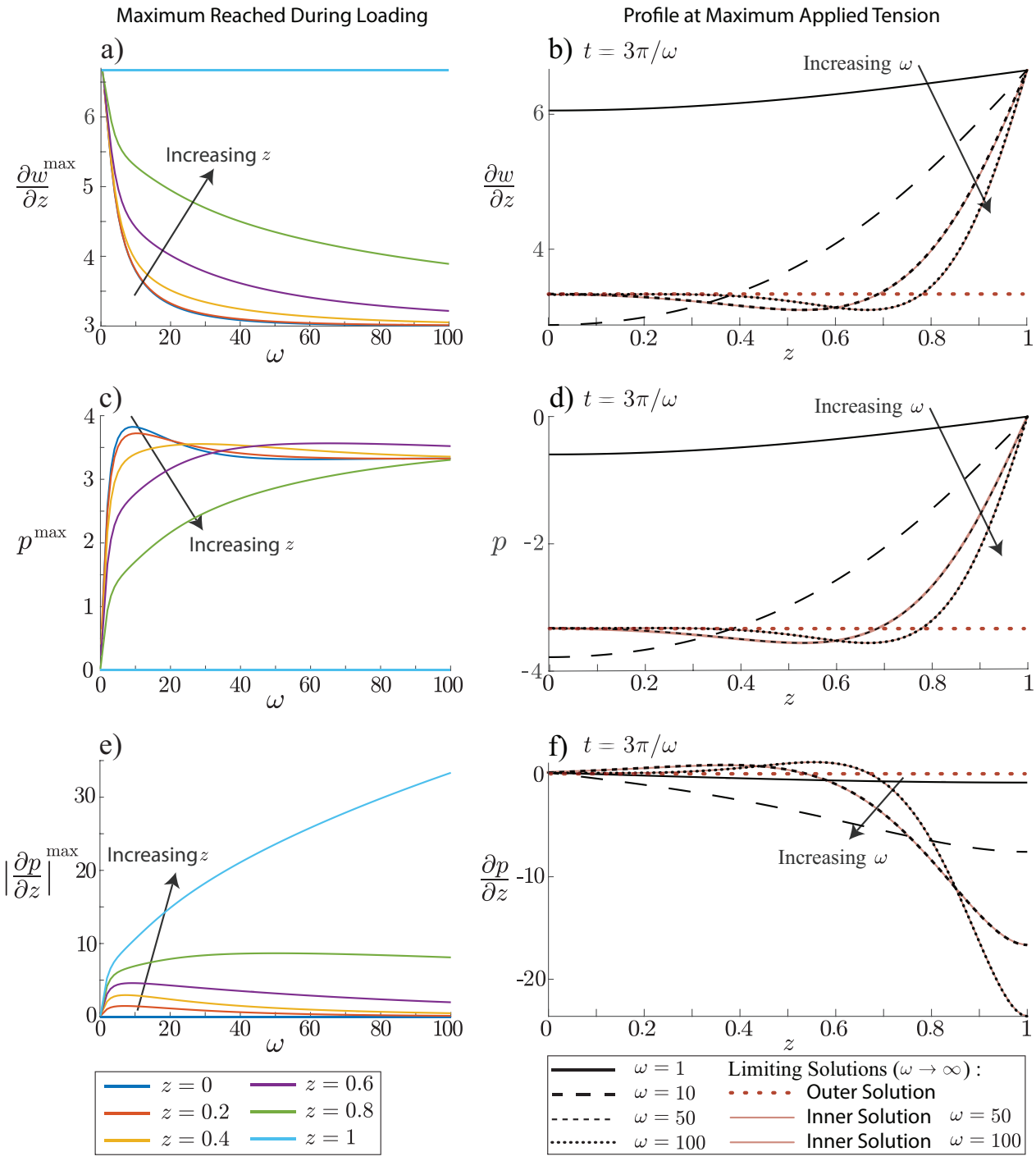


Figure 2.4: Maximum (a) strain, (c) pressure and (e) flux, as defined in (2.55), reached at varying spatial points plotted against loading frequency. Spatial profiles of (b) strain, (d) pressure and (f) flux given at the time of maximal tension $t = 3\pi/\omega$. Asymptotic solutions as $\omega \to \infty$ for the spatial profiles on in the interior $z < 1$ are also given by the dotted red line. Material parameters are set to constant $M = 1$ and $k = 1$.

homogeneous stiffness, the pressure is simply equal to the strains minus a constant in space (Equation (2.41)). In Figure 2.4c, due to this constant shift, the largest pressure changes occur at the insertion $z = 0$. However, Figure 2.4c does not show the exact profile displayed in Figure 2.4a, since, unlike the strain, the pressure maximum at each spatial point occurs at a different point in time (since the constant shift in Equation (2.41) is still time dependent). A corresponding change in the flux is also evident in Figure 2.4e,f. Larger fluxes are generated with increasing frequency, however, similar to the trends observed for the strain, this trend occurs closest to the permeable boundary at which the stress is applied. In Figure 2.4f the flux tends toward the asymptotic solution, in which there is zero flow away from the outer boundary.

2.7.3.2 Heterogeneous Stiffness and Permeability

We next consider a localised reduction in stiffness or permeability. A cyclic tensile stress is again applied to the origin, in keeping with physiological tendon loading. We induce a localised reduction in stiffness via the Gaussian bump function (Figure 2.5)

$$M(z) = 1 - s \exp\left(-\frac{(z-c)^2}{2(1/16)^2}\right), \tag{2.56}$$

where c modifies the spatial position and s modifies the magnitude[9] of the reduction. A similar expression is used to capture local reductions in the dimensionless permeability, with the spatial variation in $k(z)$ is defined similarly. We refer to $M^{\mathcal{D}} = 1 - s$ and $k^{\mathcal{D}} = 1 - s$ as the (dimensionless) minimum stiffness and minimum permeability over this 'damaged region' (with $M^{\mathcal{D}} = 1$ implying M is constant across the material). We are primarily interested in

[9]Varying the parameter $s \in [0, 0.6]$ only affects the magnitude of strain, pressure and flux increases/reductions that occurred as a result of this locally imposed reduction in stiffness/permeability. The spatial distribution of, and effect of frequency on, the strain, pressure and flux was insensitive to variations in s. As such we have only included results for $s = 0.4$.

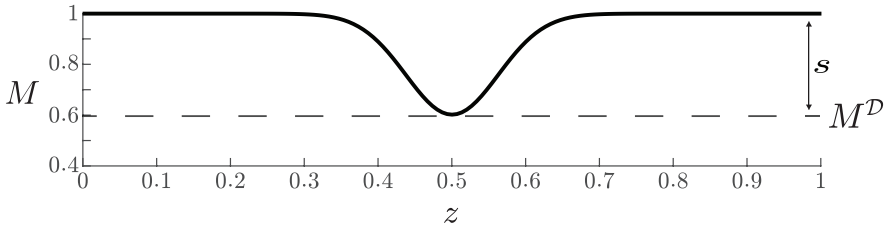


Figure 2.5: Example of profile for heterogeneous stiffness as defined in Equation (2.56) with $s = 0.4$ and $c = 0.5$.

the effects of damage at the midportion. However, to investigate how the site of damage affects the mechanical environment, we also investigate the case in which damage is imposed near the origin ($z = 1$). We again use the metrics $(\partial w/\partial z)^{\max}$, $p^{\max}$, $|\partial p/\partial z|^{\max}$ as specified by (2.55).

In Figure 2.6 we plot the maximum strain, pressure and flux at each spatial point when a cyclic stress is applied to a material with a heterogeneous stiffness. Figure 2.6a,c,e display the profiles when a reduced stiffness is imposed at the midportion, whilst Figure 2.6b,d,f display the profiles for a reduced stiffness toward the outer boundary. The profiles are given for several frequencies of loading and, in order to facilitate comparison, the overlaying black lines display the corresponding profiles for the homogeneous stiffness case. In both Figure 2.6a and b there is an observable increase in the strain in the damaged low-stiffness region. There is an interaction effect present between the loading frequency and the stiffness, in that the relative increase in the strain was less for higher frequency loading ($\omega = 50$, yellow line) compared to slow loading ($\omega = 1$, blue line). In Figure 2.6c it is evident that, when the stiffness is reduced at the centre, there is a small increase in the pressure for the lowest loading frequency and a small decrease for the highest frequency of loading. In contrast, in Figure 2.6d, when the stiffness is reduced toward the outer boundary, a small increase in the pressure is observed over this region for the two higher frequencies ($\omega = 10$ and $\omega = 50$, red and yellow lines). Contrasting Figure 2.6e and f, when the stiffness is reduced, small increases in the flux are evident toward the origin and small decreases occur toward the insertion. The relative increase appears to be larger if the reduction in stiffness is imposed at

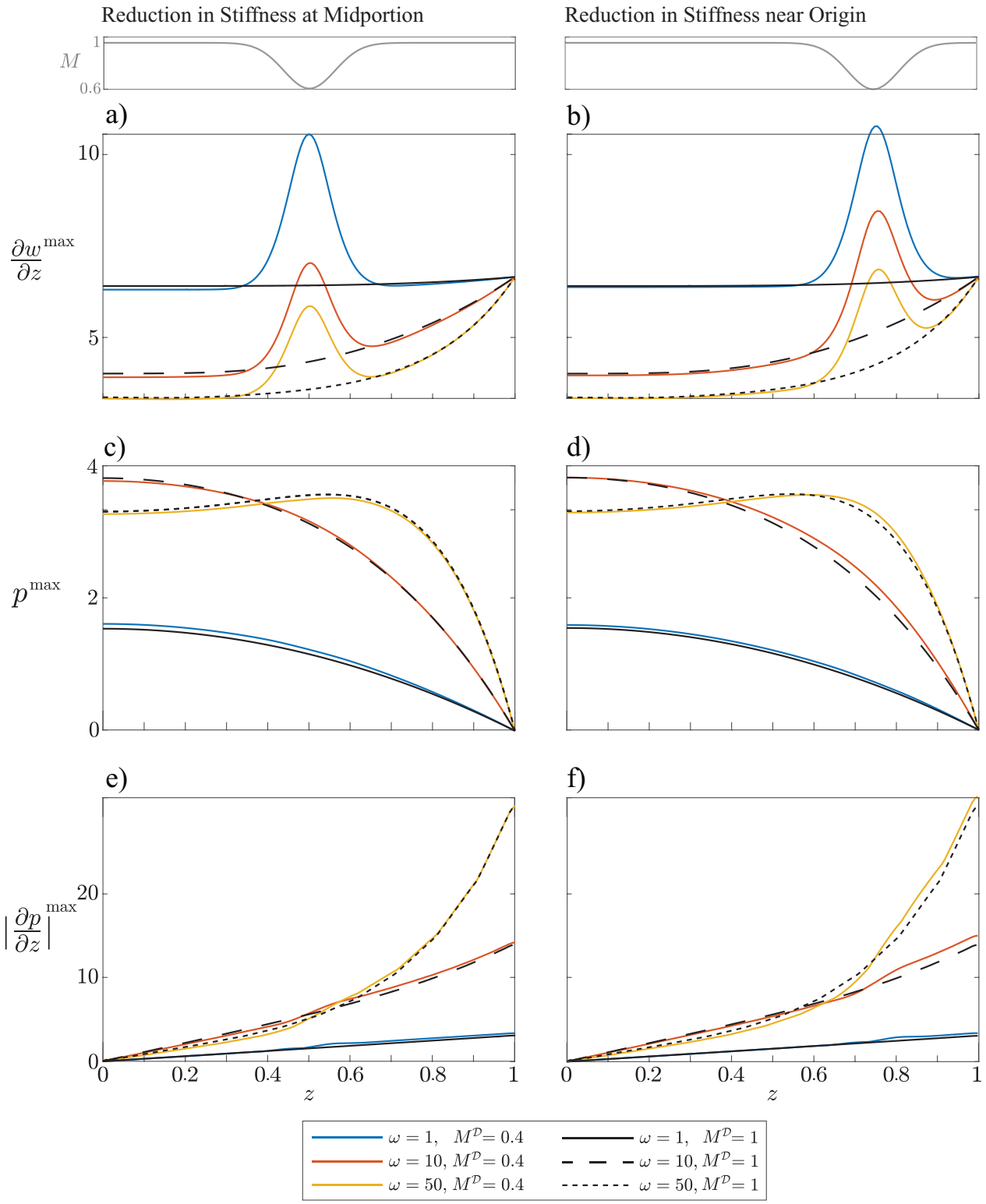


Figure 2.6: Maximum (a),(b) strain, (c),(d) pressure and (e),(f) flux reached at each spatial point during cyclic loading $\sigma^* = 1/30 - \cos(\omega t)/30$. A reduction in stiffness is either imposed at the centre (left panel) or toward the outer boundary (right panel). The same profiles in the case of homogeneous stiffness $M = 1$ are also shown (black solid and dashed lines) in order to facilitate comparison.

the outer boundary. Larger relative changes are again observed for the two higher frequencies of loading in this case. In addition to these findings, looking across all plots in Figure 2.6, it is evident that, for the ranges of stiffness and loading frequencies explored, the frequency of loading has a more substantial impact on the pressure and flux profiles than the reduction in stiffness (Figure 2.6c-f). However, the strain profiles are significantly affected by both factors (Figure 2.6a,b).

In Figure 2.7 we plot the same profiles as given in Figure 2.6, except in the setting of a reduced permeability. In this case, we can see from Figure 2.7a,b that for the same relative reductions in permeability, there is a less substantial effect on the strain than when a reduction in stiffness is imposed (Figure 2.6a,b). For the higher loading frequency, depicted by the red line ($\omega = 10$), the strain is increased on the outer boundary side of the low permeability region, whilst there is a concurrent reduction in the strain on the insertional side of the low permeability region. For the lower frequency case, there is also a small reduction in the strain, and if we contrast this to the results in the Figure 2.7c,d, we can see a concurrent increase in the pressure. This reduction in the strain and concurrent pressure increase, on the insertional side of the damaged region, appear more significant when a reduction in the permeability is imposed at the outer boundary (b,d). Similarly, looking at Figures 2.7e,f, there is a reduction in the flux, which is more significant when the damaged region is imposed at the outer boundary. This reduction occurs only for the two higher frequencies of loading and predominantly over the damaged region itself and on the outer boundary side. Looking across all plots in Figure 2.6, for the ranges of permeability and loading frequencies explored, the frequency of loading has a more substantial impact on the pressure and flux profiles than the reduction in permeability (c-f).

2.7.4 One-Dimensional Model Discussion

The one-dimensional model demonstrated that the frequency of tendon loading has a substantial effect on the solid to fluid coupling, with notable changes in the mechanical environment.

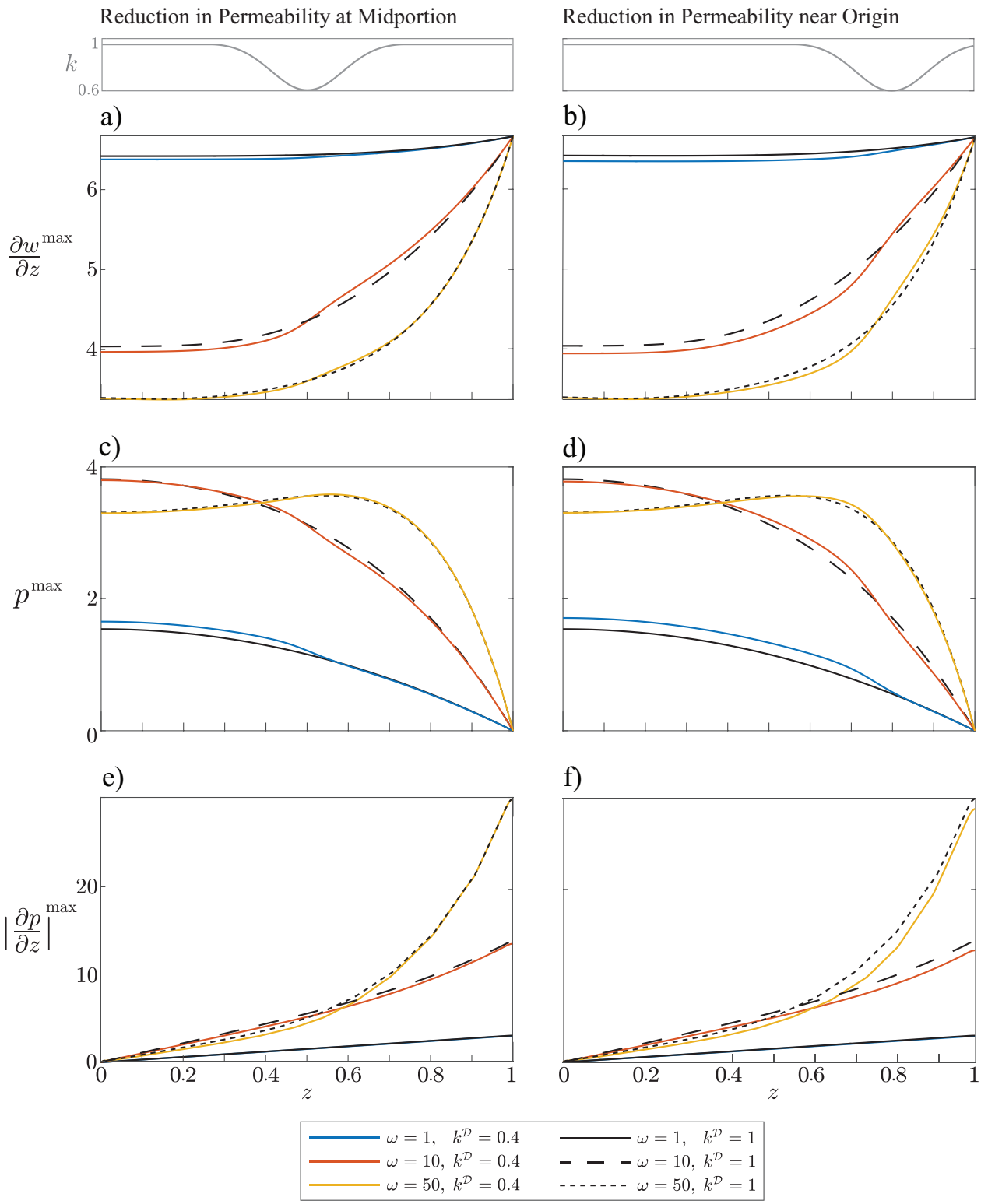


Figure 2.7: Maximum (a),(b) strain, (c),(d) pressure and (e),(f) flux reached at each spatial point during cyclic loading. A reduction in permeability is either imposed at the centre (a,c,e) or toward the outer boundary (b,d,f). The same profiles in the case of homogeneous permeability $k = 1$ are also shown (black solid and dashed lines) in order to facilitate comparison.

With an increase in the loading frequency from $\omega = 1$ to $\omega = 10$, there was a reduction in the strain and a concurrent increase in the pressure. As the loading frequency increased, there were large increases in the flux and strain magnitudes at the outer boundary, with a corresponding increase in the magnitude of the pressure changes toward the insertional impermeable boundary. These changes can be explained by the classic poroelastic response, in which there is insufficient time for pressure relaxation to occur when the loading timescale is shorter than the poroelastic timescale. With a reduction in the fluid movement possible, the fluid takes on a greater share of the applied stress, leading to a subsequent reduction in the solid strain. This behaviour was highlighted when the asymptotic limit in the frequency was taken. Our results are in good agreement with Kameo et al. (2008), who also considered the effect of loading frequency on pressure within poroelastic structures and found higher pressures to occur far from the boundary. This was despite the stress in their model being applied perpendicular to the direction of fluid movement, unlike our model in which fluid movement occurred in the same direction as the applied stress. Relating these results to physiological loading, they suggest that fluid induced stresses may be higher for high frequency loading, whilst solid strains may stay low. Since fluid and solid stresses have different mechanotransduction pathways and hence effects on the production of key tendon constituents, such as collagen and proteoglycans, such a response in tendon could lead to undesirable modifications of material properties. Furthermore, since higher loading frequencies increased the heterogeneity in the spatial distribution of stresses, certain areas may be under or over stimulated with high loading frequencies.

A key difference which has affected the spatial profile of the mechanical environment observed in our model, in contrast to previous work, is that the load in our model was applied at the permeable boundary of the material. This assumption resulted in larger deformations occurring at the site of loading and larger pressures occurring at the impermeable end. This is in contrast to MacMinn et al. (2016), who imposed a load to one impermeable boundary and allowed fluid to leave from the opposite end, and previous two-dimensional models of

cartilage in which the load was imposed perpendicular to the direction of fluid movement (Armstrong et al. 1984, Kameo et al. 2008). As such, in the work of MacMinn et al. (2016) deformation propagated from both ends, leading to high pressures and strains occurring at the centre, which decayed with time. In previous cartilage models that utilised a symmetry condition, high pressures occurred at the centre and the largest deformations occurred at the outer boundary (Armstrong et al. 1984, Kameo et al. 2008). Their assumption of plane strain in the direction normal to the applied load also meant that these authors did not observe a decay in the strain away from the site of imposed loading as observed here. In terms of boundary conditions, the model developed by Wang et al. (2001) is most similar to our set up; deformation in their model was constrained in the direction perpendicular to loading and a displacement is applied to the permeable boundary. Whilst they impose a displacement rather than a stress as we have done here, their results consistent with our predictions here. Their model predicted larger deformations to occur close to the permeable boundary, where the displacement was imposed, and higher pressures further away.

However, when trying to solve the heterogeneous case analytically, we could not separately solve over distinct homogeneous regions. From our results it is evident that localised reductions in stiffness and permeability impact the mechanical environment of the tendon. The magnitude of these effects depends on both the frequency of loading and, in the case of the pressure and flux, the proximity of the region to the permeable boundary. A localised reduction in the stiffness caused an increase in the strain over that same region. This result was also observed by Wang et al. (2001), who imposed a graded continuum of increasing material stiffness in order to model normal cartilage structure. The relative increase in strain was found to be less substantial for higher loading frequencies. Considering the results for homogeneous stiffness, the solid skeleton takes on a greater share of the applied load with slower loading. This would explain why, when a reduction in the stiffness was imposed, larger relative deformations occurred. The model also predicted a small increase in the flux when a localised reduction in stiffness was imposed, and a small decrease when there was a reduction

in the permeability. These effects were more obvious when reductions were imposed near the outer boundary, where the flux is already higher. There was a rate dependence of this effect, in which the localised reductions had minimal effect on the flux for the lower frequencies of loading. Reductions in the permeability did have an effect on the pressure at lower loading frequencies, causing an increase in the pressure on the insertional side of the damaged region, as the ability of the pressure to equalise was reduced. There was less of an effect for higher loading rates in this case, as there was already insufficient time for the pressure to equalise.

A distinction between previous modelling work on heterogeneous poroelastic tissues (Kameo et al. 2016, Ambartsumyan et al. 2019), is that we imposed a continuous heterogeneity rather than modelling a set of distinct homogeneous regions. As such, we did not need to actively ensure continuity across the tendon. Our results are in good agreement with Kameo et al. (2016) who accounted for a heterogeneous permeability when modelling fluid flow in bone. They similarly found the relative effects of a reduction in the permeability to depend on the frequency of loading and proximity to the permeable boundary.

2.7.5 Conclusions from One-Dimensional Model

There is a wealth of literature demonstrating that when poroelastic structures are subjected to higher loading rates, the interstitial fluid takes on a greater share of the applied load with a concurrent reduction in the deformation of the solid skeleton (Detournay et al. 1993). We have first reproduced these classical results in the setting of a one-dimensional model for tendon, demonstrating that fluid induced stresses are likely greater for higher frequencies of tendon loading. We explored the one-dimensional model to clearly show that there is an interaction effect between the frequency of loading and a region of localised reduction in stiffness or permeability. Furthermore, the proximity of this region to the outer boundary was shown to influence the magnitude of pressure and flux changes that resulted from a reduction in stiffness or permeability. That is, both the frequency of loading and proximity to the outer boundary affect the relevance of 'damage' induced stiffness or permeability reductions. Since

the spatial structure of damage was a key determinant of the mechanical environment, this motivates us to consider a two-dimensional model in which we do not assume the spatial variation is constant across one of the transverse dimensions.

2.8 Two-Dimensional Model

Experimental measurements of tendon are often two-dimensional. Longitudinal ultrasound images - to assess for tendinopathy - are taken as a longitudinal slice spanning the tendon thickness. As such, there is an inherent assumption in the interpretation of these images that a two-dimensional slice represents the structural changes across the entire tendon. Furthermore, measurements of the Poisson's ratio or of transverse dimensional changes pre-to-post loading usually consider only measurements across the thickness (Han et al. 2000, Hannafin et al. 1994, Grigg et al. 2009). We now assume zero strain across the tendon width and, retaining the length and thickness, consider the case in which a two-dimensional rectangular poroelastic structure is subjected to cyclic axial loading (Figure 2.8). The problem described by (2.31) and (2.32) decouples to one in (x,z) and y. We solve for a displacement of the form $\boldsymbol{u} = u\boldsymbol{e}_x + w\boldsymbol{e}_z$. The pressure, porosity, and displacement components u and w, are functions of both the transverse and axial spatial coordinates x and z, as well as time. For notational convenience we let the scaled thickness $W_{x0}/L_0 = W_0/L_0$. We impose a symmetry condition

$$u = \frac{\partial w}{\partial x} = \frac{\partial p}{\partial x} = 0 \ \text{ at } x = 0, \tag{2.57}$$

allowing us to solve over the half domain $\mathrm{D} = \{(x, z) : 0 < x < W_0/(2L_0),\ 0 < z < 1\}$ which is less computationally expensive. Our choice of a two-dimensional Cartesian coordinate system not only simplifies the problem numerically but also allows us to contrast our results with available two-dimensional imaging data in later chapters.

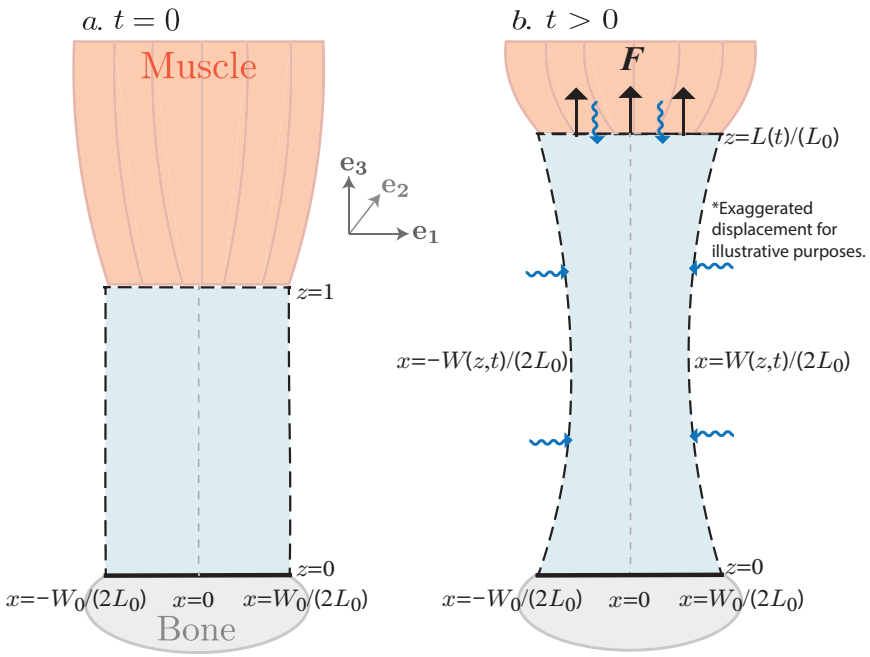


Figure 2.8: Two-dimensional depiction of tendon under load in Cartesian coordinates. The diagram is given as a schematic representation and not drawn to scale. A force $\boldsymbol{F}$(black arrows) is applied at time t > 0, generating tensile deformation of the poroelastic material and fluid movement into the tendon. Blue wavy arrows denote fluid movement into the tendon. Dashed black lines denote permeable boundaries.

2.8.1 Dimensionless Two-Dimensional System

Using (2.31) the dimensionless governing equations for the two dimensional problem are

$$\phi_f = \frac{\partial u}{\partial x} + \frac{\partial w}{\partial z}, \tag{2.58a}$$

$$\frac{\partial \phi_f}{\partial t} = k_x \frac{\partial^2 p}{\partial x^2} + k_z \frac{\partial^2 p}{\partial z^2} + \frac{\partial k_x}{\partial x}\frac{\partial p}{\partial x} + \frac{\partial k_z}{\partial z}\frac{\partial p}{\partial z}, \tag{2.58b}$$

$$\frac{\partial p}{\partial x} = \frac{\partial}{\partial x}\left(M\left(\frac{\partial u}{\partial x} + \nu\frac{\partial w}{\partial z}\right)\right) + \frac{\partial}{\partial z}\left(M\left(\frac{1-\nu}{2}\right)\left(\frac{\partial u}{\partial z} + \frac{\partial w}{\partial x}\right)\right), \tag{2.58c}$$

$$\frac{\partial p}{\partial z} = \frac{\partial}{\partial z}\left(M\left(\frac{\partial w}{\partial z} + \nu\frac{\partial u}{\partial x}\right)\right) + \frac{\partial}{\partial x}\left(M\left(\frac{1-\nu}{2}\right)\left(\frac{\partial u}{\partial z} + \frac{\partial w}{\partial x}\right)\right). \tag{2.58d}$$

We now assume that displacements and fluid movement occurs along the length and thickness of the tendon. We apply a stress free condition at the transverse boundary in which the fluid

pressure is equal to the surrounding atmospheric pressure (scaled such that $p = 0$) and the tangential components of the effective solid stress are equal to zero. Considering also (2.32), the full set of two-dimensional associated boundary conditions are then given by

$$u = \frac{\partial w}{\partial x} = \frac{\partial p}{\partial x} = 0 \qquad \text{at } x = 0, \tag{2.59a}$$

$$\frac{\partial u}{\partial x} + \left(\frac{\nu}{1-\nu}\right)\frac{\partial w}{\partial z} = \frac{\partial u}{\partial z} + \frac{\partial w}{\partial x} = 0, \;\; p = 0 \qquad \text{at } x = \frac{W_0}{2L_0}, \tag{2.59b}$$

$$u = w = \frac{\partial p}{\partial z} = 0 \qquad \text{at } z = 0, \tag{2.59c}$$

$$u = \frac{\partial w}{\partial x} = p = 0, \;\; \int_0^{W_0/(2L_0)} M\,\frac{\partial w}{\partial z}dx = \frac{A^*}{(2W_{y0}/L_0)}\left(1 - \cos(\omega t)\right), \qquad \text{at } z = 1. \tag{2.59d}$$

The condition (2.59b) represents a linearised version of the stress free condition, derived through the small strain assumption. The associated initial condition is given by

$$\phi_f = 0 \;\; \text{at } t = 0. \tag{2.60}$$

The term $A^*/(W_{y0}/L_0)$ in (2.59d) is obtained through scaling and integration of the left hand side of (2.28) over the width W_{y0}/L_0, where we have made a further simplifying assumption that the width is constant across the thickness. In all cases we have chosen the cyclic force to have a magnitude of $A^*/(2W_{y0}/L_0) = 15$ which was shown to produce global tendon strains of around 5% (results not shown), consistent with high magnitude loading regimes (Bohm et al. 2014).

We combine (2.58a) and (2.58b) to eliminate the porosity, and now solve for the pressure and displacements.

2.8.2 Numerical Scheme

We solve the system of equations (2.58)-(2.61) numerically by the method of lines; the system is discretised in space and the *MATLAB* solver *ODE15s* is used to solve over time. We again assess for spatial convergence of the numerical solution by comparison of the solution with continual refinement of the spatial grid size. Details of the numerical scheme and convergence are given in Appendix 2.C.2. To impose a 'damaged area' in which the stiffness and/or permeability is reduced, a constant local reduction is prescribed within a region of the tendon. A Gaussian filter is use to smooth the change in material properties at the border of this region. We require an initial condition on the pressure and displacements in order to solve the system numerically. Without loss of generality, we impose the following initial conditions

$$u = w = p = 0 \ \text{ at } t = 0. \tag{2.61}$$

2.8.3 Two-Dimensional Model Results

We now focus on how variations in the loading frequency and material properties affect the mechanical environment at the tendon midportion. For all cases presented in text, we fix the tendon to have a half-thickness-to-length ratio of $W_0/(2L_0) = 1/20$. The metrics used to determine the effect of the loading rate and local material property changes on the flux and strain profiles were insensitive to this parameter for the range of $W_0/(2L_0)$ applicable to tendons (Table 2.2, results not shown). In general we assume that the Poisson's ratio has a value of 0.33 and the permeability is isotropic. However, noting that there is a large variation in the reported values for these two parameters in the literature, we also investigate the sensitivity of our results to variations in these parameters within the ranges presented in Table 2.2.

We expect mechanotransduction from the fluid flux to occur through shear stress (Lavagnino et al. 2008). Although methods for estimating the shear stress from the fluid flux are available (Whittaker et al. 2009), these rely on properties of the tendon's microstructure, such as the tortuosity, which are not available. Such estimates predict that the shear stress and fluid flux are linearly related through these microscopic parameters. We are interested in the pattern of changes in the mechanical environment with increasing loading frequency and material property inhomogeneities, rather than exact dimensional values quantifying these changes. As such, we investigate changes in the fluid flux and assume that there is a linear relation between fluid flux and shear stress. We also investigate the effect of frequency, and stiffness or permeability changes, on the tensile axial strains and compressive transverse strains, as these have been suggested to cause mechanotransduction with loading (Docking et al. 2019a, Cook et al. 2012, Grigg et al. 2009).

As outlined previously (Section 1.3.1), clinical evidence suggests that loading mechanisms causing damage and positive adaptive changes occur during the elongation phase of tendon loading (as a positive tensile force is applied). While we initially also considered high pressures as a potential cell stimulus, the model predicts negative pressures (results not shown) during the elongation phase of loading. This suggests high pressures as a less likely cellular stimulus contributing to midportion damage or rehabilitation and hence we focus on investigating the solid strains and fluid flux.

2.8.3.1 Influence of Forcing Rate on Mechanical Environment

To determine why high loading rates can be provocative for tendons, we first evaluate the effect of loading rate in the setting of homogeneous stiffness and permeability. In Figure 2.9 contour plots of the axial ($\partial w/\partial z$) and transverse ($\partial u/\partial x$) strains for different loading frequencies are given. The profiles are given at the maximum point of tension during loading. For an isotropic permeability and Poisson's ratio of 0.33, both the axial (Figure 2.9a) and

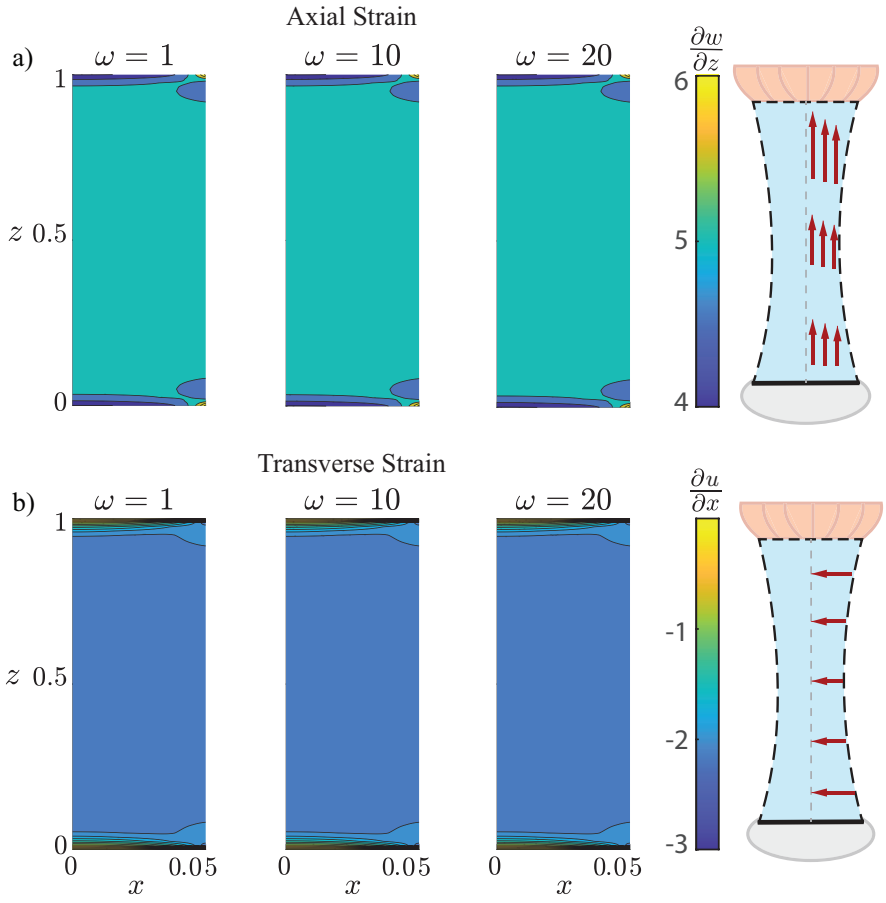


Figure 2.9: (a) Axial and (b) transverse strain profiles at maximum point of tension during loading ($t = 3\pi/\omega$) showing no observable difference in the strain profiles between different loading frequencies. Three loading frequencies are investigated: $\omega = 1$, $\omega = 10$, and $\omega = 20$. We impose a homogeneous stiffness $M = 1$, Poisson's ratio $\nu = 0.33$ and isotropic permeability $k_x = k_z = 1$.

transverse (Figure 2.9b) strain profiles were similar across different loading rates. The profiles were also homogeneous except near the longitudinal edges, which is in contrast to the one-dimensional results for similar prescribed frequencies (Figure 2.4) in which there was a gradual decrease in the strain away from the point of applied load. The insensitivity of the strain profiles to frequency was robust to reductions in either the Poisson's ratio or transverse-to-axial permeability ratio (by one order of magnitude) (results not shown). However, the loading frequency did affect the strain profiles when there was a simultaneous reduction in both parameters, with the Poisson's ratio set to zero and the transverse-to-axial permeability

ratio reduced by two orders of magnitude[10] (Figure 2.10). Figure 2.10a shows faster loading frequencies result in a loss of the homogeneous axial strain profile seen in Figure 2.9, with an increase in the strains occurring toward the site of loading and a reduction in the strains further away, consistent with the spatial strain pattern observed for the one-dimensional model (Figure 2.4). In addition, faster loading rates were shown to affect the transverse strains (2.10b) for this subset of parameter values; larger compressive transverse strains were shown to occur with faster frequencies of loading, especially toward the transverse centre.

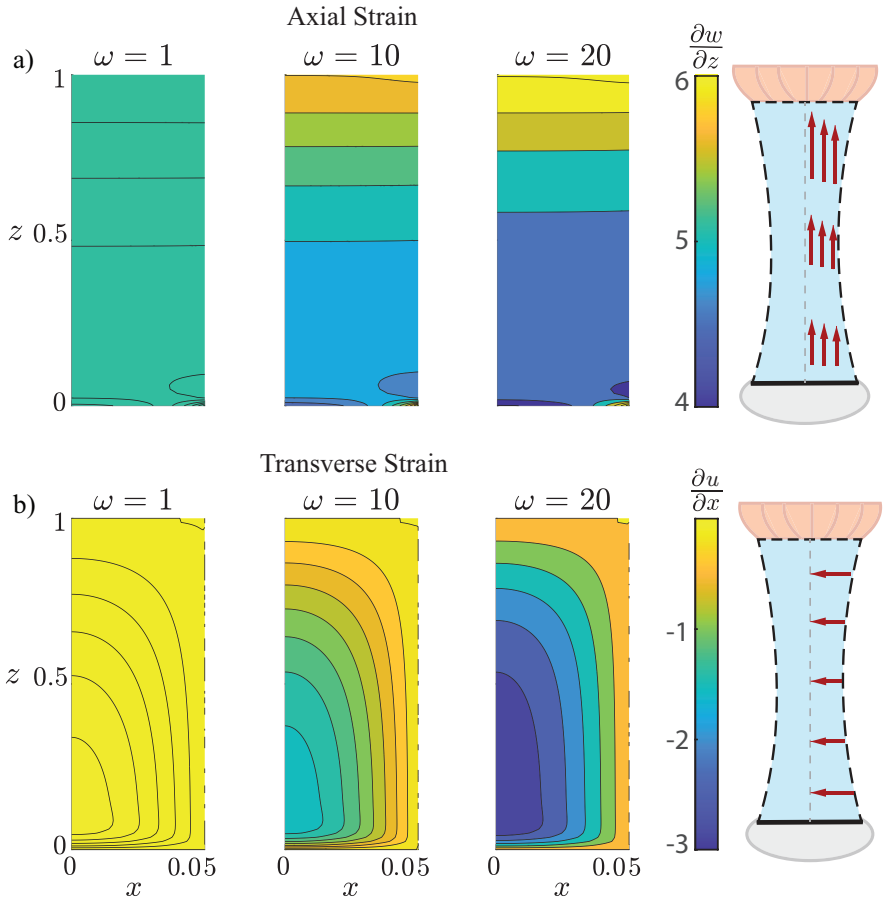


Figure 2.10: (a) Axial and (b) transverse strain profiles at maximum point of tension ($t = 3\pi/\omega$) showing variability in the strain profiles between different loading frequencies. Three frequencies of loading are investigated: $\omega = 1$, $\omega = 10$, and $\omega = 20$. We impose a homogenous stiffness $M = 1$, Poisson's ratio $\nu = 0$ and anisotropic permeability $k_x/k_z = 1/100$.

[10]Finite element modelling by Chen et al. (1998) demonstrated that this large ratio is possible in the setting of longitudinally arranged fibres.

Looking in the neighbourhood of the top and bottom right corners of Figure 2.9a, particularly large strains (yellow) can be seen. This likely arises due to an inconsistency between the two stress-boundary conditions (2.59b) and the conditions (2.59d) that prescribed the muscular origin of the tendon to act as a plate. Contrasting Figure 2.9 with Figure 2.10, these large axial strains predominantly occur in the case when a Poisson's ratio of 0.33[11] is imposed (Figure 2.9) and subsequently larger compressive transverse strains are generated. This is consistent with the fact that, when the Poisson's ratio is zero, the inconsistency with the plate condition ($\partial u/\partial x = 0$) and first stress free condition disappears. It is also evident from contrasting Figure 2.9a ($\omega = 1$) with Figure 2.10a ($\omega = 1$), that the high strains at the corners in Figure 2.9a do not appear to affect behaviour over the midportion.

In addition to the large strains observed over the corner regions, smaller axial and transverse strains (relative to the midportion) were observed at the origin and insertion away from the transverse boundary. After refining the mesh size to 160-by-160, the same boundary effects were observed (results not shown). Hence, this boundary effect is more likely the result of the plate condition, which prescribes $\partial u/\partial x = 0$, combined with the first stress free condition given in (2.59b). The first condition enforces that transverse strains near the axial boundaries must be small, while the latter condition prescribes that the axial strain must balance this small transverse strain. While we focus on understanding the mechanical environment at the midportion in this work, this finding suggests that these small regions near the origin and insertion could still exhibit interesting mechanical behaviour, warranting further investigation in future work.

In Figure 2.11 we display flux profiles at different time points within a loading cycle for varying frequencies of loading. The results are transposed onto a moving grid to assist in visualising how the flux changes throughout a loading cycle. The direction of flow is

[11] A Poisson's ratio of 0.33, when contrasted with $\nu = 0$, implies that larger compressive transverse strains occur when an axial tensile load is applied.

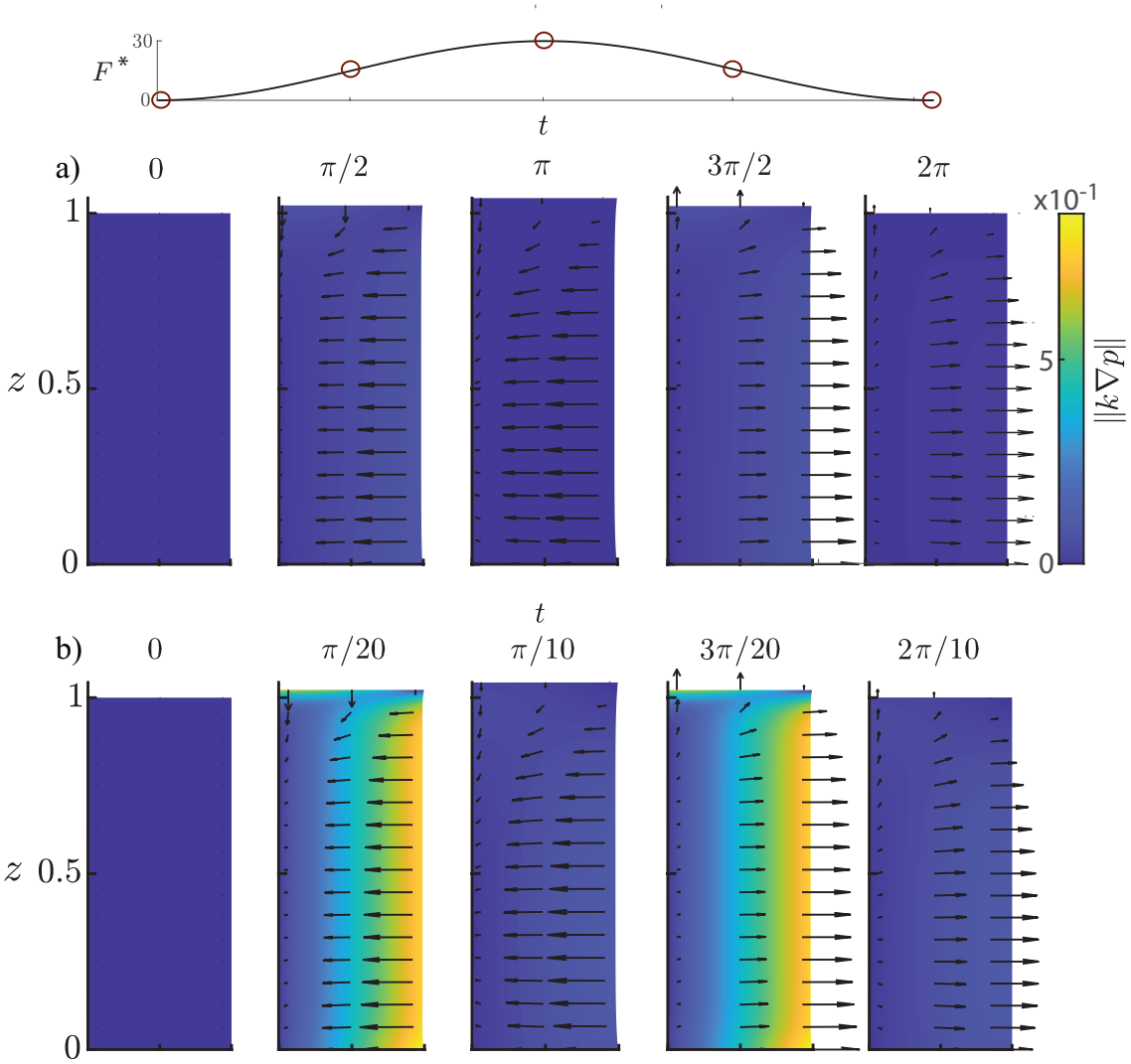


Figure 2.11: Flux at varying time points for (a) low-frequency $\omega = 1$ and (b) high-frequency loading $\omega = 10$. The heatmap gives the flux magnitude, whilst black arrows denote flow direction. Arrows are scaled for easy visualisation and hence only depict relative magnitudes within plots not between plots. The stiffness and permeability are isotropic $M = k = 1$. Results have been transposed onto a moving grid.

displayed by the black arrows while the underlying heatmap depicts the flux magnitude. It is clear that there is fluid movement into the tendon with tension. Looking at the flux magnitudes in Figure 2.11a relative to Figure 2.11b, it is apparent that the magnitude of the flux increases with increasing frequency. The highest flux occurs at the outer transverse boundary of the tendon (Figure 2.11b second and fourth plots). The pressures appear to equalise at the maximum and minimum points of forcing (Figure 2.11b third and fifth plots).

This positive relationship between the loading rate and flux magnitude was found to be insensitive to the Poisson's ratio ($\nu \in [-0.1, 0.5]$) and ratio of transverse to axial permeability ($k_x/k_z = 1/10, 1/100$) investigated. However, when a magnitude reduction in the transverse-to- axial permeability was imposed, there was a change in the spatial distribution of the flux, with higher magnitudes closer to the axial rather than transverse boundary (Appendix 2.4.1 Figure 2.21). This motivates us to focus on the isotropic case, as the literature supports fluid effects playing a role in tendinopathic changes (Lavagnino et al. 2008, Docking et al. 2013).

2.8.3.2 Effect of Material Properties on Mechanical Environment

We next look to investigate how localised reductions in the permeability or stiffness affect the mechanical environment that occurs with tendon loading. A reduction in the permeability and/or stiffness is imposed in a small region within the tendon midportion ($\mathcal{D} : W_0/(4L_0) < x < W_0/(2L_0)$, $2/5 < z < 3/5$) (Figure 2.12). The dimensionless stiffness and permeability over this region, which are constant across the region except where smoothing is imposed at the boundaries, are denoted by $M^{\mathcal{D}}$ and $k^{\mathcal{D}}$. We specifically investigate how these material property changes influence the mechanical environment with higher frequency loading ($\omega = 10$), as we are interested in how these changes modulate the tendon's tolerance to fast loading (Section 1.3.1).

Similar to the one-dimensional case, we define a metric to investigate the influence of material property changes on the maximum absolute strains and flux that occur over a cycle. As a metric, we consider the spatially averaged maximum (absolute maximum in the case of transverse strain and flux) observed over the damaged region. For example, for the axial strain we consider

$$\overline{\frac{\partial w}{\partial z}}^{\mathcal{D}} = \frac{1}{|\mathcal{D}|} \int \int_{\mathcal{D}} \max_t \frac{\partial w}{\partial z}(x, z, t) dx dz. \tag{2.62}$$

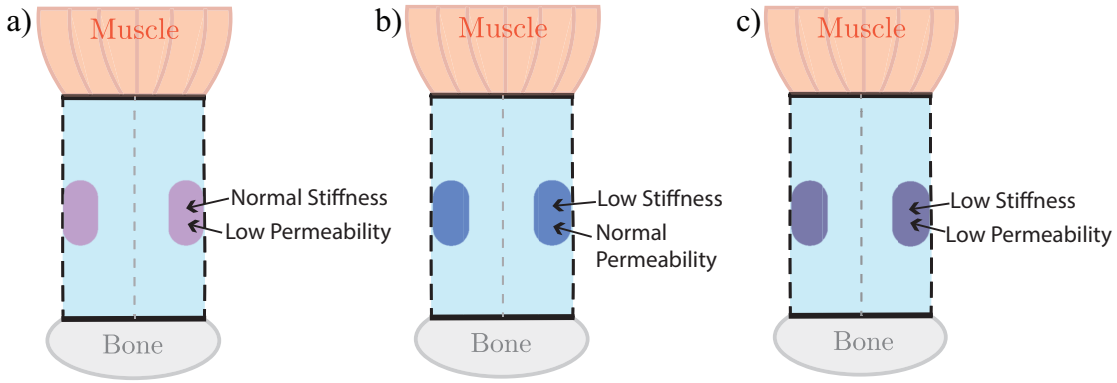


Figure 2.12: Potential damage scenarios at the tendon midportion: (a) Low permeability $k^{\mathcal{D}} = 0.6$, $M^{\mathcal{D}} = 1$ (b) Low stiffness $M^{\mathcal{D}} = 0.6$, $M^{\mathcal{D}} = 0.6$ (c) Low stiffness and permeability $M^{\mathcal{D}} = 0.6$, $M^{\mathcal{D}} = 0.6$.

Since we assume that cells are individually affected by the magnitude of local stimuli in their vicinity, we have taken the maximum at each spatial point over time independently. As such, this metric should be considered as a metric of what the average cell experiences rather than a snapshot of the global tendon strain/flux for any one time point.

In Figure 2.13 we display how localised reductions in the stiffness and permeability, imposed near the transverse boundary, influence the fluid flux during fast loading. The left

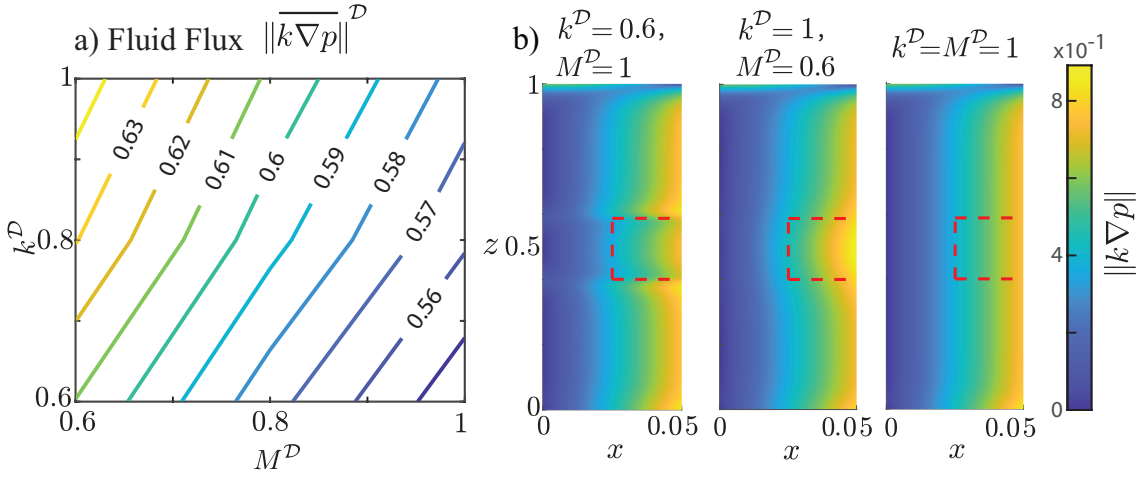


Figure 2.13: Influence of a localised reduction in stiffness and/or permeability on fluid flux for fast ($\omega = 10$) cyclic loading. The localised reduction is imposed at the outer boundary of the midportion (red dashed lines in b). (a) Average maximum flux over the damaged region for different imposed reductions in permeability and stiffness. (b) Flux magnitudes at time $t = \pi/20$ for (left to right) $k^d = 0.6$, $M^d = 0.6$ and homogeneous reference case $k^d = M^d = 1$.

contour plot displays the flux metric (equivalent to the strain metric defined in 2.62) for different relative reductions in the stiffness and strain. The right three plots in Figure 2.13b demonstrate the flux profiles when either a local reduction in the permeability or a local reduction in the stiffness is imposed, as well as the homogeneous stiffness and permeability case for reference. We have given the profiles at $\pi/20$, as larger fluxes were shown to occur at this time for the homogeneous case (Figure 2.11). However, whilst the magnitudes and direction of the flux changes throughout a loading cycle, the qualitative behaviour (in terms of relative magnitudes) shown in Figure 2.11 remained the same. Similar to the one dimensional model (Figures 2.6 and 2.7), a reduction in the stiffness served to increase the flux whilst a reduction in the permeability served to decrease it. Also in agreement with the one-dimensional model, we found that the relative effects of a reduction in either parameter were less substantial if the damaged region was imposed away from the permeable transverse boundary. In order to demonstrate this, in Appendix 2.23 we have reproduced the results given in Figure 2.13, instead accounting for a damaged region at the transverse centre.

Figure 2.14 conveys how localised reductions in the stiffness and permeability, imposed near the transverse boundary, influence the axial and transverse strains. We present contour plots showing the effects of different relative reductions in the stiffness and permeability on the axial (Figure 2.14a) and transverse (Figure 2.14c) strains. The stiffness, rather than permeability, appears to be the key property determining both the axial and transverse strains. We also show the axial (Figure 2.14b) and transverse (Figure 2.14d) strain profiles at the time point of maximum tension. Profiles are given both for the heterogeneous and homogeneous cases to facilitate comparison. It appears that substantially larger axial and transverse strains occur over damaged regions with low stiffness. Interestingly, for both the axial and transverse strain, there is a concurrent reduction in the strains occurring within the healthy tissue. In contrast to when a reduction in permeability was imposed, these findings are relatively insensitive to where the damaged region occurrs within the midportion; if we instead impose a damaged region at the transverse centre, similar patterns are observed for

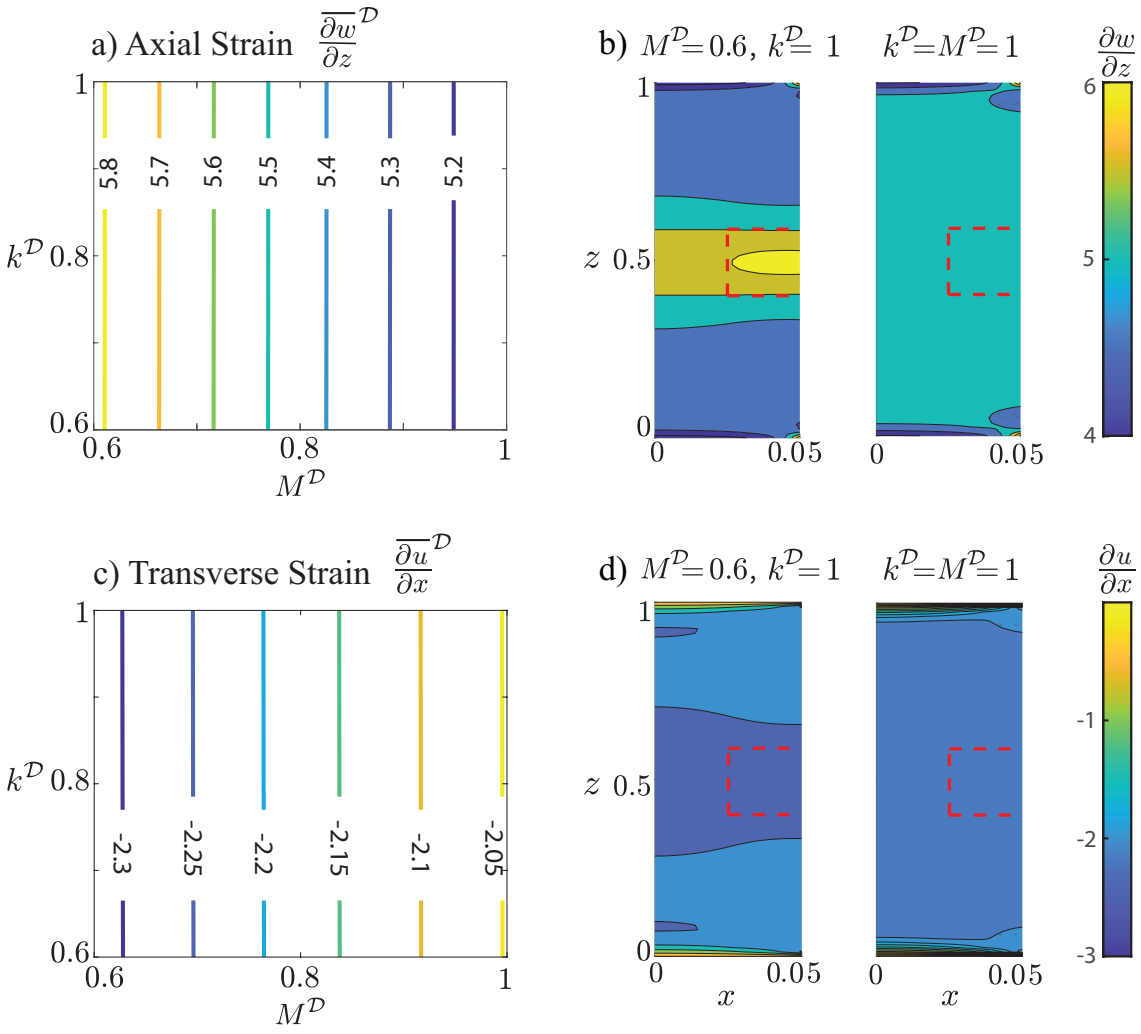


Figure 2.14: Influence of stiffness and permeability on strain for fast ($\omega = 10$) cyclic loading. The permeability is assumed isotropic and Poisson's ratio $\nu = 0.33$. The left column gives the average (a) maximum axial strain and (c) minimum transverse strain over the damaged region for different imposed reductions in permeability and stiffness. (b) Axial and (d) transverse strain profiles at time $t = \pi/10$ for $M^d = 0.4$ and $M^d = 1$ with homogeneous permeability $k^d = 1$.

the influence of stiffness on the strains occurring. If we instead impose a Poisson's ratio $\nu = 0$ and anisotropic permeability $k_x/k_z = 1/100$, a similar increase in the local strain over the region is observed, with a concurrent decrease in healthy surrounding tissue (Appendix 2.4.1 Figure 2.22).

In Figure 2.15 we contrast how reductions in the stiffness or permeability, imposed near the transverse boundary, affect the flux magnitude with the influence of the loading frequency. Across the loading frequencies explored, the loading frequency has a much more substantial

impact than a localised reduction in the stiffness or permeability.

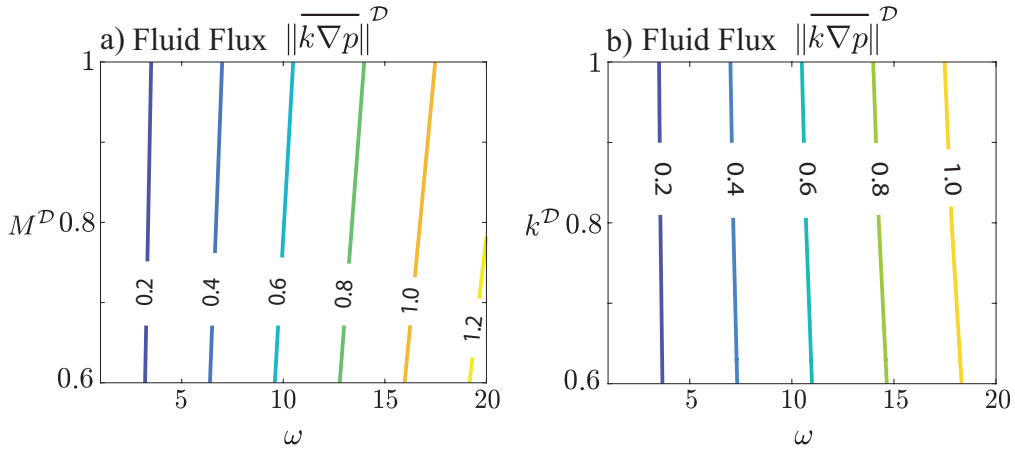


Figure 2.15: Influence of loading frequency vs a localised reduction in a) stiffness or b) permeability on maximum fluid flux over damaged region.

2.8.4 Summary of Parameter Changes on Mechanical Environment

In Table 2.3 a summary of the effects of local changes in the stiffness and permeability, and the loading frequency, on the solid strains and flux is displayed. In terms of the stiffness and permeability, we consider the effect of local reductions at the midportion, and the associated changes in the mechanical environment over those regions. In contrast, changes in the mechanical environment attributable to changes in the loading frequency refer to changes predicted for the entire tendon. An increase in the compressive transverse strain is synonymous with the transverse strain becoming more negative. Two arrows are used to denote a larger effect when contrasted with the effects from variations in other parameter values. For the loading frequency, we use $\uparrow$ /$\downarrow$ to denote an increase near the applied force and a reduction at the midportion and insertional end of the tendon (more heterogeneous).

Table 2.3: Summary of effects of material property changes and loading frequency on mechanical environment.

Parameter Changes	Axial Tensile Strain	Compressive Transverse Strain	Fluid Flux
$\nu = 0.3$, $k_x/k_z = 1$			
$\uparrow \omega$	-	-	$\uparrow\uparrow$
$\downarrow M$	$\uparrow\uparrow$	$\uparrow\uparrow$	$\uparrow$
$\downarrow k$	-	-	$\downarrow$
$\nu = 0$, $k_x/k_z = 1/100$			
$\uparrow \omega$	$\uparrow/\downarrow$	$\uparrow\uparrow$	$\uparrow\uparrow$

2.8.5 Discussion

The results for our two-dimensional poroelastic model of the tendon indicate that both the rate of loading and localised changes in the material properties affect the mechanical environment that occurs with tendon loading. Fluid stresses were shown to be highly dependent on the rate of loading whilst solid strains only showed this same rate dependence for a subset of parameter values, specifically when the transverse-to-axial permeability and Poisson's ratio were assumed to be low. Fluid was shown to flow into the tendon with tension, which was in contrast to the finite element model developed by Lavagnino et al. (2008). This is likely due to different assumptions regarding the Poisson's ratio, in which we only assessed variations in the ratio below the isotropic limit, whilst they imposed a global matrix Poisson's ratio above this. However, the pattern of fluid flow we observed was consistent with the results of Khayyeri et al. (2015) who employed a hyperelastic model. The fluid flux was influenced by both reductions in the permeability and the stiffness, whilst tendon strains were mostly impacted by changes in the stiffness.

For the case in which we assumed the permeability to be isotropic and Poisson's ratio 0.33,

the axial strain at the midportion was the same for both low and high frequencies of loading, suggesting it is unlikely a potential mechanism for maladaptation to high loading rates. However, this result also suggests a lack of positive adaptive benefit for low-frequency compared to high-frequency loading via this stimulus, at least when considered in isolation. These modelling results are in agreement with *in vivo* experimental results which have demonstrated relatively homogeneous axial strains to occur throughout the tendon with ramped loading, with the magnitude of these strains also showing no dependence on loading frequency (Kubo et al. 2002).

Given that the permeability and Poisson's ratio were two parameters in which a large range of values have been reported, we also investigated the effect of frequency on the mechanical environment with the Poisson's ratio set to zero and the transverse-to-axial permeability ratio set to 1/100. These represent a subset of reported values (Firminger et al. 2021, Federico et al. 2008, Butler et al. 1997). In this setting, we found that the loading rate had a more substantial effect on the axial strain, with higher loading rates reducing the axial strain at the midportion and toward the insertion. This results paralleled the one-dimensional model, which is unsurprising given these values for the permeability and Poisson's ratio promote fluid movement in the axial direction and reduce the transverse displacement. In this case, larger axial strains could explain the positive adaptation that occurs at the midportion with low-frequency loading. Furthermore, it suggests that fast loading could be problematic for the tendon midportion through under stimulation.

Higher fluid fluxes were shown to occur with higher rates of loading, suggesting that higher fluid shear could be implicated in the maladaptation that occurs with fast loading. Since the model also demonstrated that a reduction in permeability affected the flux but not tensile or compressive strains, this suggests that the increased deposition of proteoglycans[12] seen in

[12]Proteoglycans are key components of the tendon formed by sugar molecules attached to a protein core. Whilst their function is not fully known, their is good evidence that they, at least in part,

tendinopathy, might be a response to high fluid shear. This implication of fluid flux/shear as a mechanism for tendinopathic changes is in agreement with Lavagnino et al. (2008), who also found higher fluid shear to occur with faster loading rates. The positive relationship between loading rate and flux was insensitive to variations in the Poisson's ratio and transverse-to-axial permeability ratio. However, a reduction in the transverse-to-axial permeability ratio did affect the spatial distribution of the flux. When the permeability was assumed isotropic, large fluxes occurred toward the outer boundary of the midportion. When a reduction in the transverse-to-axial permeability was imposed, larger fluxes occurred toward the origin than at the midportion. Hence, in this parameter setting, there is less support for fluid shear causing damage at the midportion.

Whilst the fluid flux predictions in the case of a lower transverse to axial permeability ratio and zero Poisson's ratio, did not strongly support high fluid shear as a mechanism for tendinopathic changes, a notable increase in the transverse strain magnitude within the midportion occurred with increasing frequency in this case. Findings that the transverse strain magnitude is positively correlated with loading rate support the theory put forward by Cook et al. (2012) that, when detrimental forms of load are applied, the tendon cells in the Achilles mid-portion are potentially subject to compression from the solid matrix. However, in order to explain the increase in proteoglycans seen in midportion tendinopathy, previous authors (Cook et al. 2012, Grigg et al. 2009) have suggested that they may be deposited in order to reduce the permeability, thereby protecting from these high transverse strains. This hypothesis is not supported by our results, which suggest that a reduction in the permeability only serves to reduce the fluid flux. It does not however oppose the possibility that proteoglycans reduce the transverse strain in some other manner, such as by a change in the Poisson's ratio or Young's modulus. This is also a case where the results may be highly dependent on whether the Poisson's ratio is allowed to exceed the isotropic limit. We note

serve to reduce the permeability (Cook et al. 2009, Jurvelin et al. 1988, Tavakoli Nia et al. 2015).

that this theory put forward by these authors, regarding the role of proteoglycans, was based on the assumption that fluid is expelled from the tendon with tension and hence a reduction in permeability would serve to preserve fluid volume thereby reducing transverse strain. Whilst we checked that the transverse strain was independent of localised reductions in the permeability across a range of Poisson's ratios, the model does not permit us investigating ranges above the isotropic limit.

It has been suggested that rehabilitation regimes may not directly affect local areas of damage within the tendon but instead modulate the material properties of surrounding tissues (Docking et al. 2014). That is 'treat the donut not the hole'. Specifically, authors have suggested that enhanced stiffness of the outer tendon can make up for a loss of stiffness due to damage. If we assume that local axial tensile strains provide a positive stimulus to the cells, leading to an increase in local stiffness due to enhanced type I collagen deposition, then our work supports that low stiffness damaged regions may be more responsive to axial tensile loading, since these regions display proportionally larger axial strains to the rest of the tendon. Our model, however, does not incorporate microtears of collagen fibres which can occur in later stages of tendinopathy. With such tearing there is discontinuity of the fibres and hence a reduction in the stresses transferred to the cell in this region is more probable (Arnoczky et al. 2007). It has actually been suggested, in the well known continuum model for tendinopathy, that tendinopathic tendons may be quite responsive in early disease stages but that irreversible damage occurs at later stages (Cook et al. 2009). Our results fit appropriately into this picture, with our model being more applicable to the earlier disease stage. This result, regarding healthy regions of the tendon exhibiting lower axial strains, is also an important result when considering global axial strain measurements. The concurrent reduction in the strain of healthy tissue indicates that global strain measurements may not be significantly altered in the setting of local reductions in stiffness. This may explain why there is only moderate evidence supporting a reduction in stiffness with tendinopathy and demonstrates that local measurements may be of more use. These results are also

in good agreement with previous modelling work of cartilage which suggests that global strain measurements are not substantially impacted by localised reductions in the aggregate modulus (Wang et al. 2001).

Contrasting the one- and two-dimensional model results, when an isotropic permeability was imposed, the strain profile for the two-dimensional model showed a much greater degree of homogeneity than the one dimensional model which predicted a decay in the strain away from the sight of loading. Similar qualitative behaviour was observed when a zero Poisson's ratio and an anisotropic permeability were prescribed in the two-dimensional case. These parameter values served to encourage greater deformation and fluid flow along the longitudinal dimensional, making the two-dimensional model more consistent with the one-dimensional model. However, the one-dimensional model clearly does not capture variations in the transverse strain. To predict the flux and axial strain, it would be reasonable to use the one-dimensional model, should further studies support the use of parameter values in these ranges. The one-dimensional model was substantially faster[13] to implement (taking several seconds rather than several minutes) and could be easily modified to introduce further complexities. Furthermore, only one elastic constant was needed to parameterise the one-dimensional model, which is especially beneficial given uncertainty regarding the Poisson's ratio.

The analytical and finite difference approach that we have taken here serves as a useful comparison to the previous finite element and multiscale models used to investigate tendon mechanics. Our results demonstrate that high fluid fluxes occur for simple poroelastic materials exposed to high loading frequencies, are hence are not a facet of the large Poisson's ratios used, or complex microscale constitutive behaviour implemented, in previous models (Lavagnino et al. 2008, Ahmadzadeh et al. 2013). In contrast, fluid exudation out of the ten-

[13]All numerical simulations were performed on a Thinkpad Core i5 laptop.

don with tension requires the model to incorporate a component that allows for a transverse contraction of the solid matrix. Lavagnino et al. (Lavagnino et al.) predicted that the strain rate has an effect on the local strains, in contrast to our results which only demonstrated this to occur when low Poisson's ratios were implemented. This discrepancy in findings could be attributable to the anisotropy in material properties (Poisson's ratio and Young's modulus) accounted for in their model, while we only accounted for an anistropic permeability. A key benefit of the finite difference approach taken here was the speed of implementation. This will facilitate our analysis in the following chapter, in which we integrate this model into an adaptation model for tendon, requiring multiple implementations of this poroelastic mechanical model.

2.8.6 Conclusions and Future Work

In this chapter we have utilised a poroelastic model to investigate how the mechanical environment of tendons is impacted by the loading rate and localised changes in material properties consistent with damage. Using the knowledge that low-frequency high-magnitude loading causes a reduction in tendon pain, whilst high-frequency high-magnitude loading is a key aetiological factor for damage (Malliaras et al. 2013, Malliaras et al. 2017), we have identified potential mechanisms for positive and negative adaptive changes in tendinopathy. Our model predicted higher fluid fluxes to occur with high frequency loading, giving a possible mechanism for the maladaptation at the tendon midportion, which can occur with these forms of load. Specifically, the flux was especially high near the transverse boundary of the midportion, indicating that damage is most likely to occur here. Contrary to our initial hypothesis however, results also suggested that substantially larger axial strains do not occur with low-frequency loading, at least when the permeability is assumed isotropic. Hence, axial strain, when considered in isolation, may not be a potential mechanism for the positive adaptive changes with this form of load. Instead our results suggests that the fluid flux or axial strain to fluid flux ratio may be of more importance.

As we expected, we found that localised reductions in the stiffness predominantly affected solid deformation, whilst both reductions in the permeability and stiffness had a small impact on the flux. Assuming cells respond to these stresses in an adaptive manner, this suggests that proteoglycan deposition, which serves to reduce permeability, is more likely deposited in response to fluid shear. Conversely type I collagen, which modulates the tensile stiffness, is more likely deposited in response to axial strain.

Our results were relatively sensitive to the Poisson's ratio and transverse-to-axial permeability ratio. In the case of a zero Poisson's ratio and anisotropic permeability, our results suggested that either large negative transverse strains or under-stimulation due to lower axial strains, give a more likely mechanism for midportion damage with fast loading than fluid shear. In the former case, larger transverse strains occurred at the centre, indicating that damage is most likely to occur away from the transverse boundary in this case. In the succeeding chapters we aim to gain further insight into how maladaption occurs by developing an adaptation model (modelling both beneficial and maladaptive changes) which couples this poroelastic model with in vitro and clinical findings, and by using computer vision techniques to investigate the spatial distribution of tendon damage within the midportion. The lack of implication of fluid effects in the tendon's response to loading, when an anisotropic permeability was imposed, motivates us to use an isotropic permeability in the adaptation model.

There are several limitations of our model that we must consider when drawing conclusions from these results. Obviously, in reality tendons are three dimensional structures and hence our results were potentially effected by this reduction to two dimensions. However, many clinicians also use two-dimensional longitudinal tendon images to assess the degree of damage in tendinopathy, assuming this is representative of the level of damage across the entire depth. Secondly, as highlighted several times, there are discrepancies among reported values for several tendon parameters, which mean results of any poroelastic model of the tendon

must be interpreted with some caution. Another potential cause of error in our model is the assumption that tendons always operate under a linear small strain regime. Whilst this does agree with physical loading, previous authors have highlighted that such an assumption may cause issues when considering local changes in the material properties, as this may allow for finite strains to occur (MacMinn et al. 2016, Wang et al. 2001). This should be taken into consideration with further extensions to this work, especially in the case where the permeability is assumed to be strain dependent (MacMinn et al. 2016). Since we have set this model up in a way that relies on minimal constitutive relations at the micro-scale, there is great scope to build on this work depending on the key area of investigation. Extensions that would be especially pertinent to understand tendon dynamics in relation to physical loading would be the incorporation of an anisotropic stiffness and a strain dependent permeability. Should more *in vivo* evidence come to light supporting that the tendon does show viscoelastic behaviour of significance, for the rates of interest in this work, then this is also a key extension that should be included within the model. The lack of incorporation of these factors is also one of the key limitations of our model, however, as these strain dependent properties have been incorporated in previous models of tendons, we focused on incorporating heterogeneous material properties here. As such, one could impose both heterogeneous and strain dependent material properties by pairing our work with that of previous authors. Our work has also highlighted the need for further experimental work to inform mathematical modelling, specifically in the area of the Poisson's ratio and tendon permeability. Furthermore, the contribution of proteoglycans to material properties other than the Young's modulus, such as the Poisson's ratio, requires further investigation.

2.A Further Mathematical Background

2.A.1 Hooke's Law and Plane Stress Reductions

In three dimensions, Hooke's law, relating the stress and strain in a linear isotropic purely elastic material (or an isotropic purely elastic material undergoing small deformations), is given by

$$\begin{bmatrix} \varepsilon_{xx} \\ \varepsilon_{yy} \\ \varepsilon_{zz} \\ \varepsilon_{xy} \\ \varepsilon_{xz} \\ \varepsilon_{yz} \end{bmatrix} = \frac{1}{E} \begin{bmatrix} 1 & -\nu & -\nu & 0 & 0 & 0 \\ -\nu & 1 & -\nu & 0 & 0 & 0 \\ -\nu & -\nu & 1 & 0 & 0 & 0 \\ 0 & 0 & 0 & 2(1+\nu) & 0 & 0 \\ 0 & 0 & 0 & 0 & 2(1+\nu) & 0 \\ 0 & 0 & 0 & 0 & 0 & 2(1+\nu) \end{bmatrix} \begin{bmatrix} \sigma_{xx} \\ \sigma_{yy} \\ \sigma_{zz} \\ \sigma_{xy} \\ \sigma_{xz} \\ \sigma_{yz} \end{bmatrix}, \tag{2.63}$$

where ε_{ij} and σ_{ij} denote the strain and stress components, respectively. Equation (2.63) can be inverted to obtain the stresses in terms of the strains

$$\begin{bmatrix} \sigma_{xx} \\ \sigma_{yy} \\ \sigma_{zz} \\ \sigma_{xy} \\ \sigma_{xz} \\ \sigma_{yz} \end{bmatrix} = \frac{E}{(1+\nu)(1-2\nu)} \begin{bmatrix} 1-\nu & \nu & \nu & 0 & 0 & 0 \\ \nu & 1-\nu & \nu & 0 & 0 & 0 \\ \nu & \nu & 1-\nu & 0 & 0 & 0 \\ 0 & 0 & 0 & (1-2\nu)/2 & 0 & 0 \\ 0 & 0 & 0 & 0 & (1-2\nu)/2 & 0 \\ 0 & 0 & 0 & 0 & 0 & (1-2\nu)/2 \end{bmatrix} \begin{bmatrix} \varepsilon_{xx} \\ \varepsilon_{yy} \\ \varepsilon_{zz} \\ \varepsilon_{xy} \\ \varepsilon_{xz} \\ \varepsilon_{yz} \end{bmatrix}. \tag{2.64}$$

To facilitate interpretation of the Young's modulus E and Poisson's ratio ν, we consider (2.63) in the setting of uniaxial stress $\sigma_{yy} = \sigma_{zz} = \sigma_{xy} = \sigma_{xz} = \sigma_{yz} = 0$. In this case

$$\varepsilon_{xx} = \frac{1}{E}\sigma_{xx}, \;\; \varepsilon_{yy} = \varepsilon_{zz} = -\frac{\nu}{E} \tag{2.65}$$

$$\Longrightarrow \varepsilon_{yy} = \varepsilon_{zz} = -\nu\varepsilon_{xx}. \tag{2.66}$$

Hence, in the case of a unilateral applied stress, the Young's modulus represents the ratio of stress to strain: $E = \sigma_{xx}/\varepsilon_{xx}$. The Poisson's ratio represents the negative of the ratio of strain in the direction normal to the stress and the strain perpendicular to the stress: $\nu = -\varepsilon_{yy}/\varepsilon_{xx}$.

Recalling the constitutive law (2.22) presented in text:

$$\boldsymbol{\sigma}' = \Lambda tr(\boldsymbol{\varepsilon})I + (M - \Lambda)\boldsymbol{\varepsilon}, \tag{2.67}$$

to obtain M and Λ in terms of ν and E, we rearrange (2.64) into the form given by (2.67). This provides the relation (2.23) given in text:

$$M = \frac{E(1-\nu)}{(1+\nu)(1-2\nu)}, \quad \Lambda = \frac{E\nu}{(1+\nu)(1-2\nu)}. \tag{2.68a}$$

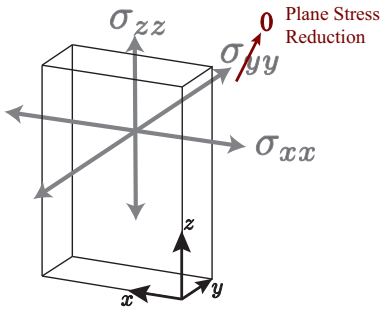


Figure 2.16: Plane stress reduction for thin material. Zero stress is assumed in the y-dimension.

Consideration must be take when inverting (2.63) in the case of a one- or two-dimensional reduction. A plane stress reduction can be used to reduce the problem from three to two dimensions (Figure 2.10). We assume zero normal and shear stress in $\boldsymbol{e_z}$: $\sigma_{yy} = \sigma_{xy} = \sigma_{yz} = 0$. This assumption is often made for a material which is thin in the third dimension. Considering Hooke's law (2.63) in this plane stress setting,

it is evident that the strains ε_{xx}, ε_{zz} and ε_{xz} are dependent only on the equivalent stresses σ_{xx}, σ_{zz} and σ_{xz}. As such, to obtain the in-plane stress-strain relations for σ_{xx}, σ_{zz} and σ_{xz}, we invert a reduced form of the matrix (2.63), excluding columns and rows corresponding to the z-dimension. This leads to

$$\begin{bmatrix} \sigma_{xx} \\ \sigma_{zz} \\ \sigma_{xz} \end{bmatrix} = \frac{E}{(1-\nu^2)} \begin{bmatrix} 1 & \nu & 0 \\ \nu & 1 & 0 \\ 0 & 0 & (1-\nu)/2 \end{bmatrix} \begin{bmatrix} \varepsilon_{xx} \\ \varepsilon_{zz} \\ \varepsilon_{xz} \end{bmatrix}. \tag{2.69}$$

The shear strain ε_{yy} can then be calculated from

$$\varepsilon_{yy} = -\frac{\nu}{E}\left(\sigma_{xx} + \sigma_{zz}\right), \tag{2.70}$$

whilst $\varepsilon_{xy} = \varepsilon_{yz} = 0$. Equation (2.69) has a different leading coefficient on the RHS when compared to (2.64). Rearranging (2.69) into the form given by (2.67), we find

$$M = \frac{E}{(1-\nu^2)}, \quad \Lambda = \frac{E\nu}{(1-\nu^2)}. \tag{2.71a}$$

In a similar manner for the one dimensional case, assuming zero stress in the other two dimensions, we obtain the relation $\varepsilon_{xx} = \sigma_{xx}/E$. Again, considering the stress-strain relation given in (2.22), it is easy to see that $E = M$ in the one-dimensional plane stress case and Λ is eliminated.

To facilitate interpretation of the oedeometric modulus M and Lamé's first parameter Λ, we consider (2.64) in the setting of uniaxial deformation $\varepsilon_{yy} = \varepsilon_{zz} = \varepsilon_{xy} = \varepsilon_{xz} = \varepsilon_{yz} = 0$ (when deformation in these directions is prevented by a solid boundary for example). In this case

$$\sigma_{xx} = M\varepsilon_{xx}, \;\; \sigma_{yy} = \sigma_{zz} = \Lambda\varepsilon_{xx}. \tag{2.72}$$

Hence, in the case of a unilateral deformation, M represents the ratio of stress to strain $M = \sigma_{xx}/\varepsilon_{xx}$ while Λ relates the transverse stress to uniaxial strain $\Lambda = \sigma_{yy}/\varepsilon_{xx}$.

2.A.2 Small Strain Theory and Lagrangian and Eulerian Descriptions

The Lagrangian description of solid or fluid mechanics involves following quantities, such as the pressure, related to a particle. The current location of the particle is given by $\boldsymbol{X}(\boldsymbol{X}_0, t)$, where $\boldsymbol{X}_0$ is some reference configuration. In contrast, the Eulerian description describes properties related to spatial points $\boldsymbol{x}$ which are constant in time, though different particles may flow through that point. The Lagrangian perspective is usually thought of as the most natural way to describe the motion of objects when finite strains occur. However, the Eulerian description is often easier to implement when only small strains occur. In continuum mechanics, small strain theory describes the approach in which the displacements of the material body are assumed to be much smaller than the dimensions of the body itself. With this approach, we can assume that the geometry and constitutive properties of the material are unchanged by this small deformation. For example, consider a quantity, such as the pressure. We can convert between the Lagrangian and Eulerian description by using the material derivative

$$\frac{Dp}{Dt}(\boldsymbol{X}, t) = \frac{dp}{dt}(\boldsymbol{x}, t) + (\boldsymbol{v}_s \cdot \nabla)p(\boldsymbol{x}, t). \tag{2.73}$$

In the small strain case, all dimensionless quantities relating to the deformation are also of order ($p \sim \nabla \boldsymbol{v}_s << 1$). Hence, at first order,

$$\frac{Dp}{Dt}(\boldsymbol{X}, t) \approx \frac{dp}{dt}(\boldsymbol{x}, t). \tag{2.74}$$

Since the quantities of interest do no differ at first order between the spatial coordinates $\boldsymbol{X}$ and $\boldsymbol{x}$, this allows us to reduce our domain to one which is stationary, and describe the

problem in a Eulerian framework.

2.B Details of Numerical Solution

Taking the derivative with respect to z (recalling Equation (2.41)) of the long-time solution for the strain (2.50), the long-time solution for the flux is given by

$$-\frac{\partial p}{\partial z} = \frac{A^*\sqrt{\omega/2}}{|\Omega_m|}\left(\frac{e^{\sqrt{\omega/2}\,(z+1)}\left(\cos(\theta_{-+})-\sin(\theta_{-+})\right)+e^{-\sqrt{\omega/2}\,(z-1)}\left(\sin(\theta_{+-})-\cos(\theta_{+-})\right)}{2\cos(2\sqrt{\frac{\omega}{2}})+e^{2\sqrt{\omega/2}}+e^{-2\sqrt{\omega/2}}}\right)$$
$$+\frac{A^*\sqrt{\omega/2}}{|\Omega_m|}\left(\frac{e^{\sqrt{\omega/2}\,(z-1)}\left(\cos(\theta_{++})-\sin(\theta_{++})\right)+e^{-\sqrt{\omega/2}\,(z+1)}\left(\sin(\theta_{--})-\cos(\theta_{--})\right)}{2\cos(2\sqrt{\frac{\omega}{2}})+e^{2\sqrt{\omega/2}}+e^{-2\sqrt{\omega/2}}}\right), \tag{2.75}$$

where θ_{ij} are as defined in 2.46.

2.C Details of Numerical Solution

2.C.1 Numerical Procedure for One-Dimensional Model

A finite difference mesh of size $N+1$ nodes, with a spatial step size of $h = 1/N$ is used. We let w_i denote the value of the displacement at the spatial point $z = i\,h$. To implement the boundary conditions (2.40) we set $w_0 = 0$ and utilise a ghost node $i = -1$ where

$$\frac{\partial^2 w_0}{\partial z^2} \approx \frac{w_1 - 2w_0 + w_{-1}}{h^2}. \tag{2.76}$$

One sided backward differences are used at the outer boundary

$$\frac{\partial w_{N_z}}{\partial z} \approx \frac{3w_{N_z} - 2w_{N_z-1} + w_{N_z-2}}{2h}, \tag{2.77}$$

$$\frac{\partial^2 w_{N_z}}{\partial z^2} \approx \frac{-2w_{N_z} - 5w_{N_z-1} + 4w_{N_z-2} + w_{N_z-3}}{h^2}, \tag{2.78}$$

$$\frac{\partial^3 w_{N_z}}{\partial z^3} \approx \frac{5w_{N_z} - 18w_{N_z-1} + 24w_{N_z-2} - 14w_{N_z-3} + 3w_{N_z-4}}{2h^3}, \tag{2.79}$$

$$\frac{\partial^3 w_{N_z-1}}{\partial z^3} \approx \frac{5w_{N_z-1} - 18w_{N_z-2} + 24w_{N_z-3} - 14w_{N_z-4} + 3w_{N_z-5}}{2h^3}. \tag{2.80}$$

We utilise central difference approximations for the first and second derivatives on the interior $i = 1, ..., N-1$, and for the third derivative at $i = 1, ..., N$:

$$\frac{\partial w_i}{\partial z} \approx \frac{w_{i+1} - w_{i-1}}{2h}, \tag{2.81}$$

$$\frac{\partial^2 w_i}{\partial z^2} \approx \frac{w_{i+1} - 2w_i + w_{i-1}}{h^2}, \tag{2.82}$$

$$\frac{\partial^3 w_i}{\partial z^3} \approx \frac{w_{i+2} - 2w_{i+1} + 2w_{i-1} - w_{i-2}}{2h^3}. \tag{2.83}$$

In order to investigate convergence of the one-dimensional model we considered the metric

$$\varphi = \frac{\left\| \int_0^{2\pi/10} \mathbf{w}_h - \mathbf{w}_{\frac{h}{2}}\, dt \right\|_2}{\left\| \int_0^{2\pi/10} \mathbf{w}_{\frac{1}{20}}\, dt \right\|_2}, \tag{2.84}$$

where $\mathbf{w}$ denotes the displacement over ten consistent equidistant nodes. The time derivative is calculated numerically by the trapezoidal rule. The loglog plot of the convergence metric for varying h is given in Figure 2.17. We chose $N = 150$ to be the final grid size, as the *ODE15s* solver was still able to find a solution in < 1 second.

Since second order accurate finite difference approximations were used to calculate all

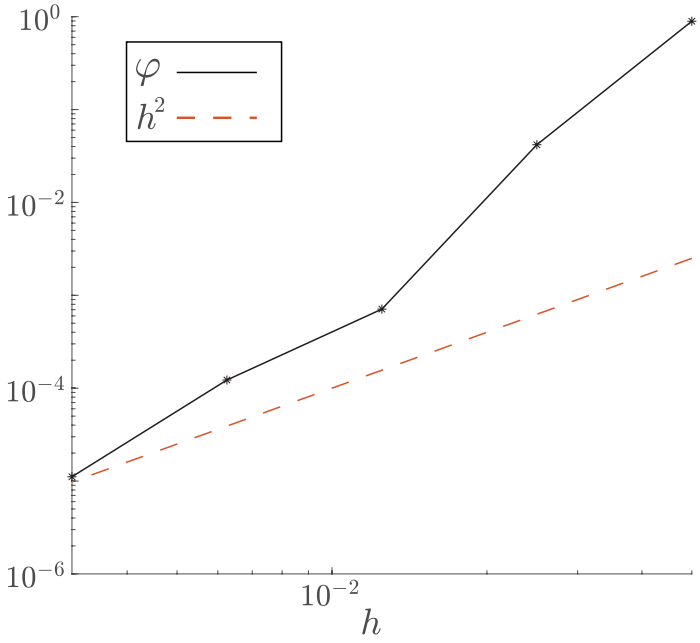


Figure 2.17: Loglog plot of relative error against spatial step size - demonstrating spatial convergence of one-dimensional numerical results. The dashed line is h^2, indicating the slope for a second order accurate scheme.

derivatives, we expect our solution to be at least accurate to second order. In Figure 2.17 we have plotted h^2 with a dashed line displaying the slope for a second order method. The one-dimensional numerical scheme converges at a slightly faster rate than given by this dashed line.

Stability of the numerical scheme is demonstrated through agreement between the analytical long-time solution and numerical solution in Section 2.7.3.1 Figure 2.3.

2.C.2 Numerical Procedure for Two-Dimensional Model

We utilised a mesh with $(N_x + 1)$-by-$(N_z + 1)$ nodes, representing the transverse and axial dimensions respectively. The governing equations (2.58) are solved on the interior nodes $i = 1, ..., N_x - 1$, $j = 1, ..., N_z - 1$, with all derivatives approximated by a second order central

difference scheme:

$$\frac{\partial u_{i,j}}{\partial x} \approx \frac{u_{i+1,j} - u_{i-1,j}}{2h_x}, \quad \frac{\partial u_{i,j}}{\partial z} \approx \frac{u_{i,j+1} - u_{i,j-1}}{2h_z}, \tag{2.85}$$

$$\frac{\partial^2 u_{i,j}}{\partial x^2} \approx \frac{u_{i+1,j} - 2u_{i,j} + u_{i-1,j}}{h_x^2}, \quad \frac{\partial^2 u_{i,j}}{\partial z^2} \approx \frac{u_{i,j+1} - 2u_{i,j} + u_{i,j-1}}{h_z^2}, \tag{2.86}$$

$$\frac{\partial^2 u_{i,j}}{\partial x \partial z} \approx \frac{(u_{i+1,j+1} - u_{i-1,j+1}) - (u_{i+1,j-1} - u_{i-1,j-1})}{4h_x h_z}, \tag{2.87}$$

where $u_{i,j}$ denotes the transverse displacement in the x-dimension, at the point $(x, z) = (i\,h_x, j\,h_z)$. The derivatives of w and p are calculated similarly. The step sizes are given by $h_x = W_0/(2L_0N_x)$ and $h_z = 1/N_z$. A one-sided difference is used to determine the displacement and pressure at the boundaries. Hence, on the exterior

$$u_{0,j} = u_{i,0} = u_{i,N_z} = p_{N_x,j} = p_{i,0} = 0, \tag{2.88a}$$

$$w_{0,j} = \frac{4w_{1,j} - w_{2,j}}{3}, \quad p_{0,j} = \frac{4p_{1,j} - p_{2,j}}{3}, \quad p_{i,0} = \frac{4p_{i,1} - p_{i,2}}{3}, \tag{2.88b}$$

whilst the displacement at $i = N_x$ is determined by setting

$$0 = \frac{3u_{N_x,j} - 4u_{N_x-1,j} + u_{N_x-2,j}}{2h_x} + \nu \frac{w_{N_x,j+1} - w_{N_x,j-1}}{2h_z}, \tag{2.89a}$$

$$0 = \frac{3w_{N_x,j} - 4w_{N_x-1,j} + w_{N_x-2,j}}{2h_x} + \frac{u_{N_x,j+1} - u_{N_x,j-1}}{2h_z}. \tag{2.89b}$$

In order to impose a force at the boundary, the boundary condition (2.59d) is discretised and the integral approximated by the trapezoidal rule:

$$\frac{h_x}{2} \sum_{i=0}^{N_x-1} \left(\frac{3w_{i,N_z} - 4w_{i,N_z-1} + w_{i,N_z-2}}{2h_z} + \frac{3w_{i+1,N_z} - 4w_{i+1,N_z-1} + w_{i+1,N_z-2}}{2h_z} \right) = \frac{A^*}{(2W_{y0}/L_0)} (1 - \cos(\omega t)) \tag{2.90a}$$

Figure 2.18 displays the finite difference grid corresponding to the two-dimensional numerical scheme. The bottom panel depicts the grid for u, w and p. White nodes display the points at which the variable is prescribed, according to boundary conditions. Black nodes display points over which the scheme solves for the variable.

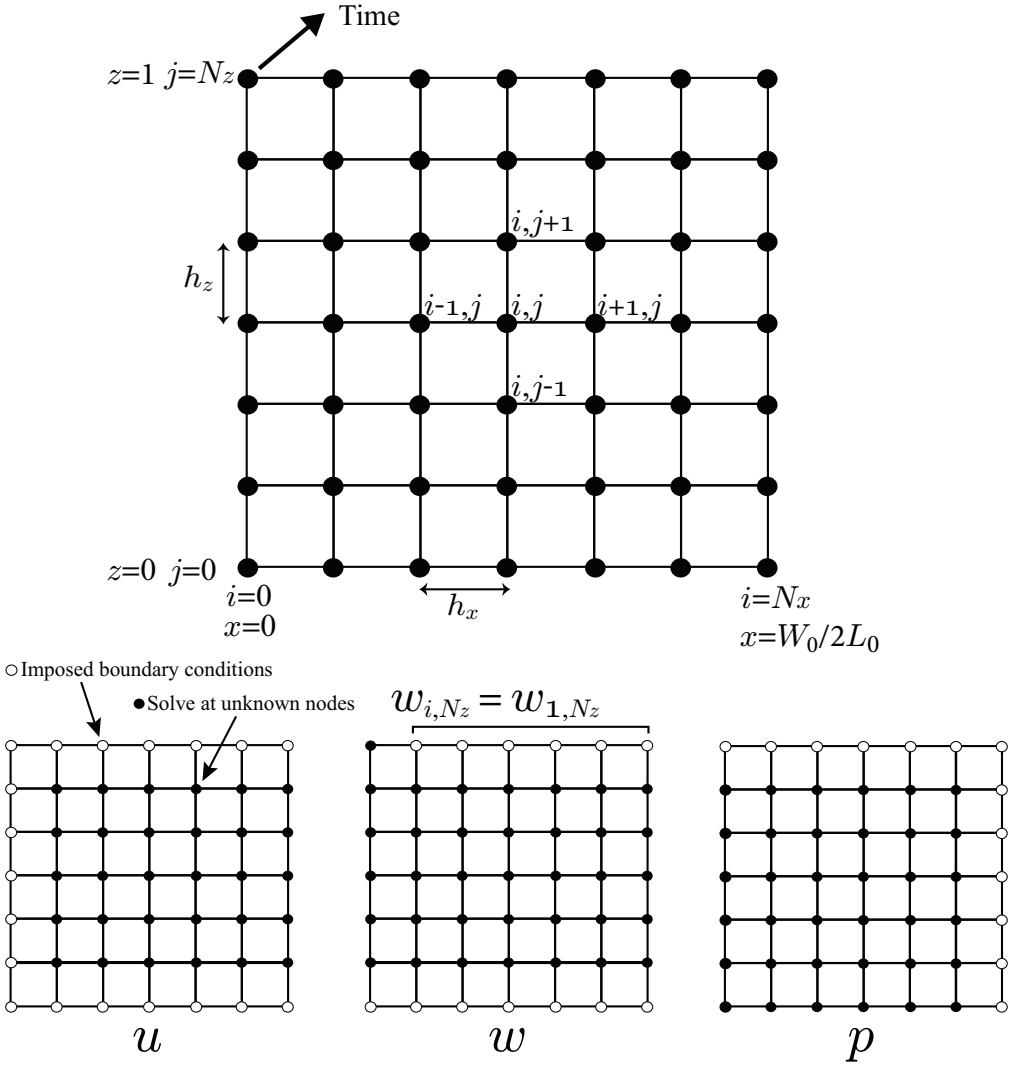


Figure 2.18: Numerical grid for two-dimensional model with bottom grids showing unknown nodes for each variable. At each time point unknown values for $u_{i,j}$, $w_{i,j}$ and $p_{i,j}$ are solved at each of the black nodes.

In order to use the *ODE15s* solver we rearrange the discretised form of the governing equations (2.58) on the interior, as well as the stress free (2.89) and forcing conditions (2.90a)

at the boundary, such that they can be expressed in the form

$$\boldsymbol{M}\frac{\partial}{\partial t}\begin{bmatrix}\boldsymbol{u}\\ \boldsymbol{w}\\ \boldsymbol{p}\end{bmatrix} = f(t, \begin{bmatrix}\boldsymbol{u}\\ \boldsymbol{w}\\ \boldsymbol{p}\end{bmatrix}),$$

where $\boldsymbol{M}$ is a mass matrix of constants, and $\boldsymbol{u}$, $\boldsymbol{w}$ and $\boldsymbol{p}$ are vectors giving the time dependent unknown displacements and pressure for which we need to solve. Here $\boldsymbol{u}$ is a vector of length $(N_x)(N_z-1)$ and includes $u_{i,j}$ at all interior nodes, in addition to the transverse boundary $i = N_x$, $j = 1, ..., N_z - 1$, such that

$$\boldsymbol{u} = (u_{1,1}, u_{1,2}, ..., u_{1,N_z-1}, u_{2,1}, u_{2,2}, ..., u_{N_x-1,N_z-1}, u_{N_x,1}, ..., u_{N_x,N_z-1})^T. \tag{2.92}$$

The vector $\boldsymbol{w}$ has length $N_x(N_z-1)+1$ and includes $w_{i,j}$ at all interior nodes, in addition to the transverse boundary $i = N_x, j = 1, ..., N_z - 1$ and one node at the muscular boundary $i = 1, j = N_z$. The vector $\boldsymbol{p}$ has length $(N_x-1)(N_z-1)$ and simply includes all interior nodes. The vectors $\boldsymbol{w}$ and $\boldsymbol{p}$ are given in a similar format to (2.92). This provides a set of $3(N_x-1)(N_z-1)+2(N_z-1)+1$ unknowns.

Consistent with the format given in (2.91), the governing equations (2.58) are rearranged

into the form

$$\frac{\partial}{\partial t}\left(\frac{\partial u_{i,j}}{\partial x}+\frac{\partial w_{i,j}}{\partial z}\right)=k_{x,i,j}\frac{\partial^2 p_{i,j}}{\partial x^2}+k_{z,i,j}\frac{\partial^2 p_{i,j}}{\partial z^2}+\frac{\partial k_{x,i,j}}{\partial x}\frac{\partial p_{i,j}}{\partial x}+\frac{\partial k_{z,i,j}}{\partial z}\frac{\partial p}{\partial z}, \tag{2.93a}$$

$$0=-\frac{\partial p_{i,j}}{\partial x}+\frac{\partial}{\partial x}\Big(M_{i,j}\Big(\frac{\partial u_{i,j}}{\partial x}+\gamma\frac{\partial w_{i,j}}{\partial z}\Big)\Big)+\frac{\partial}{\partial z}\Big(M_{i,j}\Big(\frac{1-\gamma}{2}\Big)\Big(\frac{\partial u_{i,j}}{\partial z}+\frac{\partial w_{i,j}}{\partial x}\Big)\Big), \tag{2.93b}$$

$$0=-\frac{\partial p_{i,j}}{\partial z}+\frac{\partial}{\partial z}\Big(M_{i,j}\Big(\frac{\partial w_{i,j}}{\partial z}+\gamma\frac{\partial u_{i,j}}{\partial x}\Big)\Big)+\frac{\partial}{\partial x}\Big(M_{i,j}\Big(\frac{1-\gamma}{2}\Big)\Big(\frac{\partial u_{i,j}}{\partial z}+\frac{\partial w_{i,j}}{\partial x}\Big)\Big). \tag{2.93c}$$

where $\gamma=\nu/(1-\nu)$ and the derivatives are discretised according to the central difference scheme outlined previously. The transverse and axial permeability, k_x and k_z, and the stiffness M are also given as discrete values over the grid. This provides a set of $3(N_x-1)(N_z-1)$ equations. The mass matrix rows associated with the second two equations are given by the zero vector. The stress free boundary conditions are kept in the form (2.89), providing an additional $2(N_z-1)$ equations for the solver. Again, the mass matrix rows associated with the stress free equations are given by the zero vector. Finally, taking the time derivative of the discretised force (2.90a) at $i=1$, and recalling $w_{i,Nz}=w_{1,N_z}$ for $i\neq 1$, we obtain

$$\frac{\partial}{\partial t}\Bigg(\sum_{i=1}^{N_x-1}(6w_{1,N_z}-8w_{i,N_z-1}+2w_{i,N_z-2}) \tag{2.94a}$$

$$+6w_{1,N_z}+4w_{0,N_z-1}+4w_{Nx,N_z-1}+w_{0,N_z-2}+w_{Nx,N_z-2}\Bigg) \quad=\frac{4A^*L_0h_z}{(2W_{y0}h_x)}\sin(\omega t), \tag{2.94b}$$

which provides the last equation necessary to solve for the unknown displacements and pressure.

Regarding the remaining displacements and pressures at the boundary: at each time step, the ODE function, provided to the *ODE15s* solver, specifies the displacements and pressures at the boundary according to (2.88). In addition we set $w_{i,Nz}=w_{1,N_z}$ for $i\neq 1$.

2.3.2.1 Convergence for Two-Dimensional Scheme

We have used the same number of grid points in both the axial and transverse dimension; we found transverse dimension required greater grid refinement. We denote $h_z = h$ and note that $h_x = h_z(W_0/L_0)$. To verify numerical convergence of the scheme, the homogeneous case was run over one loading cycle $(2\pi/10)$ for $\omega = 10$, using a range of different grid sizes $N_x = N_z = 5, 10, ..., 80, 160$. We then compared the metric

$$\varphi = \frac{\left\| \int_0^{2\pi/10} \mathbf{f}_h - \mathbf{f}_{\frac{h}{2}} \, dt \right\|_2}{\left\| \int_0^{2\pi/10} \mathbf{f}_{\frac{1}{5}} \, dt \right\|_2}, \tag{2.95}$$

where $\boldsymbol{f} = (\boldsymbol{u}, \boldsymbol{w}, \boldsymbol{p})$ is the solution taken for consistent equidistant spatial points across grid sizes. The time integral is integrated numerically using the trapezoid rule. In Figure 2.19 we show the plot of φ against the grid step size h. Results are shown for a forcing frequency of $\omega = 10$, and homogeneous stiffness and permeability. We found the convergence results were unaffected by forcing frequency or inhomogeneities in the stiffness/permeability (results not shown). A final grid size of 80-by-80 was chosen.

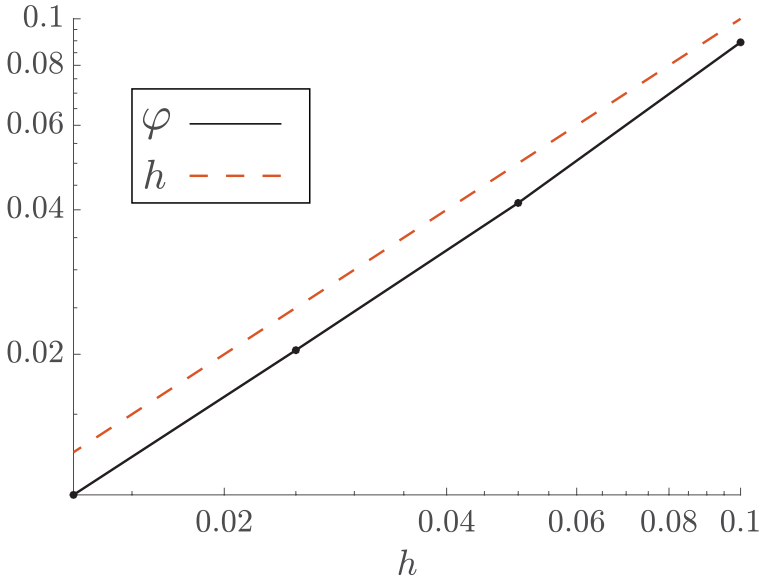


Figure 2.19: Loglog plot of relative error against spatial step size - demonstrating spatial convergence of two-dimensional numerical results. Dashed line is h, indicating slope for first order method.

Whilst second order accurate finite difference approximations were used to calculate all derivatives, the trapezoidal rule implemented in 2.90a is a first order method. Hence, we expect our solution to be at least accurate to first order. Since the true solution is unknown we cannot contrast the numerical and true solution to obtain the order of accuracy. Instead we approximate the order of accuracy p of the numerical solution by considering

$$\frac{\left\| \int_0^{2\pi/10} \mathbf{f}_h - \mathbf{f}_{\frac{h}{2}} \, dt \right\|_2}{\left\| \int_0^{2\pi/10} \mathbf{f}_{\frac{h}{2}} - \mathbf{f}_{\frac{h}{4}} \, dt \right\|_2} \approx p^2. \tag{2.96}$$

For the grid sizes $h = 40, 80, 160$, we find that the approximate order of accuracy $p > 1$. Consistent with this result, Figure 2.19 demonstrates a slightly steeper for the convergence of the numerical scheme relative to that indicated for a first order scheme.

The *MATLAB* stiff solver *ODE15s* uses a variable time-step size. We expect the stability of the solution to improve as the prescribed tolerance for the ODE solver is refined. In Figure 2.20 we have plotted the parameter

$$\varphi_2 = \frac{\left\| \int_0^{2\pi/10} \mathbf{f}_{\text{rel_tol}} - \mathbf{f}_{\text{rel_tol}/2} \, dt \right\|_2}{\left\| \int_0^{2\pi/10} \mathbf{f}_{\text{rel_tol}=0.01} \, dt \right\|_2}, \tag{2.97}$$

where rel_tol denotes the relative tolerance (where the absolution tolerance is given by 100$*$rel_tol), demonstrating the solution converges with a reduction in the relative tolerance.

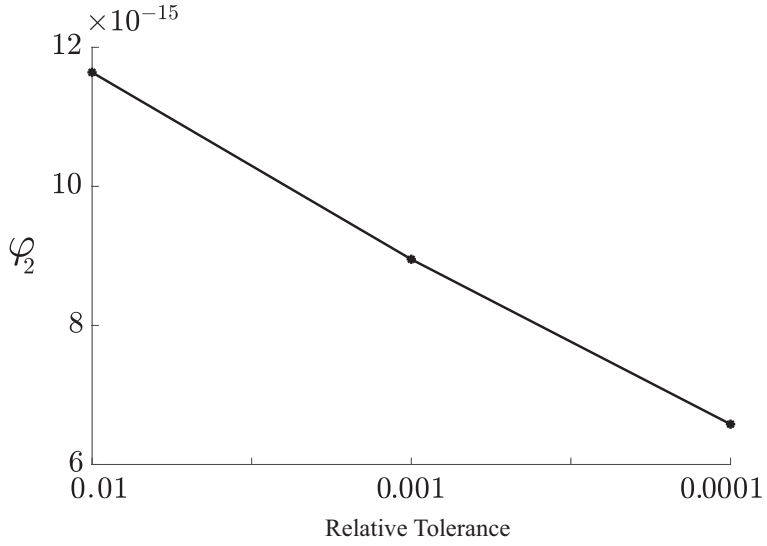


Figure 2.20: Plot of relative error against relative tolerance used for *ODE15s* - demonstrating convergence of two-dimensional numerical results.

2.4 Additional Results

2.4.1 Sensitivity to Transverse to Axial Permeability Ratio

In Figure 2.21 the flux magnitude is shown for different points within a loading cycle, in the setting of an anisotropic permeability ($k_x/k_z = 1/10$). The flux magnitudes are seen to be higher with the faster loading rate, consistent with the isotropic permeability case presented in text (Section 2.8.3.1 Figure 2.11). However, in contrast to the isotropic case, the largest flux magnitudes occur at the muscular origin.

In Figure 2.22 the axial and transverse strain profiles at the maximum point of tension when a Poisson's ratio of zero and anisotropic permeability are imposed. We have accounted for a localised reduction in the stiffness, and hence the plots represent the same scenario as given in Figure 2.14b,d, except in Figure 2.14b,d an isotropic permeability was imposed and the Poisson's ratio $\nu = 0.4$. Here, results are similar; we also observe substantially larger axial and transverse strains over the low stiffness regions and there is a concurrent reduction in the strains occurring within the healthy tissue.

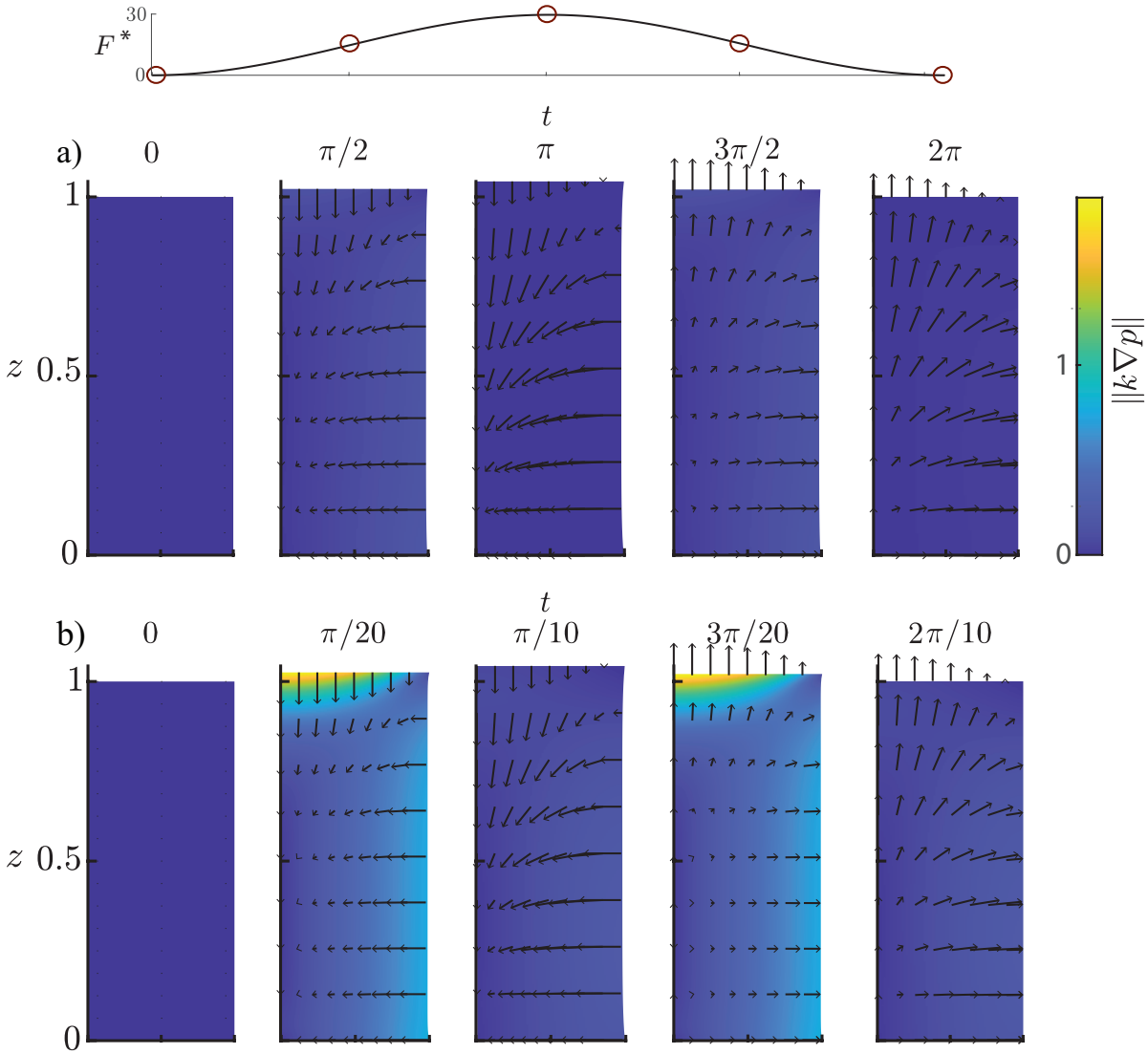


Figure 2.21: Flux magnitude at varying time points for (a) slow $\tilde{\omega} = 1$ and (b) fast loading $\tilde{\omega} = 10$ when an anisotropic permeability is imposed $k_x/k_z = 1/10$. Arrows are scaled for easy visualisation and hence only depict relative magnitudes within plots not between plots. The stiffness and permeability are assumed constant $M/M_0 = k_z/k_0 = 1$. Results have been transposed onto a moving grid.

2.4.2 Sensitivity to Location of Damage

In Figure 2.23 we have reproduced Figure 2.13, except instead imposing a damaged region at the centre of the transverse dimension (red dashed line). In this case, it is evident that the flux magnitude is already lower here than at the outer boundary, and hence any reduction in the permeability or stiffness at the centre, only serves to slightly further reduce the flux

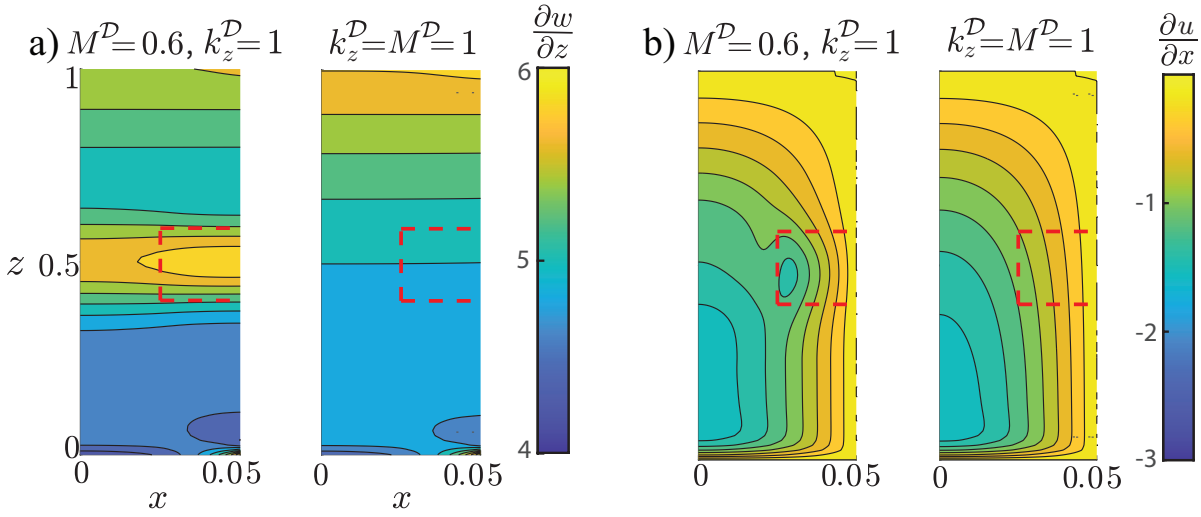


Figure 2.22: Influence of stiffness and permeability on strain for fast ($\omega = 10$) cyclic loading. (a) Axial and (b) transverse strain profiles at time $t = \pi/10$ for $M^d = 0.4$ and $M^d = 1$. The permeability is homogeneous and anisotropic $k^z = 1$ and $k^x = 1/100$, and the Poisson's ratio $\nu = 0$.

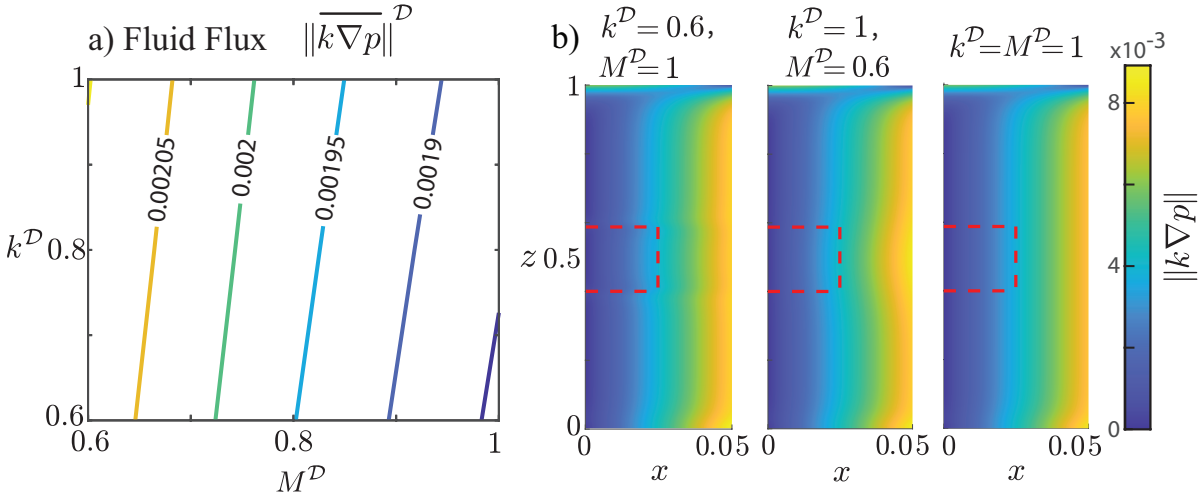


Figure 2.23: Influence of a localised reduction in stiffness and/or permeability on fluid flux for fast ($\omega = 10$) cyclic loading. The localised reduction is imposed at the centre of the midportion (red dashed lines in b). (a) Average maximum flux over the damaged region for different imposed reductions in permeability and stiffness. (b) Flux magnitudes at time $t = \pi/20$ for (left to right) $k^d = 0.6$, $M^d = 0.6$ and homogeneous reference case $k^d = M^d = 1$.

here. The contour plot in Figure 2.23a comparative to the contour plot shown in Figure 2.13a shows much lower relative reductions in the flux when either the permeability or stiffness is locally reduced. Complementing this result, in Figure 2.23b no observable difference in the profiles of the flux magnitude are evident.

CHAPTER 3

A Load-Driven Adaptation Model for Tendon

3.1 Synopsis

In this chapter we develop an adaptation model to investigate the time dependent changes in material properties that occur within tendon in response to cyclic tensile loading. The model couples poroelastic modelling with a set of phenomenological rules for material property changes in response to local mechanical stimuli. We utilise the poroelastic model developed in Chapter 2 and impose a series of loading bouts over a period of multiple weeks. Alterations in the tendon collagen and proteoglycan content are assumed to occur in response to loading and are represented indirectly through changes in the stiffness and permeability of the poroelastic material. In response to each loading bout, material properties change continuously until implementation of the subsequent loading bout. The adaptation model is designed to capture both reductions in the stiffness and increases in the permeability of the poroelastic material, maladaptive changes consistent with tendinopathic changes, in response to high frequency loading. It also captures increases in tendon stiffness observed to occur with low loading frequencies which is considered to be a beneficial adaptive response. Based on previous *in vitro* work which investigated the effect of individual local mechanical stimuli on the production of collagen and proteoglycans in both tendons and cartilage, we assume that local tensile axial strains promote an increase in the stiffness, through type I collagen synthesis, and high local fluid fluxes promote a reduction in the stiffness and increase in the

permeability, through collagen degradation and proteoglycan synthesis. Two variations of the phenomenological rules governing the material property changes in response to a bout of loading are trialled: material property changes are either dependent only on the previous loading bout, or are also affected by earlier loading bouts. The model is executed to simulate physiological loading regimes, as described in previous clinical studies, allowing us to contrast material property changes predicted by the model with those reported *in vivo*. Whilst we focus on specific loading scenarios and phenomenological models here, the model provides a general tool to investigate different phenomenological models for structural changes in response to loading or the impact of different loading scenarios in the clinical setting.

3.2 Introduction

A key barrier to optimising rehabilitation regimes is an incomplete understanding of the time dependent changes in tendon constituents and material properties that occur in response to loading. The chemical environment in tendon is complex and measuring *in vivo* changes in tendon constituents is difficult. There are also multiple confounding factors that prohibit the direct translation of *ex vivo* or *in vitro* experiments - which investigate the impact of mechanical stimuli on the production of tendon constituents by cells - to the clinical setting. Examples of such confounding factors include: the species the tendon was taken from, the tendon type examined and the experimental test conditions (Burgio et al. 2022).

Mathematical modelling provides a useful tool to investigate the mechanical behaviour of tendons and associated changes in constituents that can not be investigated easily experimentally. Only in recent years has the theory of tendinopathy occurring as a maladaptive process, rather than as a microtearing event, become more prominent. Hence, despite more recent evidence demonstrating that many of the changes in tendinopathy represent a cartilagenous response[1] (Burssens et al. 2013, Cook et al. 2009), there is a sparsity of poroelastic dam-

[1]The tendon structure starts to share similarities with cartilage due to increase protoeoglycan

age models investigating the potential for mechanical stimulation with loading to promote a maladaptive cartilagenous response. This has also lead to a lack of modelling of the time-dependency of changes in response to loading, as previous damage models for tendinopathy (Mehdizadeh et al. 2017, Bontempi 2009) assumed that micro-damage occurred immediately at the time of loading (with a cumulative effect occurring when multiple loading bouts were undertaken).

Two key aspects of the time-dependent response of tendon cells to load require further investigation. Firstly, the individual local mechanical stimuli that are responsible for the stimulation of collagen and proteoglycan production in tendon have not been fully elucidated. Results from Chapter 2 suggest that fluid shear may promote proteoglycan production in response to fast loading frequencies and that local axial tensile strains alone do not explain the increased type I collagen deposition that is posited to occur with low loading frequencies (Section 2.8.3.1 Figure 2.9). Secondly, greater insight is needed into the time dependence of collagen and proteoglycan changes, and the resulting changes in material properties, following loading. There is experimental work investigating collagen synthesis following loading (Magnusson et al. 2010), however, additional work is needed to understand how collagen and proteoglycan synthesis are affected by loading frequency. Whilst the limitations of experimental work poses challenges when trying to accurately inform modelling work, it also motivates the development of an adaptation model, as one can explore the implications of *in vitro* and *ex vivo* results in terms of a broader understanding of the tendon's response to load.

3.3 Chapter Outline

In Section 3.4.1 we start by reviewing existing adaptation and damage models for tendon and other musculoskeletal tissues. To model how the local mechanical environment contributes

deposition, a loss of collagen I, and cell rounding.

to changes in the stiffness and permeability, in Section 3.4.2 we first review how the local mechanical environment affects proteoglycan and collagen production, and then in Section 3.4.3 how these constituents affect material properties. We focus specifically on collagen and proteoglycans, as these constituents are modulated in response to loading and appear to be the key determinants of the Young's modulus and tendon permeability (Jurvelin et al. 1988, Tavakoli Nia et al. 2015, Fessel et al. 2011). In Section 3.6 we then present an adaptation model that captures the understanding gained from the integration of previous experimental work. We utilise the adaptation model to simulate a single bout or several bouts of loading, gaining basic insight into the model behaviour (Section 3.8.2). We then simulate a longer series of loading bouts as is applied in clinical practice, contrasting the material property changes predicted by our model with those observed in previous clinical studies (Section 3.8.3), and demonstrating how the model can be used to investigate the effect of different loading regimes on tendon material properties (Sections 3.8.4 and 3.8.5).

3.4 Literature Review

3.4.1 Previous Damage and Adaptation Models

To our knowledge, only one mathematical model has been used to investigate tendinopathy as a maladaptive mechanotransduction response and only changes in proteoglycan content in response to fluid induced stresses were accounted for (Wren et al. 2000). A larger proportion of models have assumed that tendinopathy occurs as a set of fibre tearing events, as only more recent evidence has challenged this hypothesis (Cook et al. 2009). More general adaptation models for mesenchymal[2] tissue differentiation are also relevant to the work here, as they are informed by much of the same underlying biology and consider similar phenomenological principles.

[2]Connective tissue of undifferentiated cells that forms blood vessels, bone, muscle, cartilage and tendon Pountos et al. 2005.

Wren et al. (2000) developed a poroelastic damage model to investigate the potential for load-induced pressure changes to cause a cartilagenous response at the tendon insertion. A finite element package was utilised to model the Achilles tendon. The geometry of the tendon at the insertional end differed from the set up we utilised in Chapter 2; they imposed curvature of the tendon at the insertional end, with a small section of the transverse boundary wrapping around bone (Figure 3.1).The curvature of the tendon around the bone generated external compressive forces to the tendon with tensile loading. A plane strain condition was used in the axial direction and emphasis was placed on investigating the effects of transverse deformation. The poroelastic model was run iteratively with one bout of loading simulated per day. The permeability was updated after each loading bout according to a phenomenological rule which depended on the maximum hydrostatic pressure occurring at each spatial location within the tendon during the entire loading bout. The time-dependence of the material property changes was not explored, with each loading bout invoking an immediate change in the permeability. Changes in permeability were not affected by the duration of a loading bout, a reasonable assumption given evidence that the magnitude of the global tendon stress plays a much more significant role than the number of loading cycles (Magnusson et al. 2010). The model predicted that low permeability zones will develop around the tendon insertion in response to loading, which is in good agreement with an experimental damage model developed by Malaviya et al. (2000).

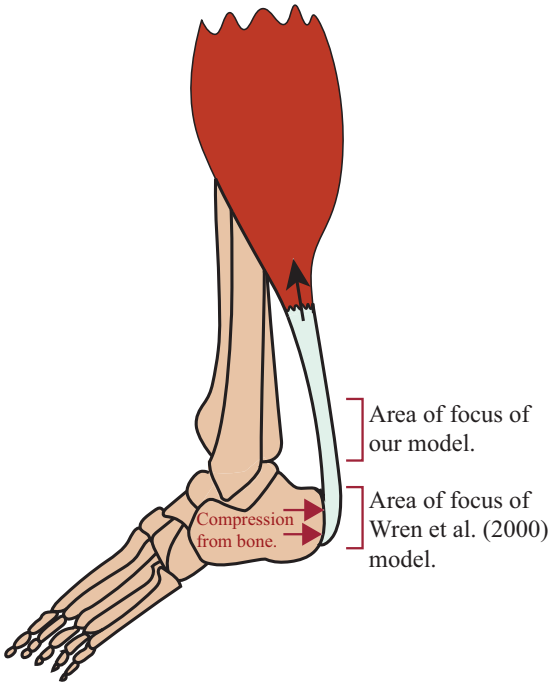


Figure 3.1: Schematic of Achilles tendon showing areas of focus when modelling insertional (Wren et al. 2000) vs midportion tendinopathy (our model).

As a result of mechanotransduction, mesenchymal stem cells (Section 1.2.2) both differentiate into specific cell types and control tissue differentiation. Loboa et al.(2003) developed

a poroelastic phenomenological model for tissue differentiation from multipotent mesenchymal tissue in response to loading. Rather than simulate loading, they simply specified a daily pressure and tensile stress stimulus. Similar to Wren et al. (2000), the model was run iteratively, with material properties updated after each iteration (day) according to a phenomenological rule: mechanical stimuli affected the proteoglycan, collagen I and collagen II deposition, which in turn affected the global material properties of the tissue (Young's modulus, permeability, and oedometric modulus - recalling 2.23). It was assumed that the pressure, rather than fluid shear stress, was the driver for proteoglycan deposition, and that proteoglycan deposition affects both the permeability and aggregate modulus. Similar to Wren et al. (2000) they assumed that the magnitude of loading has a much more substantial affect on mechanotransduction than duration. Loboa et al.(2003) imposed that the more extreme the mechanical stresses, the more quickly the material properties adapted in response (and to a larger degree). This does not follow normal tendon adaptation, where there is an initial reduction in collagen content, and hence proposed weakening, in the initial period following loading (Magnusson et al. 2010). The model predicted that a low daily tensile stress and high fluid pressure would lead to the formation of cartilage, while a higher daily tensile stress and low fluid pressure would lead to the formation of fibrous tissue.

Mehdizadeh et al. (2017) utilised a fatigue damage model to investigate changes in concentrations of signalling, structural and effector[3] molecules in response to loading. They introduced the notion of an elementary cell response (ECR), defined as "a normal reference secretion profile of a molecule by a [tendon cell] in response to the [tendon cell's] local strain". Tensile cell strain was the only local mechanical cell stimulus assumed to affect the ECR. A solid model consisting of parallel fibres subject to uniform strains was used. Based on previous experimental results for fatigue loading of the tendon (Wren et al. 2003), a phenomenological law that predicts the probability of local fibre breakage with fibre strain was imposed. They

[3]Effector molecules bind to and regulate protein activity.

used a phenomenological law to prescribe changes in several tendon constituents in response to loading, including collagen, glycosaminoglycans, and an array of enzymes. A sigmoidal curve was used to model concentration changes of each constituent in response to cell strain. The time dependence of the ECR to tendon cell strain was not investigated (an immediate response was assumed). The authors were able to reproduce a variety of *in vitro* results with their model, however, there were several predictions and facets of the model that are not necessarily in agreement with clinical evidence. Firstly, the authors predicted that high strains result in fibre breakage. This then resulted in a significant decrease in the strains observed in damaged regions (solid stresses were not transmitted through broken fibres) and the subsequent under-stimulation of tendon cells. This is despite high strains being essential in slow heavy resistance training - rehabilitation regimes which have been shown to produce the largest adaptive increase in the Young's modulus and tendon stiffness (Arampatzis et al. 2007). Secondly, neither the effects of fluid-induced stresses nor loading frequency were investigated (Lavagnino et al. 2008, Malliaras et al. 2017). Finally, they assumed that under-stimulation of cells is responsible for tendinopathic changes. Evidence suggests this is an unlikely mechanism for tendinopathy development but may be relevant in later stage tendinopathy (Cook et al. 2016) and, accordingly, this model may be more applicable to late stage disease.

To our knowledge no poroelastic model has been used to investigate how a cartilagenous response occurs in the tensile midportion of tendons. Furthermore, no study has yet investigated how a cartilagenous response occurs with regard to damage-inducing or rehabilitative loading scenarios, nor has any model of tendon incorporated both localised changes in both permeability and stiffness to mimic damage or maladaptation. In contrast to previous work, we account for the material properties being modulated over continuous time between loading bouts, rather than implementing an automatic step change. This will allow us to capture the important effects of recovery time between loading and gain insight into the time dependency of material property changes in response to loading.

3.4.2 Effect of Local Mechanical Stimulation on Proteoglycan and Collagen Content

To understand how the local mechanical environment indirectly contributes to changes in the local stiffness and permeability, we first consider how the local mechanical environment affects proteoglycan and collagen production. As there is a much denser literature on the effects of local mechanical stimuli on cartilage cells than tendon cells, experimental work in this area also informs our model. It is reasonable to assume that this literature is applicable to tendon, given tendon cells are derived from the same cell lineage as cartilage cells, and under certain conditions tendon cells take on a more cartilaginous cell phenotype (Mos et al. 2009).

There is reasonable evidence to suggest that type I collagen deposition occurs primarily as a response to cellular tensile strains, as would occur with tensile loading of the tendon (Arnoczky et al. 2002). Huisman et al. (2014) demonstrated an upregulation of type I collagen production by tendon cells in response to local tensile strains greater than 3-4 % *in vitro*, whilst Howard et al. (1998) showed the same response *in vitro* by cells taken from a ligament, musculoskeletal structures which share similar properties to tendon. Since type I collagen is the key contributor to the tensile properties of tendon, allowing the tendon to withstand large tensile loads (Fessel et al. 2011), these findings suggest that this response to strain represents a beneficial adaptive mechanism for the tendon. When considering the duration of each loading bout, there appears to be a ceiling effect in which additional loading repetitions have no impact on collagen synthesis following loading (Magnusson et al. 2010). That is, collagen synthesis in response to load is independent of loading duration once some given threshold has been exceeded.

Whereas type I collagen synthesis appears to increase with tensile cyclic loading, *in vivo* evidence suggests for certain forms of exercise there may be an initial period over which degra-

dation also occurs so that the net synthesis is negative (Figure 3.2) (Langberg et al. 2000, Magnusson et al. 2010). The main evidence for this assertion comes from a study involving participants undertaking 36km of running (Langberg et al. 1999b), in which molecules associated with collagen production or degradation were measured from fluid surrounding the tendon over succeeding days. Several authors have assumed that this pattern of net collagen synthesis also applies to rehabilitation regimes (Murtaugh et al. 2013, Magnusson et al. 2010), however, to our knowledge the medium-term (days) time dependence of collagen synthesis in response to low-frequency rehabilitative loading has not been investigated. It is essential to elucidate whether the pattern of collagen synthesis following loading is affected by the loading frequency, as this would guide intervention design. Another critical question left unanswered by previous work is how these time dependent changes in collagen synthesis (Figure 3.2) are affected when subsequent bouts of loading are undertaken at intervals less than 72 hours apart. That is, there is no clear evidence to suggest whether, following subsequent loading, the same process is restarted or if there is some cumulative effect. Finally, it is it has yet to be confirmed whether collagen synthesis and degradation both occur as a result of local tensile strains, or whether degradation occurs due to another local stimuli.

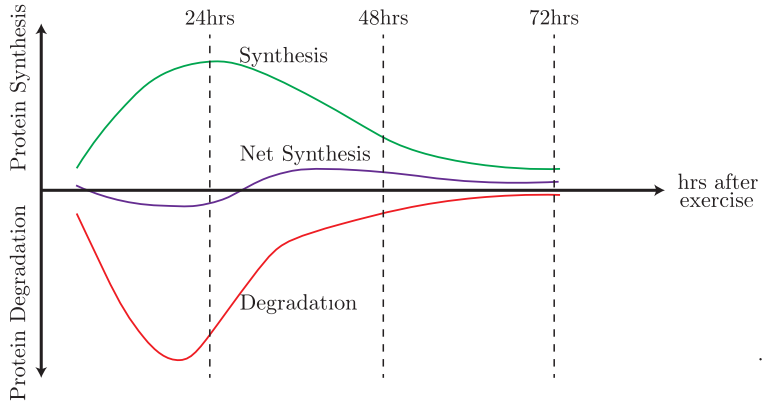


Figure 3.2: Schematic of acute collagen changes in response to exercise in humans, based on prior experimental and *in vivo* results (Langberg et al. 1999b, Miller et al. 2005, Langberg et al. 1999a). Loading is followed by an increase in both the synthesis and degradation of collagen. There is a net loss of collagen over the first 24 hours, followed by a net synthesis over the next 48 hours. Reprinted with permissions from S. Magnusson et al. 2010. "The pathogenesis of tendinopathy: balancing the response to loading". *Nature Reviews Rheumatology* 6 (5): 262–268.

Whilst the *net* collagen synthesis following fast and slow loading bouts has not been compared over the 72 hours following loading, there is evidence that the synthesis of collagen is similar. No significance difference in collagen synthesis was found at 24 hours following one hour of running (patellar and Achilles), knee extensions undertaken until total fatigue (patellar), and heavy slow resistance training involving knee extensions (patellar) (Kjær et al. 2009). This suggests that, if lower loading frequencies promote greater net collagen synthesis relative to fast loading, it is more likely because higher loading frequencies promote greater degradation. There is evidence that shear stress, as well as tensile strain, may alter collagen production. Fong et al. (2005) and Jones et al. (2005) demonstrated a reduction in collagen type I and an increase in enzymes implicated in collagen degradation (Oshiro et al. 2003, Del Buono et al. 2013), for tendon cells exposed to shear stress. Combining this evidence with the high fluid flux we observed with fast loading in Chapter 2, this gives a potential mechanism for enhanced collagen degradation with fast loading, and hence lower net synthesis. The assumption that fluid shear and axial strain have differential effects on collagen synthesis/degradation in tendon is reasonable, given that this holds for other musculoskeletal tissues (Fitzgerald et al. 2006, Owan et al. 1997). Modelling work on bone has demonstrated that cell deformations induced by fluid shear and solid strain are qualitatively different (McGarry et al. 2005), explaining the experimentally observed difference in bone cell responses to fluid shear and solid strain (Owan et al. 1997).

Large proteoglycans are most commonly present in tissues subject to high external compressive stresses (Grad et al. 2011, Docking et al. 2013). They are also abundant in midportion tendinopathies where external compressive forces are absent (Cook et al. 2012). Evidence suggests that proteoglycan deposition is affected by both compressive solid, and fluid induced, stresses (Buschmann et al. 1999, Shieh et al. 2007). Results from Chapter 2 indicate that an increase in proteoglycans is most likely an adaptive response to high fluid shear, rather than compressive transverse strains. Buschmann et al. (1999) also demonstrated that cyclic fluid shear resulted in an up regulation of aggrecan production in *ex vivo* cartilage

specimens. They isolated the effect of fluid shear through mathematical modelling of the experimental set up. One study reported a down regulation of aggrecan production with fluid shear (Lee et al. 2002), however, fluid shear was applied steadily over a minimum of two hours. This type of loading does not represent the physiological loading of interest in this work; proteoglycan production is differentially regulated by cyclically and statically applied stimuli (Wang et al. 2007). There are no studies investigating the time frame of aggrecan production following exercise in tendons, only in cartilage. In response to mechanical loading of the temperomandibular joint, aggrecan was produced in cartilage over a time frame of four to eight hours (Schätti et al. 2013). Similarly, cartilage cells *in vitro* demonstrated an increase in aggrecan net synthesis by 24 hours following loading (De Croos et al. 2006). This suggests that a net increase in aggrecan content may occur more rapidly than a net increase in collagen.

Based on the preceding literature, in Table 3.1 we have provided a summary of the effect of different local mechanical stimuli on type I collagen and proteoglycan content.

Table 3.1: Influence of individual mechanical stresses on collagen and proteoglycan deposition over succeeding 72 hours (early: <24 hrs, late: 24 - 72 hrs) (Buschmann et al. 1999, Shieh et al. 2007, Fong et al. 2005, Jones et al. 2013, Magnusson et al. 2010, Huisman et al. 2014).

Mechanical Stimulus	Collagen I [Ref]		Large PGs [Ref]	
	Early	Late	Early	Late
Fluid Flux/Shear Stress	↓ ? [F,J]	-	↑ [S]	-
Transverse Strain	-	-	↑ [B]	-
Axial Strain	↓ ? [M]	↑ [H]	-	-

3.4.3 Effect of Micro-Structural Changes on Material Properties

We now consider evidence regarding how changes in the local collagen and proteoglycan content affect the local tendon stiffness and permeability. Large proteoglycans play a dominant role in determining the permeability of cartilage, in which an inverse power law relationship is observed, whereby increases in proteoglycans can results in corresponding large reductions in permeability (Jurvelin et al. 1988, Tavakoli Nia et al. 2015, Comper et al. 1987, Zamparo et al. 1989). Type I collagen appears to be a more important determinant of the tensile modulus than proteoglycans (Fessel et al. 2011). Evidence suggests that the collagen content and Young's modulus are positively correlated for small strain scenarios, also sharing a power law relationship with the reported exponent ranging from one (a simple linear relation) to three (Roeder et al. 2002, Jansen et al. 2018). Taking the first order approximation of the power law relations[4], we simplify our model by assuming a linear relation between the proteoglycan content and permeability, as well as between the collagen content and Young's modulus.

Whether proteoglycans modulate the material properties of the tendon, other than the permeability, is largely unknown. Proteoglycans appear to play some role in determining the aggregate modulus in cartilage, albeit secondary to collagen changes (Jurvelin et al. 1988). For simplicity we assume that proteoglycans only influence the permeability in our model.

Further supporting the notion that exercise induces material property changes, exercise has been shown to modulate both the permeability of horse tendons and Young's modulus of human tendons *in vivo* (Murray et al. 1999, Arampatzis et al. 2007, Arampatzis et al. 2010, Bohm et al. 2015). Exercise was shown to induce a decrease in the permeability and most studies have shown an increase in the Young's modulus with exercise (Bohm et al. 2014). As these studies did not involve overloading specimens (high frequency loading bouts had several days recovery between), these changes are more likely representative of healthy adaptation

[4]Consider the first two terms of the Taylor series expansion.

to exercise, rather than tendinopathic changes where a reduction in the Young's modulus has been observed (Arya et al. 2010). Furthermore, large variations in the permeability of tendon (Eckstein et al. 1999) and Young's modulus of cartilage (Westh et al. 2008) have been detected between individuals, supporting the notion that previous loading history and personal factors determine the person's baseline material properties of connective tissues.

3.4.4 Loading Scenarios

Several authors have investigated long-term changes in material parameters following a loading intervention. Arampatzis et al. (2007), Arampatzis et al. (2010) and Bohm et al. (2015) investigated changes in the stiffness, Young's modulus[5] and cross-sectional area (CSA), for different loading regimes. Measurements of stiffness changes following intervention were reported as the ratio of the global stiffness post-intervention to the global stiffness pre-intervention, and were reported similarly for the Young's modulus and CSA. The authors investigated changes following a 14 week loading intervention with four loading bouts spaced over a week. Only the loading rates and magnitudes were varied within and across studies: cyclic loading was performed with a dimensional frequency of 0.17 Hz or 2.4 Hz and was undertaken with a magnitude of either 55% or 90% MVC[6] (Section 1.3.1). A summary of the loading interventions and material property changes are given in Table 3.2. Changes in material properties are given as the ratio of post-intervention to pre-intervention values. A dash denotes no significant change.

In-season management is a form of rehabilitation which is used when an athlete or individual can not avoid high frequency loading. In-season management regimes entail the incorporation of low frequency loading bouts, whilst still allowing the individual to complete

[5]The global stiffness/Young's modulus were calculated by linear regression as the slope of the tendon force-displacement/stress-strain curve, taken between 50% and 100% of the maximum force/stress.
[6]The maximum load magnitude possible for the subject if they were to perform only one repetition/cycle.

Table 3.2: Changes in material properties with clinical loading interventions (Arampatzis et al. 2007, Arampatzis et al. 2010, Bohm et al. 2015).

Loading Protocol	Loading Parameters		Material Property Change Post:Pre Intervention		
	Frequency (Hz)	% MVC	Young's Modulus	Stiffness	Average CSA
Heavy-Slow	0.17	90	1.29- 1.57	1.4	1.1
Light-Slow	0.17	55	-	-	-
Hopping (Fast)	2.4	≈ 90	-	-	-

regular high frequency loading (though often an increase in the recovery time between high frequency loading bouts is required). The aim is to minimise damage to tendon structure whilst allowing an athlete to continue to undertake high frequency loading over multiple weeks so that they can complete their sporting season. Whilst the individual can continue to engage in high frequency loading, the frequency of individual loading bouts often needs to be reduced to some degree (for example the individual can continue to run but at a slower pace) (Cook et al. 2014). In contrast to the experimental work investigating the effects of classic rehabilitative loading, as outlined above (2007), Arampatzis et al. (2010), less is known about the effects of in-season management on tendon structure.

3.5 Aims of Model

Informed by the preceding literature, we proceed to develop an adaptation model for tendon which describes the material property changes which occur in response to different forms of long-term loading. We model a series of macroscopic loading bouts using the poroelastic model from Chapter 2, predicting the associated mechanical environment which occurs within the tendon and the change in tendon material properties in response to this environment (Figure 3.3). While the change in material properties in response to mechanical stimulation is due to collagen and proteoglycan deposition, for simplicity and due to a lack of experimental

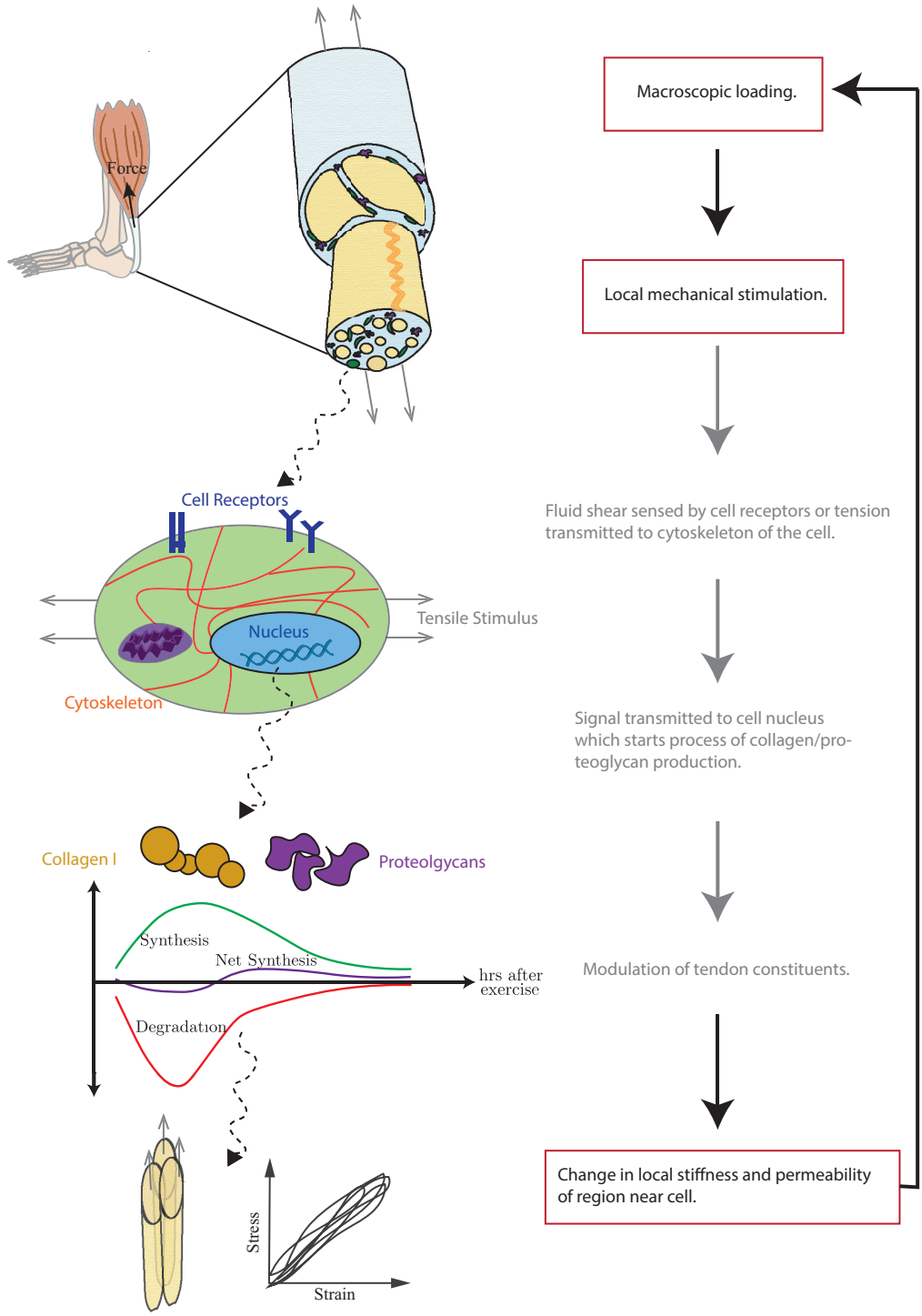


Figure 3.3: Schematic of the iterative loading and mechanotransduction process that the adaptation model aims to emulate. Macroscopic loading causes a change in the mechanical environment of the tendon, invoking mechanical stimuli which are sense by the cells. Cells respond by altering the local surrounding collagen and proteoglycan content, leading to a change in the local material properties. The intermediate step of cellular production of tendon constituents is omitted in the adaptation model.

data, we do not explicitly consider a model for the protein dynamics and instead prescribe a direct relation between material properties and mechanical stimulation. This model aims to serve several purposes. Firstly, we investigate whether the tendon having a positive response to large (4-6%) tensile axial strains, with an increase in stiffness, and a maladaptive response to high fluid fluxes/shear, with a reduction in stiffness and permeability, can explain the material property changes that have been observed with rehabilitative and damage-inducing loading. Secondly, by prescribing a model that implements time-dependent changes in the material properties in response to loading, we investigate how the recovery times between loading affect the long-term material property changes that occur in response to a series of loading bouts. Finally, we demonstrate how the model can be used to contrast the material property changes for different loading regimes, with the aim to provide a tool for identifying optimal loading regimes given different baseline tendon structures and patient loading requirements (e.g. whether they want to continue engaging in high-frequency loading).

3.6 Model Setup

A series of loading bouts $1, ..., b, ..., B$ are implemented (Figure 3.4) using the two-dimensional poroelastic model investigated in Chapter 2 (Equations (2.58)-(2.61)). The variables and parameters of the poroelastic model are presented in Table 2.1. In each loading bout, an axial force is applied to the tendon and we solve for the displacement $\boldsymbol{u}$ and pressure p, and subsequently the strain $\nabla \boldsymbol{u}$ and flux $k\nabla p$ (Darcy's law, Equation (2.12)). Two elastic constants describe the solid behaviour: the stiffness M and the Poisson's ratio ν. We assume that the stiffness M and permeability k are isotropic and heterogeneous. We use dimensionless variables, implementing the scalings given in Section 2.6.1.

As loading bouts are administered at a minimum of 24 hours apart, there is a separation of timescales: the time over which a loading bout occurs is an order of magnitude less that the time between loading bouts. We introduce a new dimensional variable τ to denote the larger

timescale over which the series of loading bouts takes place and impose that the loading bouts occur instantaneously over this larger timescale. We scale τ by one hour such that all variables are now considered in their dimensionless form.

The time frame between loading bouts b and $b+1$ is given by $\Delta\tau_b$ for $b \in \{1, 2, ..., B-1\}$, which can vary within a series of loading bouts. The first loading bout $b = 1$ (or equivalently the first implementation of the poroelastic model) is initiated at time $\tau = 0$. Subsequent loading bouts $b = 2, 3, ..., B$ are then implemented instantaneously at time $\tau_b = \sum_{i=1}^{b-1} \Delta\tau_i$. The magnitude of loading is kept constant across loading bouts, whilst the frequency ω varies across, but not during, a bout of loading. We let ω_b denote the frequency of loading bout b for $b \in \{1, 2, ..., B\}$. We assume that the stiffness $M = M(\boldsymbol{x}, \tau)$ (we hold the Poisson's ratio constant and recall M is linearly proportional to the Young's modulus E in this case) and the permeability $k = k(\boldsymbol{x}, \tau)$ change over the continuous time between loading bouts. We let $M_b(\boldsymbol{x}, \tau = \tau_b)$ and $k_b(\boldsymbol{x}, \tau = \tau_b)$ denote the stiffness and permeability of the tendon during the loading bout b and assume that there is no change in material properties during a loading bout. We note that changes in stiffness can be considered as a surrogate for collagen content and changes in permeability serve as a surrogate for proteoglycan content (inversely proportional).

Since evidence suggests that the tendon's adaptive response to loading is insensitive to the time frame of loading, when loading is implemented for a sufficiently long time (Magnusson et al. 2010), we assume that all loading bouts exceed this amount of time. We prescribe Δt_b, representing the duration of loading bout b, to be constant across loading bouts: $\Delta t_b = \Delta t \ \forall b$,

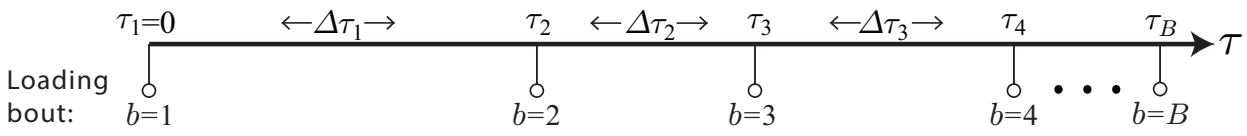


Figure 3.4: Schematic showing how a series of B loading bouts are administered over time. Loading bouts are administered instantaneously at time τ_b and with a subsequent recovery time of $\Delta\tau_b$, for $b = 1, 2, ..., B$.

such that the long-time oscillatory state is reached when implementing the poroelastic model. We assume the magnitude, but not the duration, of the stimulus at each spatial location within the tendon affects whether an adaptive response to loading occurs. The local stiffness $M(\boldsymbol{x}, \tau)$ is assumed to change in response to large tensile strains and high fluid fluxes, whilst the permeability $k(\boldsymbol{x}, \tau)$ varies in response to high fluid fluxes. In reality, we expect fluid flow to exert a mechanical stimulus to the cell through shear stress; however, we again (Section 2.8.3) use the fact that we expect the shear and fluid flux to be approximately linearly related and use the fluid flux magnitude as a surrogate for shear stress. The outputs from each loading bout b, which we use to determine material property changes, are the maximum axial strain $\partial w_b^{\max}/\partial z\,(\boldsymbol{x}, t^*)$ and maximum flux magnitude $\|k\nabla p\|_b^{\max}(\boldsymbol{x}, t^*)$ reached at each location $\boldsymbol{x}$, during loading (Figure 3.5). Here t^* is the time at which the maximum value is obtained and takes a value between 0 and Δt. At each spatial location $\boldsymbol{x}$ we then take the maximum value for the strain and flux magnitude over the interval $(0, \Delta t)$, such that

$$\frac{\partial w_b^{\max}}{\partial z}(\boldsymbol{x}) = \max_{t^*(\boldsymbol{x})\in(0,\Delta t)} \frac{\partial w_b}{\partial z}\left(\boldsymbol{x}, t^*(\boldsymbol{x})\right), \quad \|k\nabla p\|_b^{\max}(\boldsymbol{x}) = \max_{t^*(\boldsymbol{x})\in(0,\Delta t)} \|k_b(\boldsymbol{x}, \tau_b)\nabla p\|_b\left(\boldsymbol{x}, t^*(\boldsymbol{x})\right). \tag{3.1}$$

We draw attention to the fact that the maximum at each spatial point may occur at different time points $t^* = t^*(\boldsymbol{x})$ during loading. However, in the case of the strain stimulus, it does occur for all spatial points at the time point of maximal applied force.

In Figure 3.6 we display a schematic of the adaptation model that outlines the iterative process used to model a set of loading bouts.

We consider two options for how the material properties are influenced by previous loadings bouts. In the first case, we assume that material properties are only influenced by the stimuli (Equations (3.1)) which occurred during the immediately prior loading bout. The alternate case we consider is when the material property changes occur as a summation of the responses to previous loading bouts. We still assume that material properties do not change during a

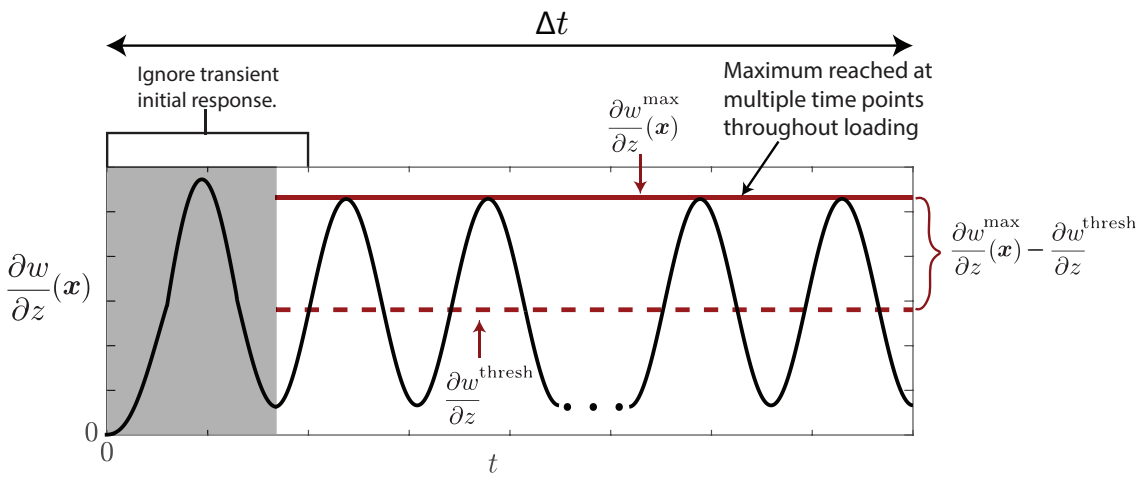


Figure 3.5: A cyclic tensile force is applied to the tendon with some prescribed frequency and magnitude $F/(M_0L_0) = A/2 - A\cos(\omega)/2$. The maximum axial strain reached for each spatial point is recorded. Since the loading magnitude does not change, this maximum is reached for each cycle. If the strain exceeds some threshold strain at any location within the tendon, then an adaptive response is initiated at that location, proportional to the amount by which the maximum strain exceeds the threshold strain.

loading bout itself. We refer to these models as the *reset* and *cumulative* models, respectively.

The initial stiffness and permeability are given by $M(\boldsymbol{x}, \tau = 0)$ and $k(\boldsymbol{x}, \tau = 0)$ and are prescribed to be either initially homogeneous or with a local reduction in the stiffness/permeability imposed over the midportion, described in further detail in the subsequent section. For the reset model, the material parameters are updated according to

$$\begin{aligned}\frac{\partial M(\boldsymbol{x},\tau)}{\partial \tau} = \sum_{b=1}^{B-1} \left(\frac{\partial w_b}{\partial z}^{\max}(\boldsymbol{x}) - \frac{\partial w}{\partial z}^{\text{thresh}} \right)^+ f_1(\tau - \tau_b)\mathbf{1}_{\{\tau_b \le \tau < \tau_{b+1}\}} \\ + \left(\|k\nabla p\|_b^{\max}(\boldsymbol{x}) - \|k\nabla p\|^{\text{thresh}} \right)^+ f_2(\tau - \tau_b)\mathbf{1}_{\{\tau_b \le \tau < \tau_{b+1}\}}, \qquad (3.2)\end{aligned}$$

$$\frac{\partial k(\boldsymbol{x},\tau)}{\partial \tau} = \sum_{b=1}^{B-1} \left(\|k\nabla p\|_b^{\max}(\boldsymbol{x}) - \|k\nabla p\|^{\text{thresh}} \right)^+ g(\tau - \tau_b)\mathbf{1}_{\{\tau_b \le \tau < \tau_{b+1}\}}, \qquad (3.3)$$

where $(\cdot)^+$ denotes the positive part and $0 \le \tau < \tau_B$. The parameters $\partial w^{\text{thresh}}/\partial z$ and $\|k\nabla p\|^{\text{thresh}}$ are the strain and flux thresholds at which a mechanical stimulus to the cells is

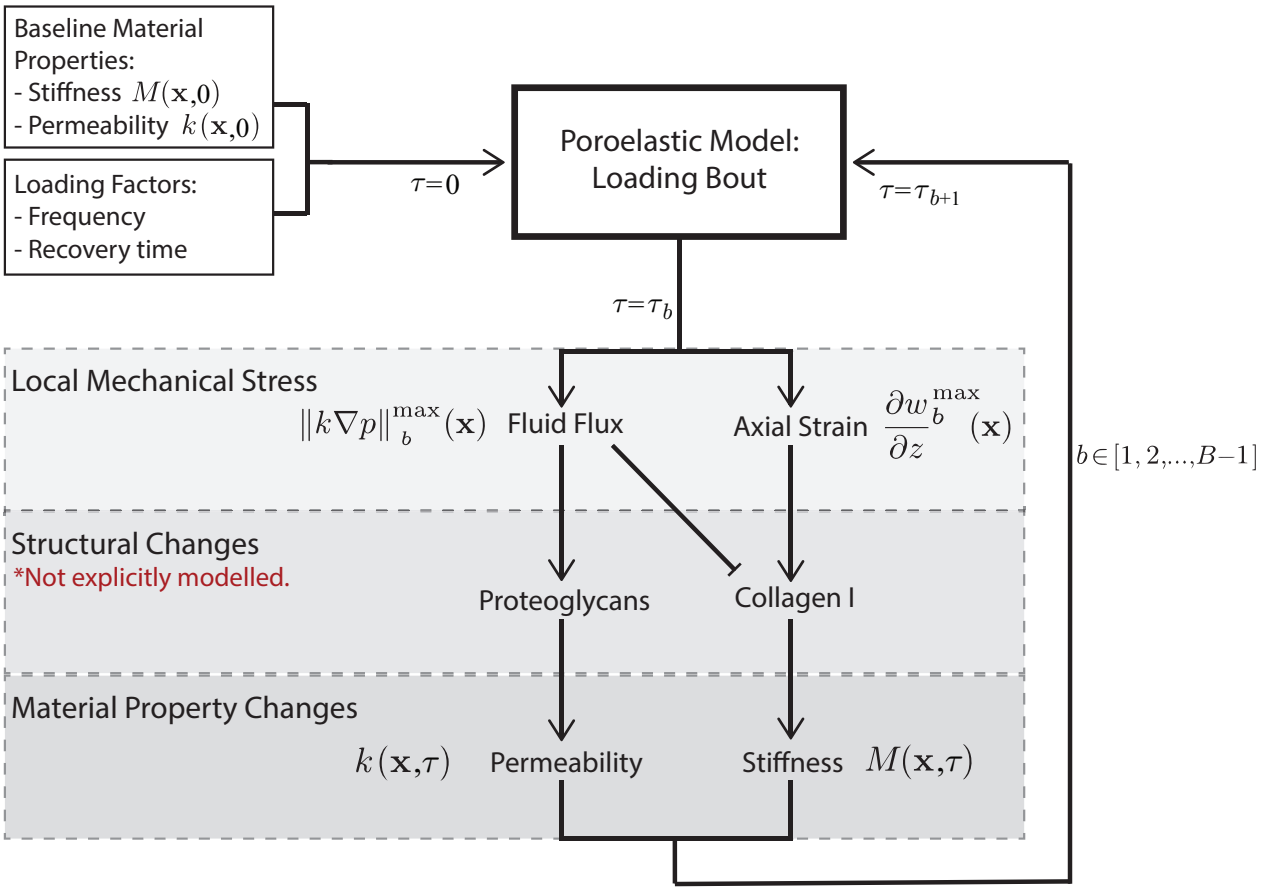


Figure 3.6: Schematic representation of adaptation model. The cells are mechanically stimulated during each loading session, leading to subsequent local changes in the tendons constituents. These micro-structural changes in tendon constituents lead to downstream affects on the material properties, which subsequently affects mechanical stimulation with future loading.

generated. We assume that these thresholds do not change during a series of loading bouts. The indicator function $\mathbf{1}_{\{\tau_b\leq\tau<\tau_{b+1}\}}$ serves to switch on the stimulus from loading bout b over the time period $\tau_b \leq \tau < \tau_{b+1}$ and off at all other times.

To reproduce the time dependent relationship given in the schematic Figure 3.2, we choose $f_1(\tau)$ and $f_2(\tau)$ to be of the form

$$f_1(\tau) = \frac{c_1\tau - c_2\tau^2}{c_3\tau^3 - c_4\tau^2 + c_5\tau + c_6}, \quad f_2(\tau) = -\frac{c_7\tau - c_8\tau^2}{c_9\tau^3 - c_{10}\tau^2 + c_{11}\tau + c_{12}}. \tag{3.4}$$

where c_1-c_{12} are constants, and the functions f_1 and f_2 represent the synthesis (green/top curve in Figure 3.2) and degradation (red/bottom curve in Figure 3.2) respectively. Using the

constitutive rule (3.2), we assume that the axial strain promotes an increase in the stiffness (synonymous with an increase in local tendon collagen content or change in collagen type - from type III to I), whilst the fluid flux magnitude (shear) reduces the stiffness (synonymous with a reduction in local tendon collagen content). There is little knowledge surrounding the time dependence of proteoglycan changes following loading. Hence we assume a simple form for the function $g(\tau)$, motivated by the acute increase in proteoglycans observed when cartilage cells are exposed to load (Section 3.4.2):

$$g(\tau) = -\left(c_{13}\tau^2 - c_{14}\tau -\right)\mathcal{H}(24-\tau) \quad \text{where} \quad \mathcal{H}(24-\tau) := \begin{cases} 1 & \tau < 24 \\ 0 & \tau \geq 24. \end{cases} \tag{3.5}$$

The parameter values for c_1-c_{14} are given in Appendix 3.A.1 and are assumed to be the same for the reset and cumulative model to facilitate comparison. In Figure 3.7 we display the functions (3.4) and (3.5). The strain stimulus, which serves as a coefficient to $f_1(\tau)$ in (3.2), is found to be larger than the flux stimulus, which serves as a coefficient to $f_2(\tau)$ in (3.2). Hence, $f_1(\tau)$ is parameterised to have a smaller magnitude than $f_2(\tau)$ (otherwise only increases in the stiffness would be observed).

For the cumulative model, the material properties are updated according to

$$\begin{aligned} \frac{\partial M(\boldsymbol{x},\tau)}{\partial \tau} = &\sum_{b=1}^{B-1} \mathcal{H}\left(\tau-\tau_b\right)\left(\frac{\partial w_b}{\partial z}^{\max}(\boldsymbol{x}) - \frac{\partial w}{\partial z}^{\text{thresh}}\right)^{+} f_1(\tau-\tau_b) \\ &+ \mathcal{H}\left(\tau-\tau_b\right)\left(\|k\nabla p\|_b^{\max}(\boldsymbol{x}) - \|k\nabla p\|^{\text{thresh}}\right)^{+} f_2(\tau-\tau_b), \end{aligned} \tag{3.6}$$

$$\frac{\partial k(\boldsymbol{x},\tau)}{\partial \tau} = \sum_{b=1}^{B-1} \mathcal{H}\left(\tau-\tau_b\right)\left(\|k\nabla p\|_b^{\max}(\boldsymbol{x}) - \|k\nabla p\|^{\text{thresh}}\right)^{+} g(\tau-\tau_b), \tag{3.7}$$

where $0 \leq \tau < \tau_B$. Conceptually (3.6) and (3.7) suggest that the cellular response to loading is a cumulative phenomena in which additional cell stimulation builds on the previous response rather than resetting it. In contrast to the indicator functions used in the reset

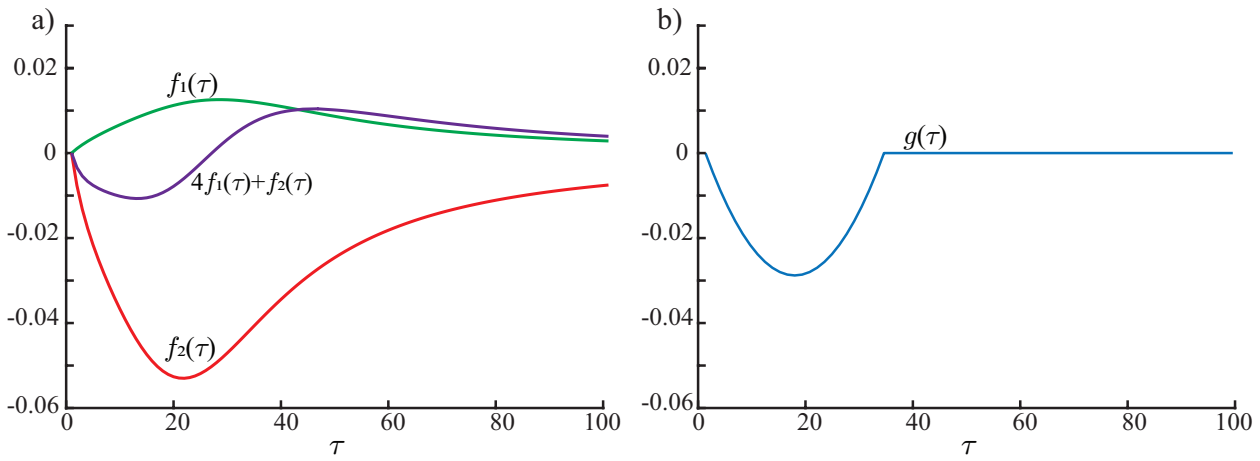


Figure 3.7: Plot of functions (3.4) and (3.5) describing time-dependence of material property changes following loading. a) Positive (f_1) and negative (f_2) contributions to changes in stiffness from the strain and flux stimulus, respectively. The purple line shows an example of the summative effect of the positive and negative contributions to the change in stiffness, dependent on the stimulus magnitudes in (3.2). b) Function governing changes in permeability. An acute change in the permeability occurs over 24 hours with no subsequent changes.

model, the heaviside function $\mathcal{H}(\tau - \tau_b)$ serves to switch on the stimulus from the loading bout b without switching it off.

We note that, by prescription (Equation (3.5)) there are no further changes to the permeability using either the reset (Equation (3.3)) or cumulative (Equation (3.7)) model after 24 hours following loading. As such, differences in the permeability for the cumulative model, when contrasted with the reset model, occur only indirectly through cumulative effects of loading on the stiffness which in turn affects the strain and subsequently the flux stimulus.

In Figure 3.8 we display a schematic of the loading simulation which shows how the material properties are updated between loading bouts for each model.

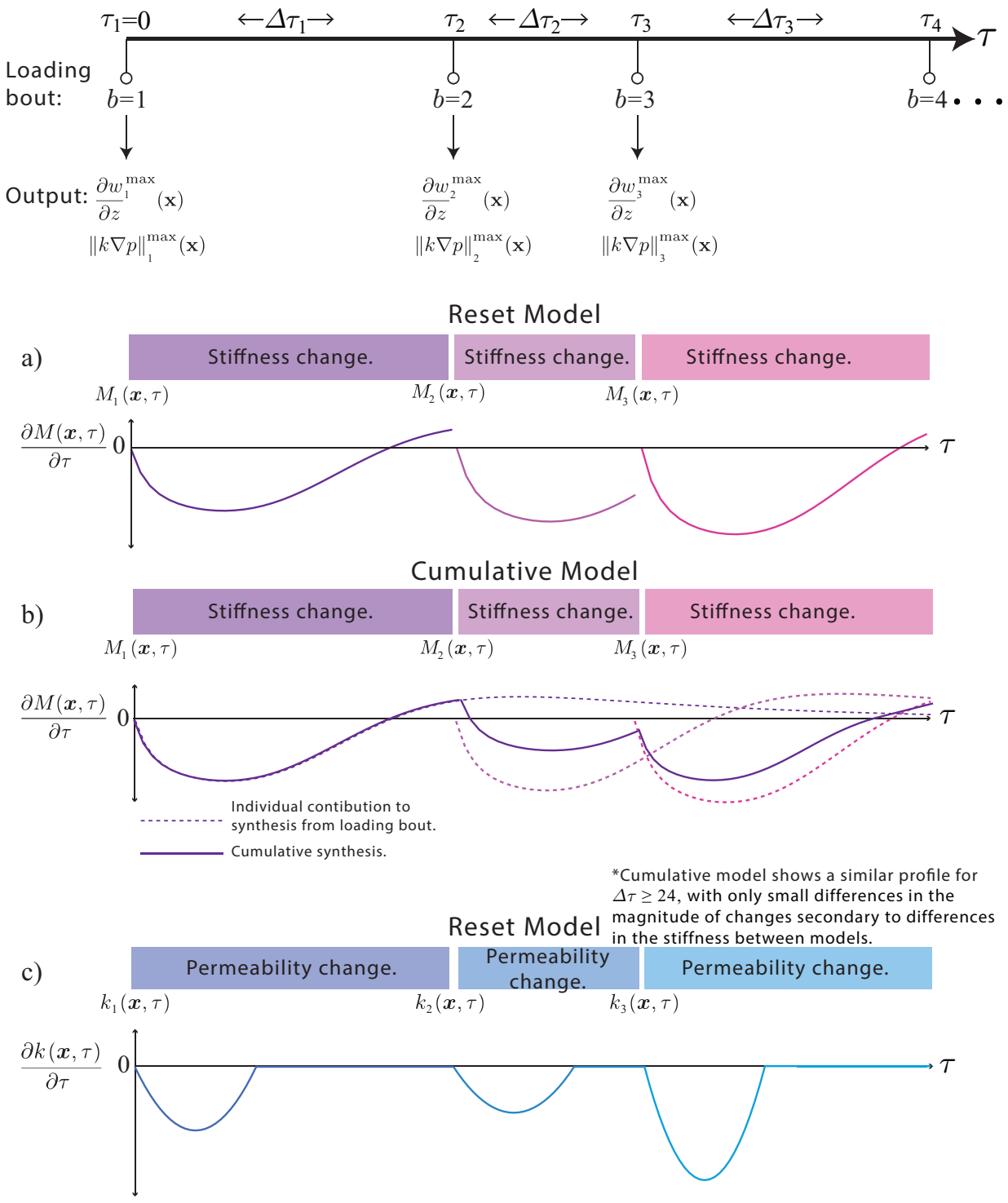


Figure 3.8: Material property changes for the reset and cumulative models in response to a series of loading bouts when a large flux stimulus is imposed. a) Rate of change in stiffness following three separate loading bouts for reset model. b) Rate of change in stiffness following three separate loading bouts for cumulative model. Dashed lines in varying shades of pink and purple indicate individual contributions from separate loading bouts. Solid purple line indicates cumulative rate of change in stiffness. c) Rate of change in permeability for reset model.

A summary of the parameter and variable definitions used throughout this chapter are given below.

Symbol	Definition
B	Number of loading bouts undertaken.
b	Subscript to denote the loading bout number $b = 1, 2, ..., B$.
ω_b	Frequency of loading bout b.
τ	Macroscopic timescale over which a series of loading bouts occur.
Δt_b	Duration of loading bout b.
$\Delta\tau_b$	Duration of time between loading bouts b and $b+1$.
τ_b	Time loading bout b occurs.
$\frac{\partial w_b}{\partial z}^{\max}(\boldsymbol{x})$	Maximum axial strain during loading bout b at each spatial location.
$\|k\nabla p\|_b^{\max}(\boldsymbol{x})$	Maximum flux magnitude during loading bout b at each spatial location.
$\frac{\partial w}{\partial z}^{\text{thresh}}$	Axial strain threshold at which adaptation occurs.
$\|k\nabla p\|^{\text{thresh}}$	Flux threshold at which adaptation occurs.
$M(\boldsymbol{x}, \tau)$	Tendon stiffness.
$k(\boldsymbol{x}, \tau)$	Tendon permeability.
$f_i(\tau)$	Function for synthesis/degradation ($i = 1$ or $i = 2$) of collagen I, and hence increase/decrease in stiffness.
$g(\tau)$	Function for net synthesis of proteoglycans, and hence net reduction in permeability.

3.7 Model Implementation

As before (Chapter 2), we consider a two-dimensional poroelastic model for the tendon, spanning the width and thickness (Figure 3.9). We impose a symmetry condition at the longitudinal axis, and only consider the domain $\mathrm{D} = \{(x, z) : 0 < x < W_0/(2L_0),\ 0 < z < 1\}$.

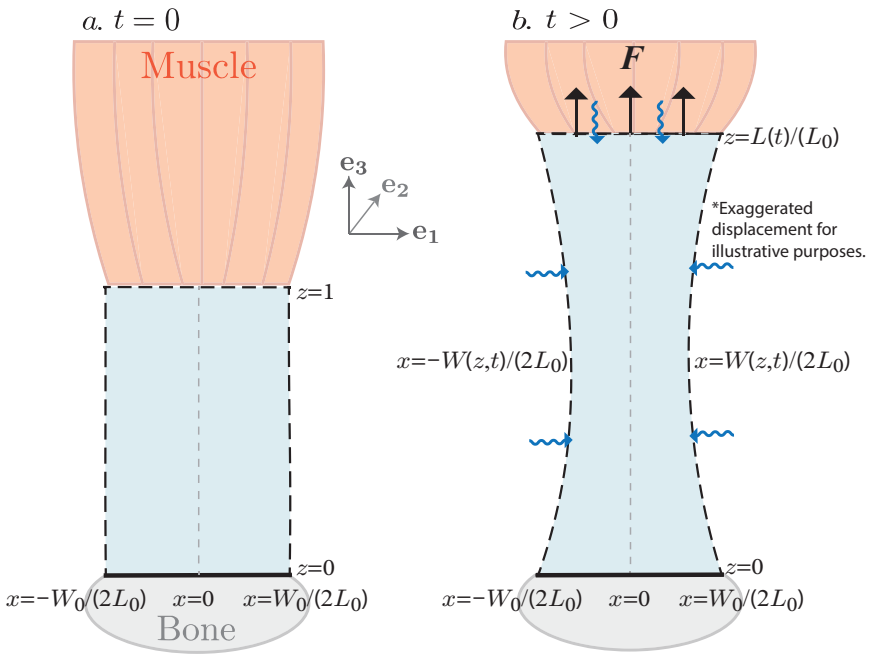


Figure 3.9: Two-dimensional depiction of tendon under load in cartesian coordinates. The diagram is a schematic and not drawn to scale. An axial force is applied at the muscular boundary at time t > 0, generating tensile deformation of the poroelastic material and fluid movement into the tendon. Fluid moves in and out of the tendon (blue wavy arrows).

3.7.1 Pseudocode

Pseudocode for the adaptation model is given in Algorithm 1 and a schematic is depicted in Figure 3.6. To incorporate loading into the adaptation model, for each loading bout the poroelastic model developed in Chapter 2 is subject to load and the output (maximum flux and axial strain at each spatial point) used to determine how the material parameters dynamically evolve (Equations (3.2)-(3.3) or (3.6)-(3.7)) prior to the next loading bout.

Algorithm 1 Pseudocode for Adaptation Model of Tendinopathy

Inputs:
Number of louding bouts B
Baseline material properties $M_0(\boldsymbol{x})$, $k_0(\boldsymbol{x})$, ν
Duration between loading bouts $\{\Delta\tau_1, ..., \Delta\tau_B\}$
Frequency of loading implemented at each bout $\{\omega_1, ..., \omega_B\}$
Loading magnitude A (constant across loading bouts).
Initialise:
    Implement poroelastic model at time $\tau_1 = 0$ with forcing parameters: $\{\omega_1, A\}$.
    Output: Maximum axial strain and fluid flux reached at each spatial point.
for $b = 1 : B$ **do**
    Calculate material properties at time of loading, $M_b(\boldsymbol{x})$, $k_b(\boldsymbol{x})$, by integrating (3.2)-(3.3)
    or (3.6)-(3.7) over Δt.
    Implement poroelastic model:
        Input forcing parameters: $\{\omega_b, A\}$.
        Output: Maximum axial strain and fluid flux reached at each spatial point.

3.7.2 Loading Interventions

We simulate several loading interventions and assess the impact of different forms of long term (14 weeks) loading on the stiffness and permeability. To gain insight into the system dynamics, we first investigate changes due to a single loading bout, and then proceed to investigate changes when a series of loading bouts are delivered over multiple weeks. We investigate how classic rehabilitation regimes, in which low-frequency high-magnitude loads (0.17 Hz, $\geq 70\%$ MVC, 72 hrs between bouts) are applied to damaged tendon over a period of 14 weeks, affect the material properties, and assess whether the model predictions are in line with both qualitative observations and global material property change measurements recorded clinically (Table 3.2).

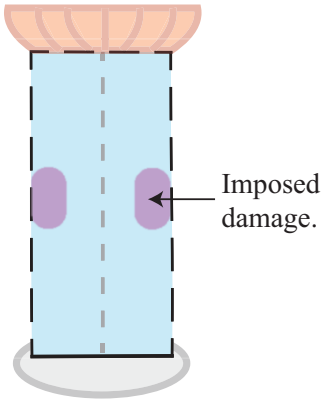


Figure 3.10: A damaged region within the tendon is imposed over $\{W_0/(4L_0) \leq x \leq W_0/(2L_0),\ 2/5 \leq z \leq 3/5\}$.

We mimic midportion damage by imposing a constant localised reduction in the stiffness $M(x,z) = M^d < 1$ and permeability $k(x,z) = k^d < 1$ over the region $\{W_0/(4L_0) \leq x \leq W_0/(2L_0),\ 2/5 \leq z \leq 3/5\}$. We again apply a Gaussian filter (Section 2.8.2) to ensure a smooth (gradient) change in the stiffness and permeability at the edge of this region. We then investigate damage-inducing forms of loading ($\geq$ 2 Hz, $\geq$ 70% MVC, 24 hrs between bouts), applied to initially healthy tendon, and assess whether the qualitative predictions of material properties changes are consistent with those observed clinically. Finally, we proceed to use the model to investigate loading interventions which feature a mixture of low- and high-frequency loading, for which less is known about the material property changes that occur.

3.7.3 Parameter Values

We prescribe a tendon length of 3 cm, thickness of 0.3 cm, and, for a healthy tendon, an initial homogeneous Young's modulus of 1 GPa (Arampatzis et al. 2007, Arampatzis et al. 2010, Bohm et al. 2015). The Poisson's ratio is 0.33 and hydraulic permeability $3.98e^{-14}m^4/N \cdot s$ (Chapter 2 Table 2.2). Recalling that low-frequency loading in rehabiltation regimes is completed at a speed of 0.17 Hz and running is completed at speeds >2 Hz, scaling ω by the classic poroelastic timescale $t_c = \mu L_0^2/(k_0 M_0)$ given in Section 2.6.1, this leads to a dimensionless frequency of $\omega = 2$ for low-frequency rehabilitative loading protocols and $\omega = 10 - 20$ for running (Section 1.3.1) (Arampatzis et al. 2007, Rowlands et al. 2007). The force magnitude is chosen to produce strains of 4.5-5%, consistent with global strains observed for high magnitude (90% MVC) loading (Arampatzis et al. 2007, Arampatzis et al. 2010, Bohm et al. 2015). The strain threshold for all simulations is set to $\partial w^{\text{thresh}}/\partial z = 4$ (corresponding to a 4% dimensional strain), motivated by previous *in vitro* work (Huisman

et al. 2014). The dimensionless flux threshold is set to $\|k\nabla p\|^{\text{thresh}} = 0.03$[7], taken from the upper reference range of the flux magnitude observed in Chapter 2. A summary of the baseline parameters used is given in Appendix 3.A.1 Table 3.3.

3.7.4 Metrics

While we implement the adaptation model for the entire tendon, we are especially interested in how the stiffness and permeability change over the midportion ($0 \leq x \leq W_0/(2L_0)$, $2/5 \leq z \leq 3/5\}$) in response to different frequencies of loading. A diagram displaying the region over which the metric is calculated is shown in Figure 3.11. We also display the areas of damage imposed when we initialise the simulation with a tendinopathic tendon (a healthy tendon - not shown - is initialised with no areas of damage). The metric is calculated for the entire midportion while the damage is only imposed over half of this region.

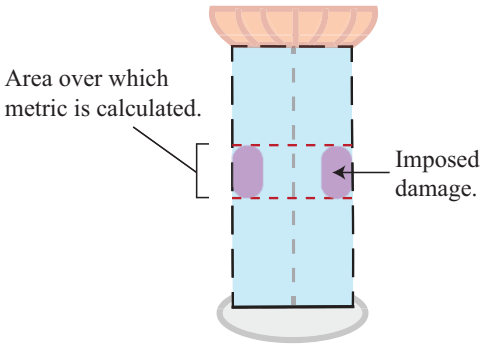


Figure 3.11: Tendon displaying metric area and damaged region.

As a metric, we consider the spatially averaged stiffness and permeability over the midportion

$$M_{av}(\tau) = \frac{2L_0}{5W_0}\int_{2/5}^{3/5}\int_0^{W_0/2L_0} M(\boldsymbol{x},\tau)\,d\boldsymbol{x}, \quad k_{av}(\tau) = \frac{2L_0}{5W_0}\int_{2/5}^{3/5}\int_0^{W_0/2L_0} k(\boldsymbol{x},\tau)\,d\boldsymbol{x}, \qquad (3.8)$$

as well as the maximum and minimum stiffness and permeability over the midportion ($M_{max}(\tau)$, $M_{min}(\tau)$, $k_{max}(\tau)$, $k_{min}(\tau)$). We are also interested in determining how local material property changes affect the tensile axial strains and flux magnitudes at the midportion that occur during loading. We use, as a metric, the spatial average (over the midportion) of the local

[7]For a hydraulic permeability of $3.98e^{-14}m^4/N \cdot s$, Young's modulus of 1 GPa and this correlates to a flux of $\approx 5.9e^{-6}$ m/s, consistent with the magnitudes predicted by the experimental and finite element work of Safa et al. (2020).

stimulus-response-producing quantities defined in (3.1)

$$\varphi_s = \frac{2L_0}{5W_0}\int_{2/5}^{3/5}\int_0^{W_0/2L_0} \frac{\partial w}{\partial z}^{\max}(\boldsymbol{x})\, d\boldsymbol{x}, \quad \varphi_f = \frac{2L_0}{5W_0}\int_{2/5}^{3/5}\int_0^{W_0/2L_0} \|k\nabla p\|^{\max}(\boldsymbol{x})\, d\boldsymbol{x}, \tag{3.9}$$

which we refer to as the *average strain stimulus* and *average flux stimulus* respectively. These metrics can be considered as the average stimulus felt by the cells over the midportion which promotes the cells to produce a change in the collagen/proteoglycan content of surrounding tissue. Consistent with the finite difference scheme used to implement the poroelastic model (Section 2.8.2), the integrals are approximated numerically using the trapezoidal rule.

A summary of the loading scenarios investigated and metrics used to measure changes are given in Figure 3.12.

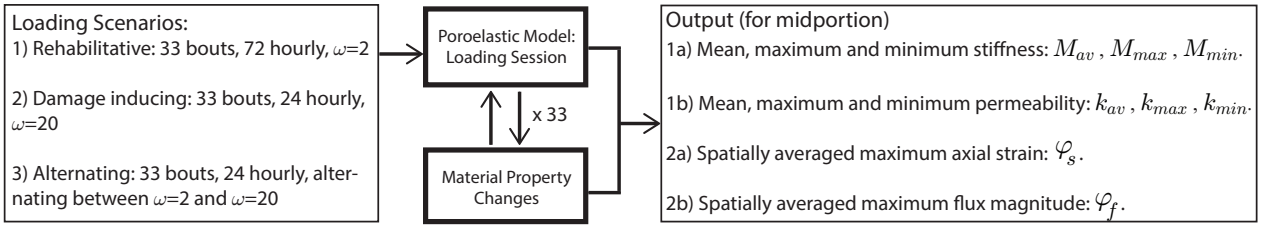


Figure 3.12: Schematic of loading simulations implemented and metric output.

3.8 Results

3.8.1 Parameter Sensitivity

In this chapter we have introduced several new parameters, including the strain (3.2) and flux thresholds (3.3), and a set of parameters governing the time dependence of material property changes in response to loading (Equations (3.4) and (3.5)). In Appendix 3.A.2 we investigate and discuss the sensitivity of the material property changes to these parameters when a single loading bout is completed at two different frequencies ($\omega = 2, 20$). Overall, the axial strain threshold and parameters governing the magnitude of $g(\tau)$ (Equation (3.5))

had the most significant effects on changes in stiffness and permeability occurring over the midportion.

3.8.2 Changes in Stiffness Following a Single Loading Bout

We expect changes due to a single loading bout to be small, and that more substantial changes to occur as a result of multiple bouts of loading (investigated in subsequent sections). However, to build intuition of the adaptation model, we first investigate how the stiffness changes in response to a single bout of loading. We have parameterised the model such that material property changes following a single bout of loading should be small, and hence substantial changes in material properties should only occur after a period of multiple weeks, consistent with the clinical observations detailed in Section 3.4.4. To indicate changes in the stiffness driven by the strain stimulus and flux stimulus, we consider the decomposition of Equation (3.2)

$$\begin{aligned}\frac{\partial M_b(\boldsymbol{x},\tau)}{\partial \tau} &= \left(\frac{\partial w_{b-1}}{\partial z}^{\max}(\boldsymbol{x}) - \frac{\partial w}{\partial z}^{\text{thresh}}\right)^{+} f_1(\tau-\tau_{b-1})\mathbf{1}_{\{\tau\geq\tau_b\}} \\ &\quad + \left(\|k\nabla p\|_{b-1}^{\max}(\boldsymbol{x}) - \|k\nabla p\|^{\text{thresh}}\right)^{+} f_2(\tau-\tau_{b-1})\mathbf{1}_{\{\tau\geq\tau_b\}} \qquad (3.10)\\ &= \frac{\partial M_s(\boldsymbol{x},\tau)}{\partial \tau} + \frac{\partial M_f(\boldsymbol{x},\tau)}{\partial \tau}, \qquad (3.11)\end{aligned}$$

where $\partial M_s/\partial\tau$ and $\partial M_f/\partial\tau$ are the changes in stiffness attributable to the strain and flux stimuli, respectively.

In Figure 3.13a we plot the rate of change in stiffness, and in Figure 3.13b the actual stiffness change, at the time τ following a single loading bout for an initially homogeneous tendon ($M(\boldsymbol{x},\tau=0)=k(\boldsymbol{x},\tau=0)$). The stiffness changes are taken at the point $\boldsymbol{x}^*=(W_0/(4L_0),1/2)$, the midpoint of the half plane identified by a red cross, following a loading bout completed with a frequency of $\omega=2,17$ or 20. We have assumed the tendon is initially

homogeneous with $M(\boldsymbol{x}) = 1$ ($M_s(\boldsymbol{x}) = M_f(\boldsymbol{x}) = 0$). In Figure 3.13a i and Figure 3.13b i the loading frequency is sufficiently low that the flux threshold is not exceeded and hence changes in the stiffness are strictly positive. It is evident from Figure 3.13a that, as the loading frequency increases, a larger flux stimulus (red dashed line) occurs, which contributes to a reduction in the stiffness. Figure 3.13b shows that the time point of subsequent loading will affect the tendon stiffness for that loading bout, especially between the ranges of $\tau \in [0, 72]$. In Figure 3.13c we plot the final stiffness following a single loading bout. There is a global increase in stiffness for the lower loading frequency and a heterogenous change for the higher frequencies, with an increase in stiffness toward the transverse centre and progressive decrease in the stiffness closer to the transverse boundary. If we instead consider a point at the transverse centre $\boldsymbol{x}^* = (0, 1/2)$, we find that the pattern of stiffness changes are the same as Figure 3.13a i and Figure 3.13b i for all three frequencies ($\omega = 2, 17, 20$), as the flux threshold is not exceeded at any point and the axial strain is almost exactly uniform across the midportion (results not shown). Conversely, stiffness profiles taken for a point at the transverse boundary $\boldsymbol{x}^* = (W_0/(2L_0), 1/2)$ are displayed in Appendix 3.B.1. In this case, for $\omega = 20$, the flux stimulus during loading is higher than at the point $\boldsymbol{x}^* = (W_0/(4L_0), 1/2)$, and hence there is a greater decrease in the stiffness following a single loading bout. The profile for $\omega = 2$ at the outer boundary is still the same as Figure 3.13a i, as the flux threshold is not exceeded for this lower frequency of loading (results not shown). In Appendix 3.B.1 Figure 3.14 we carry out a similar analysis, considering the midpoint of the half plane $\boldsymbol{x}^* = (W_0/(4L_0), 1/2)$. In Appendix 3.B.2 Figure 3.25 we consider how the stiffness may change across the tendon when the tendon is already damaged, with a local reduction in stiffness.

In Figure 3.14a we plot the rate of change in permeability, and in Figure 3.14b the actual permeability, at the time τ following a single loading bout for an initially homogeneous tendon ($M(\boldsymbol{x}, \tau = 0) = k(\boldsymbol{x}, \tau = 0)$). We investigate the loading frequencies $\omega = 17$ and 20, as $\omega = 2$ produces no change in the permeability since the flux threshold is not exceeded.

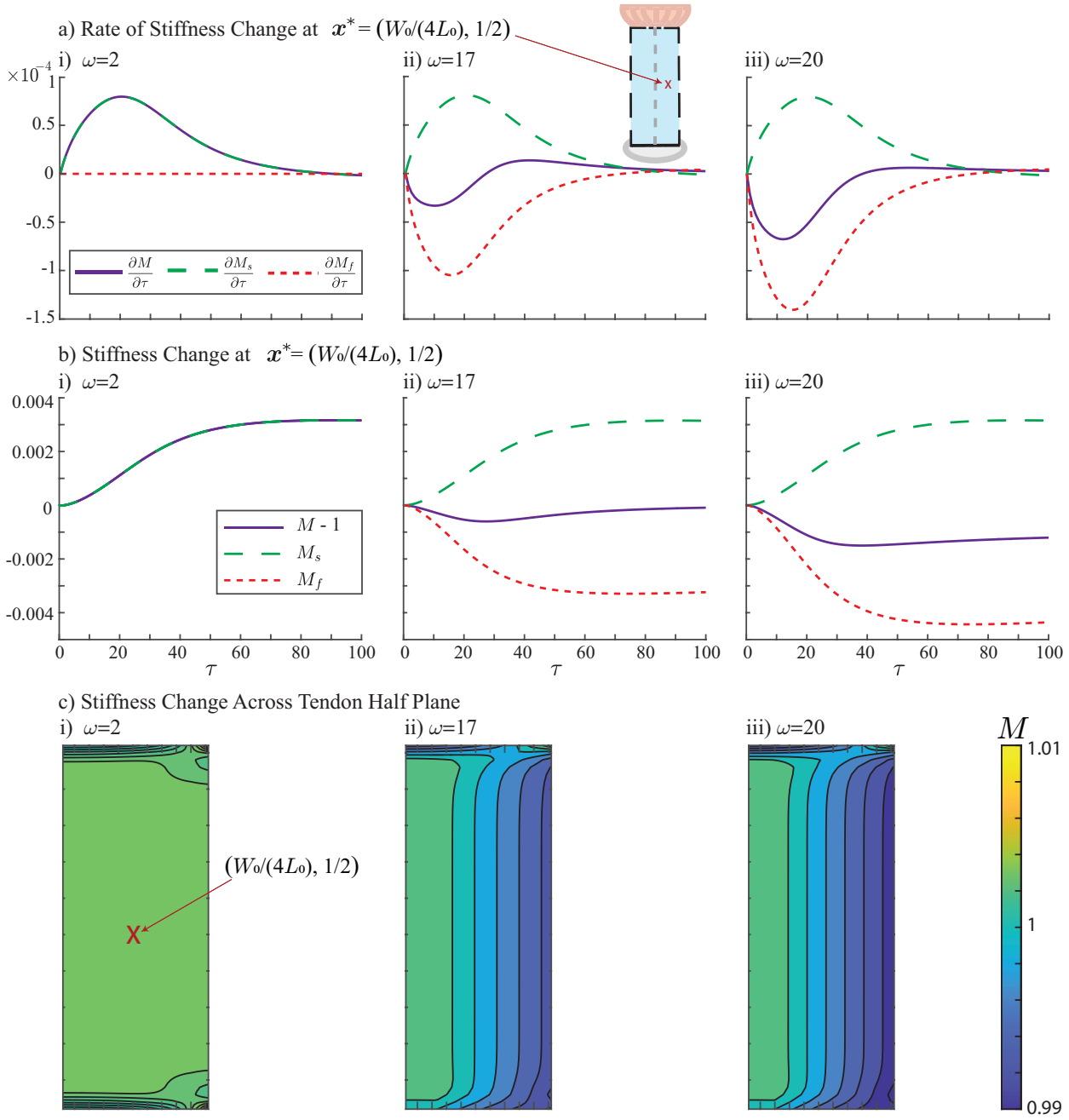


Figure 3.13: a) Rate of change in tendon stiffness and b) stiffness change against time τ at the midpoint of half plane $\boldsymbol{x}^* = (W_0/(4L_0), 1/2)$, and c) stiffness change over whole tendon half plane after a bout of loading. Loading frequency: i) $\omega = 2$, ii) $\omega = 17$, iii) $\omega = 20$. Initially homogeneous tendon: $M(\boldsymbol{x}, \tau = 0) = k(\boldsymbol{x}, \tau = 0) = 1$ and $M_s(\boldsymbol{x}, \tau = 0) = M_f(\boldsymbol{x}, \tau = 0) = 0$.

Consistent with Equation (3.5), the permeability changes rapidly over the first 24 hours and, assuming no subsequent loading, remains stable thereafter. The time-dependency of permeability changes are similar for $\omega = 17$ and 20, with the magnitude of reductions in the

permeability increasing with increasing frequency.

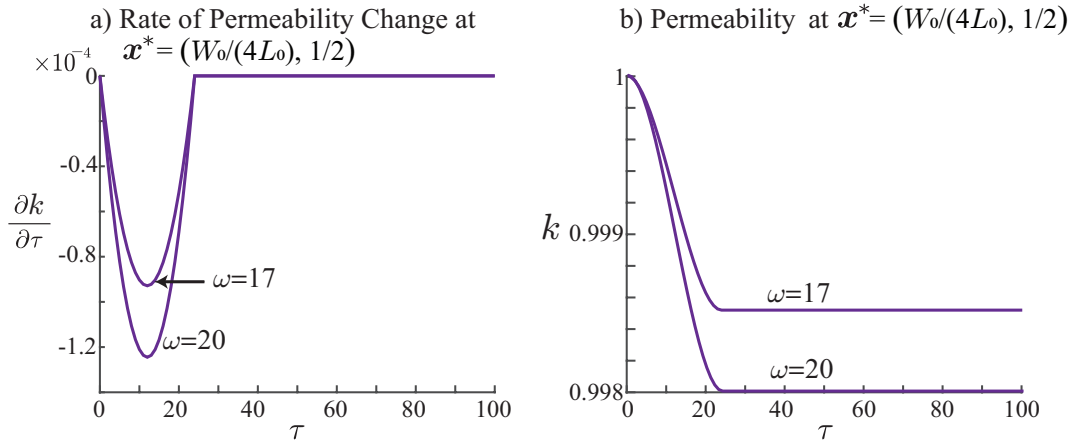


Figure 3.14: a) Rate of change in tendon permeability and b) permeability at time τ for the midpoint of half plane $\boldsymbol{x}^* = (W_0/(4L_0), 1/2)$ after a bout of loading. Loading frequency: i) $\omega = 17$, ii) $\omega = 20$.

In Figure 3.15 we display the stiffness at $\boldsymbol{x}^* = (W_0/(4L_0), 1/2)$ when the cumulative model is implemented for four bouts of loading (black arrows indicate delivery of a loading bout). Four loading bouts are implemented with 72 (Figure 3.15a) or 24 (Figure 3.15b) hours recovery and with a frequency of $\omega = 2, 17$ or 20. For the slow loading scenario $\omega = 2$, since the flux threshold is not exceeded at any point, the change in stiffness is strictly positive for $\Delta = 24, 72$. A larger increase in the stiffness is observed for a recovery period of 72 hours between loading bouts, as the rate of stiffness change stays strictly positive over this time. When $\omega = 17$ there is a small decrease in the stiffness, which is larger when the recovery time is shorter with 24 hours between loading bouts. For $\omega = 20$ there is also a decrease in stiffness, but with a larger decrease observed for a recovery period of 72 hours, a consequence of the rate of stiffness change staying negative past 24 hours (Figure 3.13a iii). Overall, the cumulative model predicts that the stiffness is higher with a longer recovery period, except in the case of the fastest loading frequency $\omega = 20$.

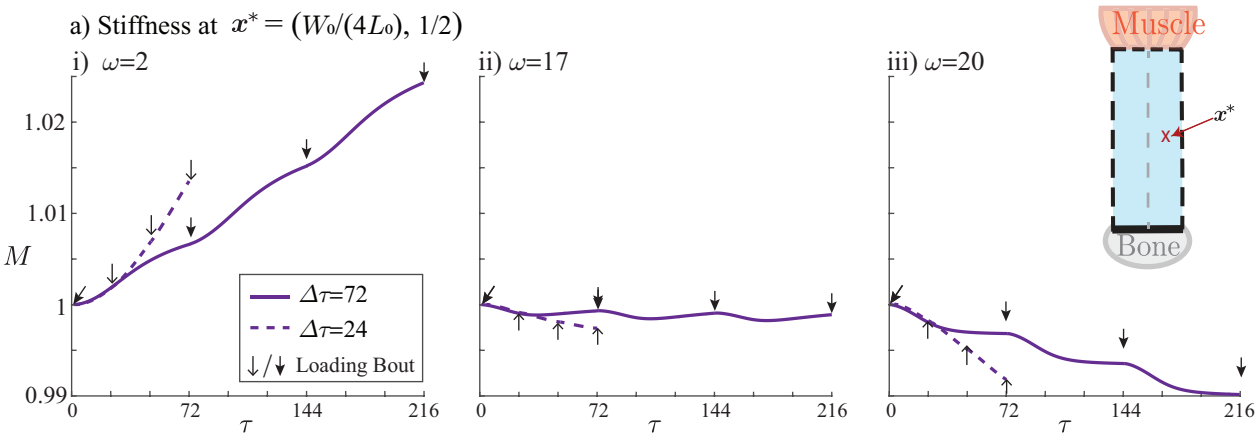


Figure 3.15: Stiffness using cumulative model against time τ at the midpoint of half plane $\boldsymbol{x}^* = (W_0/(4L_0), 1/2)$, for three bouts of loading with a recovery period of 24 or 72 hours. Loading frequency: i) $\omega = 2$, ii) $\omega = 17$, iii) $\omega = 20$.

3.8.3 Rehabilitative Loading

We now consider the case in which a person with midportion tendinopathy undertakes 14 weeks of rehabilitative loading with the aim of improving tendon structure. We simulate 33 bouts of loading with a dimensionless frequency of $\omega = 2$ and a recovery period of 72 hours. To mimic damage, the initial tendon structure is characterised by a localised reduction in stiffness and permeability at the midportion: $M^d = k^d = 0.4$ over the region $\{W_0/(4L_0) \leq x \leq W_0/(2L_0), 2/5 \leq z \leq 3/5\}$ (Figure 3.12). The averaged, maximum and minimum midportion stiffness at commencement of each loading bout are given in Figure 3.16a. The stiffness across the entire midportion increases with each loading bout. The slope of the minimum stiffness M_{min}, for both the reset model and cumulative model, is slightly steeper than that of the average and maximum stiffness, M_{av} and M_{max} (results not shown). This indicates that the strain stimulus with loading is slightly higher in these low stiffness regions and hence they are slightly more responsive than the healthy regions, where $M = 1$, in terms of increases in stiffness following low frequency loading.

In Figure 3.16b the corresponding average strain stimulus (Equation (3.9)) which occurs during each bout of loading is displayed. Results for the reset and cumulative models are

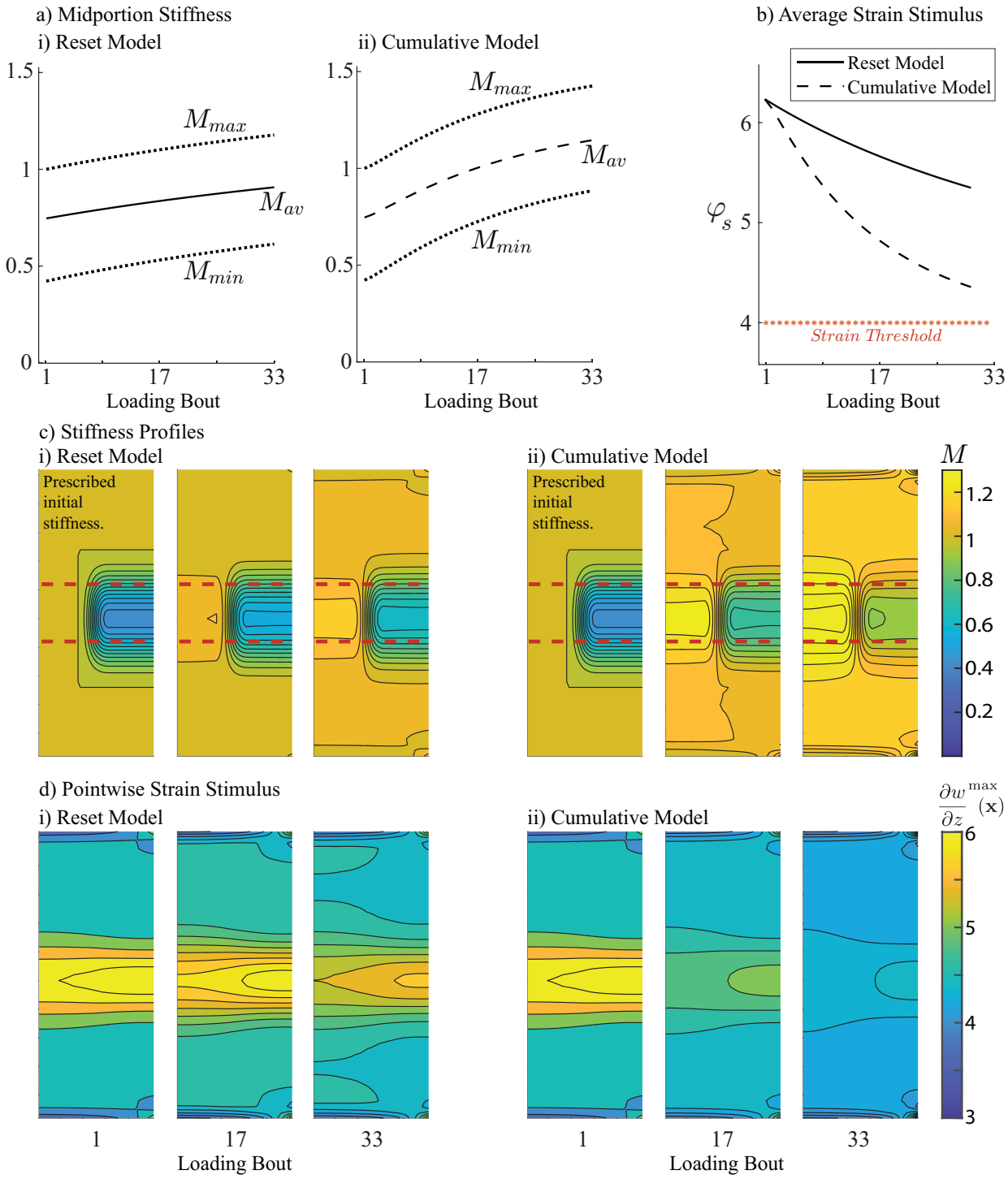


Figure 3.16: Changes in the midportion (red dashed lines) stiffness and the local mechanical environment with 33 bouts of slow loading ($\omega = 2$, $\Delta\tau = 72$). a) Averaged stiffness over the midportion at commencement of loading bout (Equation (3.8)). b) Averaged axial strain stimulus during each loading bout (Equation (3.9)).c) Stiffness profiles for loading bouts $b = 1, 17, 33$ for the i) reset and ii) cumulative model. d) Strain stimulus associated with loading bouts $b = 1, 17, 33$ for the i) reset and ii) cumulative model.

given by a solid and dashed line, respectively. At no point is the flux threshold exceeded (results not shown) and hence changes in the stiffness are positive and occur only as a result of large axial strains. Because of the direct influence of the stiffness on the axial strain, the curves given in 3.16a and 3.16b are inversely correlated with the average stiffness increasing as the average strain stimulus decreases. The cumulative model predicts a larger increase in the stiffness and reduction in the strain over time. This occurs because there is a very small positive net synthesis past 72 hours following loading (Figure 3.13a i - solid purple line) which, for the cumulative model, contributes to increases in the stiffness in the subsequent recovery time frame. In Appendix 3.B.3 the corresponding long-term profiles for Figures 3.16a and 3.16b are given. As the number of loading bouts increases, the increases in stiffness becomes smaller and the average strain stimulus asymptotes toward the strain threshold.

In Figure 3.16c the stiffness profiles are shown for several time points in the 14 week period for both the reset and cumulative models. In Figure 3.16d the corresponding strain stimulus that occurred during the loading bout is shown. This is equivalent to the strain profile at the maximum point of tension during loading (as the strain stimulus for each location occurs at the time point of maximal tendon displacement). The stiffness profile for the first loading bout displays the initial profile implemented to mimic damage. The initial permeability profile was prescribed similarly, however, since the flux threshold was not exceeded, there was no change to the permeability profile over time. The largest increase in stiffness occurs in the damaged region and directly adjacent to it, where, in Figure 3.16d, a larger strain stimulus is seen to occur. This finding is in keeping with results from Chapter 2 (Figure 2.14) that demonstrated larger axial strains is regions adjacent to damage than observed throughout the rest of the healthy tissue. Both the reset and cumulative models suggest that the stiffness profile will revert to a more homogeneous profile eventually, except for a region transversely adjacent to the region of damage which will show an increase in the stiffness.

Simulating the global stiffness measurement protocol used clinically (Section 3.4.4), the

ratio of post-to-pre intervention global stiffness[8] is 1.06 for the reset model and 1.18 for the cumulative model. If the same loading protocol is simulated but $\Delta\tau = 24$ (results not shown) there is a small reduction in the global stiffness changes, with a post-to-pre intervention global stiffness of 1.03 (reset model) and 1.17 (cumulative model) after 33 loading bouts. If loading is performed with a recovery period of $\Delta\tau = 72$ but at a frequency of $\omega = 20$ (results not shown) then there is a small decline (relative to baseline stiffness $M = 1$) in the global stiffness for both the reset and cumulative model after 21 loading bouts. The cumulative model breaks down numerically (the *MATLAB* ODE15s solver fails) after this due to non-physical stiffness values. We discuss this issue in the subsequent section and chapter discussion. By 21 loading bouts the ratio of post-to-pre intervention global stiffness is 0.99 for the reset model and 0.97 for the cumulative model. In this case, the stiffness and permeability values in the damaged region decline throughout the simulation, however, this is paired with an increase in the stiffness of the transversely adjacent region. This minimises the reduction in global stiffness and explains why the global stiffness values are only slightly less than one at the point the model breaks down, despite the model breaking down due to small non-physical stiffness values occurring locally.

3.8.4 Damage-Inducing Loading

We next consider the scenario in which a person with an initially healthy tendon engages in repetitive high-frequency loading with short recovery periods. We simulate 33 bouts of loading, at a dimensionless frequency of $\omega = 20$ and with a recovery period of 24 hours. We initialise the simulation with a healthy tendon, prescribing a homogeneous stiffness and permeability of $M(\boldsymbol{x}) = k(\boldsymbol{x}) = 1$. Both the axial strain and flux contribute to adaptation, and we consider them in turn.

[8]Stiffness is measured by applying a constant force of varying magnitudes, recording the global tendon displacement, and then taking the slope of the force-deformation curve.

The midportion stiffness at commencement of each loading bout is given in Figure 3.17a. There is a gradual reduction in the average midportion stiffness for both the reset and cumulative models, with a larger reduction seen for the cumulative model. For both models the minimum stiffness M_{min} lies further from the average M_{av} than the maximum M_{max}. The cumulative model predicts very low stiffness values for certain regions, which would lead to non-physical values and the numerical implementation breaking down with a continuation of the trend ($M_{min} \to 0$).

In Figure 3.17b the average axial strain stimulus (Equation (3.9)) which occurs during each bout of loading is displayed. While there is a linear increase in the average strain stimulus for the reset model, the cumulative model predicts a nonlinear change in the strain over time with an initial reduction in the average strain stimulus followed by an increase. This was not due to competing effects of the stiffness and permeability changes, as the same result was observed if the permeability was held constant (results not shown). Hence, it appears the nonlinear change in the average strain stimulus is more likely a result of the heterogeneous stiffness changes seen in Figure 3.17a ii, leading to competing effects from high and low stiffness regions on the strain. The healthy high stiffness regions may initially balance the low stiffness regions and prevent large strains occurring, however, as local regions continue to decline in stiffness (M_{min}), a turning point occurs in which the average strain starts to increase.

Figure 3.17c displays the stiffness profiles at commencement of several loading bouts and Figure 3.17d shows the corresponding strain stimulus that occurred during the loading bout. In contrast to the global increase in stiffness seen in Figure 3.16, in Figure 3.17c the changes in stiffness are more heterogeneous for both models: there is an increase in the stiffness toward the transverse centre and a concurrent damaged region with a reduction in stiffness closer to the transverse boundary. Greater heterogeneity is seen for the cumulative model, compared to the reset model, as the summative effect of a high flux stimulus from each

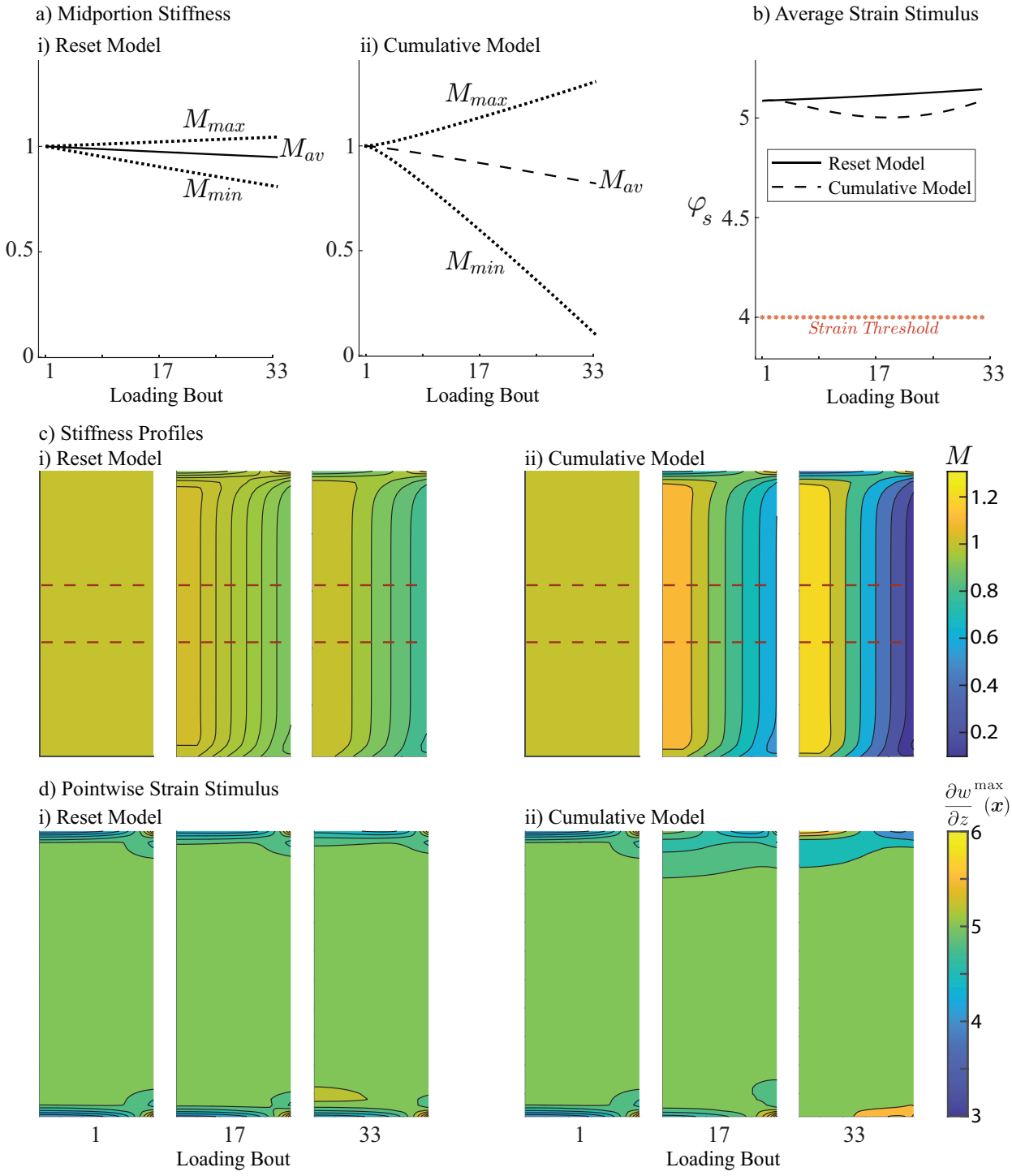


Figure 3.17: Changes in the midportion stiffness and maximum axial strain with 33 bouts of fast loading ($\omega = 20$, $\Delta\tau = 24$). a) Averaged (Equation (3.9)), maximum and minimum stiffness over the midportion at commencement of loading for the i) reset and ii) cumulative models. b) Average axial strain stimulus during each loading bout (Equation (3.9.c)) Stiffness profiles for loading bouts $b = 1, 17, 33$ for the i) reset and ii) cumulative model. d) Strain stimulus associated with loading bouts $b = 1, 17, 33$ for the i) reset and ii) cumulative model.

loading bout contributes to a greater reduction (greater damage) in the stiffness near the transverse boundary where high fluxes occur. In contrast to Figure 3.16, the strain stimulus (and equivalently strain profile at maximum point of tension) remains relatively homogeneous throughout the simulation. In Figure 3.16d the model predicted that healthy areas which are transversely adjacent to low stiffness damaged regions will undergo similarly large strains to the damaged low stiffness region. As such, in this case, where a reduction is stiffness occurs along the entire length of the tendon near the transverse border, rather than the reduction just being confined to the midportion (as was imposed in the previous section, Figure 3.16c), the model predicts a relatively homogeneous strain profile. This is potentially an effect of the boundary conditions (Section 2.8 Equations (2.59c) and (2.59d)) in which a tensile load is applied to the tendon as if it is attached to two plates at its axial ends, which may restrict differences in the axial tensile strain occurring across the tendon thickness.

The ratio of post-to-pre global intervention stiffness is 0.986 for the reset model and 0.988 for the cumulative model. It again appears that global measurements do not capture the degree of local stiffness reductions. In the case of the cumulative model, local increases in the stiffness (Figure 3.17c ii lead to a very slightly higher global stiffness for this model when compared to the reset model, despite local regions of very low stiffness.

The permeability at commencement of each loading bout for both the reset and cumulative models is given in Figure 3.18a. There is minimal difference between the reset and cumulative models, with a linear decline in the average permeability, indicating damage within the midportion, occurring. In Figure 3.18b the corresponding average flux stimulus (Equation (3.9)) which occurs during each bout of loading is displayed. In contrast to Figure 3.16c, in Figure 3.18b the flux threshold is exceeded during every loading bout which, for both models, leads to a reduction in both the permeability and stiffness (Figure 3.17a). It is evident that the reductions in permeability do not appear to have a strong reciprocal effect on the flux for this simulation, with the average flux stimulus remaining high relative to the

flux threshold. In fact, the average flux stimulus changes in a similar manner to the average strain stimulus shown in Figure 3.17b, suggesting that these small changes in the flux may be attributable to changes in stiffness (leading to a change in strains that in turn affects the porosity and subsequently the flux - Section 2.8 Equations (2.58)) rather than permeability. Figure 3.18c displays the corresponding permeability profiles at commencement of several loading bouts for the reset model. As the permeability is only affected by the flux, the profile for the flux stimulus exhibits the same spatial pattern as Figure 3.18c with higher flux magnitudes occurring near the transverse boundary (results not shown). The spatial pattern of permeability changes and flux stimulus for the cumulative model were also not observably different (results not shown). Consistent with the phenomenological rules prescribed, the heterogeneity in the permeability shows a similar pattern to that of the stiffness (Figure 3.17c).

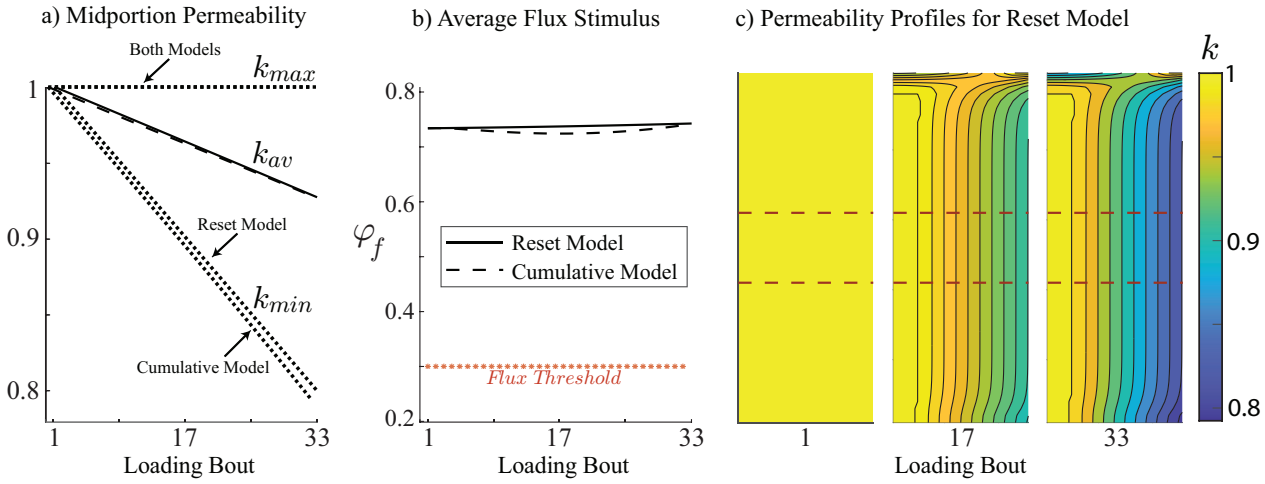


Figure 3.18: Changes in the midportion permeability and maximum flux magnitude with 33 bouts of fast loading ($\omega = 20$, $\Delta\tau = 24$). a) Averaged (Equation (3.8)), maximum and minimum permeability over the midportion at commencement of loading for the reset and cumulative models. b) Average flux stimulus during each loading bout (Equation (3.9)). c) Permeability profiles for loading bouts $b = 1, 17, 33$ for the reset model.

To further investigate how changes in the permeability and average flux stimulus, shown in Figure 3.17, are related to changes in the stiffness, we simulate the same high-frequency loading scenario but hold the stiffness fixed. If the stiffness is held constant across the

simulation with $M(\boldsymbol{x}) = 1$, the permeability profile for the cumulative model is exactly equivalent to the reset model in Figure 3.18a (results not shown). Hence, the small difference in k_{min} between the two models seen in Figure 3.17a is a downstream effect from differences in the stiffness changes for the two models, as the stiffness affects the local flux magnitudes through changes in the strain profile. The flux changes for this constant stiffness scenario are shown in Figure 3.19. In Figure 3.19a the average flux stimulus over time is shown while in 3.19b the maximum flux magnitude at a point in the inner and outer midportion reached during each loading bout is shown. The changes in the flux stimulus observed in Figure 3.19a are even smaller than those observed in Figure 3.18b and interestingly there is an increase in the flux stimulus despite a reduction in the average permeability. This can be

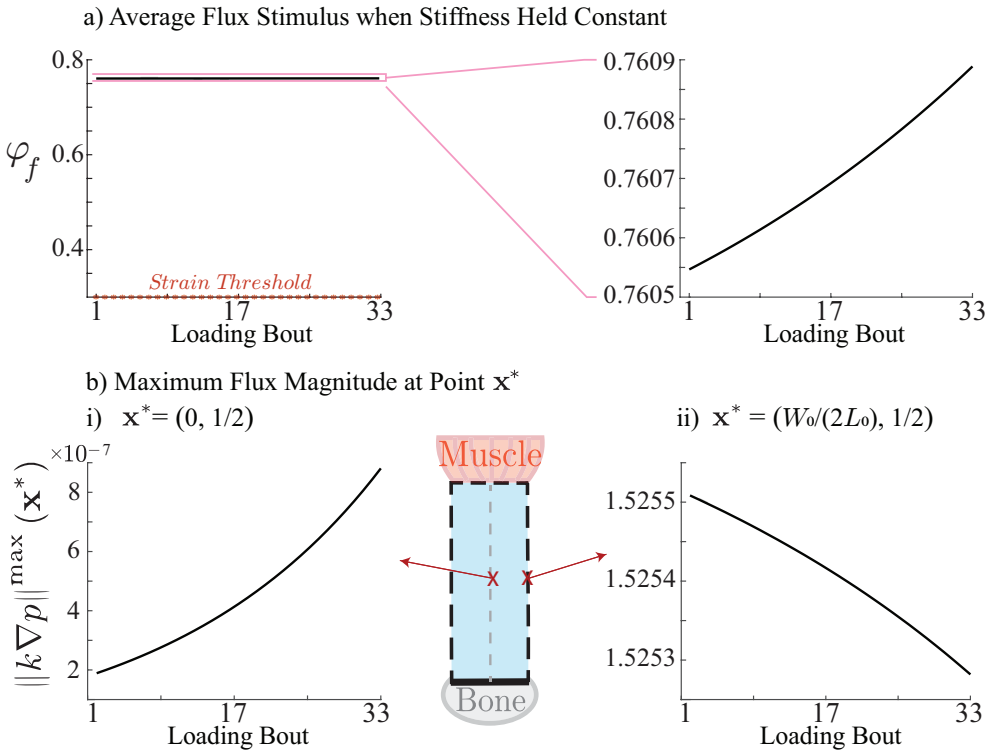


Figure 3.19: Changes in the midportion permeability and maximum flux magnitude with 33 bouts of fast loading ($\omega = 20$, $\Delta tau = 24$) when stiffness is held fixed. The flux and permeability profiles are the same for the reset and cumulative models in the case of constant stiffness. a) Flux stimulus during each loading bout with magnification to demonstrate small changes. b) Maximum flux magnitude at i) $\boldsymbol{x}^* = (0, 1/2)$ and ii) $\boldsymbol{x}^* = (W_0/(2L_0), 1/2)$ occurring during each loading bout.

explained by the pattern observed in Figure 3.19b in which, while there is a reduction in the flux magnitude at the outer boundary, there is a concurrent increase in the flux magnitude at regions where the flux magnitude was initially lower. Clearly, the spatially averaged flux stimulus φ_f displayed in 3.19b may then under predict changes in the point-wise stimulus.

3.8.5 In-Season Loading Regimes

Whilst the low and high frequency loading scenarios simulated in Sections 3.8.3 and 3.8.4 are known to increase and decrease tendon stiffness respectively (Bohm et al. 2014, Arya et al. 2010, Obst et al. 2018), it is unclear how tendon structure is effected when a mixture of loading frequencies are performed. We simulate in-season management with 33 weeks of loading in which bouts alternate between a frequency of $\omega = 2$ and $\omega = 20$ or $\omega = 2$ and $\omega = 10$, with recovery periods of 24 hours. We first investigate how such a regime would impact an initially healthy tendon with $M(\boldsymbol{x}) = k(\boldsymbol{x}) = 1$. Figure 3.20a and b display the stiffness and permeability at commencement of each loading bout for the combination of $\omega = 2, 20$ and $\omega = 2, 10$ respectively. The final stiffness and permeability profiles at the end of the simulation are given in Figure 3.20c and d.

In Figure 3.20a i and ii, in contrast to the stiffness changes observed in Figure 3.17a, the average midportion stiffness is maintained close to one for both the reset and cumulative models. Assessing the maximum and minimum stiffness over the midportion, in both cases there are still areas within the midportion that exhibit a local reduction and those that exhibit a local increase. This can also be observed in the final stiffness profiles in Figure 3.20c. There are larger increases/reductions in the stiffness for the cumulative model, leading to a more heterogeneous final stiffness profile. The introduction of different loading frequencies within a simulation leads to competing influences on the stiffness. From the previous section, the higher frequency loading bouts ($\omega = 20$) promote a local reduction in the stiffness near the transverse boundary (Figure 3.17) and the lower frequency loading bouts ($\omega = 2$) promote a more global increase (Figure 3.16). Hence, when alternating between $\omega = 2$ and $\omega = 20$,

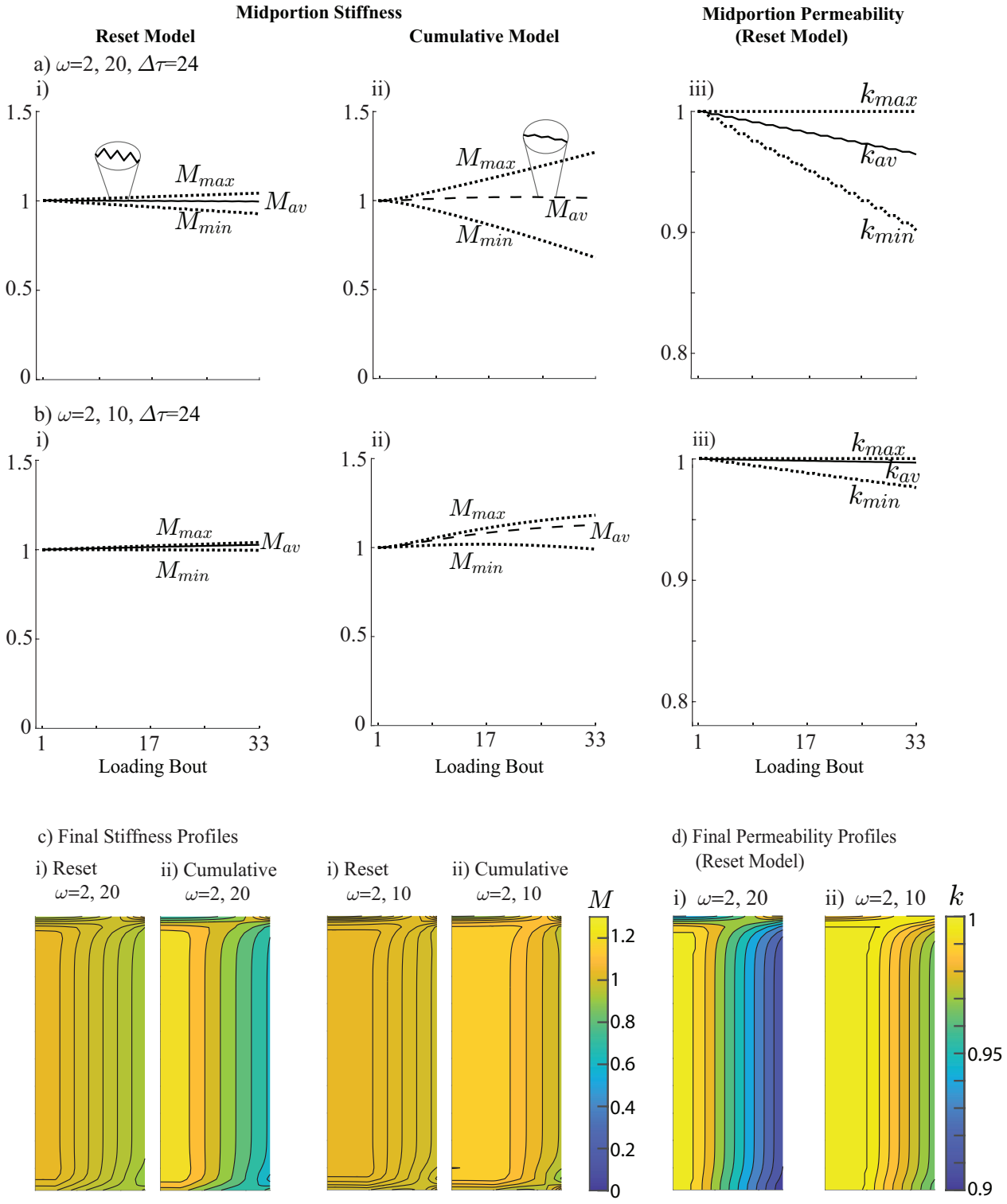


Figure 3.20: Changes in the midportion stiffness and permeability with 33 bouts of fast loading ($\Delta\tau = 24$). Frequency alternating between a) $\omega = 2$ and $\omega = 20$ or b) $\omega = 2$ and $\omega = 10$. Averaged, maximum and minimum stiffness over the midportion at commencement of loading for the i) reset and ii) cumulative models and iii) averaged, maximum and minimum permeability for reset model. c) Final stiffness profiles. d) Final permeability profiles ($b = 33$).

near the transverse boundary, the higher frequency loading stimulus dominates throughout the series and a local reduction occurs. Conversely, closer to the transverse centre there is an increase in the stiffness attributable to the high tensile axial strains and low fluxes occurring over this region with both loading frequencies. For the reset model, loading bouts undertaken for the two different loading frequencies exert their effects iteratively with a stepwise change in the stiffness (zoomed in region Figure 3.20a i). For the cumulative model, there is direct competition between stimuli from previous loading bouts, as the stimulus to the cells is not reset with subsequent loading (Figure 3.8). This results in a smaller difference in the stimulus for subsequent loading bouts and hence changes in stiffness over time exhibit a smoother profile (zoomed in region Figure 3.20a ii).

In Figure 3.18b there is an increase in the average stiffness for both the reset and cumulative models and, in contrast to 3.18a, there are only minor localised reductions in the stiffness over some regions (M_{min}). This occurs because the flux stimulus is lower for loading undertaken with a frequency of $\omega = 10$ than $\omega = 20$ (Chapter 2 Figure 2.15) and hence reductions in stiffness, near the transverse boundary, due to the higher frequency ($\omega = 10$) loading stimulus do not dominate to the same degree over the increases in stiffness attributable to lower frequency ($\omega = 2$) loading bouts being undertaken. Thus, the combination of loading with $\omega = 2$ and $\omega = 20$ appears to be sufficient to maintain the average stiffness but a combination of $\omega = 2$ and $\omega = 10$ leads to a more optimal general increase in the stiffness, though this is only minor for the reset model.

In Figure 3.20a iii there is a decline in the permeability (k_{min},k_{av}) for the reset model, similar to that seen in Figure 3.18a though less extreme. The cumulative model results for the permeability were similar to the reset model (results not shown). In Figure 3.20b iii there is also only a minor reduction in the average permeability, though some midportion regions show a larger localised reduction which can be seen in Figure 3.20d ii.

In addition to contrasting different frequency combinations, we investigated whether an

increase in the recovery period would affect the stiffness and permeability changes given in Figure 3.18. There was no observable difference in the results if a recovery period of 48 hours after every loading bout was imposed instead of 24 hours (results not shown).

Since this alternating frequencies form of loading protocol is often used for in-season management of damaged tendons, we repeat the preceding simulation for a tendon with a local area of damage $M^d = k^d = 0.4$ at the outer midportion (Figure 3.21). In this case, for both combinations of loading frequencies ($\omega = 2, 20$ and $\omega = 2, 10$) there is an increase in the average stiffness, though the increase is very small for Figure 3.21a i. The reduction in the minimum midportion stiffness in Figure 3.21a is also less than that in Figure 3.20. The reduction in midportion permeability is also much less in Figure 3.21 iii than observed in Figure 3.20 iii. If we consider the average midportion stiffness, the latter combination of $\omega = 2, 10$ does again appear more optimal, with a larger increase in the average midportion stiffness and smaller reductions in the average permeability. However, in Figure 3.21c it can be seen that the higher frequency combination $\omega = 2, 20$ leads to larger increase in stiffness near transverse centre but this is paired with a larger reduction in stiffness near tranvserse boundary, leading to a greater difference between maximum and minimum stiffness.

In Appendix 3.B.4 we investigate whether the initial state of damage impacts the optimal loading regime. We repeat the analysis given in Figure 3.21 for a tendon with damage given by $M^d = k^d = 0.6$. The pattern of stiffness and permeability changes were similar to those in Figure 3.21 with the alternative loading scenario $\omega = 2, 10$ generating a notable increase in stiffness and minimising the reduction in permeability when compared to $\omega = 2, 20$.

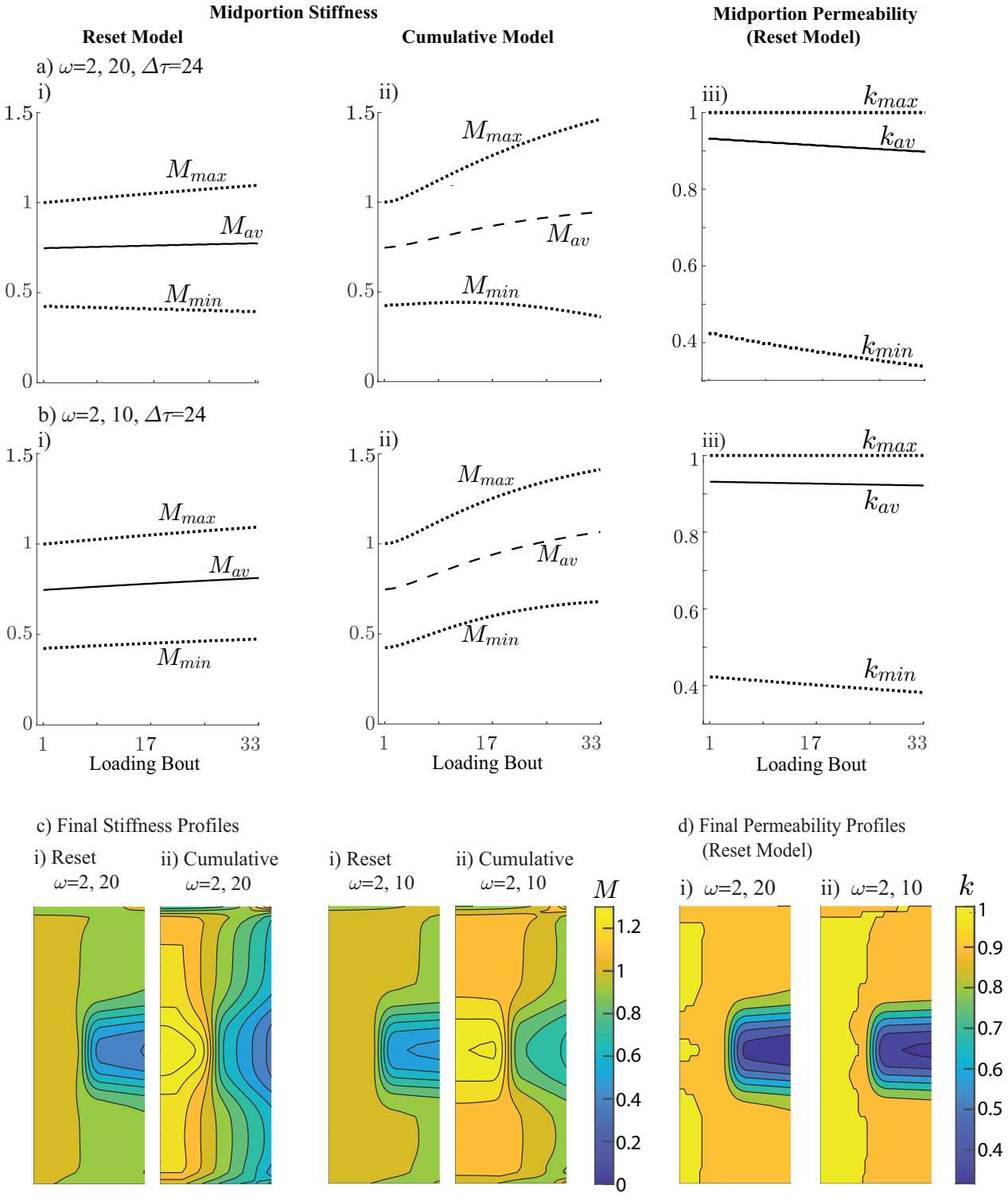


Figure 3.21: Changes in the midportion stiffness and permeability with 33 bouts of loading ($\Delta\tau = 24$) in the setting of damage: a local reduction in the stiffness and permeability ($M^d = k^d = 0.4$) at the midportion at initialisation of loading. Frequency alternates between a) $\omega = 2$ and $\omega = 20$ or b) $\omega = 2$ and $\omega = 10$. Averaged, maximum and minimum stiffness over the midportion at commencement of loading for the i) reset and ii) cumulative models and iii) averaged, maximum and minimum permeability for reset model. c) Final stiffness profiles. d) Final permeability profiles ($b = 33$).

3.9 Discussion

Based on clinical findings, we expected to see a local reduction (leading to a global reduction for whole tendon measurements) in stiffness at the midportion when simulating high-frequency, high-magnitude loading with short recovery periods (24 hrs), and an increase when simulating low-frequency, high-magnitude loading with long recovery periods (3 days). By considering a phenomenological rule which assumed collagen synthesis occurs in response to tensile axial strain and collagen degradation occurs in response to fluid flux (equivalently shear), we were able to reproduce these clinical findings with our adaptation model. Global stiffness measurements predicted by the cumulative and reset model were qualitatively consistent with changes observed clinically. However, while the cumulative model measurements took similar values to those observed clinically (Table 3.2), the reset model was found to slightly under predict expected changes in the stiffness (both the averaged midportion stiffness and globally).

As well as global changes in the stiffness, we considered the spatial pattern of local changes. The changes in stiffness were highly heterogeneous when simulating damage-inducing forms of load and more uniform when simulating slow rehabilitative loading. This is attributable to the heterogeneity in the flux magnitudes observed with loading, whilst the local axial strains were much more homogeneous (Section 2.8.3.1 Figure 2.9). Because of this heterogeneity, the global reductions in stiffness with damage inducing loading were found to be much smaller than those observed locally. These results highlight the importance of taking local measurements when trying to gain a complete picture of the tendon's material properties and hence capabilities to handle different loading regimes. Global measurements may in fact provide a falsely positive picture of the tendon's stiffness.

An interesting facet seen when simulating rehabilitation loading was that healthy regions transversely adjacent to a low stiffness region were particularly responsive in terms of in-

creasing stiffness. These regions underwent larger tensile strains and hence a larger strain stimulus was generated. Future structural and imaging analyses should seek to elucidate whether adjacent regions to damage show changes that may indicate a higher density of collagen I. Aside from the transversely adjacent regions, other healthy regions of the tendon were slightly less responsive to the rehabilitation. This is consistent with changes in collagen observed clinically, in which the upregulation of Achilles peritendinous collagen was found after 12 weeks of rehabilitative loading but only in injured tendons (Langberg et al. 2007), suggesting damaged tendon is more responsive to rehabilitation.

As expected, changes in the permeability were relatively consistent between the reset and cumulative models. Reductions in the permeability had minimal impact on the average flux stimulus across the midportion. Rather, the loading frequency, and to some degree the stiffness, appeared to be the key determinant in whether any reduction in the permeability was observed. This is consistent with results from Chapter 2 in which the loading frequency was found to have a larger increase on the flux, the stimulus for permeability changes, than the material properties (Figure 2.15). Changes to the stiffness had a more substantial effect on the spatially averaged flux stimulus (Equation (3.9)) than changes to the permeability. This occurs because a reduction in permeability in one region leads to an increase in the flux magnitude in adjacent regions (3.19). In contrast, local increases in the stiffness lead to a small global reduction in the strain, which in turns causes a global reduction in the flux (results not shown). These findings suggest that high fluxes will occur with high frequency loading regardless of how the permeability has changed from the previous loading history. Hence, loading bouts at low loading frequencies are potentially necessary to maintain the tendon stiffness.

The phenomenological component of our work here shares many similarities with the model presented by Loboa et al. (2003). In a similar manner we assume that both fluid and solid induced stresses lead to a change in collagen and proteoglycan content, thereby affecting the

material properties. In contrast to Loboa et al., we consider the time dependency of material properties changes in our phenomenological component. We also utilise a mechanical model of the tendon to predict the fluid and solid induced stresses that occurs within the tendon when a force is applied at the tendon origin. This allows us to capture the spatial profile of damage which is not captured in the work by Loboa et al. since they focus on global tissue adaptation. Our model is slightly more simplistic in terms of the constituents and material properties affected, as we do not consider changes in collagen II content[9] or aggregate modulus. Our results are consistent with Loboa et al. 2003 in that high solid tensile stresses, in the absence of high fluid-induced stresses, lead to a higher density of collagen without an accumulation of proteoglycans (in our model this is synonymous with an increase in the stiffness but no change in the permeability).

One issue with the model here was that, for the faster loading frequency investigated ($\omega = 20$), the model predicted that a shorter recovery period would better preserve the stiffness than a longer recovery period, assuming the same number of loading bouts (Figure 3.15 iii). This was an unexpected result as it is known that shorter recoveries between high-frequency loading can be detrimental to tendon structure (Cook et al. 2014). It may be that peak collagen I synthesis occurs slightly later than suggested in Figure 3.2[10] and more experimental work is needed to determine the exact time-dependency of changes. Modifying the time-dependent functions (3.4) to account for this would promote a greater benefit in terms of preserving stiffness with longer recovery times.

In Section 3.8.5 it was shown that the initial damage state of the tendon (degree of local stiffness/permeability reductions) had minimal affect on which in-season management protocol was most optimal to maintain the midportion tendon stiffness. Furthermore, increases in

[9]Collagen II is not a prominent constituent in midportion tendinopathy (Cook et al. 2012).
[10]Figure 3.2 is a schematic derived from experimental results taken at large (hours) intervals apart rather than an exact recording of time-dependent changes.

the recovery time from 24 to 72 hours had minimal effect (results not shown). The changes in stiffness and permeability were much more sensitive to modifications in the loading frequency. Based on clinical findings (Cook et al. 2014, Maffulli et al. 2004), it is not surprising to find that the loading frequency has the most substantial effect on rehabilitation outcomes. However, we would expect that the baseline material properties and recovery time frames would have a more substantial effect than observed. This suggests that, as discussed above, the peak collagen I synthesis may occur later than specified here and in Figure 3.2, or there may some additional benefit of increased recovery time frames that is not captured by the model and needs further experimental investigation.

The cumulative model predicted global stiffness changes in response to rehabilitative (post-to-pre intervention stiffness of 1.18 for cumulative model compared to 1.06 for reset model) that were more consistent with those observed clinically (Table 3.1). However, for damage inducing regimes, the cumulative model predicted that certain regions of the tendon would continue to decrease in stiffness, taking non-zero values if the trend continued. This suggests that either the parameter thresholds for the reset model should be adjusted to predict larger changes, or the cumulative model needs to be modified in some way to prevent non-physical stiffness values occurring. One possibility would be incorporating a saturating function into the constitutive laws for material property changes, such that change in stiffness/permeability are also dependent on the current stiffness/permeability at that time point. This would prevent the stiffness and permeability a from declining to non-physical values and has been used in previous work on tendon (Mehdizadeh et al. 2017). Another simpler approach would be to simply impose a upper and lower bound for each material property, an approach employed by Loboa et al. (2003).

3.10 Conclusion and Limitations

One of the key gaps in research on tendinopathy is the lack of approaches which integrate experimental results, clinical findings and modelling work. In this chapter we have proposed a mathematical adaptation model for the tendon's response to loading, informed by previous clinical and experimental work. We were able to capture a range of clinical findings in terms of stiffness changes in response to loading and predicted changes in the permeability consistent with *in vivo* findings.

Since this model was informed by the combined synthesis of multiple experimental results for tendon and cartilage cells, many of which are not conclusive, there is the possibility than certain components of the model are inaccurate due to the generalisations we have made from this experimental work. Furthermore, this is compounded by limitations of our poroelastic model which were outlined in our previous chapter. As such, this model should not be considered as a perfectly accurate depiction of how damage and positive adaptive changes occur. Rather, we aim for this work to guide future experimental and clinical studies and also to be a framework for future modelling, as new experimental results become available.

There are several other limitations that are present in this model and should be considered for future work. We have assumed that proteoglycans solely affect the permeability. There is however, the potential that proteoglycans may modulate the material properties in some other manner, as aggrecan has been suggested to play a role in the compressive stiffness of cartilage (Zhang et al. 2015). Another factor that we do not address in this work is the effect of deloading, which can also be a factor in the development of tendinopathy (Docking et al. 2019a). However, whilst we do not model any degradation resulting from the absence of a load stimulus, such catabolic effects only appear to be important with greater than two weeks of deloading (Kubo et al. 2004). In our work here, we only simulate recovery periods with a maximum of 72 hours, and hence neglecting this component is reasonable.

Another key gap in the literature and limiting factor in deriving our model, is the lack of knowledge surrounding the biochemical pathways and mechanotransduction process that allows the tendon to adapt to load. This made it difficult to parametrise the model in terms of the time-dependence of the response to load (Equation (3.4)), and hence for simplicity we applied the same parameter values to the reset and cumulative model. We have also assumed that the strain and flux thresholds for cellular adaptation to occur remain constant, thereby assuming that cells have a consistent response to load. There is, however, the possibility that cell behaviour changes in response to load, with the same stimulus having different effects over time. We have also either assumed that cells continue to respond to a loading bout, regardless of the time frame since that loading bout has occurred (cumulative model), or that the cellular response is completely dependent on the previous loading bout (reset model). Future work may consider incorporating a time-dependent weighting function for the continuous model, such that more recent loading bouts serve as a stronger stimulus to the cells.

The model developed here provides an accessible and cheap tool to investigate potential effects of different loading scenarios. This is especially important when considering damage inducing scenarios, as ethical constraints often limit the degree to which we can investigate these. The model can also be used to inform future studies and can be modified in light of new results. Specifically, the results for the simulations explored with our model here suggest that future experimental cell setups should consider both the strain and fluid flux/shear ratios experienced by the cell, rather than considering these in isolation. Future *in vivo* work should also focus on local material property measurements as global measurements may be misleading.

3.A Adaptation Model Parameterisation

3.A.1 Parameter Values

The parameter values used to prescribe $f_1(\tau)$, $f_2(\tau)$, and $g(\tau)$, are given by

$$f_1(\tau) = \frac{0.5852\tau - 0.0065\tau^2}{0.0570752\tau^3 - 1.96\tau^2 + 52.78\tau + 512}, \tag{3.12}$$

$$f_2(\tau) = -\frac{0.3642\tau - 0.0049\tau^2}{0.0584402\tau^3 - 1.69\tau^2 + 37.44\tau + 158} \tag{3.13}$$

$$g(\tau) = -\frac{(\tau^2 - 24\tau)}{5000}\mathcal{H}(24 - \tau). \tag{3.14}$$

Table 3.3: Default parameter values for implementation of adaptation model.

Parameter		Value	Parameter		Value
Length	L_0	3 cm	Hydraulic Permeability	k/μ	$3.98e^{-14}$ $m^4/N \cdot s$
Thickness	W_0	0.3 cm	Strain Threshold	$\frac{\partial w}{\partial z}^{\text{thresh}}$	0.04
Baseline Young's Modulus	E	1	Flux Threshold	$\|k\nabla p\|^{\text{thresh}}$	0.003 ($5.9e^{-6}$ m/s)
Poisson's Ratio	ν	0.3			

3.A.2 Parameter Sensitivity

To evaluate the parameter sensitivity we consider the effect of parameter variations on the change in material parameters following a single loading bout, $M_{b+1}(\boldsymbol{x}^*) - M_b(\boldsymbol{x}^*)$ and $k_{b+1}(\boldsymbol{x}^*) - k_b(\boldsymbol{x}^*)$, at the point $\boldsymbol{x}^* = (W_0/(4L_0), 1/2)$. We also evaluate parameter sensitivity for the point $\boldsymbol{x}^* = (W_0/(2L_0), 1/2)$, where the flux is higher. We let $M_b(\boldsymbol{x}^*) = 1$ and

evaluate changes in stiffness at 72 hours following a loading bout with frequency $\omega = 2$, the change in stiffness at 24 hours following a loading bout with frequency $\omega = 20$, and the change in permeability at 24 hours following a loading bout with frequency $\omega = 20$. Letting the superscript *baseline* denote the stiffness/permeability calculated for the parameter values given in Sections 3.4.4 and 3.A.1, and $\pm 10\%$ refer the stiffness/permeability calculated when an increase or decrease in the baseline parameter values by 10% is imposed, we consider the metrics

$$\frac{M_{b+1}^{\pm 10\%}(\boldsymbol{x}^*) - 1}{M_{b+1}^{\text{baseline}}(\boldsymbol{x}^*) - 1} \times 100 \quad \text{and} \quad \frac{k_{b+1}^{\pm 10\%}(\boldsymbol{x}^*) - 1}{k_{b+1}^{\text{baseline}}(\boldsymbol{x}^*) - 1} \times 100. \tag{3.15}$$

We investigate the impact of changing the strain or flux thresholds from baseline: $\partial w^{\text{thresh}}/\partial z = 0.04$, $\|k\nabla p\|^{\text{thresh}} = 0.003$. We also modify the magnitude of the time dependent functions $f_1(\tau)$, $f_2(\tau)$ and $g(\tau)$ used in Equations (3.4) and (3.5): we multiply each function in by some coefficient α, β or γ such that $f_1(\tau) \to \alpha f_1(\tau)$, $f_2(\tau) \to \beta f_2(\tau)$ and $g(\tau) \to \gamma g(\tau)$, and hence $\alpha = \beta = \gamma = 1$ can be considered as baseline parameter values. The percentage difference in the stiffness and flux changes, when a 10% increase or decrease is applied (individually) for each of these five parameters is given in Figure 3.22. In Figure 3.23 the same evaluation has been carried out as in Figure 3.22 except at an outer boundary point $\boldsymbol{x}^* = (W_0/(2L_0), 1/2)$. If we consider the point at the transverse centre of the half plane $\boldsymbol{x}^* = (W_0/(4L_0), 1/2)$, the change in stiffness, following both low and high frequency loading, is most sensitive to changes in the axial strain threshold $\partial w^{\text{thresh}}/\partial z$. For low frequency loading (Figure 3.22a) small changes to the flux threshold have no effect (as the flux threshold is not exceeded). Considering the point at the outer midportion $\boldsymbol{x}^* = (W_0/(2L_0), 1/2)$, the change in stiffness, following both low and high frequency loading, is more sensitive to changes in the time dependent parameters governing the flux response ($f_2(\tau)$) in Equation (3.2). Regardless of whether we consider a point at the outer or inner region of the midportion, the change in permeability is most sensitive to the magnitude of parameters given in Equation (3.5)).

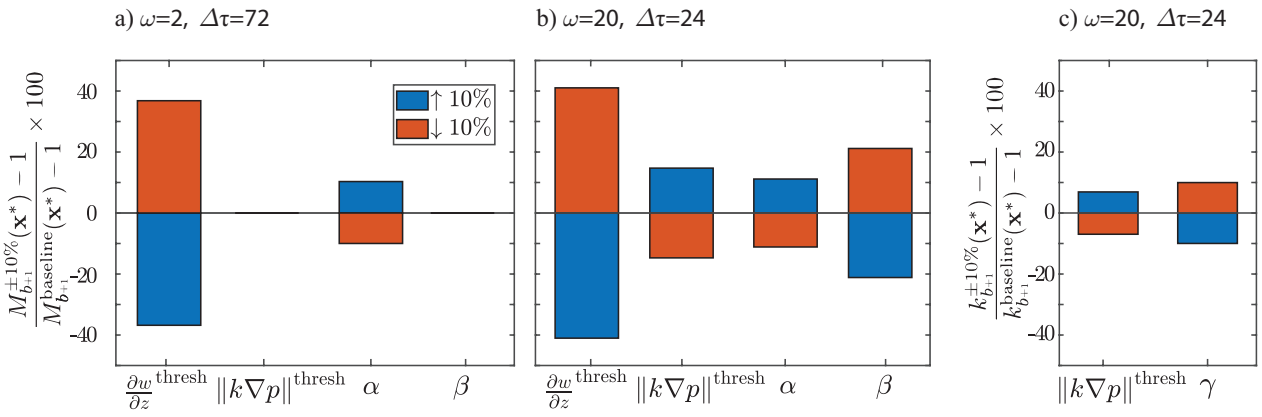


Figure 3.22: Percentage change in the material differences at the point $\boldsymbol{x}^* = (W_0/(4L_0), 1/2)$ following loading after a 10% change in the parameter values from baseline: $\partial w^{\text{thresh}}/\partial z = 0.04$, $\|k\nabla p\|^{\text{thresh}} = 0.003$, $\alpha = 1$, $\beta = 1$, $\gamma = 1$. a) Increase in the stiffness at 72 hours follow a loading bout with a frequency $\omega = 2$. b) Decrease in the stiffness at 24 hours follow a loading bout with a frequency $\omega = 20$. c) Decrease in the permeability at 24 hours follow a loading bout with a frequency $\omega = 20$.

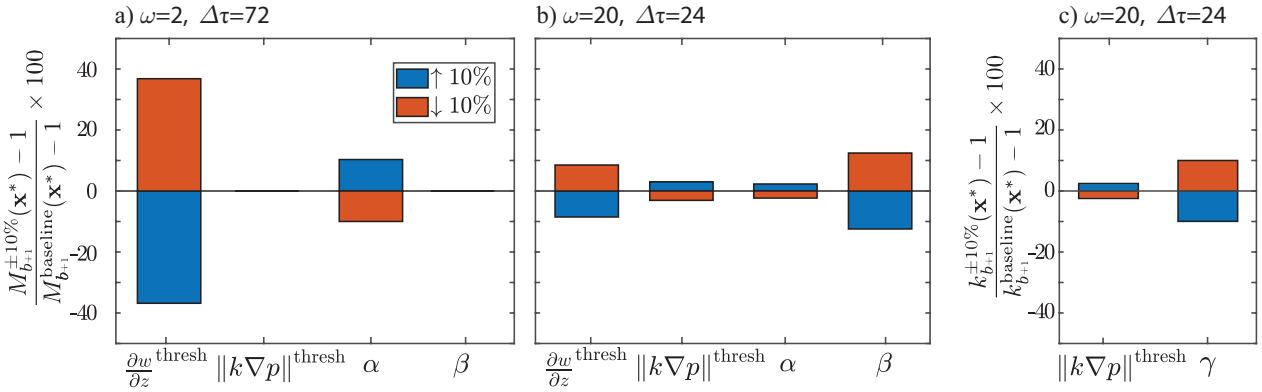


Figure 3.23: Percentage change in the material differences at the point $\boldsymbol{x}^* = (W_0/(2L_0), 1/2)$ following loading after a 10% change in the parameter values from baseline: $\partial w^{\text{thresh}}/\partial z = 0.04$, $\|k\nabla p\|^{\text{thresh}} = 0.003$, $\alpha = 1$, $\beta = 1$, $\gamma = 1$. a) Increase in the stiffness at 72 hours follow a loading bout with a frequency $\omega = 2$. b) Decrease in the stiffness at 24 hours follow a loading bout with a frequency $\omega = 20$. c) Decrease in the permeability at 24 hours follow a loading bout with a frequency $\omega = 20$.

3.B Additional Results

3.B.1 Changes in Stiffness at Transverse Boundary Following a Single Loading Bout

In Figure 3.24a we plot the rate of change in stiffness, and in Figure 3.13b the actual stiffness, at the time τ following a single loading bout. The stiffness changes are taken at the point $(x = W_0/(4L_0),\, z = 1/2)$, the midpoint of the half plane, following a loading bout completed with a frequency of $\omega = 10$ or 20. We have assumed the tendon is initially homogeneous with $M(\boldsymbol{x}) = 1$. It is evident from Figure 3.24a that, as the loading frequency increases, a larger flux stimulus occurs, which contributes to a reduction in the stiffness.

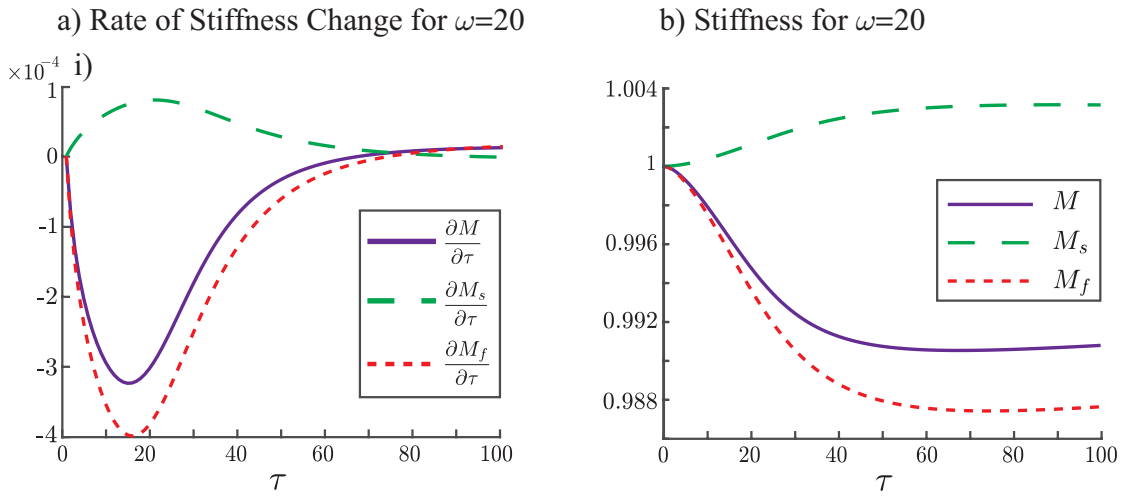


Figure 3.24: a) Rate of change in tendon stiffness and b) stiffness at time τ for the midpoint of half plane $(x = W_0/(2L_0), z = 1/2)$ after a bout of loading. Frequency: $\omega = 20$.

3.B.2 Changes in Stiffness Following a Single Loading Bout

In Figure 3.25 we plot the final stiffness following a single loading bout for a damaged tendon (Figure fig:indiv_e2_dmga displays initial damage). There is decrease in the stiffness closer to the transverse boundary for the faster two loading frequencies $(\omega = 17, 0)$. For the slower loading frequency $\omega = 2$, in contrast to Section 3.8.2 Figure 3.13, there is a very small

reduction in the stiffness globally, with a small increase in stiffness over the very edges of the damaged region.

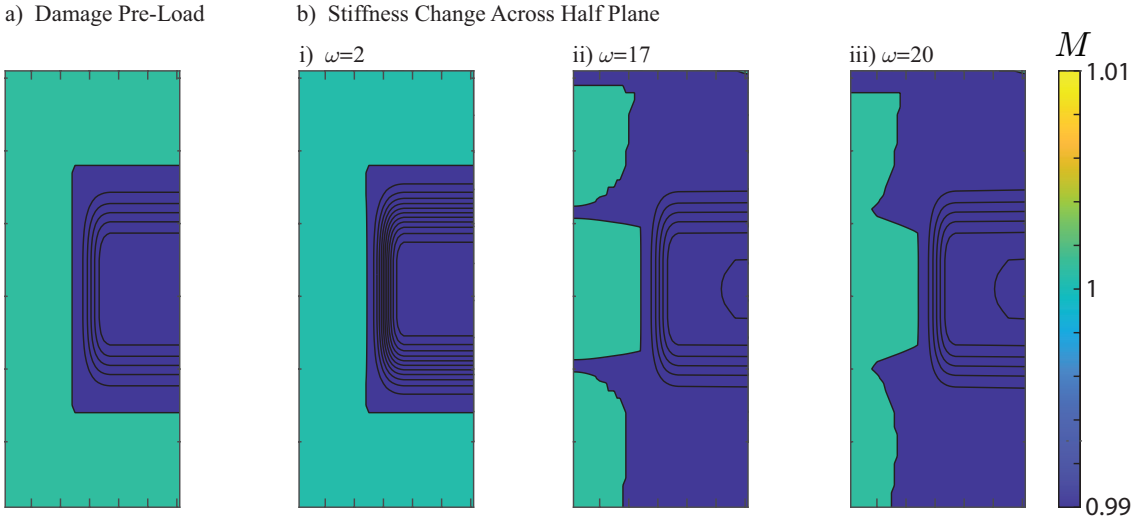


Figure 3.25: Stiffness change over whole tendon half plane after a bout of loading for a damaged tendon. a) Original imposed damage showing local reduction in stiffness. b) Change in stiffness following a single loading bout with frequency: i) $\omega = 2$, ii) $\omega = 17$, iii) $\omega = 20$.

3.B.3 Long-Time Behaviour

In Figure 3.26 the long term stiffness profiles corresponding to Figure 3.16a,b and as described in Section 3.8.3. It is evident that as the number of loading iterations increases, the changes in the stiffness and strain stimulus get smaller and smaller. The strain threshold represents an asymptote for the cumulative model. This is not so apparent for the reset model which exhibits smaller changes in stiffness following each iteration when contrasted with the cumulative model. However, it appears that a similar trend toward the strain threshold would take place but a substantial number of loading bouts would be required for this trend to become more apparent. If loading is commenced when the stiffness is high everywhere, and the flux threshold is not exceeded locally anywhere, then no adaptation simply takes place (results not shown).

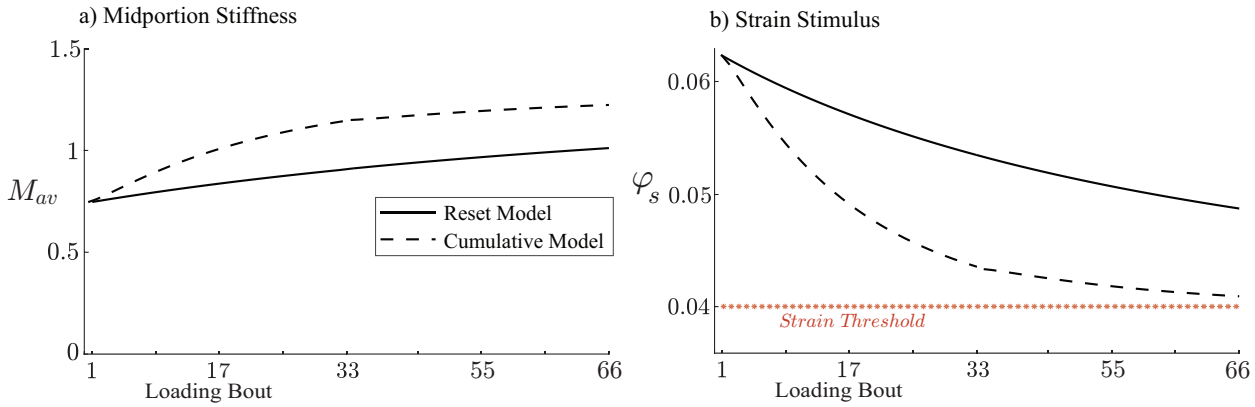


Figure 3.26: Changes in the midportion stiffness and the local mechanical environment with 66 bouts of slow loading ($\omega = 2$, $\Delta\tau = 24$). a) Averaged stiffness over the midportion at commencement of loading. b) Averaged axial strain stimulus during each loading bout.

3.B.4 Model-Based Prescription of Loading

We simulate 3 weeks of loading in which bouts alternated between a frequency of $\omega = 2$ and $\omega = 20$, or $\omega = 2$ and $\omega = 10$ with recovery periods of 24 hours. In Figure 3.27 we display the resulting stiffness and permeability changes. In contrast to Figure 3.21, we have initialised the simulation imposing a local area of damage: $M^d = k^d = 0.6$. Similar to Figure 3.21, the latter combination of $\omega = 2, 10$ does again appear more optimal, with a larger increase in the overall midportion stiffness and smaller reductions in the permeability. The most notable difference is that the reduction in the minimum midportion stiffness is greater for $M^d = k^d = 0.6$.

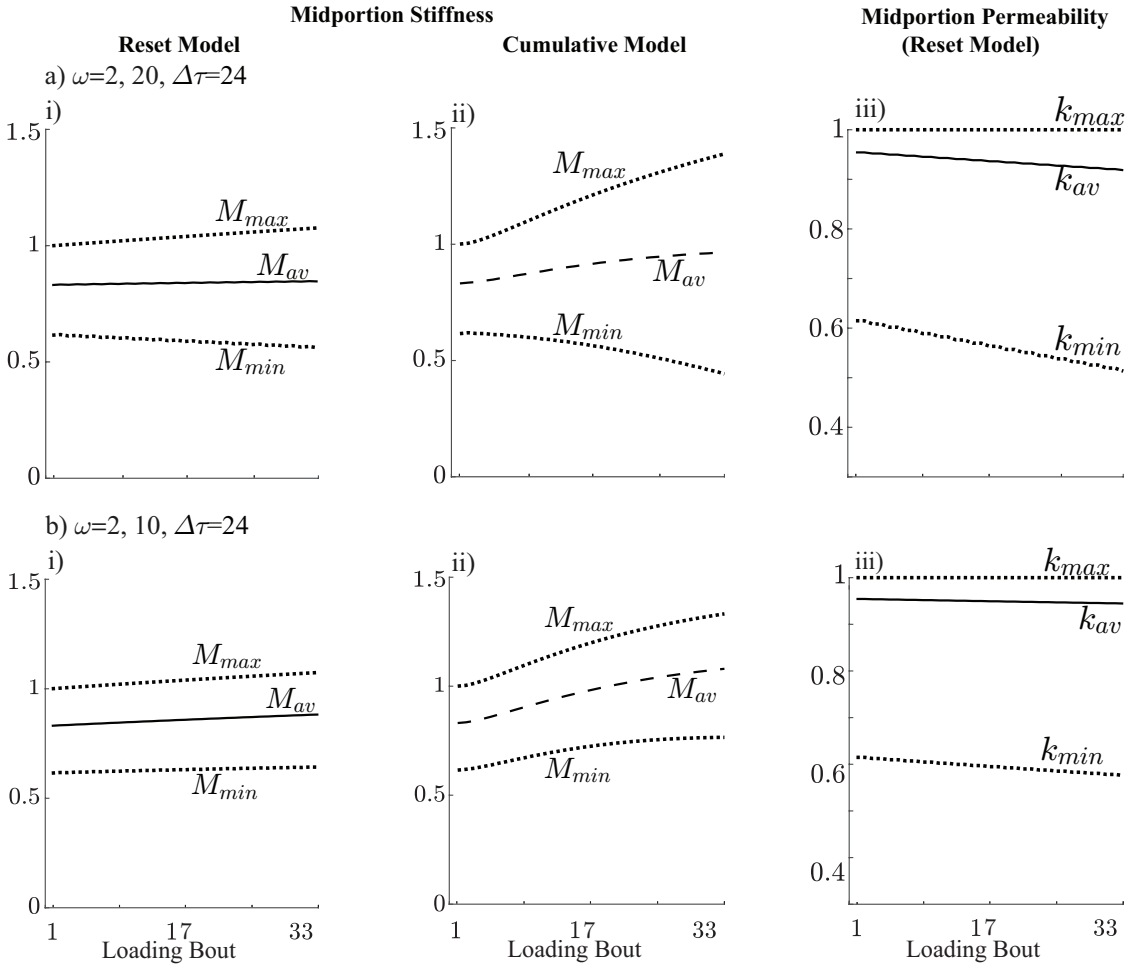


Figure 3.27: Changes in the midportion stiffness and permeability with 33 bouts of fast loading($\Delta\tau = 24$) in the setting of a local reduction in the stiffness and permeability ($M^d = k^d = 0.6$) at the midportion at initialisation of loading. Frequency alternates between a) $\omega = 2$ and $\omega = 20$ or b) $\omega = 2$ and $\omega = 10$. Averaged, maximum and minimum stiffness over the midportion at commencement of loading for the i) reset and ii) cumulative models and iii) averaged, maximum and minimum permeability for reset model.

CHAPTER 4

Tendon Image Segmentation

4.1 Synopsis

To produce a quantitative and automated means of inferring potential structural changes from ultrasound (US) images, we develop and implement an algorithm that performs a texture-based segmentation of tendon US images. A model-based segmentation approach is used which combines Gaussian mixture models, Markov random field theory and grey-level co-occurrence (GLCM) features. We also trial the use of a set of exemplar filter bank responses, termed *textons*, to capture texture information. However, the GLCM features are found to be superior in differentiating between tendinopathic and healthy tendons. The algorithm is implemented on a data set of B-mode ultrasound images of the Achilles tendon, provided by *Imaging at Olympic Park* in Melbourne, Australia. The images are labelled as *tendinopathic* or *healthy* but no ground truth segmentation is available. Hyperparameters are tuned on a proportion of the dataset to provide a segmentation which allows us to classify the tendons as tendinopathic or healthy. We also use this training set to identify which texture class labels are predominant in each image class, and hence represent tendinopathic or healthy tissue. We then use a texture proportion cut-off threshold to classify the remaining images, allowing us to validate that the segmentation correlates to disease state. Our approach successfully detects a difference in the texture profiles of tendinopathic and healthy tendons. Results for the tendinopathic images are collated in order to gain insight into the spatial pattern

of structural changes that occur with tendinopathy. It is evident that distinct textures, which are predominantly present in tendinopathic tendons, appear most commonly near the transverse boundary of the tendon, though there was a large variability among diseased tendons.

4.2 Introduction

Texture-based medical image segmentation involves the segmentation of medical images based on a set of texture features assigned to each pixel (or group of pixels). It is a useful means to objectively identify disruption to healthy collagen fibre architecture (Mostaço-Guidolin et al. 2011) and hence is applicable to tendon, in which there is an increase in fibre spacing and loss of the parallel fibre arrangement (Hodgson et al. 2012). A range of methods are available for medical image segmentation but relatively few have been trialled on tendon, especially those that do not involve a set of gold standard segmentations carried out by the radiologist.

Motivated by the lack of objective tools for quantifying tendinopathic changes on ultrasound imaging, the purpose of this chapter is to develop a machine learning tool for segmenting ultrasound images of the tendon and subsequently capturing changes in the texture profiles of healthy and tendinopathic tendons. An example texture-based segmentation of an unhealthy tendon image is given in Figure 4.1. Specifically, given a set of 49 greyscale masked[1] tendon images provided by *Imaging at Olympic Park*, Melbourne, we seek to provide a segmentation of each image by assigning a texture class label to each pixel within the image. We assume that distinct texture labels will correspond to healthy and tendinopathic tissue. We further assume that the proportion of pixels assigned to each texture label within an image provides a measure which can accurately determine whether the image is of a healthy

[1]A corresponding logical array is created for each image, specifying which pixels lying outside of the tendon boundary are are to be excluded from the analysis.

or tendinopathic tendon. The dataset of images available are labelled at the image level, as *healthy* or *tendinopathic*, but no ground truth segmentation of the image is available. However, several tendinopathic images within the dataset showed coarse regions of more extreme tendinopathic changes which we also use in validating our segmentation approach; we expect the algorithm to build on a radiologists' capabilities rather than contradict them.

4.2.1 Literature Review

The related work for this chapter can be divided into two broad categories: (1) current quantitative approaches for tendon image classification and segmentation and (2) methods for the automated segmentation of medical images. Over recent years a wealth of techniques have become available for the quantitative analysis of medicals images. Segmentation of a medical image involves the labelling of each individual pixel to a tissue class. The term *tissue class* not only refers to distinct tissues types, but also to tissues of the same type with different levels of damage, depending on the segmentation problem of interest. There is no one gold standard approach for medical image segmentation. There are a multitude of factors that affect how successful an approach may be, such as the modality by which the images were taken, the size of the dataset, whether a labelled dataset is available for supervised

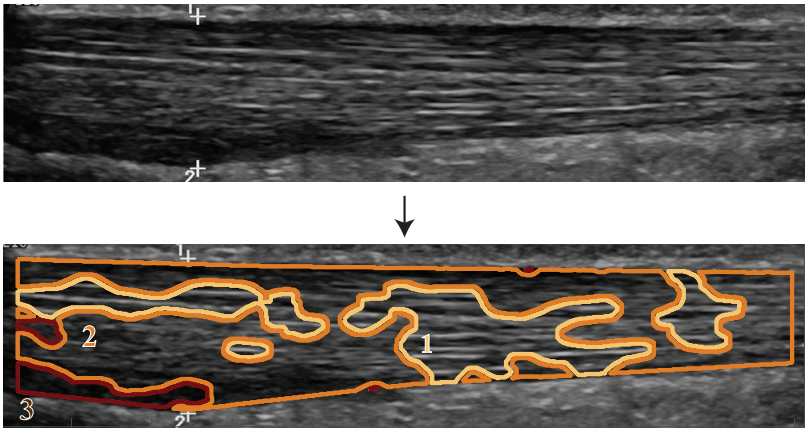


Figure 4.1: Texture-based segmentation of tendinopathic tendon into three distinct texture classes: yellow outline (1), orange outline (2) and red outline (3).

learning, and where any potential clinical or industrial benefit lies. For ultrasound (US) images, methods that are robust to noise are assumed to be more successful (Meiburger et al. 2018).

Segmentation of an image is usually based on some set of features for each image. The features can be simple, such as pixel grey-level intensities, or a multivariate variable, such as a set of filter bank responses (Appendix 4.A.2 provides a description of image filtering). Classically, machine learning approaches to image segmentation utilise a training and test dataset. The training dataset is used to parameterise the model, whilst the test set is used to test the model accuracy. Segmentation of images through machine learning approaches can utilise supervised or unsupervised learning. In the context of segmentation, supervised learning requires a ground truth segmentation over every pixel in the training set. Unsupervised learning would require no labelling of the images. When labels are present at the image level (for example *healthy* vs *tendinopathic* tendons) but no ground truth segmentation is known, then this constitutes weakly supervised learning.

Ultrasound Tissue Characterisation (UTC) is the only method of quantitatively analysing and segmenting static US images of tendons that has been widely adopted by the clinical research community (Van Schie et al. 2010, Docking et al. 2016, Wezenbeek et al. 2017). Several other methods for the quantitative analysis and segmentation of tendon images have been investigated. Of these, statistical image descriptors and filtering approaches have shown promise.

4.2.1.1 Quantitative Approaches to Tendon Imaging

The algorithm for UTC, developed by Van Schie et al. (2010), compares grey level variability between adjacent transverse images and subsequently segments the tendon tissue on US into four distinct classes, based on the continuity of greyscale values across images. A series of

transverse images are taken along the entire length of the tendon approximately 0.2mm apart. It is assumed that low variability in pixel intensities across corresponding points in contiguous transverse images represents healthy continuous collagen alignment (Schie et al. 2003, Van Schie et al. 2010). Whilst it has become a popular method for tendon image analysis among clinical researchers, research suggests limited diagnostic and prognostic capabilities (Ark et al. 2018, Docking et al. 2019b). In a study on 179 male football players, UTC provided no additional diagnostic or prognostic benefit over grey-scale US (Docking et al. 2019b). One potential explanation for these findings may be that pixel intensity-based approaches to image segmentation, such as UTC, are often more sensitive to noise than filtering or statistical model-based approaches (Brattain et al. 2018). UTC also requires specialised and expensive ultrasound equipment, and a large number of images must be taken in order to span the entire tendon length.

Grey-level statistics have been investigated as a means of quantifiably analysing tendon images (Tsai et al. 2014, Schie et al. 2000, Park et al. 2016). First- and second-order grey-level statistics are simple and fast to calculate. They capture information regarding the pixel intensities and, in the case of second-order statistics, the spatial relationship between pixels in an image. The image is assessed either in its entirety or scanned using a smaller window, and the distribution of grey levels within the image or small windows are assessed. The grey-level co-occurrence-matrix (GLCM) is commonly used to generate second-order statistics. Grey-level co-occurrence-matrices describe the orientation and distance between pixels with similar grey level values within some window, or the entirety, of an image (Haralick et al. 1973). Using *ex vivo* specimens, in which the true disease state of a section of tissue can be determined by invasive histological analysis, the sensitivity of first-order grey-level statistics to capture deviations from healthy tendon structure was found to be low (Schie et al. 2000, Lalumiere et al. 2020). Second-order statistics, which are considered as a texture marker (Lalumiere et al. 2020), have shown more promise in quantifying damage. Lalumiere et al. (2020) and Nadeau et al. (2016) compared first- and second-order grey-level statistics

between healthy and tendinopathic images of the Achilles tendon. The grey-level statistics were calculated for, and compared between, images, but were not used to contrast regions within the image in the context of segmentation. In both cases, second-order, but not first-order, statistics were significantly correlated to the presence of tendinopathy. Because of the variable accuracy, Nadeau et al. (2016) suggested more work is needed to evaluate the use of second-order statistics. The positive findings by these authors suggests that quantitative texture measurements have promise in tendon image analysis. In addition to the use of GLCM features in tendon image analysis, GLCM features have shown to have a high correlation with collagen morphology of blood vessels on microscopy (Mostaço-Guidolin et al. 2011), supporting that GLCM features can capture microscopic changes in collagen structure.

Wavelet transforms have been used to define texture features for tendon images and utilised to segment the image (Fernández et al. 2002, Kim et al. 1998). For this approach, a filter bank of varying scales is used to perform wavelet decomposition of an image (Huang et al. 2018). In this way the image is decomposed into a set of subimages (or subbands), each of the same size as the original image, according to varying spatial frequencies (they each capture details occurring at different scales). The resulting decomposition is used to define texture features which can then be clustered in some way to achieve a texture-based segmentation of the image. Kim et al. (1998) used this approach to segment tendon images from 24 horses who exhibited an identifiable tear on US. Their segmentation results showed good agreement with those carried out by a radiologist. Curvelet transforms are an extension of wavelet transforms, which have been used for the detection of shoulder tendon tears in humans (Gupta et al. 2014). Similar to wavelets, curvelet representations are generated by applying a set of filters to the image. Curvelets have a higher degree of directionality[2] than wavelets, and hence are particularly useful in image analysis which requires the detection of curved regions (Candes et al. 2006). For the interested reader, a mathematical description of

[2]The filters used to apply to transformation each have a scale and direction/orientation.

wavelets and curvelets in the setting of image segmentation is given by AlZubi et al. (2011).

Convolution neural networks (CNNs) are another distinct approach to image segmentation. A series of convolution filters are applied to the image and fed into a neural network - a series of simple algorithms (neurons) that are weighted and combined in layers - to produce a segmentation of the image. Convolution neural networks have classically been used for supervised segmentation, in which parameterisation of the model is carried out by using a labelled training set of images. A limitation of convolution neural networks is that several hundred images are usually required, at a minimum (Rawat et al. 2017). Jahanifar et al. (2020) and Alzyadat et al. (2020) investigated the use of CNNs in the automatic segmentation of tendinopathic regions in the supraspinatus[3] and Achilles tendon, respectively. To cope with the small dataset Jahanifar et al. (2020) had available, they used transfer learning in which their network was partially trained by using a set of publicly available segmented nerve images. Hence, the accuracy of their approach is dependent on the nerve and tendon imaging datasets being similar enough. In contrast, Alzyadat et al. (2020) simply augmented their data to increase the dataset size. In this case, the predictive accuracy of their approach is dependent on whether the augmentation techniques produce a representative dataset of tendinopathic tendons that captures the diversity of imaging presentations. Both authors utilised fully supervised learning in which a segmentation carried out by a radiologist was considered as ground truth, and hence the approach is unlikely to surpass the accuracy of the radiologist.

There is currently no gold standard technique for automated tendon image segmentation in the setting of tendinopathy. Collectively, quantitative approaches to tendon image analysis show promise but further research in this area is needed to generate a clinically reliable tool. A much wider range of machine learning approaches are available than have been used in

[3]A positional tendon of the shoulder.

tendon image analysis, and hence there is great scope to identify more reliable methods for quantifying tendinopathy on imaging.

4.2.1.2 Segmentation of Medical Images

A Gaussian Mixture model (GMM) is a statistical model which is commonly used for medical image segmentation (Ilea et al. 2011). The model is used to represent a set of normally distributed sub-populations (tissue classes in the context of medical image segmentation). Pixel intensities, or other descriptors associated with each pixel, such as the grey-level statistics, constitute realisations of random variables belonging to these sub-populations. Inference methods are then used to determine to which sub-population the pixel most likely belongs - providing a segmentation of the image. A limitation of GMMs is the lack of spatial information they encode, as pixels are considered as independent random variables. Markov random fields are often coupled with GMMs, termed hidden Gaussian Markov random fields (HGMRFs), in order to introduce spatial dependence into the GMM. Markov Random Fields (MRFs) have been widely used in medical image segmentation, including ultrasound, due to their ability to encode spatial information. The entire image is modelled as a probabilistic network of pixels rather than considering pixel values in isolation. The key feature of MRFs is that the assignment of a pixel to a certain tissue class is encouraged if neighbouring pixels also belong to this tissue class (Azmi et al. 2011). For this reason, approaches using MRFs work well for noisy images. Hidden Gaussian Markov random fields have been used successfully in breast lesion and brain lesion detection on US and MRI imaging (Azmi et al. 2011, Zhang et al. 2000).

Textons are a popular means for the texture-based segmentation of medical images (Morgado et al. 2013, Acharya et al. 2019). In 1981 the term *texton* was coined by Julesz (1981) to define micro-structures in natural images which form the the basic elements of pre-attentive perception. That is, *texton* was a name given to the repeating primitive elements which form

textures. It was then suggested by Zhu et al. (2005) that these primitive elements could be automatically identified by applying a set of filter banks to a set of textures image and then clustering the set of filter bank responses across pixels, with cluster centres representing distinct textons. That is, mathematically, textons are defined as a set of exemplar filter bank responses. Textons represent an approach which is grounded in both filtering and structural descriptions of texture. Several authors have extended the use of textons to incorporate a stochastic element, incorporating the randomness of how primitive units occur. Varma et al. (2005) modelled the joint distribution of primitive elements belonging to a texture by utilising a frequency histogram of textons in some small window around each pixel. Distinct histograms were then identified by again clustering the results, with distinct histograms representing distinct textures. The window over which texton histograms are built is chosen to be larger than the filter size, allowing primitive units to be detected at the microscale, and then the repetition of these primitive units to be characterised over a larger scale. The choice of both the filter sizes and the window size for the frequency histogram can be challenging as it is dependent on the image resolution and the scale over which primitive units repeat. Petroudi et al. (2006) combined the use of textons and HGMRFs. Rather than use pixel intensities, they used the texton assignment as an observable multivariate random variable for a HGMRF. They were able to successfully match a radiologists segmentation of breast images to detect different densities of breast tissue.

More recently, advances have been been made in weakly supervised segmentation by CNNs through the use of post-hoc spatial attention maps Li et al. 2018. Parametrisation is carried out using a training dataset with image level labels (for example whether the tendon is healthy or unhealthy would constitute an image level label). The resulting network is then analysed to create a series of spatial attention maps for each image: heatmaps which show the degree to which each pixel contributed to the choice of image level labelling for that image. A problem with such post-hoc analysis, in the setting of weak supervised learning, is that it

does not control for the machine exploiting confounding information[4] (Zech et al. 2018). This could be problematic in the setting of tendon, as the machine could end up predominantly using the tendon thickness as a means for classification, despite the thickness not directly correlating to severity (Docking et al. 2015, Hirschmüller et al. 2012).

There are a vast array of machine learning approaches that are available for medical image segmentation and have the potential to provide a more reliable segmentation of the tendon than prior approaches. However, not all approaches are applicable, due to potential limitations in terms of dataset size or the lack of availability of a fully accurate ground truth segmentation. Importantly, we are not limited to considering any approach in isolation. We can combine approaches to provide additional local texture information and hence a segmentation of the image which better correlates with the disease state. To our knowledge, no one has yet investigated the use of textons or GLCM features, in combination with HGMRFs, for the texture-based segmentation of tendons on ultrasound.

4.3 Key Mathematical Concepts

We now outline the key mathematical background and algorithm components used in our approach here. Whilst each component of the approach detailed here has been used within some imaging segmentation individually, to our knowledge the exact overall combination of texture features and framework used to segment the images has not been implemented before.

4.3.1 Notation

The notation that is used throughout this chapter is given as follows.

- Upper case letters denote a random variable and associated lowercase letters denote a

[4]For example, a CNN, trained to classify severity of lung disease on chest x-ray, ended up classifying the images based on the presence of a "metallic L token" which was placed on any patient lying down (which would be the case if they were quite ill) (Zech et al. 2018).

realisation (observed outcome or event) of the random variable.

- For a random variable X, the state space denoting all possible realisations is given by $x \in \mathcal{X}$.
- For a discrete random variable, the probability of a realisation occurring is given by $P(X = x) = p(x)$, where $p(x)$ is termed the probability mass function.
- For a continuous random variable Y, the probability of Y taking a value between a and b is given by $P(a \leq Y \leq b) = \int_a^b f(y)\, dy$. In the case of a continuous random variable, the probability of Y equalling any exact value is zero.
- In general, p is used to denote a probability mass function for a discrete variable and f or g shall be used to denote a probability density function for a continuous random variable.
- The subscript i is used for a collection of random variables from the same population: X_i for $i \in \{1, 2, ..., N\}$.
- For a vector-valued multivariate random variable, the random variable and its associated realisation are denoted in bold.
- For two dependent random variables X and Y, the *conditional probability* of a realisation x, given the realisation y of Y is known, is given by $P(X = x|Y = y) = p(x|y)$.
- The function $\mathbf{1}_0(x)$ denotes an indicator function that takes a value of one for $x = 0$ and zero otherwise.
- We use $I(x, y)$ to denote the pixel intensity for an n-by-m rectangular image I where $x = 1, ..., n$ and $y = 1, ..., m$ denote the row and column pixel coordinates.

Throughout this chapter we also rely on several fundamental statistical principles for calculations, detailed in Appendix 4.A.1, including Baye's rule and deriving the marginal distribution in the setting of dependent variables.

4.3.2 Hidden Gaussian Markov Random Fields

A multivariate Gaussian mixture model (GMM), first introduced by Newcomb (1886) and Pearson (1894), describes a population formed by a set of discrete multivariate Gaussian distributed subpopulations $k \in \{1, ..., K\}$. For the entire population, we use the set of indices $i \in \mathcal{S}$ where $\mathcal{S} = \{1, ..., N\}$. Each random variable $\boldsymbol{Y}_i$ has a multivariate Gaussian distribution, with the parameters dependent on the subpopulation $X_i = k$ (where X_i is itself a univariate random variable) to which the variable belongs. Hence, the distribution of $\boldsymbol{Y}_i$ conditioned on $X_i = k$, termed the emission distribution, is multivariate Gaussian with mean vector $\boldsymbol{\mu}_k$ and covariance matrix $\boldsymbol{\Sigma}_k$: $\boldsymbol{Y}_i | X_i = k \sim \mathcal{N}(\boldsymbol{\mu}_k, \boldsymbol{\Sigma}_k)$. We let $\boldsymbol{\mu} = (\boldsymbol{\mu}_1, ..., \boldsymbol{\mu}_K)$ and $\boldsymbol{\Sigma} = (\boldsymbol{\Sigma}_1, ..., \boldsymbol{\Sigma}_K)$ denote the parameter set describing the entire set of Gaussian subpopulations. It is assumed that, for all $j \neq i$ where $i, j \in \mathcal{S}$, the variables X_i and X_j (and similarly $\boldsymbol{Y}_i$ and $\boldsymbol{Y}_j$) are independent. Usually we observe a set of variables $\boldsymbol{Y}_1, ..., \boldsymbol{Y}_N$ and wish to infer the subpopulations $X_1, ..., X_N$ to which they belong. In the case of texture-based image segmentation, this constitutes observing a set of features associated with each pixel, and using this information, in the context of a GMM representation of the image, to assign an appropriate texture class label to each pixel.

Unifying GMM and Markov random field (MRF) theory, Hidden Gaussian Markov random fields (HGMRFs) (Rue et al. 2005) introduce a set of dependencies between variables. Figure 4.2 displays a probabilistic graphical representation of how GMMs and MRFs are combined to create a graph of directly and indirectly connected random variables. Vertices represent random variables and edges represent dependencies between these variables. We refer the reader to Appendix 4.A.4.2 for a detailed description of MRFs. In HGMRFs, similar to GMMs, two types of variables are present: *observable variables* $\{\boldsymbol{Y}_1, ..., \boldsymbol{Y}_N\}$, which have a Gaussian distribution when conditioned on the subpopulation to which they belong, denoted by the *hidden variables* $\{X_1, ..., X_N\}$. The terms *hidden* and *observable* are derived from the fact that these models are used when the realisations $\boldsymbol{y} = \{\boldsymbol{y}_1, ..., \boldsymbol{y}_N\}$ are known, and inference

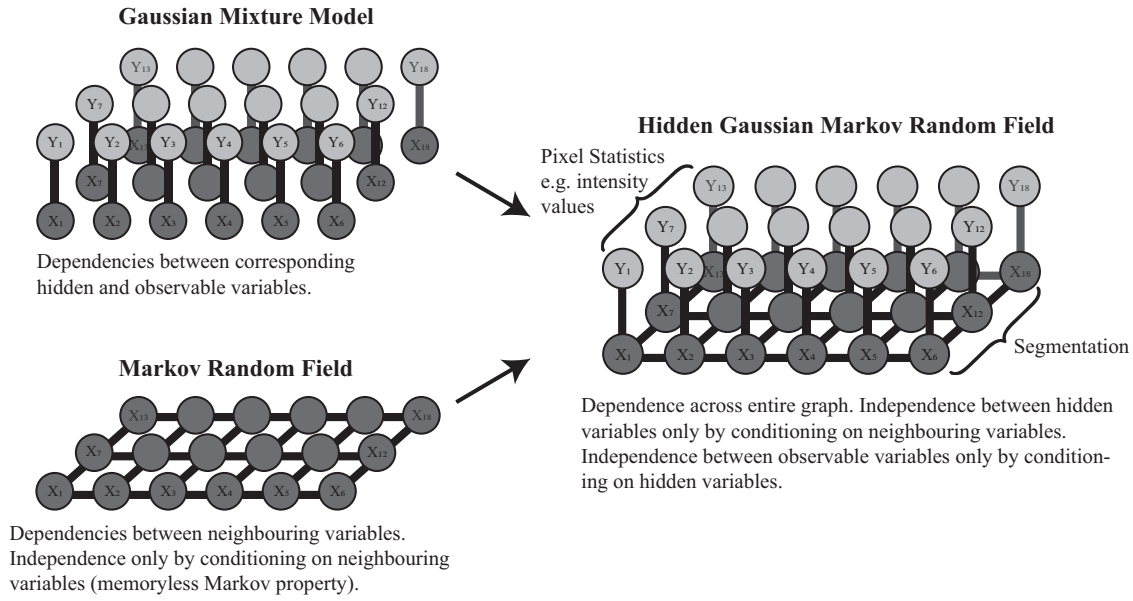


Figure 4.2: Illustration of dependencies within a Hidden Gaussian Markov Random Field. Black edges denote dependence between random variables. The observable variables $\{\boldsymbol{Y}_1, ..., \boldsymbol{Y}_N\}$ are independent when conditioned on their associated hidden random variables $\{X_1, ..., X_N\}$, which gives the subgroup to which the variable Y_i belongs.

methods are then used to approximate the unknown hidden field $\boldsymbol{x} = \{\boldsymbol{x}_1, ..., \boldsymbol{x}_N\}$, representing a segmentation of the image. The observable variables $\{\boldsymbol{Y}_1, ..., \boldsymbol{Y}_N\}$ are conditionally independent when conditioned on the associated hidden variables $\{X_1, ..., X_N\}$. Denoting $\mathcal{N}(i)$ to be the neighbouring indices of i, a hidden variable X_i is independent of the rest of the hidden field, $\boldsymbol{X}_{-\{i\}}$, when conditioned on its neighbours X_j where $j \neq i, j \in \mathcal{N}(i)$. In the case of images, the neighbours constitute neighbouring pixels (Zhang et al. 2000). This neighbourhood dependence is termed the *Markov property*:

$$P(X_i|\boldsymbol{X}_{-\{i\}}) = P(X_i|\boldsymbol{X}_{\mathcal{N}(i)}), \tag{4.1}$$

where $\boldsymbol{X}_{\mathcal{N}(i)}$ denotes the hidden variables (texture class labels) associated with pixels in the neighbourhood surrounding i. In Figure 4.2 grey edges connect neighbouring hidden variables; there are four neighbours seen for each interior variable. Neighbours of a pixel need not constitute only directly adjacent pixels (Figure 4.3a), but may include surrounding

pixels within some larger defined window (Figure 4.3c), with the neighbourhood window size representing a hyperparameter of the model.

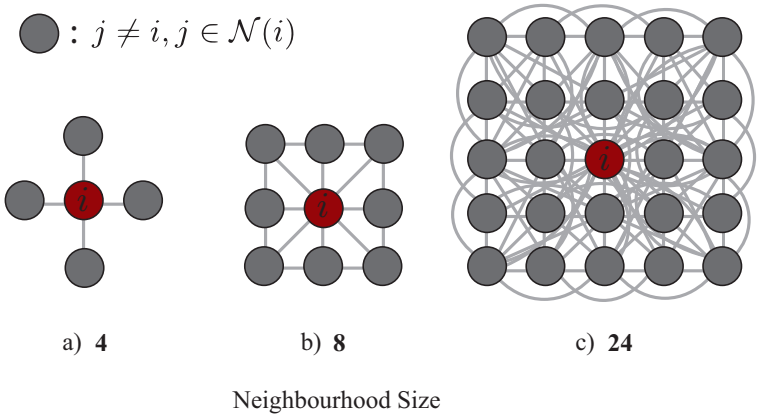


Figure 4.3: Examples of three potential neighbourhood configurations. The pixel of interest is coloured is conveyed by a red circle. Neighbours of the pixel of interest are given by grey circles. An adjoining grey line between two pixels conveys that they are neighbours.

The joint distribution for a HGMRF is given by

$$p(\boldsymbol{x}, \boldsymbol{y}) = p(\boldsymbol{x})p(\boldsymbol{y}|\boldsymbol{x}) = p(\boldsymbol{x}) \prod_{i=1}^{N} f(\boldsymbol{y}_i|x_i, \boldsymbol{\mu}_{x_i}, \boldsymbol{\Sigma}_{x_i})$$

$$= \frac{\exp\left(-\sum_{c \in C} V_c(\boldsymbol{x}_c, \beta)\right)}{Z(\beta)} \prod_{i=1}^{N} \left\{ \frac{1}{(2\pi)^{\frac{p}{2}} |\boldsymbol{\Sigma}_{x_i}|^{\frac{1}{2}}} \exp\left(-\frac{1}{2}(\boldsymbol{y}_i - \boldsymbol{\mu}_{x_i})^T \boldsymbol{\Sigma}_{x_i}^{-1} (\boldsymbol{y}_i - \boldsymbol{\mu}_{x_i})\right) \right\}, \tag{4.2}$$

where p is the length of $\boldsymbol{y}_i$ and $\boldsymbol{\Sigma}_{x_i}^{-1}$ is the inverse of the variance matrix. The second term corresponds to a multiplication over the conditionally independent multivariate Gaussian variables $\boldsymbol{y}_i$. The first term $\exp(\cdot)/Z(\beta)$, corresponds to the MRF component $p(\boldsymbol{x})$ and represents a Gibb's distribution (Appendix 4.A.4.2 Equation (4.34)). The term $V_c(\boldsymbol{x}_c, \beta)$ is a potential function associated with each clique in the graph (Appendix 4.A.4.1), and $\sum_{c \in C} V_c(\boldsymbol{x}_c, \beta)$ constitutes a factorisation over the cliques: all subsets of directly dependent random variables within the hidden field (cliques are discussed in Appendix 4.A.4.1). The choice of potential function is arbitrary and dependent on the application. We choose the

common Isling form (Winkler 2003)

$$\sum_{c \in C} V_c(\boldsymbol{x}_c, \beta) = \sum_{i \in S} \sum_{j \in \mathcal{N}(i)} \beta \, \mathbf{1}_0(x_i - x_j), \tag{4.3}$$

where β is termed the Gibb's parameter, usually taking a value between $\beta \in [0.5, 1]$. This choice of potential function reflects prior knowledge that neighbouring pixels tend to share the same class label. The normalisation factor $Z(\beta)$ in (4.2) is given by

$$Z(\beta) = \sum_{\boldsymbol{x} \in \boldsymbol{\mathcal{X}}} \exp\left(- \sum_{c \in C} V_c(\boldsymbol{x}_c, \beta) \right), \tag{4.4}$$

where $\boldsymbol{\mathcal{X}}$ denotes all possible segmentations of the image.

4.3.3 Extension of the Expectation-Maximisation Algorithm to Hidden Gaussian Markov Random Fields

Using the HGMRF model, we seek to determine the most probable segmentation of an image $\boldsymbol{x} = (x_1, ..., x_N)$ and parameter set $\boldsymbol{\varphi} = (\boldsymbol{\mu}, \boldsymbol{\Sigma}, \beta)$, given a set of observed local texture features associated with each pixel $\boldsymbol{y} = (\boldsymbol{y}_1, ..., \boldsymbol{y}_N)$. In line with previous authors (Zhang et al. 2000), to estimate the segmentation $\boldsymbol{x}$ we maximise the posterior probability

$$\hat{\boldsymbol{x}} = \underset{\boldsymbol{x}}{\operatorname{argmax}} \, p(\boldsymbol{x} | \boldsymbol{y}, \boldsymbol{\varphi}), \tag{4.5}$$

which is termed a maximum-a-posteriori (MAP) estimate. Simultaneously, we approximate the parameter set $\boldsymbol{\varphi}$ by finding the maximum likelihood estimate (MLE): the parameters which maximise the likelihood[5] of generating the observed data. The marginal likelihood of

[5]The likelihood is the probability of observing the data when a given parameter set is taken to be true.

observing the data $\boldsymbol{y}$, with consideration of the unknown data $\boldsymbol{x}$, is given by

$$\mathcal{L}(\boldsymbol{\varphi}) = p(\boldsymbol{y}|\boldsymbol{\varphi}) = \int p(\boldsymbol{y}, \boldsymbol{x}|\boldsymbol{\varphi}) d\boldsymbol{x}. \tag{4.6}$$

Rather than maximise the likelihood directly, we equivalently maximise the log-likelihood

$$\hat{\boldsymbol{\varphi}} = \underset{\boldsymbol{\varphi}}{\operatorname{argmax}}\ \ell(\boldsymbol{\varphi}) = \underset{\boldsymbol{\varphi}}{\operatorname{argmax}}\ \log \mathcal{L}(\boldsymbol{\varphi}). \tag{4.7}$$

The Expectation-Maximisation (EM) algorithm, developed by Dempster et al. (1977), is a widely used approach for approximating the MLE for GMMs. The algorithm was extended by Zhang et al. (2000) to approximate the GMM parameters and hidden realisations in a HGMRF. They called this the HMRF-EM algorithm, a procedure which iteratively approximates the MLE for the parameter set $\boldsymbol{\varphi}$ (Equation (4.7)), whilst simultaneously finding an approximation of the MAP estimate of the segmentation $\hat{\boldsymbol{x}}$ (Equation (4.5)). Only approximations are possible for both estimates, as $\boldsymbol{x}$ represents a graph of events in which the possible realisations $\boldsymbol{\mathcal{X}}$ increase exponentially with the number of pixels. This makes both the integral given in (4.6), and maximising directly over $\boldsymbol{x}$ in (4.5), intractable.

We now introduce the reader to the EM algorithm, and then detail how extensions of the algorithm can be incorporated to simultaneously approximate (4.5) and (4.7) in the setting of a HGMRF. The EM algorithm seeks to determine the MLE (4.6-4.7) by maximising the expected value of the log likelihood with respect to the complete data $(\boldsymbol{x}, \boldsymbol{y})$. The EM procedure iterates between estimating the unknown data $\boldsymbol{x}$, given the current parameter set $\boldsymbol{\varphi}^t$, and estimating $\boldsymbol{\varphi}$ by maximising over the expectation of the complete log likelihood $E[\log p(\boldsymbol{x}, \boldsymbol{y}|\boldsymbol{\varphi})]$. A proof that the EM procedure finds a local maximum of the marginal likelihood (4.6-4.7) is given by Dempster et al. (1977). The EM procedure involves iterating between two steps:

1. Expectation Step

Define the expected value of the complete log likelihood of $\boldsymbol{\varphi}$ (using the joint distribution $p(\boldsymbol{y}, \boldsymbol{x}|\boldsymbol{\varphi})$) , with respect to the conditional distribution $\boldsymbol{x}|\boldsymbol{y}, \boldsymbol{\varphi}^t$:

$$Q(\boldsymbol{\varphi}; \boldsymbol{\varphi}^t) = E[\log p(\boldsymbol{y}, \boldsymbol{x}|\boldsymbol{\varphi})|\mathbf{Y} = \mathbf{y}, \boldsymbol{\varphi} = \boldsymbol{\varphi}^t]. \tag{4.8}$$

Here $\boldsymbol{\varphi}^t$ is the current parameter estimate at iteration t.

2. Maximisation Step

Find the parameter set $\boldsymbol{\varphi}$ which maximises $Q(\boldsymbol{\varphi}; \boldsymbol{\varphi}^t)$

$$\boldsymbol{\varphi}^{t+1} = \underset{\boldsymbol{\varphi}}{\operatorname{argmax}}\, Q\left(\boldsymbol{\varphi}; \boldsymbol{\varphi}^t\right). \tag{4.9}$$

In the case of a HGMRF, the expected value of the log likelihood of $\boldsymbol{\varphi}$, with respect to the conditional distribution $\boldsymbol{x}|\boldsymbol{y}, \boldsymbol{\varphi}^t$, is given by

$$\begin{aligned} Q(\boldsymbol{\varphi}; \boldsymbol{\varphi}^t) &= E[\log p(\boldsymbol{y}, \boldsymbol{x}|\boldsymbol{\varphi})|\boldsymbol{y}, \boldsymbol{\varphi}^t] \\ &= \sum_{\boldsymbol{x} \in \boldsymbol{\mathcal{X}}} p\left(\boldsymbol{x}|\boldsymbol{y}, \boldsymbol{\varphi}^t\right) \log p\left(\boldsymbol{y}, \boldsymbol{x}|\boldsymbol{\varphi}^t\right) \\ &= \sum_{\boldsymbol{x} \in \boldsymbol{\mathcal{X}}} \frac{p\left(\boldsymbol{y}|\boldsymbol{x}, \boldsymbol{\mu}^t, \boldsymbol{\Sigma}^t\right) p\left(\boldsymbol{x}|\beta\right)}{p\left(\boldsymbol{y}|\boldsymbol{\varphi}^t\right)} \log\left(p\left(\boldsymbol{y}|\boldsymbol{x}, \boldsymbol{\mu}^t, \boldsymbol{\Sigma}^t\right) p\left(\boldsymbol{x}|\beta\right)\right) \quad \text{(Baye's Rule).} \end{aligned} \tag{4.10}$$

Due to the number of potential realisations $\boldsymbol{\mathcal{X}}$, the problem of calculating or maximising over Q is intractable. Hence an approximation of the marginal distribution of $\boldsymbol{x}$ is required.

4.3.3.1 Mode Field Algorithm

In order to make the calculation of the expectation of Q tractable, we consider the method of mean field-like approximations presented by Celeux et al. (2003) in which we fix values of the neighbouring sites $j \in \mathcal{N}(i)$ when calculating probabilities at site i. Denoting $\boldsymbol{x}^t_{\mathcal{N}(i)}$ to be the values of the neighbouring sites at iteration t, the marginal distribution of $\boldsymbol{x}$ is approximated by the pseudo-likelihood (Besag 1975)

$$p(\boldsymbol{x}|\beta) \approx \prod_{i \in S} p\left(x_i | \boldsymbol{x}^t_{\mathcal{N}(i)}, \beta\right). \tag{4.11}$$

To calculate (4.11), and subsequently approximate Q at each iteration, we also need an approximation of the neighbours $\boldsymbol{x}_{\mathcal{N}(i)}$. Consistent with our aim to simultaneously approximate the MAP estimate (4.5), we use the mode field algorithm in which the neighbours are sequentially updated at each iteration via

$$\overline{x}^t_i = \underset{x_i}{\operatorname{argmax}}\, p\left(x_i | y_i, \boldsymbol{x}^{t-1+\frac{i-1}{n}}_{\mathcal{N}(i)}, \boldsymbol{\varphi}^{t-1}\right), \tag{4.12}$$

or updated simultaneously

$$\overline{x}^t_i = \underset{x_i}{\operatorname{argmax}}\, p\left(x_i | y_i, \boldsymbol{x}^{t-1}_{\mathcal{N}(i)}, \boldsymbol{\varphi}^{t-1}\right). \tag{4.13}$$

with all neighbours based on the previous iteration. If sequential updating (4.12) is used, convergence to a local maximum is guaranteed. Conversely, if simultaneous updating is used, updating is substantially faster and directional effects (from iterating across an image) are eliminated, but convergence to a local maximum is not guaranteed. We choose the mode field algorithm with simultaneous updating as it provides a faster and more convenient approximation. This allows us to consider large neighbourhoods $\mathcal{N}(i)$, as convolution filters can be used numerically to allow for rapid calculations of the clique potentials (4.3). We also

differ from Zhang et al. (2000) in this component of the HMRF-EM algorithm, as they used a sampling method to generate at MAP assignment for $\boldsymbol{x}$ at each iteration, which is more computationally expensive.

Using (4.11), the joint distribution $p(\boldsymbol{y}, \boldsymbol{x}|\boldsymbol{\varphi})$ is replaced by

$$\prod_{i \in S} p\left(y_i, x_i | \boldsymbol{x}^t_{\mathcal{N}(i)}, \boldsymbol{\varphi}^t\right) = \prod_{i \in S} \left\{ f\left(y_i | x_i, \boldsymbol{\mu}^t_{x_i}, \boldsymbol{\Sigma}^t_{x_i}\right) p\left(x_i | \boldsymbol{x}^t_{\mathcal{N}(i)}, \beta\right) \right\}. \tag{4.14}$$

As a result, the new objective function we seek to maximise over is

$$\begin{aligned} Q(\boldsymbol{\mu}, \boldsymbol{\Sigma}; \boldsymbol{\varphi}^t) &\approx \sum_{i=1}^{N} \sum_{x_i=1}^{K} p\left(x_i | \boldsymbol{x}^t_{\mathcal{N}(i)}, y_i, \boldsymbol{\varphi}^t\right) \log f\left(y_i | x_i, \boldsymbol{\mu}_{x_i}, \boldsymbol{\Sigma}_{x_i}\right) \\ &\quad + \sum_{i=1}^{N} \sum_{x_i=1}^{K} p\left(x_i | \boldsymbol{x}^t_{\mathcal{N}(i)}, y_i, \boldsymbol{\varphi}^t\right) \log p\left(x_i | \boldsymbol{x}^t_{\mathcal{N}(i)}, \beta\right) \\ &= Q_1\left(\boldsymbol{\mu}, \boldsymbol{\Sigma}; \boldsymbol{\varphi}^t\right) + Q_2\left(\beta; \boldsymbol{\varphi}^t\right) \end{aligned} \tag{4.15a}$$

where

$$p(x_i | \boldsymbol{x}^t_{\mathcal{N}(i)}, y_i, \boldsymbol{\varphi}^t) = \frac{f(\boldsymbol{y}_i | x_i, \boldsymbol{\mu}^t_{x_i}, \boldsymbol{\Sigma}^t_{x_i}) p(x_i | \boldsymbol{x}^t_{\mathcal{N}(i)}, \beta)}{\sum\limits_{x_l=1}^{K} f(\boldsymbol{y}_i | x_l, \boldsymbol{\mu}^t_{x_l l}, \boldsymbol{\Sigma}^t_{x_l}) p(x_l | \boldsymbol{x}^t_{\mathcal{N}(i)}, \beta)}. \tag{4.16}$$

Here $f(\cdot)$ simply represents the multivariate Gaussian density function, and

$$p(x_i | \boldsymbol{x}_{\mathcal{N}(i)}, \beta) = \frac{\exp\left(- \sum\limits_{j \in \mathcal{N}(i)} \beta \, \mathbf{1}_0(x_i - x_j) \right)}{\sum\limits_{x_l=1}^{K} \exp\left(- \sum\limits_{j \in \mathcal{N}(i)} \beta \, \mathbf{1}_0(x_l - x_j) \right)} \tag{4.17}$$

For simplicity, and similar to previous work (Zhang et al. 2000), we set β to be a fixed hyperparameter and find the MLE for the Gaussian parameters only. To obtain the MLE

estimates for $\boldsymbol{\mu}$ and $\boldsymbol{\Sigma}$, we maximise Q_1 by setting[6]

$$\frac{\partial}{\partial \boldsymbol{\mu}_k}\left(\sum_{i=1}^{N} P\left(x_i = k|\boldsymbol{x}^t_{\mathcal{N}(i)}, y_i, \boldsymbol{\varphi}^t\right)\log f\left(y_i|x_i = k, \boldsymbol{\mu}_k, \boldsymbol{\Sigma}_k\right)\right) = 0 \;\text{ for } k = 1, ..., K \tag{4.18}$$

$$\frac{\partial}{\partial \boldsymbol{\Sigma}_k}\left(\sum_{i=1}^{N} P\left(x_i = k|\boldsymbol{x}^t_{\mathcal{N}(i)}, y_i, \boldsymbol{\varphi}^t\right)\log f\left(y_i|x_i = k, \boldsymbol{\mu}_k, \boldsymbol{\Sigma}_k\right)\right) = 0 \;\text{ for } k = 1, ..., K \tag{4.19}$$

The MLE estimates at iteration t are then given by

$$\hat{\boldsymbol{\mu}}_k = \frac{\sum\limits_{i=1}^{N} P\left(x_i = k|\boldsymbol{x}^t_{\mathcal{N}(i)}, y_i, \boldsymbol{\varphi}^t\right)\boldsymbol{y}_i}{\sum\limits_{i=1}^{N} P\left(x_i = k|\boldsymbol{x}^t_{\mathcal{N}(i)}, y_i, \boldsymbol{\varphi}^t\right)} \;\text{ for } k = 1, ..., K, \tag{4.20}$$

$$\hat{\boldsymbol{\Sigma}}_k = \frac{\sum\limits_{i=1}^{N} P\left(x_i = k|\boldsymbol{x}^t_{\mathcal{N}(i)}, y_i, \boldsymbol{\varphi}^t\right)(\boldsymbol{y}_i - \hat{\boldsymbol{\mu}}_k)(\boldsymbol{y}_i - \hat{\boldsymbol{\mu}}_k)^T}{\sum\limits_{i=1}^{N} P\left(x_i = k|\boldsymbol{x}^t_{\mathcal{N}(i)}, y_i, \boldsymbol{\varphi}^t\right)} \;\text{ for } k = 1, ..., K. \tag{4.21}$$

4.3.4 Grey-Level-Co-Occurrence-Matrix

We let the observable variables $\boldsymbol{Y}_i$ in the HGMRF model constitute texture features generated from the grey-level co-occurrence matrix (GLCM), which is calculated for a window surrounding each pixel within an image. We divide the intensity range $[0, 255]$ into N_{CM} equal width bins. One of these N_{CM} grey-levels, which we denote by $I^*(x, y) \in (1, 2, ..., N_{CM})$, is assigned to each pixel, corresponding to the bin its intensity value $I(x, y)$ belongs. For an $w_{CM1} \times w_{CM2}$ window within an image, the GLCM is an N_{CM}-by-N_{CM} matrix specifying the number of grey-level pixel pairings within the image that occur at a chosen pixel offset

[6]We also use the property $(\boldsymbol{y}_i - \boldsymbol{\mu}_k)^T\boldsymbol{\Sigma}_k^{-1}(\boldsymbol{y}_i - \boldsymbol{\mu}_k) = \text{tr}((\boldsymbol{y}_i - \boldsymbol{\mu}_k)^T\boldsymbol{\Sigma}_k^{-1}(\boldsymbol{y}_i - \boldsymbol{\mu}_k)) = \text{tr}((\boldsymbol{y}_i - \boldsymbol{\mu}_k)(\boldsymbol{y}_i - \boldsymbol{\mu}_k)^T\boldsymbol{\Sigma}_{ki}^{-1})$.

$(\Delta x, \Delta y)$. Each component (i,j) of the GLCM $\boldsymbol{C}$ is defined mathematically by

$$\boldsymbol{C}_{\Delta x,\Delta y}(i,j) = \sum_{x=1}^{w_{CM1}} \sum_{y=1}^{w_{CM2}} \mathbf{1}_0 \left(I^*(x,y) - i\right) \mathbf{1}_0 \left(I^*(x+\Delta x, y+\Delta y) - j\right). \tag{4.22}$$

The matrix is then normalised so that entries represent estimates of the co-occurrence probabilities. An example of the normalised GLCM, for an offset of $(-1,0)$, corresponding to one row up and zero columns across, is given in Figure 4.4.

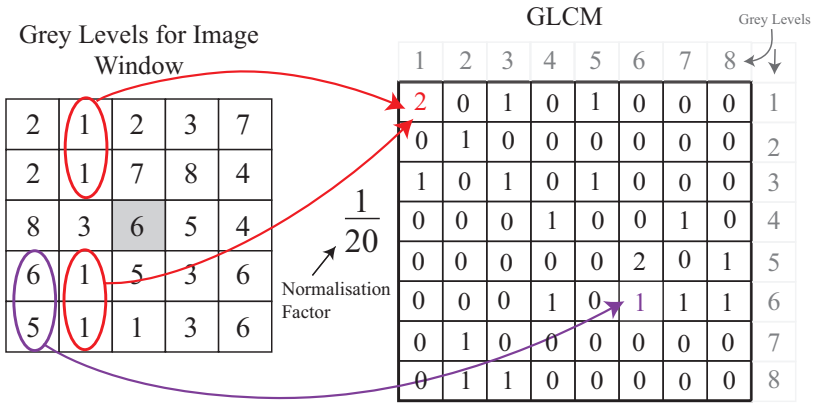


Figure 4.4: Left: Grey-level assigned to each pixel based on the pixel's intensity. There are 8 grey levels prescribed. Right: Corresponding normalised GLCM detailing the number of co-occurring pairs for the offset $(-1,0)$. There are 20 total pairs so a normalisation factor of $1/20$ is used.

Various metrics of the GLCM are then used to define a set of texture features, called Haralick features (Haralick et al. 1973). Examples of features which have been used in tendon (Collinger et al. 2010) include

$$\text{contrast: } \sum_{i,j} |i-j|^2 C(i,j) \quad \text{Range} = [0,\ (N_{CM}-1)^2], \tag{4.23}$$

$$\text{energy: } \sum_{i,j} C(i,j)^2 \qquad \text{Range} = [0,\ 1], \tag{4.24}$$

$$\text{homogeneity: } \sum_{i,j} \frac{C(i,j)}{1+(i-j)^2} \qquad \text{Range} = [0,\ 1]. \tag{4.25}$$

The *contrast* gives a measure of the contrast in intensities between neighbouring pixels within

the region and takes a value of zero for a constant image. *Energy* is a measure of uniformity, taking a value of one for a constant image. If there are no dominant grey levels and hence all values of the GLCM take similar values, then the energy is small. The *homogeneity* measures the closeness of the distribution prescribed by the GLCM to that of a diagonal GLCM matrix. *Homogeneity* in the context of a GLCM feature is distinct from the use of the term by the radiologist, where the term *homogeneity* gives a qualitative description of the entire tendon structure. The former refers to the grey-level distribution within a window of the image, whilst the latter is used to describe the homogeneity of texture across the entire image and is usually used in reference to a healthy tendon (Hodgson et al. 2012). In terms of GLCM features, it has been proposed that the loss of repeating bright and dark lines, seen in tendinopathic images on US, would result in an increase in the homogeneity and energy, and reduced contrast (Collinger et al. 2010).

4.3.5 Textons

Rather than using the GLCM features for the observable variable $\boldsymbol{Y}_i$, we also consider the texton histogram for each pixel. The texton histogram is a concept introduced by Varma et al. (2005) which builds on the mathematical description of textons, first introduced by Zhu et al. (2005). A set of N_{fil} filters are applied to an image, or set of images. Considering the filter bank responses for each pixel as an individual data point of dimension N_{fil}, data points are then clustered into N_{tex} clusters using the K-Means algorithm (Appendix 4.A.3). The set of exemplar filter bank responses that constitute the cluster centres define a *texton dictionary*. Next, for some window around each pixel, which is larger than the filter bank scales, the texton responses are aggregated to give a histogram of responses. The histogram at each pixel location i gives the statistical distribution of textons within the surrounding window, and can be represented as a multivariate data point $\boldsymbol{y}_i$ of dimension N_{tex}. Finally, these data points are again clustered, with each individual cluster representing a distinct texture. The cluster label of each pixel provides a texture-based segmentation of the image.

It is at this final clustering stage where we utilise the HGMRF clustering approach detailed earlier. A flow diagram for the algorithm is given in Figure 4.5.

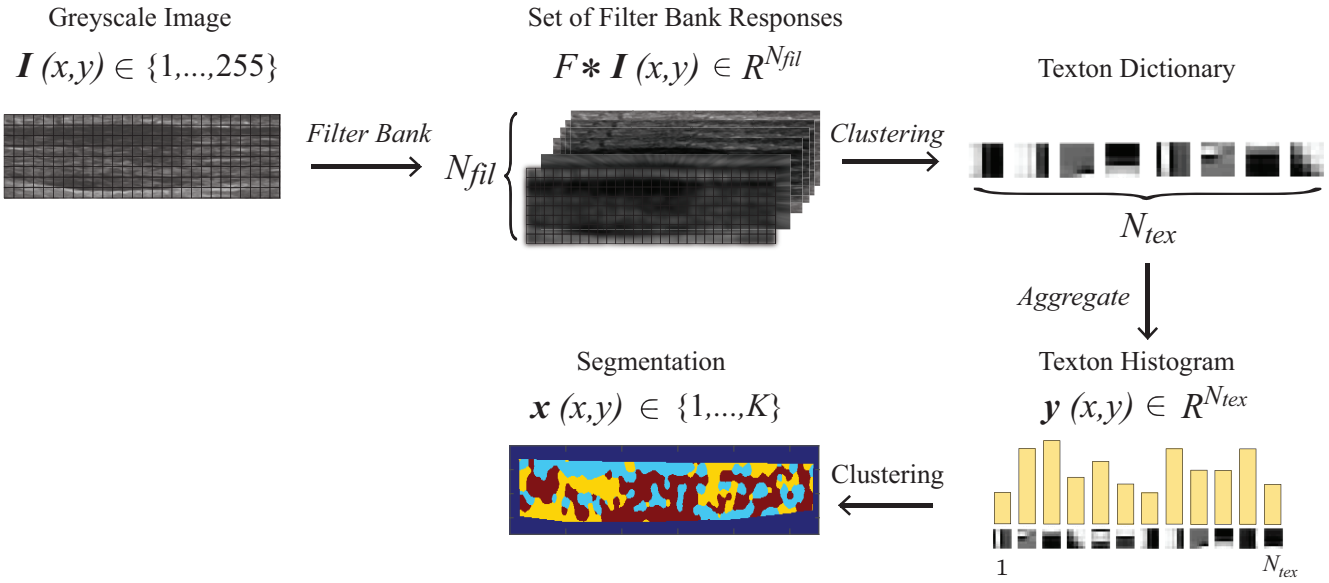


Figure 4.5: Flow diagram for texton generation and subsequent texton-based texture segmentation.

An array of filter banks are available for texton generation. We use the Maximum Response (MR8) filter bank developed by Varma et al. (2002). The filter bank consists of 38 filters but only 8 filter responses; filters are applied at multiple orientations but only the maximum filter response across all orientations is recorded. The filter bank is therefore rotationally invariant. The dimension of the responses is less than other popular filter banks (Varma et al. 2002), contributing to a reduction in the computational overhead in clustering responses. Varma et al. (2002) showed the MR8 filter bank was superior in texture discrimination when analysing the popular Columbia-Utrecht Reflectance and Texture Database (CUReT) database of textured images, when compared to the popular Leung and Malik (LM) (Leung et al. 2001) and Schmid (S) (Schmid 2001) filter banks.

4.3.6 Decision Trees

Decision trees provide an easy way to use segmentation results for image level classification and provide a high level of interpretability. For each image, we calculate the proportion of pixels assigned to each texture class $P_1, ..., P_k$ and use this as input to the decision tree. Using the well known CART model, a set of binary rules are tested which allow for accurate classification of the training set. The CART algorithm uses a greedy approach in which the best discriminatory binary split is chosen at each stage (branching in the tree). In Figure 4.6 we display an example for $K = 3$ texture classes. The process continues until the tree is capable of accurately classifying all images or another user defined criterion is met to prevent over-fitting.

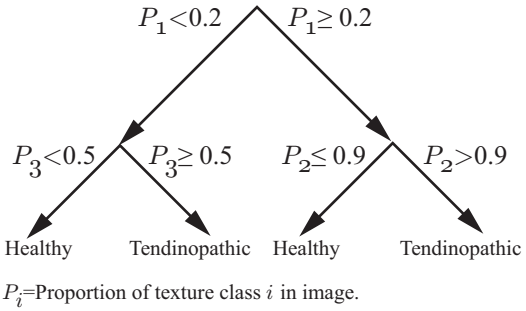


Figure 4.6: Example of decision tree for classification.

4.4 Image Collection and Pre-Processing

A set of longitudinal greyscale US images of Achilles tendons with midportion tendinopathy were collected as part of another study conducted between Monash University and *Imaging at Olympic Park* (IOP). A diagnosis of tendinopathy was determined by both clinical symptoms (pain related to loading) and a deviation from the normal healthy texture profile on imaging. For comparison, a set of healthy images were obtained from patients and employees of IOP. Images were uploaded to a secure database and fully anonymised. Ethical approval was obtained through Monash University. All images were obtained by an ultrasonographer with experience in tendon imaging. An example image from the database is given in (Figure 4.1a). All images were high resolution *tif* images.

Images were masked to include a 4cm long segment (including the entire thickness along that length) over the tendon midportion. A Gaussian filter was applied to all images to reduce

noise. In the case where texton histograms were utilised as the texture features, reflective padding[7] was used at the mask edges to prevent a loss of edge information with subsequent filtering of the image.

4.5 Algorithm for Texture-Based Segmentation of Tendon Images

We model each $m \times n$ image as a hidden Gaussian Markov random field (HGMRF), in which there is both an observable multivariate random variable $\boldsymbol{Y}_i$ and a univariate hidden variable X_i associated with each pixel $i = 1, ..., N = mn$. The variable $\boldsymbol{Y}_i$ gives a set of texture features associated with each pixel. The hidden variable X_i is a categorical variable denoting the texture class label $k \in \{1, ..., K\}$. A realisation of the hidden field $\boldsymbol{x}$ represents a texture-based segmentation of the image. The variables $\boldsymbol{Y}_i$, when conditioned on X_i, are i.i.d[8] with a multivariate Gaussian distribution $\boldsymbol{Y}_i | X_i = k \sim N(\boldsymbol{\mu}_k, \boldsymbol{\Sigma}_k)$. We apply the HMRF-EM algorithm (Zhang et al. 2000), described in Section 4.3.3, to each image individually. In contrast to Zhang et al. (2000), to obtain the maximum-a-posteriori (MAP) estimate for the HMRF-EM procedure, we utilise the mode field algorithm described by Celeux et al. (2003) and detailed in Section 4.3.3.1. The algorithm is first run on 25 of the images which form a training set. We use the final texture proportions for each training image to fit a decision tree with $K - 1$ splits, using the *MATLAB* function *fitctree*. This generates a set of simple binary predictive rules that allows for the classification of each image based on its texture class label proportions. The prediction accuracy of the decision tree on a subsequent test set, consisting of the remaining 24 images, provides a means for hyperparameter tuning and

[7]To generate filter responses for edge pixels during convolution, *padding* of the edges is required: data values are added to extend the region for analysis so the convolution filter does not overlap an empty/masked region. To avoid information loss, we use symmetric padding in which the image is reflected at the mask edges.

[8]Suggesting the texture features assigned to each pixel are independent of those assigned to the surrounding pixel, when conditioning on the texture class label $k \in \{1, ..., K\}$.

assists in validating the segmentation results.

The training algorithm consists of three main stages:

1. For all images, generate a set of texture features (GLCM features or texton histogram) $\boldsymbol{y}_i$ for each pixel. Use K-Means clustering to provide an initial label for each pixel $x_i^{t=0}$.

2. For each image, using the HMRF-EM algorithm with the observable data $\boldsymbol{y}_i$, generate a segmentation of the image $\boldsymbol{x}$.

3. For each image, calculate the proportion of pixels assigned to each texture class. Using the image-level labels and texture class proportions, generate a decision tree to form a predictive rule for classification of *healthy* and *tendinopathic* tendon images.

Pseudocode for the generation of GLCM- and texton-based features are given by Algorithm 2a and 2b. To calculate the GLCM and associated features, we utilise the built-in *MATLAB* functions *graycomatrix* and *graycoprops*. The set of filters which is required to generate the texton histogram, is obtained by using the *makeRFSfilters* function, provided by the Oxford Visual Geometry Group *Texture classification - filters*. We refer to the initial feature generation and K-Means segmentation, excluding latter HMRF-EM processing, as the *GLCM-based K-Means* and *texton-based K-Means* algorithms. Pseudocode for the subsequent HRMF-EM analysis is given in Algorithm 3. We use the terms *GLCM-based HMRF-EM* and *texton-based HMRF-EM* algorithms to refer to the entire algorithms (inclusive of feature generation, K-Means clustering and subsequent HMRF-EM processing).

Algorithm 2a GLCM Feature Generation and K-Means Clustering

Inputs:
N_{img} greyscale images.
N_{img} corresponding image masks.
Number of grey levels for GLCM generation N_{CM}.
Window size for GLCM generation $W_{CM1} = w_{CM2} \times w_{CM}$.
Number of texture class labels K.
for each image **do**
  for each pixel **do**
    Using *graycomatrix*: generate GLCM for surrounding window W_{CM}.
    Using *graycoprops* on GLCM: Calculate (energy, contrast, homogeneity*)$^T \leftarrow \boldsymbol{y}_i$.
  *The homogeneity was removed due to a high correlation with the energy, see Section 4.6.1.
  for all images and pixels **do**
    Cluster $\boldsymbol{y}_i$ into K clusters.
    Use cluster label $k \in \{1, ..., K\}$ to provide initial segmentation $k \leftarrow x_i^{t=0}$.

Algorithm 2b Texton Histogram Generation and K-Means Clustering

Inputs:
N_{img} greyscale images.
Filter bank of size N_{fil}.
Number of textons N_{tex}.
Window size for texton aggregation $W_{tex} = w_{tex} \times w_{tex}$.
Number of texture class labels K.
for each image **do**
  Generate a set of N_{fil} filter bank responses: I (size $m \times n$) $\rightarrow \boldsymbol{F}$(size $m \times n \times N_{fil}$).
for all images and pixels **do**
  Cluster filter bank responses into N_{tex} clusters.
  Assign each pixel to corresponding cluster centroid ('texton').
  Calculate texton histogram (N_{tex} bins) in window W_{tex} surrounding pixel $\leftarrow \boldsymbol{y}_i$.
  Cluster histogram responses $\boldsymbol{y}_i$ into K clusters.
  Use cluster label $k \in \{1, ..., K\}$ to provide initial segmentation $k \leftarrow x_i^0$.

Algorithm 3 HMRF-EM Segmentation

Inputs:
Texton histogram for each pixel $\boldsymbol{y}_i$.
Initial pixel class labels $x_i^{t=0}$.
Number of clusters for segmentation K.
Max iterations T.
Gibbs parameter β.

for texture class labels k=1:K **do**
  Compute initial mean: $\boldsymbol{\mu}_k^0 = \sum_{i:\, x_i=k} \boldsymbol{y}_i \Big/ \sum_{i:\, x_i=k} 1.$
  Compute initial variance: $(\boldsymbol{\Sigma}_k^0)^2 = \sum_{i:\, x_i=k} (\boldsymbol{y}_i - \boldsymbol{\mu}_k)^2 \Big/ \sum_{i:\, x_i=k} 1.$

repeat
  Neighbour Assignment
  for pixels i=1:n **do**
    for class labels k=1:K **do**
      Calculate probably of class label assignment: $P_G(x_i = k|y_i, \boldsymbol{x}_{\mathcal{N}(i)}^{t-1}, \boldsymbol{\varphi}^{t-1})$.
      Assign pixel most probable label: $\overline{x}_i^t \leftarrow \underset{x_i}{\operatorname{argmax}}\, P_G(x_i|y_i, \boldsymbol{x}_{\mathcal{N}(i)}^{t-1}, \boldsymbol{\varphi}^{t-1})$.
  Expectation
  for pixels i=1:n **do**
    for class labels k=1:K **do**
      Calculate probability of class assignment based on newly assigned neighbours: $P(x_i = k|y_i, \boldsymbol{x}_{\mathcal{N}(i)}, \boldsymbol{\varphi}^{t-1}) = f(y_i|x_i, \boldsymbol{\varphi}^{t-1}) P(x_i|\boldsymbol{x}_{\mathcal{N}(i)}^t, \beta) \Big/ f(y_i|\boldsymbol{\varphi}^{t-1})$.
  Maximisation
  for class labels k=1:K **do**
    Compute mean and variance:
    $(\boldsymbol{\mu}_k^t, \boldsymbol{\Sigma}_k^t) = \underset{(\mu_k, \boldsymbol{\Sigma}_k)}{\operatorname{argmax}} \sum_{i \in S} \sum_{x_i \in \mathcal{X}} P_{\overline{\boldsymbol{x}}^t}(x_i|y_i, \boldsymbol{\varphi}^t) \log f(y_i|x_i, \boldsymbol{\mu}, \boldsymbol{\Sigma})$.

until $\boldsymbol{\varphi}$ converges or iterations $t > T$: =0

For subsequent testing of individual images, the three main stages are:

1. Generate a set of texture features for each pixel as above. Assign each pixel to the nearest cluster centroid, calculated from the K-Means output for the training set.

2. Implement the HMRF-EM algorithm, using the texton histogram $\boldsymbol{y}_i$ data, in order to generate a segmentation of the image $\boldsymbol{x}$.

3. Determine whether the image represents a healthy or tendinopathic tendon based on decision tree model learned from training set.

After the first stage in processing both the training and test images, the texture class labels $\{1, 2, ..., K\}$ across all images refer to subpopulations from the same Gaussian mixture population. After the second step, since the HMRF-EM generates small updates to the mean and variance for each image individually, labels between images no longer refer to the exact same mixture population. However, since the HMRF-EM mainly serves to reduce noise and provide a more distinct segmentation, we expect corresponding labels between images to refer to approximately the same subpopulations and are hence comparable.

4.6 Code Validation

We first test the code on several modified images from the Columbia-Utrecht Reflectance and Texture Database (CuRET). Since the CuRET database provides images in which only one unique texture is present, we collate several images in order to test our algorithm in terms of segmentation. We contrast results for K-Means texton clustering and HMRF-EM. An example is given in Figure 4.7. Both approaches are able to clearly segment the images into appropriate textures. The HMRF-EM serves to reduce the small amount of noise present and produces a more defined segmentation. A thin mask is applied to the images (dark blue outline) and reflective padding is used, in order to ensure there are no issues from the pre-processing (Section 4.4).

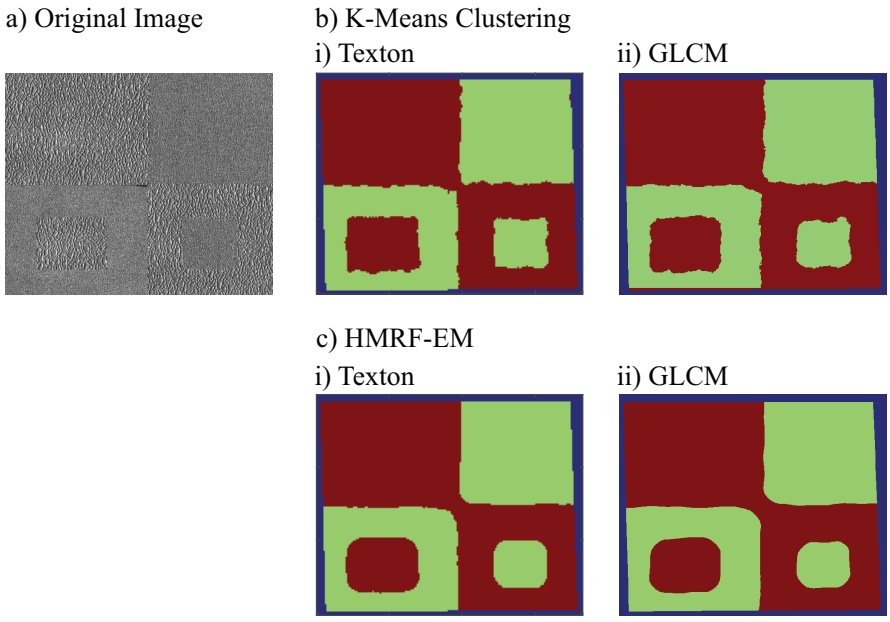


Figure 4.7: Adapted textured images from CuRET database with dimensions (i/ii) 1460×1210 and (iii) 1210×1460. Texture classes $K = 2$, number of textons $N_{tex} = 20$, texton histogram window size 20×20. For the HMRF-EM, a neighbourhood window size of 60×60 was used and $\beta = 1$. Red and green denote The pixel assignments to one of the two texture classes are given in red and green. The blue outline is a thin mask of the image.

4.6.1 Hyperparameter Optimisation and Variable Selection

Based on the resolution of our dataset we use the default filter size of the MR8 filter bank (Varma et al. 2002), as the filter size spans the width of the smallest units of interest (fibres). A GLCM offset of $(-1, 0)$ is used to capture increases in fibre spacing consistent with tendinopathy (Hodgson et al. 2012); this offset is perpendicular to the fibre axis in a healthy longitudinal tendon image. The remaining hyperparameters that are tuned during training are listed in Table 4.1. A grid-based search is used with parameter ranges based on previous values utilised in the literature, as well as the scale of physical units within the image. Because the HMRF-EM component is sensitive to the accuracy of the initialisation, hyperparameters are divided into two sets: the initial texton/GLCM feature generation and K-means clustering, and the HMRF-EM components, which are tuned sequentially. The optimal hyperparameters are defined to be those that provide clear class proportion thresholds that can be used for classification. Thus we choose hyperparameters which produce a decision

Table 4.1: Model hyperparameters and tuning ranges explored.

Hyperparameter	Definition	Range [max, min]	Selection
N_{tex}	Number of textons	[10, 20]	20
W_{tex}	Texton window size	[10^2, 30^2]	25
N_{CM}	Number of GLCM grey level bins	[4, 10]	8
W_{CM}	GLCM window size	[10, 30]×[10, 30]	10×20
K	Number of texture classes	[2, 4]	3
β	Gibbs parameter	[0.5, 2]	1
$\mathcal{N}(i)$	Markov neighbourhood (square window)	[1^2, 30^2]	30×30

tree fit with the highest classification accuracy and minimum number of splits.

Texton and GLCM parameter ranges are based off previous work (Rıos-Dıaz et al. 2012, Li et al. 2014). The texton and GLCM window sizes are also partially informed by knowledge of the scale of physical units within the image, prescribed to capture several fibres within a window. Calculation and visualisation of the GLCM features given in Equation (4.23) demonstrate that the homogeneity and energy display a strong positive linear correlation; after tuning of other hyperparameters, a loss of homogeneity has no impact on clustering and subsequent classification performance (results not shown). Consequently, only the energy and contrast aree used as texture features. The parameter range for the Gibbs parameter is informed by previous work (Wang 2012). The classification accuracy is only mildly improved by changes to the HMRF-EM parameters. The upper end of the neighbourhood size is chosen to provide a more distinct segmentation.

4.7 Segmentation Results

Since the HMRF-EM is sensitive to the initial segmentation, we first evaluate how well GLCM-and texton-based features serve to distinguish between tendinopathic and healthy

tendons. We investigate whether either set of features, via K-Means clustering, provides a segmentation that allows us to distinguish between tendinopathic and healthy tendons. We then proceed to analyse the use of further HMRF-EM processing.

4.7.1 Texture Features and Initial K-Means Clustering

In Figure 4.8a a scatter plot of the GLCM features is given for all pixels belonging to images within the training set. Pixels belonging to tendinopathic images are denoted by blue points and those belonging to healthy images are denoted by green points. There is a distinct difference in the distribution of local GLCM features between tendinopathic and healthy tendons, with pixels belonging to tendinopathic tendons tending to have a lower contrast and

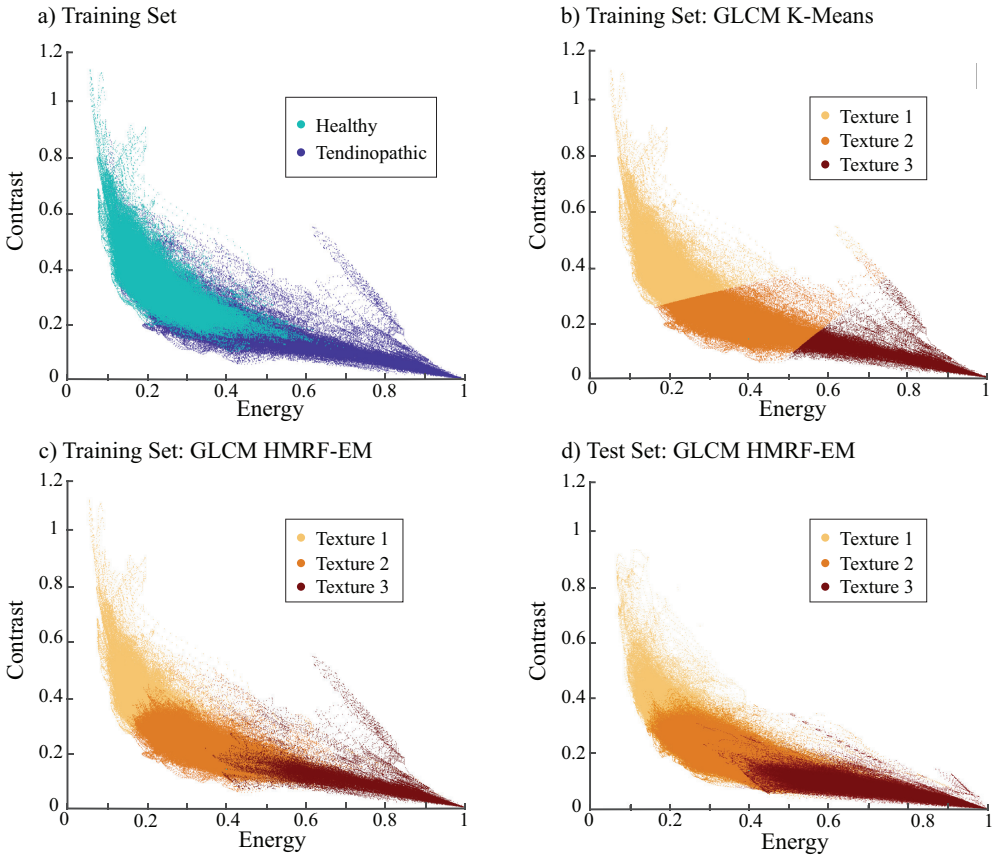


Figure 4.8: Scatter plot of GLCM features for all pixels within the training set showing a) different distributions between values for pixels within healthy and tendinopathic tendons, b) K-Means cluster assignments, and c) HMRF-EM cluster assignments. d) Scatter plot of GLCM features for all pixels within the test set showing associated HMRF-EM cluster assignments.

higher energy. In Figure 4.8b a scatter plot of the same training data shows the texture label assigned to each pixel after GLCM-based K-Means clustering. GLCM feature generation for the training set took 460 seconds while initial clustering of the training set using the *kmeans*[9] function in *Matlab* took 561 seconds. The data is clustered into three texture classes: the first class is indicated in yellow and corresponds to high contrast and low energy values, the second class is indicated in orange and corresponds to moderate contrast and energy values, and the third class is indicated in red and corresponds to low contrast and high energy values. In Figure 4.8c a scatter plot of the training data after GLCM-based HMRF-EM implementation is carried out. Contrasting this plot with Figure 4.8b, it is evident that a small proportion of the pixels lying at the edge of the initial clusters were reassigned after HMRF-EM implementation. A scatter plot for the test set after GLCM-based HMRF-EM implementation is given in Figure 4.8d. It is evident that the test data shows a similar spread of energy and contrast values to the training data.

To visualise the texton histograms for each pixel, a dimensionality reduction is required. We have used principal component analysis, which produces an orthogonal linear transformation of the data. The first and second linear combinations of the data (the first and second principal components) account for the majority of variance in the data and provide a way to visualise the data in two dimensions. Using this method, the texton histograms for pixels belonging to healthy and tendinopathic tendons were compared, and no apparent difference in the distribution of principal components was identified (results not shown).

Two examples for the GLCM- and texton-based K-Means segmentations are given in Figure 4.9. The texture class labels $k \in \{1, 2, 3\}$ are consistent between images processed by the same algorithm only. In Figure 4.9a and 4.9c, the GLCM-based K-Means segmentations for a tendinopathic and healthy image are shown. The GLCM-based K-Means clustering appears

[9]The number of replicates was set to three which served to increase the reliability but also increased computational time.

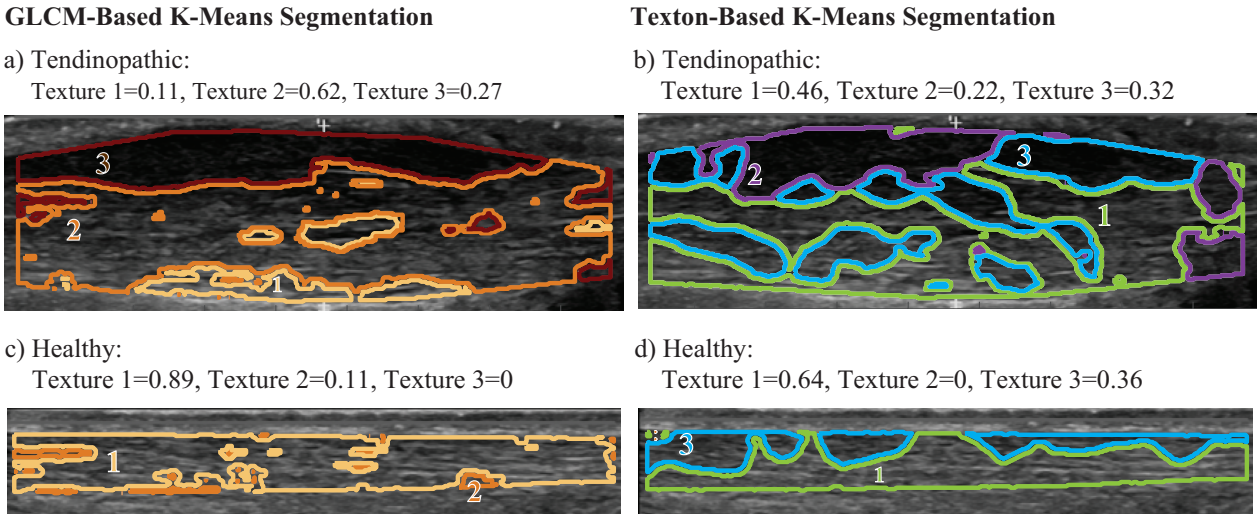


Figure 4.9: Two segmentation examples from the training set, generated from using K-means clustering on either GLCM features (a,c) or texton histograms (b,d) for each pixel. Image (a/b) is of a tendinopathic tendon whilst (c/d) is of a healthy tendon. Texture labels are consistent for the same algorithm but not between algorithms.

to provide a segmentation that assigns the first texture class (yellow outline) to regions with clearly visible collagen fibres and interfibre spacing, the second class (orange outline) to regions in which the fibres are visible but with less clarity, and the third class (red outline) is assigned to regions in which fibres are barely visible. The results are qualitatively in good agreement with our expectations: the first texture class is predominant in the healthy image, and the second and third classes constitute the majority of the tendinopathic image. Over the entire training set there is some variability but generally high proportions of the first texture class are seen in the healthy images, and high proportions of the second and third texture class are seen in tendinopathic images (Appendix 4.B Figure 4.17).

In Figure 4.9b and 4.9d, the texton-based K-Means segmentations for a tendinopathic and healthy image are shown. These are the same two images as shown in Figure 4.9a and 4.9c. Analysing the regions assigned to each texture class, it not completely visually apparent why the three classes are considered as distinct textures. Potentially, the first texture (green outline) class appears to be assigned to brighter regions whilst the second (purple outline in Figure 4.9c only) and third (blue outline) classes appear to have lower pixel intensity values.

Over the entire training set there is a general trend that larger proportions of the second texture are assigned to tendinopathic tendons (Appendix 4.B Figure 4.18). However several images of healthy tendons exhibit small proportions of the second texture class, comparable to the second texture class proportions seen in several of the tendinopathic images. Contrasting the results with the GLCM-based K-Means segmentations seen in Appendix 4.B Figure 4.17, the texton-based K-Means algorithm provides a less distinct segmentation between tendinopathic and healthy tendons. In both cases, the K-Means segmentation results appear noisy, warranting further HMRF-EM processing.

In Table 4.2 the mean and standard deviation of texture proportions within the training set are given after the GLCM-based segmentation has been generated. Values after initialisation through K-means clustering, and following further HMRF-EM processing, are displayed. Consistent with the visual segmentations shown in Appendix 4.B Figure 4.17, there is a clear difference in texture class proportions between tendinopathic and healthy tendons. The first texture class appears predominantly in healthy tendons whilst the second class is more predominant in the tendinopathic tendons. The third class is only present in the tendinopathic tendons. As expected, following HMRF-EM implementation, there are only minimal changes to the mean texture class proportions.

Table 4.2: Mean and standard deviation of segmentation proportions for training set after K-Means clustering of GLCM features.

Image Set	Texture Class Proportion: Mean (SD)		
	1	2	3
Tendinopathic - GLCM K-Means	0.15 (0.10)	0.67 (0.16)	0.18 (0.17)
Healthy - GLCM K-Means	0.69 (0.14)	0.31 (0.14)	0.00 (0.00)
Tendinopathic - GLCM HMRF-EM	0.12 (0.10)	0.72 (0.19)	0.16 (0.18)
Healthy - GLCM HMRF-EM	0.73 (0.18)	0.27 (0.18)	0.00 (0.00)

Table 4.3: Mean and standard deviation of segmentation proportions for training set after K-Means clustering of texton features.

Image Set	Texture Class Proportion: Mean (SD)		
	1	2	3
Tendinopathic - Texton K-Means	0.48 (0.10)	0.22 (0.14)	0.30 (0.09)
Healthy - Texton K-Means	0.62 (0.06)	0.02 (0.02)	0.37 (0.06)
Tendinopathic - Texton HMRF-EM	0.50 (0.12)	0.21 (0.14)	0.29 (0.10)
Healthy - Texton HMRF-EM	0.68 (0.10)	0.01 (0.02)	0.30 (0.10)

In Table 4.3 the mean and standard deviation of texture proportions within the training set are given after the texton-based segmentation has been generated. Again, values after initialisation through K-means clustering, and following further HMRF-EM processing are displayed. There is a slightly higher proportion of the first texture class in healthy tendons whilst there is a slightly higher proportion of the second class seen in the tendinopathic tendons. There is minimal difference in terms of proportions of the third class. These results are consistent with the visual segmentations shown in Appendix 4.B Figure 4.18. Overall, whilst there is a difference in the mean texture class proportions between tendinopathic and healthy tendons, the differences between means are not as large as those seen in Table 4.2. Again, following HMRF-EM implementation, there are only minimal changes to the mean texture class proportions.

The GLCM-based K-Means algorithm, when compared with the texton-based K-Means algorithm, provided a clearer and more interpretable segmentation that clearly correlated with the presence of tendinopathy. Hence, we focus on the results for the GLCM-based HMRF-EM algorithm herein.

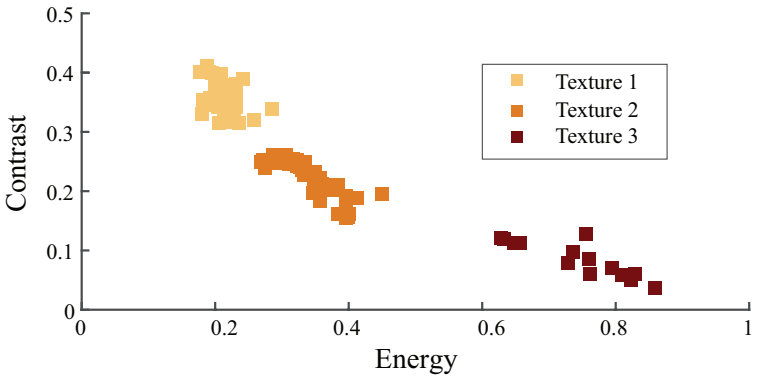


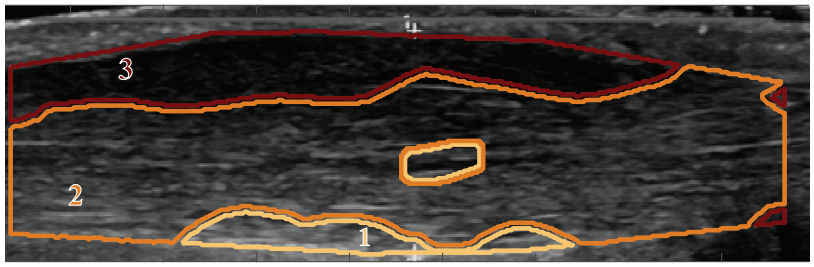
Figure 4.10: Mean energy and contrast for images after GLCM-based HMRF-EM segmentation.

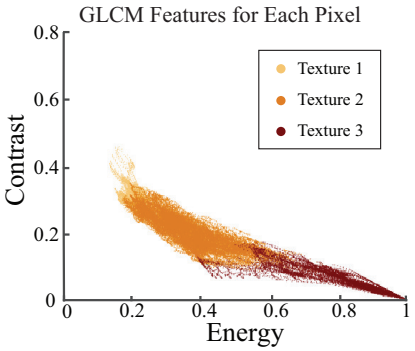
4.7.2 GLCM-Based HMRF-EM Segmentation

In Figure 4.10 a plot of the means μ_k for the texture class labels $k \in \{1, 2, 3\}$, after implementation of the GLCM-based HMRF-EM algorithm, is displayed. The mean is calculated for each individual image in the dataset. Across the images, the means for each label can be seen to form distinct clusters. Hence, the texture class labels $k \in \{1, 2, 3\}$ are comparable across images, referring to high contrast and low energy, moderate contrast and energy, and low contrast and high energy, respectively.

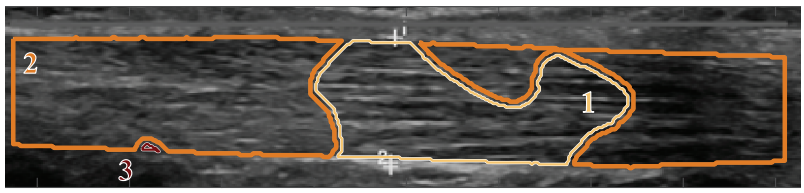
Figure 4.11 gives the GLCM-based HMRF-EM segmentation for four examples from the training set. The corresponding scatter plots of GLCM features for each pixel within the image are given on the right. The colour of scatter points indicates the texture class assignment (one - yellow, two - orange, three - red). Figure 4.11a and 4.11b give image segmentations for two tendinopathic tendons. In Figure 4.11a a tendon segment has been assigned to the third texture class, outlined in red, with associated low contrast and high energy values occurring for the encompassed pixels. This region was prospectively identified as showing a clear deviation from the normal texture profile seen in healthy tendons: the region is hypoechoic and collagen fibres are barely visible. Similar to Figure 4.11a, across the training set, regions assigned to the third texture class occurred most commonly near the transverse border of the tendon (Appendix 4.B Figure 4.19). In Figure 4.11b tendon regions are predominantly

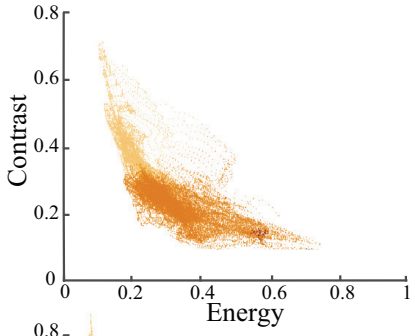
a) **Tendinopathic:** Texture 1=0.08, Texture 2=0.67, Texture 3=0.24



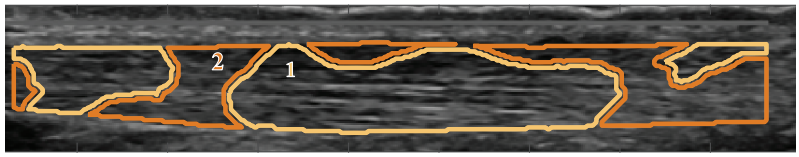


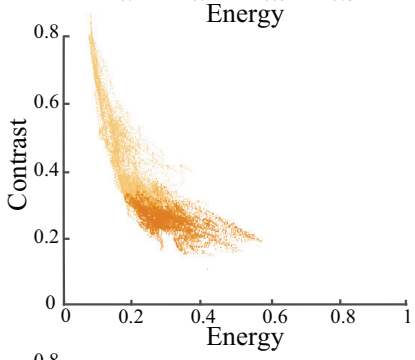
b) **Tendinopathic:** Texture 1=0.3, Texture 2=0.7, Texture 3=0



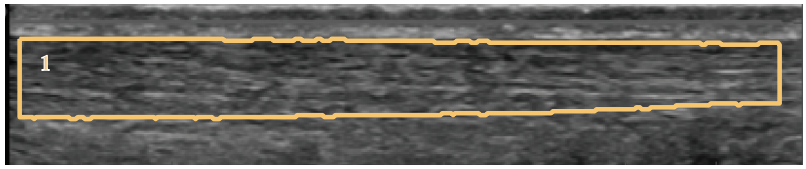


c) **Healthy:** Texture 1=0.62, Texture 2=0.38, Texture 3=0





d) **Healthy:** Texture 1=1, Texture 2=0, Texture 3=0



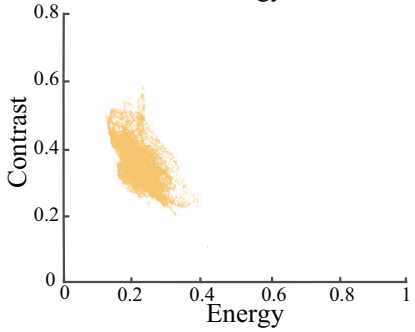


Figure 4.11: Segmentation results, and associated GLCM features for each pixel, for four images within the training set. Images (a) and (b) are of tendinopathic tendons, and (c) and (d) are of healthy tendons. Regions labelled as texture class one are outlined in yellow and constitute areas with high contrast and low energy. Areas assigned to texture class two are outlined in orange and refer to areas with moderate contrast and energy. Areas outlined in red have been assigned to texture class three and constitute areas with low contrast and high energy. The same colour scheme is used to denote each pixel's texture class label with the scatter plots.

labelled to the first (yellow outline) and second (orange outline) textures. In contrast to Figure 4.11a, more extreme high energy and low contrast values were not observed, however, a large region was classified as the second texture - with medium contrast and energy. Figure 4.11c and 4.11d are the image segmentations for two healthy tendons. In Figure 4.11c pixels were still assigned to the second texture class but in lower proportions than seen in Figure 4.11b. Figure 4.11d displays a tendon tendon with a consistent texture pattern throughout and hence only the first texture class is assigned. In Figure 4.11b-4.11d the first texture class has been assigned to regions in which there is clear visibility of the collagen fibres with darker hypoechoic spaces between. In Figure 4.11a-4.11c the second texture class has been assigned to regions that do not have the same degree of clarity between the fibres and interfibre spacing, but also do not have the same degree of hypoechogenicity as the region assigned to the third class in Figure 4.11a. This qualitative pattern was consistent across the training set (results not shown).

Contrasting the segmentation given by the GLCM-based K-Means algorithm in Figure 4.9a and 4.9c with the GLCM-based HMRF-EM based segmentation of the same images given in Figure 4.11a and 4.11d, further HMRF-EM processing provides a visible noise reduction and clearer well-defined segmentation. This result was consistent across the training set, comparing all images clustered using the GLCM-based K-Means (Appendix 4.B Figure 4.17) with that using the full GLCM-based HMRF-EM approach (Appendix 4.B Figure 4.19).

The computational time taken for analysis of an image by the HMRF-EM algorithm was quick, taking several seconds. This in in contrast to the initial k-means segmentation of the 12 training images, which took approximately 12 minutes, and generation of the GLCM-features, which took approximately over 10 seconds per image.

To test robustness of the algorithm to noise, in Appendix 4.B Figure 4.21 we have rerun the segmentations of the training set after additional speckle noise has been applied. The segmentations for corrupted images showed minimal difference from the original segmenta-

tions for the training set, suggesting that the algorithm is robust to a reasonable amount of noise. However, care should be taken for especially poor quality images.

We next consider how the algorithm performs on the test set of images. In Figure 4.12 we present the GLCM-based HMRF-EM segmentation for two tendinopathic and two healthy images from the test set. The segmentation boundaries are outlined left and the corresponding scatter plots of GLCM features for each pixel within the image are given right. In Figure 4.12a and 4.12b two tendinopathic images are displayed. Qualitatively, Figure 4.12a displays a clearly tendinopathic tendon, with a large degree of thickening and hypoechogenicity. In Figure 4.12c and 4.12d two healthy images are displayed. There is good qualitative agreement with the segmentations given for the training examples in Figure 4.11, in which the third texture is assigned to hypoechoic regions with lower contrast and minimal visible fibres, and the first texture is assigned to regions with higher contrast and more clearly visible fibres. Similar to the segmentation results for the training set (Figure 4.11a and Appendix 4.B Figure 4.19), across the test set, regions assigned to the third texture class occurred most commonly near the transverse border of the tendon (Appendix 4.B Figure 4.20).

The decision tree produced from the training set are given in Figure 4.13. Images are classified as tendinopathic if the proportion of the first texture, calculated for the masked 4cm region, is less then 0.37. Otherwise, the tendon is considered healthy. Using this simple binary cut-off, the decision tree was able to classify all training images accurately. Using the decision tree on the test set, 22 of the 24 images were accurately classified. All tendinopathic images were successfully classified, whilst two healthy images were misclassified as tendinopathic due to low proportions of the first texture. Since radiologist based classification is not completely accurate, there is the potential that these tendons were misclassified. Figure 4.14a displays the tendinopathic im-

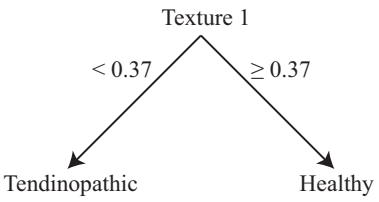


Figure 4.13: Decision tree for classifying tendon images as tendinopathic or healthy based on GLCM-based HMRF-EM segmentation results.

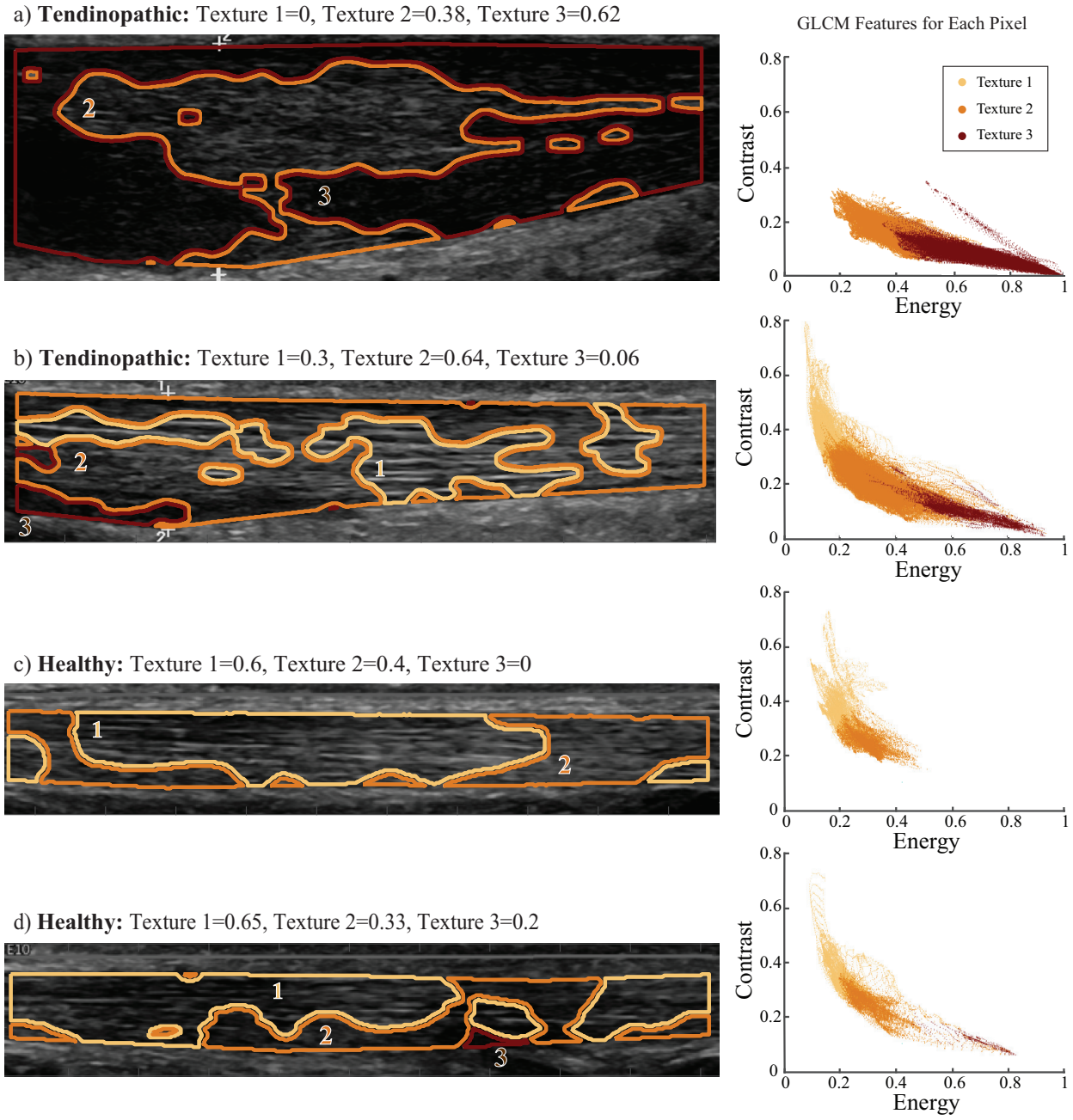


Figure 4.12: Segmentation results, and associated GLCM features for each pixel, for four images within the test set. Images (a) and (b) are of tendinopathic tendons, and (c) and (d) are of healthy tendons. Regions labelled as texture class one are outlined in yellow and constitute areas with high contrast and low energy. Areas assigned to texture class two are outlined in orange and refer to areas with moderate contrast and energy. Areas outlined in red have been assigned to texture class three and constitue areas with low contrast and high energy. The same colour scheme is used to denote each pixel's texture class label with the scatter plots

age from the test set which exhibits the highest proportion of the first texture (0.33) and was correctly classified. This is contrasted with the two misclassified healthy images from the test set in Figure 4.14b and 4.14c. The proportions of the first texture present in these images is 0.23 and 0.36 respectively. Comparing the associated scatter plots of GLCM features (right panel), despite the misclassification, there is still a difference in the GLCM distributions between the tendinopathic and healthy tendons. The tendinopathic tendon has a greater spread of contrast and energy values amongst its pixels than the misclassified healthy images. The tendinopathic tendon also exhibits a small region classified as the third texture whilst the other two images do not have a region with such low contrast and high energy values.

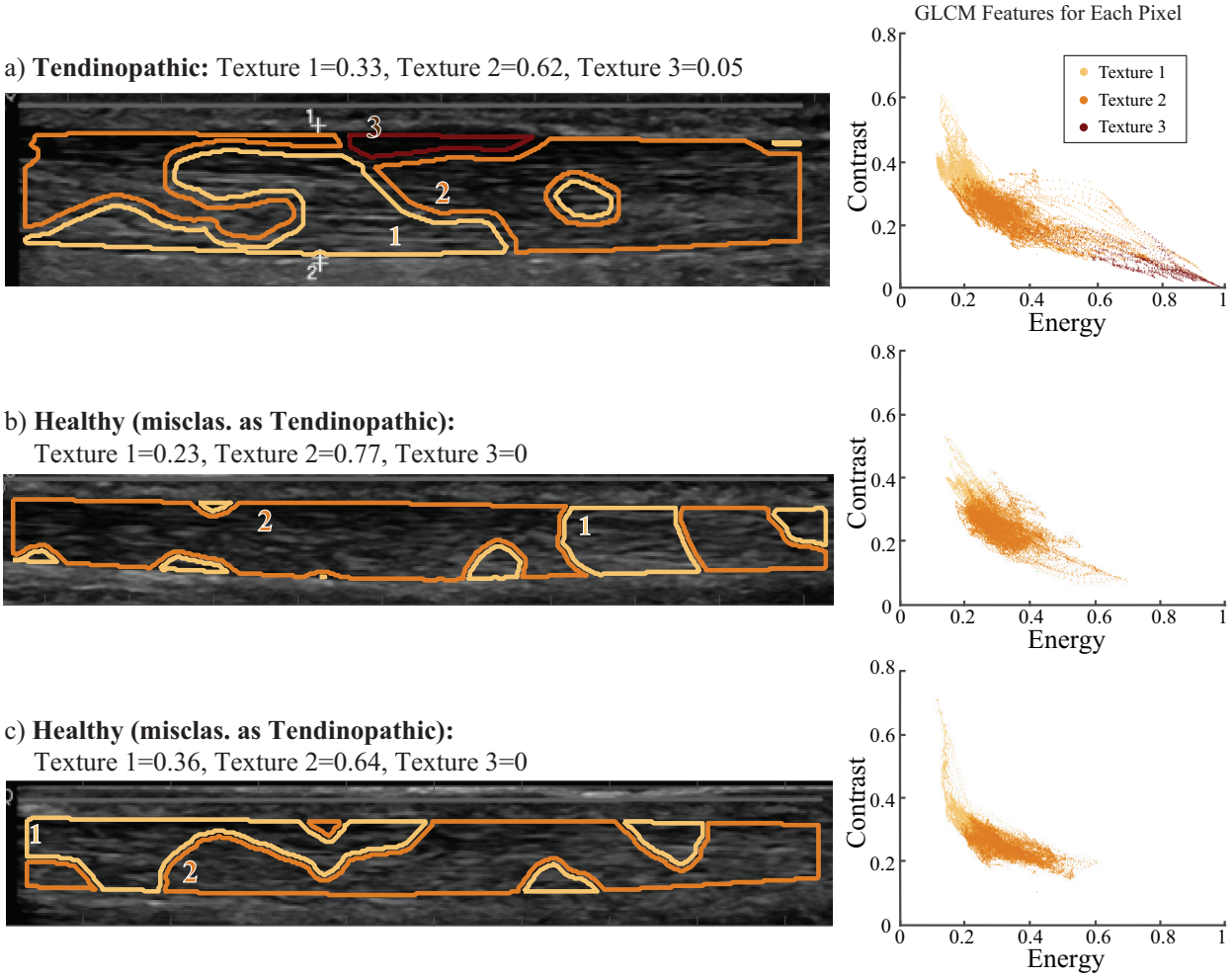


Figure 4.14: Segmentation examples, and associated GLCM features for each pixel, for three images within the test set. a) Successfully classified tendinopathic image with the largest proportion of texture one of all tendinopathic test images. b, c) Misclassified healthy images from the test set.

4.8 Discussion

Local texture features based on the grey-level co-occurrence matrix (GLCM) and textons were both analysed as a means for providing a segmentation that could differentiate between tendinopathic and healthy tendons on imaging. Texture features based on the GLCM were shown to have a stronger correlation with disease state and provided a more distinct segmentation between tendinopathic and healthy tendon images. Another benefit of the GLCM feature-based approach is that only two features were required to capture difference between tendinopathic and healthy tendon images, and these two features - the energy and contrast - have meaningful interpretations. This is in contrast to texton histograms, which provide a statistical description of filter bank responses, and hence are both higher dimensional and do not have a direct interpretation. It is more desirable for texture features to have a direct interpretation, as this facilitates integration of these methods into the clinical community.

A continuum of changes in the GLCM contrast and energy appear to occur with tendinopathy. Collectively, the GLCM-based HMRF-EM segmentation results suggest that a reduction in the contrast, and an increase in the energy, of a region is indicative of potential tendinopathic changes. The results also suggest that regions with the lowest contrast (< 0.2) and highest energy (> 0.6) may represent a higher level of damage. Visually these findings correlated with a loss of fibre clarity, extending to a complete loss of fibre visibility. This could suggest a loss of collagen fibres in that region or an accumulation of denser substances such as fluid (for example due to proteoglycan deposition preventing fluid expulsion) which obscure the fibres on US. There was a wide variety of topological presentations, however, there was a general trend that these more extreme low contrast and high energy regions occurred closer to the transverse tendon boundaries (Appendix 4.B Figures 4.19 and 4.20). This finding is consistent with predictions from the adaptation model in Chapter 3, in which higher fluid fluxes/shear occurred near the transverse boundary of the midportion. The model predicted a reduction in stiffness as a result, which was prescribed to be synonymous with a reduction

in type I collagen (or change in collagen from type I from type III leading to disruption of healthy collagen architecture).

Whilst the second texture in the GLCM-based HMRF-EM segmentation, corresponding to moderate contrast and energy values, was predominantly present in tendinopathic tendons, it was also present in lower proportions amongst the healthy tendon images. These regions may still correspond to early tendinopathic changes, as several longitudinal studies have demonstrated that tendinopathic changes on imaging often precede pain and suggest a higher risk for later symptom development (Fredberg et al. 2002, Khan et al. 1997, Cook et al. 2000). This could also be a result of the use of K-Means as the initial clustering algorithm. Since, in the setting of overlapping clusters, the K-Means algorithm allocates points in a way that roughly equalises the spatial variance of the clusters, it can perform poorly if clusters have a large difference in the number of points. It may be that facilitating larger differences in cluster sizes is necessary to provide an even better distinction between tendinopathic and healthy tendons.

The purpose of this work was to identify a segmentation technique that could be used as a quantitative tool to measure disease severity. Since a prognostic labelled dataset was not available, we correlated the segmentation results with disease state to first provide a proof of concept. A simple decision tree approach was chosen to validate whether the segmentation could be used to accurately classify images, as we desired a segmentation that would provide readily interpretable quantifiable predictors for the clinician. A simple cut-off value for one texture allowed us to classify 47 of 49 images correctly, with 100% accuracy for the tendinopathic images. Evaluation of GLCM features for the misclassified healthy images suggested there was still a difference between the distribution of GLCM features of healthy tendons and the tendinopathic set. This suggests a more refined decision tree may improve

the classification accuracy, such as if we had used K-fold cross-validation[10] in training the model and allowed for a higher number of splits within the tree. The focus of this work was in providing a novel segmentation approach, and use the classification step to simply validate the segmentation approach. For this reason, and due to the computational runtime associated with generating the initial clustering of GLCM features, we did not further optimise our approach to achieve the highest classification accuracy.

Future clinical work should seek to elucidate whether the output from this algorithm correlates with factors such as pain severity or response to rehabilitation. In order to do so, a range of quantitative metrics may be produced in addition the the texture class segmentation proportions. Within class variance for the GLCM features may be used to determine the heterogeneity within regions of the tendon. It may also be of interest to measure the variance in the GLCM features for each pixel across the entire tendon, to get a picture of the heterogeneity. The Shannon entropy, which would require assigning the GLCM feature values to N bins ($N >> K$ for K texture classes), is another metric for determining heterogeneity which has been used machine learning analysis of bone images (Ryou et al. 2022). A continuous analogue of the Shannon's entropy also exists (Jaynes 1957).

The GLCM-based HMRF-EM segmentation algorithm presented here has several advantages over Ultrasound Tissue Characterisation (UTC) (Schie et al. 2003). In contrast to UTC, which captures the continuity of fibres in the longitudinal direction, the GLCM-based HMRF-EM segmentation algorithm also captures information about the relationship of collagen fibres in the transverse direction. Our approach can also be used on the output of standard B-mode US devices, whilst UTC requires expensive specialised equipment. Furthermore, the HMRF-EM segmentation algorithm requires only one masked longitudinal

[10]The dataset if split into 'K' groups, with one used as the test set and the others used as the training set. The model is trained and tested, with the process repeated using each of the unique groups as the test set.

image, in contrast to UTC which requires a hundredfold greater number of masked transverse images to span the length of the tendon. This can also be considered as a limitation of our approach, as UTC may provide a more comprehensive coverage of tendon changes.

4.9 Conclusions and Limitations

In this chapter we have developed a segmentation approach which has shown to correlate well with the classification of tendons as healthy or tendinopathic. We utilised a Hidden Gaussian Markov Random Field model to segment each image based on a set of local grey-level co-occurrence features. The model was fit using a modified version of the HMRF-EM algorithm developed by Zhang et al. (2000). We also trialled the use of texton histograms as the texture features for the model, but this performed sub-optimally compared to the use of GLCM features. The segmentation output from this approach provides a tool which can be used as an adjunct to the radiologist. It provides both quantifiable and interpretable information regarding the texture profiles within the image, as well as a segmentation of the image which the radiologist can use to ensure they have detected all segments of interest. In good agreement with the literature (Cook et al. 2016, Fredberg et al. 2002, Cook et al. 2000), our segmentation results and analysis of texture features suggest that tendinopathic changes occur as a continuum and early structural changes may precede pain. The results also gave insight into the topology of changes which occur in tendinopathy, demonstrating that more severe tendinopathic changes are most likely to occur nearest to the transverse tendon boundary.

A key weakness of this study in the limited size of the dataset and the lack of additional clinical features to correlate with the segmentation results, such as pain levels. This would allow for more accurate hyperparameter tuning and allow us to confirm whether the texture profiles exhibited correlate with disease severity, as well as disease state. With an increase in dataset size modifications to the initial K-Means clustering may be required. The use

of scalable K-Means alternatives should be considered. The reduction in computational runtime associated with alternative initial clustering methods may also facilitate the use of K-fold cross-validation. We also note that the hyperparameters were tuned according to the resolution of the dataset available. The resolution between images in our dataset was similar and hence the same hyperparameters values were used throughout. To ensure generalisability, future work should consider identifying a resolution dependent scaling for the hyperparameters which would be affected by resolution, such as GLCM window size. Despite the above limitations, the results from this study are promising and support the collection of a larger prognostic dataset. The segmentation approach we have developed here has the potential to provide a readily accessible tool for the quantitative analysis of tendon images in both the research and clinical setting.

4.A Key Mathematical Concepts

4.A.1 Fundamental Statistical Principles

Throughout this chapter we rely on several fundamental statistical principles for calculations. In the case of two discrete multivariate random variables, $\boldsymbol{X}$ and $\boldsymbol{Y}$, Bayes' rule states that the *posterior probability*, or equivalently the *conditional probability*[11], of $\boldsymbol{X} = \boldsymbol{x}$ is given by

$$p(\boldsymbol{x}|\boldsymbol{y}) = \frac{p(\boldsymbol{x}, \boldsymbol{y})}{p(\boldsymbol{y})} = \frac{p(\boldsymbol{y}|\boldsymbol{x})p(\boldsymbol{x})}{p(\boldsymbol{y})}. \tag{4.26}$$

The same rule applies for continuous random variables, except in (4.26) the probability mass functions are replaced by density functions.

Secondly, given a set of N independent random variables $\boldsymbol{X} = (X_1, ..., X_N)$, the total

[11]We usually use the term *posterior probability* in the context of Bayes' rule - as we consider $\boldsymbol{y}$ as relevant evidence. The term *posterior* pertains to taking into account this relevant evidence.

probability of $\boldsymbol{X} = \boldsymbol{x}$ is given by

$$p(\boldsymbol{x}) = \prod_{i=1}^{N} p(x_i). \tag{4.27}$$

In the case of dependent variables, the marginal probability distribution of X_i is given by

$$p(x_i) = \sum_{\boldsymbol{x}_{-\{i\}}} p(x_i, \boldsymbol{x}_{-\{i\}}), \tag{4.28}$$

where $\boldsymbol{x}_{-\{i\}} = (x_1, ..., x_{i-1}, x_{i+1}, ..., x_N)$ is a realisation of the random vector $\boldsymbol{X}$ excluding the realisation x_i. The summation over $\boldsymbol{x}_{-\{i\}}$ denotes all possible realisations of $\boldsymbol{x}_{-\{i\}}$.

4.A.2 Convolution Filters

Convolution filters, also known as kernals, are small matrices used to derive information from or transform an image. At each pixel in an image we assign some linear weighted combination of its neighbouring pixel intensities, which we achieve through discrete convolution of the image with a filter. Mathematically, given an $m \times n$ image I, with pixel intensities $I(x, y)$, $x = 1, .., m$ and $y = 1, .., n$, and filter g, the discrete convolution of I with g is given by

$$h(x, y) = I(x, y) * g(x, y) = \sum_{i=0}^{w-1} \sum_{j=0}^{h-1} I(i, j) g(x - i, y - j), \tag{4.29}$$

where w and h are the filter width and height respectively. This equates to flipping the filter in both the horizontal and vertical access, then sliding it across the image: we multiply the overlapping filter and image elements, sum these, and assign the value to the central pixel. For example, consider the convolution of an image with the 2-D Gaussian which is of the form:

$$G(x, y) = \frac{1}{2\pi\sigma^2} \exp - \frac{x^2 + y^2}{2\sigma^2}. \tag{4.30}$$

We approximate (4.30) by an integer valued convolution kernel. The function (4.30) is technically non-zero everywhere, however we approximate it to be zero for points lying greater than three standard deviations from the mean. Hence, the corresponding discrete kernel can be truncated at this point (Figure 4.15). As a result, the kernel size and subsequent degree of blurring generated by the gaussian filter are governed by the choice of σ.

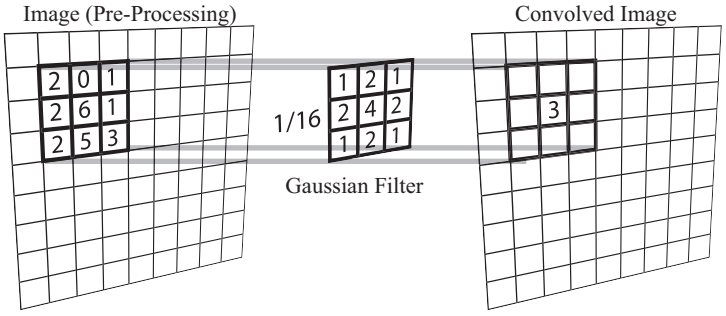


Figure 4.15: Convolution of an image with a 3-by-3 Gaussian filter. The value at the pixel given in the convolved image is calculated by $(1/16)\cdot(1\cdot 2+2\cdot 0+1\cdot 1+2\cdot 2+4\cdot 6+2\cdot 1+1\cdot 2+2\cdot 5+1\cdot 3)$.

[scale=0.35, trim=0cm 7cm 2cm 3cm]

Image filtering has multiple applications in image processing. Often we pre-process an image by applying a blurring filter such as the Gaussian filter, which is especially useful in medical imaging to reduce noise. Filters are also use to extract information, such as where values in the imaging are rapidly changing (e.g. to extract edges in an image).

4.A.3 K-Means Clustering

K-Means is a simple clustering algorithm that has enjoyed widespread use among the mathematical community. Given a prescribed number of K clusters, and a set of n observations of some dimension p, it gives us a means of grouping these observations based on a Euclidean similarity measure. Let $\boldsymbol{C} = \{C_1, C_2, ..., C_K\}$ denote the individual clusters containing some proportion of the total n observation such that the union of the clusters contains all observations and the intersection of any two clusters is empty. The k-means algorithm seeks to

minimise the within-cluster variance

$$\underset{\boldsymbol{C}}{\operatorname{argmin}} \sum_{i=1}^{K} \sum_{\boldsymbol{x} \in C_i} \|\boldsymbol{x} - \boldsymbol{\mu}_i\|^2. \tag{4.31}$$

Here $\boldsymbol{\mu}_i$ is the mean of group i and is given by

$$\boldsymbol{\mu}_i = \frac{1}{|C_i|} \sum_{j \in C_i} x_j \tag{4.32}$$

Considering the objective function (4.31), it is evident that K-Means incorporates two assumptions about the variance: the variance of each attribute is assumed spherical, and a constant variance is assumed across all variables. This objective function (4.31) is minimised through the following procedure:

K-Means Algorithm:

1. Initialisation: Randomly assign each observation to one of the clusters $C_1, C_2, ..., C_k$.
2. Iterate the following steps until the cluster assignments stop updating
   (a) For each cluster i compute the cluster mean μ_i.
   (b) Re-assign all observations to the cluster with the closest mean, as calculated by the Euclidean distance.

The k-means algorithm achieves a local but not global solution to this objective function and hence is sensitive to the initial random cluster assignment. This is especially the case when the prior probability of each cluster is not the same, as is usually assumed in the initialisation step of K-Means. As such, it is worthwhile running several repetitions of the procedure (which can be specified as an input to the MATLAB function), with the clustering which gives the lowest measure of the object function then selected. Due to the iterative nature of the algorithm, K-Means is computationally expensive for large data sets which is

problematic when several repetitions of the procedure are desired.

K-means clustering can be considered as a special case of a clustering with a Gaussian mixture model (Section 4.3.2) in which we assume that all variances are equal, covariances are zero, and mixture weights are equal (the probability of a cluster assignment is $1/k$). The Expectation-Maximisation algorithm, a means of determining the GMM (4.3.3), reduces to the K-Means algorithm in the case of $\mathbf{\Sigma}_K = \sigma^2 \boldsymbol{I}$ and $\sigma \to 0$. As a result, the underlying cluster shapes are limited be spherical and hard assignments are produced, making k-means a more restrictive form of clustering in this sense.

4.A.4 Stochastic Modelling of Image Textures

4.A.4.1 Graphs

Denoted by $\mathcal{G} = (\mathcal{V}, \mathcal{E})$, a graph is a mathematical structure consisting of vertices (or nodes) $\mathcal{V}$ and edges $\mathcal{E}$. Graphs represent a useful way of analysing complex structures formed by a collection of interrelated variables. An edge connecting two vertices represents some relationship between these vertices. Edges can be directed or undirected, depending on whether this is a reciprocal relationship or not. A directed graph contains directed edges. Probabilistic graphical models combine probability and graph theory. In this case, each vertex $i \in \mathcal{V}$ is associated with a random variable X_i. Edges between two connected vertices i and j then represent conditional probabilites $p(x_i|x_j)$ and $p(x_j|x_i)$ in the case of an undirected graph. Hence, the realisation of the entire graph $\boldsymbol{X} = (X)_{i\in\mathcal{V}} \in \mathcal{X}_i$, is given by $\boldsymbol{x} = (x)_{i\in\mathcal{V}}$. A clique, $i \in \mathcal{C}$, is a subset of vertices in an undirected graph such that every set of two vertices in the clique are connected by an edge. A clique can be considered as a complete subgraph in the graph. Realisations of a clique are denoted by $\boldsymbol{x}_c = (x)_{i\in\mathcal{C}}$.

4.A.4.2 Markov Random Fields

Markov random fields (MRFs) can be modeled as an undirected graph in which each vertex represents a random variable. Conditional probabilities between random variables, termed transitional probabilities in the case of MRFs, are represented by the adjoining edges. A visual example of this field, which can be used to represent a rectangular image, is given in Figure 4.16. Consistent with the name, Markov Random Fields exhibit the memoryless

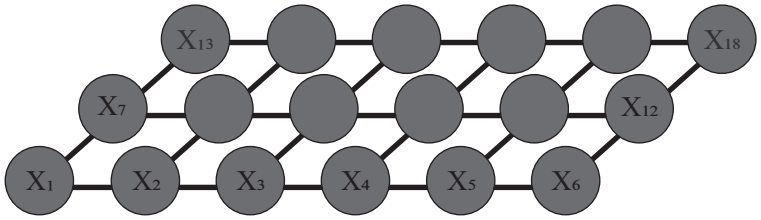


Figure 4.16: Markov random field representation of an image. Each pixel is donated by a vertex X_i. In this case the maximal clique size is two, and as such each pixel, or vertex, is a member of four different cliques (excluding edge pixels).

property of a stochastic process, termed the 'Markov property'. That is, the probability of any random variable, conditioned on its neighbours, is independent of the remaining graph. Mathematically this equates to

$$P(X_i|\boldsymbol{X}_{-\{i\}}) = P(X_i|\boldsymbol{X}_{\mathcal{N}(i)}) \tag{4.33}$$

where $\boldsymbol{X}_{-\{i\}}$ denotes a realisation of the entire graph, excluding the location i, whilst $\boldsymbol{X}_{\mathcal{N}(i)}$ denotes a realisation of the random variables in the neighbourhood surrounding i. Since we model images as an entirely connected graph, this allows for the stochastic propagation of local interactions throughout the entire graph. The stochastic MRF model is consistent with the fact that textures represent repetitions of local structures in a stochastic manner.

Because of the conditional independence present in a MRF, the probability density function for the state of the field can be factorised across each clique such that the joint probability

of the hidden state takes the form

$$p(\boldsymbol{x}) = \frac{\exp\left(-U(\boldsymbol{x}, \beta)\right)}{Z(\beta)} \tag{4.34}$$

where $U(\boldsymbol{x}, \beta)$ is the energy potential given by

$$U(\boldsymbol{x}, \beta) = \sum_{c \in C} V_c(\boldsymbol{x}_c, \beta). \tag{4.35}$$

Here V_c is termed the clique potential and Z is a normalising constant. This type of distribution is called a Gibbs distribution, and its equivalence to MRFs is well extablished by the Hammersley-Clifford theorem which states that the density of such a graph can be factorised over the cliques (or complete subgraphs) of the graph. The clique potential functions are functions that give a probabilistic score to the joint distribution of variables within the clique, representing a level of compatibility. They need not be true probabilities and can be somewhat arbitrary, dependent on the application, however they must be non-negative. This is easier to understand if we consider the example of a clique potential that we shall use throughout our work here:

$$\sum_{c \in C} V_c(\boldsymbol{x}_c, \beta) = \sum_{j \in \mathcal{N}(i)} \beta \delta(x_i - x_j), \tag{4.36}$$

in which it is clear to see that the clique potential is higher when there is more heterogeneity in the values assigned to $x_i \in \mathcal{C}$. In this case, the probability of a realisation of the field, as given in (4.34), increases if neighbouring vertices (or pixel labels in the case of images) take the same value.

4.B Additional Results

Segmentation results for the entire training set using GLCM-based and texton-based K-Means clustering are given in Figures 4.17 and 4.18 respectively. In Figure 4.17, the first texture class

is coloured in yellow, the second in orange and the third in red. The first class corresponds to high contrast and low GLCM energy values, the second class corresponds to moderate values for both variables, and the third class corresponds to low contrast and high energy values. There is clearly a larger proportion of tendinopathic tendons which show moderate and low contrast, and moderate and high energy, values. In Figure 4.18 the first texture class is coloured green, the second class purple and the third class blue. The distinction between segmentations for tendinopathic and healthy tendons is less clear. A larger proportion of the second class is present in tendinopathic tendons but this is variable. The third class is assigned in similar portions for tendinopathic and healthy tendons, predominantly near the transverse boundary.

Segmentation results for the training and test sets using GLCM-based HMRF-EM algorithm are given in Figures 4.19 and 4.20 respectively. Using the same colour scheme as for Figure 4.17 detailed above, for both sets of images, a larger proportion of the second and third textures are found in tendinopathic tendons. Contrasting these results to the segmentations generated from only K-Means, provided in Figure 4.17, the segmentations are visibly more distinct.

To test robustness of the GLCM-based HMRF-EM algorithm to noise, in Figure 4.21 we have repeated the segmentation of the training set after speckle noise has been applied. Speckle noise was applied through the *MATLAB* function imnoise, where the default degree of noise (mean=0, variance 0.04) was used. The algorithm was robust to this small degree of additional noise, with only small differences in the segmentations evident in Figure 4.21. As the variance parameter increased, the segmentations further diverged from the original segmentations produced in Figure 4.19, suggesting that caution may need to be taken when images have an abnormally large amount of noise present.

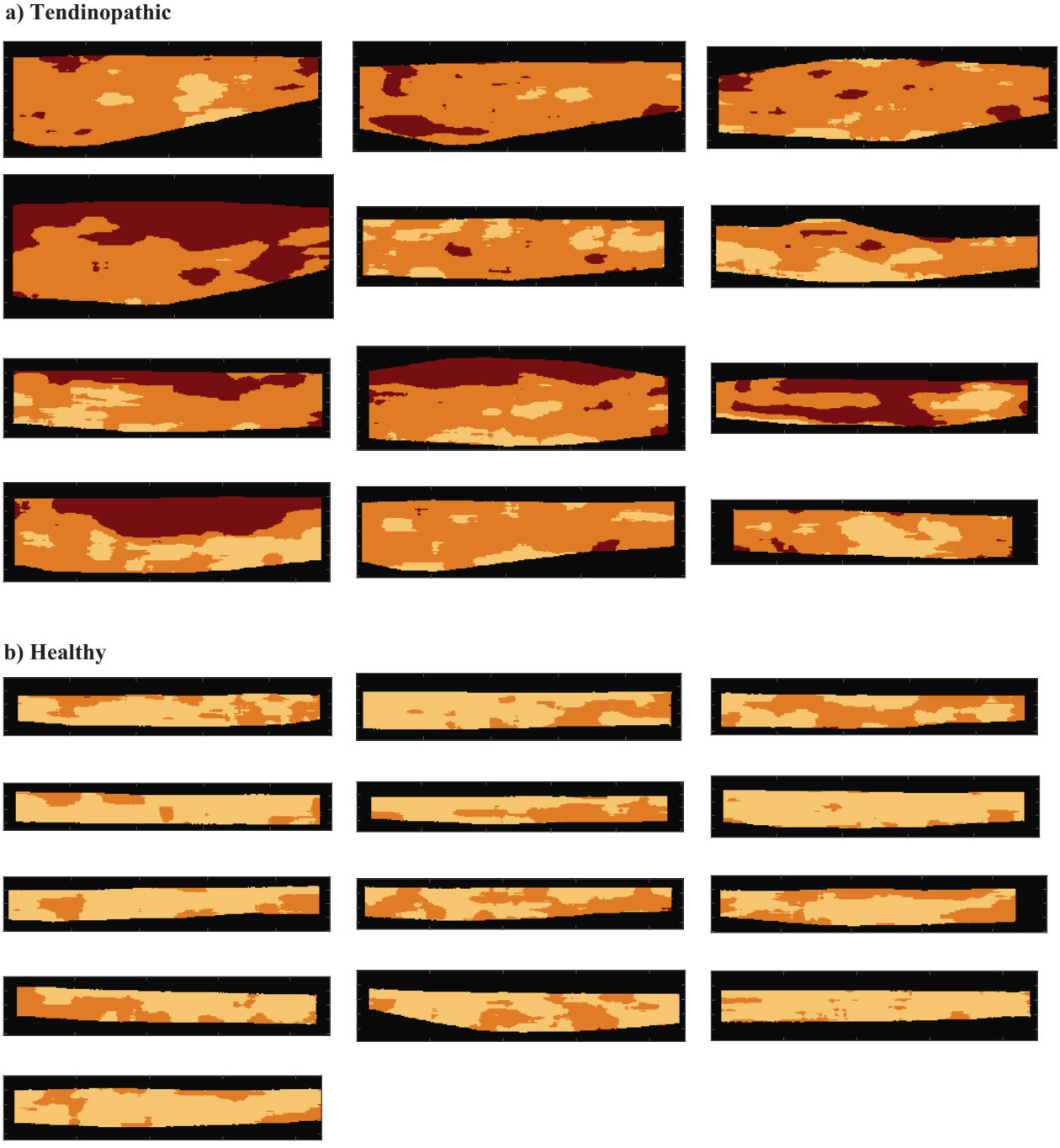


Figure 4.17: GLCM-based K-Means segmentation results for the training set. Regions labelled as texture class one are coloured yellow and constitute areas with high contrast and low energy. Areas assigned to texture class two are coloured in orange and refer to areas with moderate contrast and energy. Areas coloured in red have been assigned to texture class three and constitute areas with low contrast and high energy.

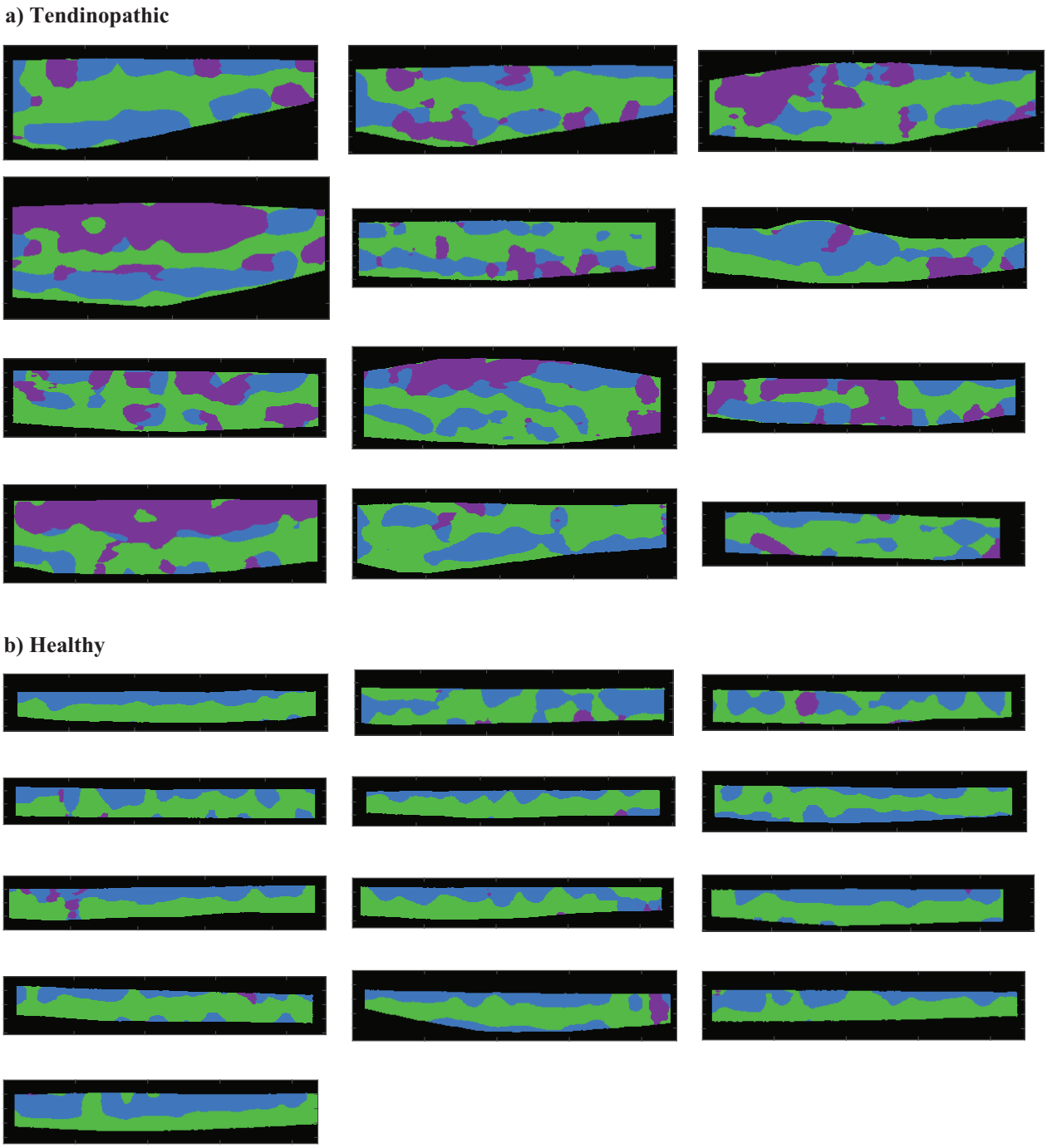


Figure 4.18: Texton-based K-Means segmentation results for the training set. Regions labelled as texture class one are coloured green, two are coloured purple, and three are coloured blue.

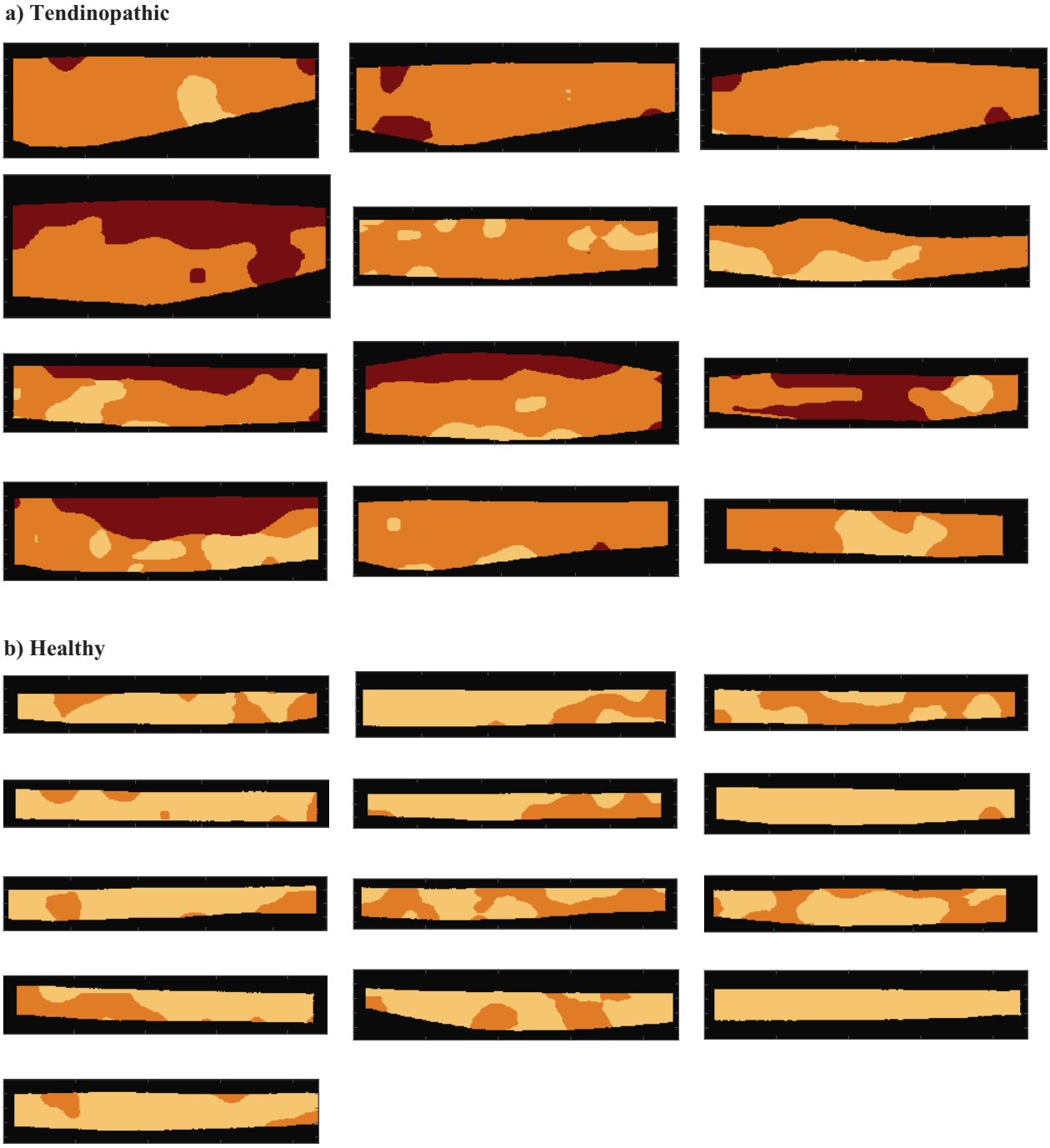


Figure 4.19: GLCM-based HMRF-EM segmentation results for the training set. Regions labelled as texture class one are coloured yellow and constitute areas with high contrast and low energy. Areas assigned to texture class two are coloured in orange and refer to areas with moderate contrast and energy. Areas coloured in red have been assigned to texture class three and constitute areas with low contrast and high energy.

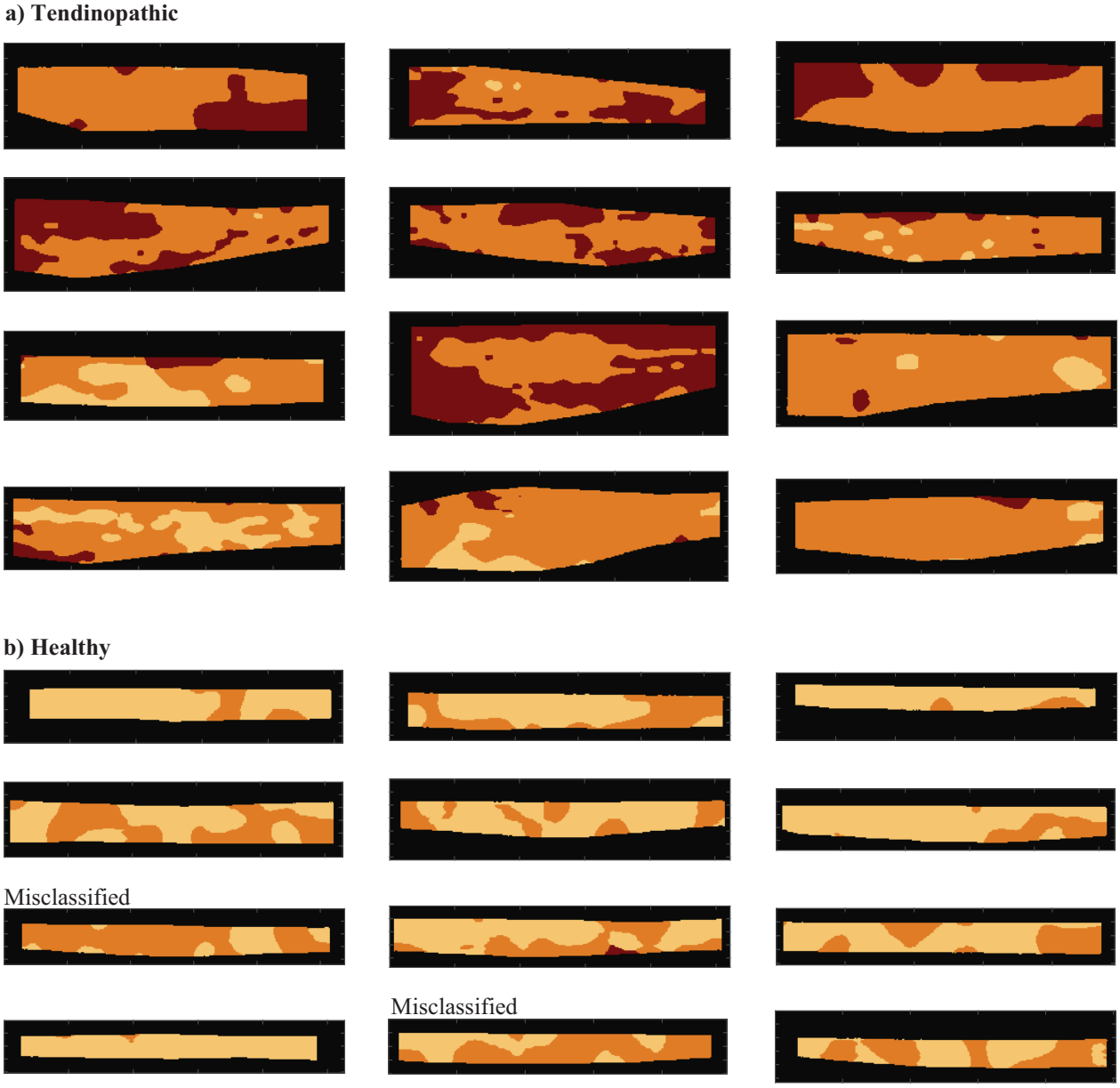


Figure 4.20: GLCM-based HMRF-EM segmentation results for the test set. Regions labelled as texture class one are coloured yellow and constitute areas with high contrast and low energy. Areas assigned to texture class two are coloured in orange and refer to areas with moderate contrast and energy. Areas coloured in red have been assigned to texture class three and constitute areas with low contrast and high energy. The two healthy tendons which were misclassified during testing are labelled.

a) Tendinopathic



b) Tendinopathic with speckle noise applied.



c) Healthy



d) Healthy with speckle noise applied.



Figure 4.21: GLCM-based HMRF-EM segmentation results for half of training set, with and without speckle noise applied. Regions labelled as texture class one are coloured yellow and constitute areas with high contrast and low energy. Areas assigned to texture class two are coloured in orange and refer to areas with moderate contrast and energy. Areas coloured in red have been assigned to texture class three and constitute areas with low contrast and high energy.

CHAPTER 5

Summary and Future Work

5.1 Summary of Thesis

This thesis has focussed on understanding the mechanical environment that occurs within tendons subject to different forms of loading, and how this may contribute to changes in tendon structure in response to long-term loading. We began by introducing the reader to the background anatomy, physiology and pathology pertaining to tendon. We detailed experimental evidence that tendinopathy occurs as a cartilagenous maladaptive response to high-frequency loading, in which there is a loss of collagen and increase in proteoglycans, motivating the approach taken in this thesis. We provided the reader with a brief background into poroelastic theory and summarised the current state of the art mathematical models for tendon. We also outlined the limitations of current imaging methods in detecting the local structural changes that occur in tendinopathy, incentivising further research in machine learning approaches for detecting structural changes in tendon images.

In Chapter 2 we developed a linear poroelastic small strain model for tendons subject to load. We investigated the local mechanical environment that occurs with different frequencies of physiological loading. We also investigated how local reductions in the stiffness or permeability, as have been posited to occur with collagen disruption and proteoglycan accumulation, affect the local mechanical environment when the tendon is subject to load.

We demonstrated that high fluid fluxes occur with high-frequency loading. We also demonstrated that axial strain remained comparable across the loading frequencies investigated, though we acknowledge further research into the parameter values for tendon permeability and Poisson's ratio are needed to support this result. Since the axial strain was high for both low- and high-frequency loading whilst the fluid flux increased with loading frequency, we inferred that fluid shear is the most likely cause of a maladaptive cellular response to high-frequency loading and that the axial strain may provide an adaptive response. A reduction in permeability was found to decrease the flux but had minimal effect on the transverse or axial strains. This suggests that proteoglycan deposition is most likely a response to high fluid shear with high-frequency loading, serving to reduce the permeability and hence fluid shear stimulus. However, further analysis demonstrated that the loading frequency has a much more substantial effect on the flux than the permeability, and hence reductions in permeability may be limited in their ability to prevent high flux occurring in the setting of very high-frequency loading.

Building on the results from Chapter 2, in Chapter 3 we coupled the poroelastic model with a set of time dependent phenomenological rules that prescribed material property changes in response to loading. We simulated several weeks of loading and contrasted the predicted macroscopic stiffness changes with those observed clinically. Using a model which assumed that high fluid fluxes caused proteoglycan deposition and collagen degradation, whilst axial strain promoted collagen synthesis, we were able to accurately predict global reductions in stiffness consistent with clinically observed values. We simulated a range of different loading regimes and predicted associated material property changes, demonstrating how the model could potentially be used to identify optimal rehabilitative loading regimes based on current tendon structure and patient characteristics, such as how much exercise they need to continue to engage in. We highlighted several issues with the model, including predicting non-physical stiffness values and suggesting further amendments that could be made to the model in future work.

In Chapter 4, we developed an automated segmentation approach for ultrasound images of the tendon based on texture. We were motivated by the absence of reliable imaging tools to quantify, and understand the topology of, structural changes which occur in tendinopathy. Not only does the work in this chapter complement the preceding work, but it also serves to provide a novel quantitative imaging approach in tendon that has clinical viability in its own regard. We implement a hidden Gaussian Markov random field modelling approach to segment each image, based on local texture features generated from the grey-level co-occurrence matrix. Segmentation labels correlating with tendinopathic tendons were deemed as tendinopathic areas. Analysing the segmentation results across the tendinopathic tendons, there was a clear trend that tendinopathic regions most commonly occurred closer to the transverse boundaries. This supported by our findings in Chapter 2 and 3, which suggested damage is more likely to occur near the transverse tendon boundary where higher local fluid fluxes/shear occurs with high-frequency loading.

5.2 Future Work

The approach taken here provides a fundamental backbone for future mechanical and adaptation or damage models to build on. There are several extensions to the mechanical modelling and image analysis work here that would provide a model which is more representative of true tendon structure. As well as future modelling work, the challenges identified within, and results from, this thesis motivate several areas of future experimental and clinical research.

5.2.1 Parameter Accuracy and Sensitivity for Mechanical Modelling of Tendon

In Chapter 2 we derived a linear poroelastic model for tendon that utilised the Young's modulus, Poisson's ratio and permeability as input parameters to the model. A major source of uncertainty for this poroelastic model was the wide range of experimentally reported parameters values for the Poisson's ratio and permeability, as well as the lack of knowledge

surrounding whether any anisotropy exists. In Chapter 2 we investigated the sensitivity of our model to these parameters and demonstrated that the axial strain and flux profiles, resulting from a given applied load, differed between subsets of parameter values reported. These results motivate the need for further experimental work to determine more refined parameters ranges for tendon and whether any anisotropy exists, for example in the permeability. This is essential if we are to draw strong conclusions from mathematical modelling of the tendon. Such future experimental work would be complemented by further parameter sensitivity analyses. A range of approaches and computational packages are available for sensitivity analysis depending on factors such as the computational expense of running the simulation, whether parameters could be correlated, and output metrics of interest. A simple *one-at-a-time* approach was used here but more advanced methods are available, such as those in which parameter values are sampled randomly. Further insight into accurate parameter ranges and the sensitivity of the mechanical model to these parameters would contribute to our understanding of how material properties of the tendon influence the mechanical environment of tendon subject to load.

5.2.2 Three-Dimensional Heterogeneous Anisotropic Model for Tendon

One- and two-dimensional models were used for the tendon in this work. Given the inhomogeneity in material properties incorporated, this provides a useful starting point to explore the effect of loading frequency and material property changes on the local mechanical environment within tendon subject to load. However, tendons are three-dimensional structures in which the thickness and width can vary along the length of the tendon (Firminger et al. 2021). Whilst several previous authors have used an axisymmetric model for the tendon (Lavagnino et al. 2008, Butler et al. 1997), recent work has also suggested that the material properties taken across the width may vary to those taken across the thickness of the tendon (Hannafin et al. 1994). Aside from exploring the effects of an anisotropic permeability, we

have assumed that the tendon is an isotropic structure. This is a simplifying assumption that is likely false for tendon since tendons contain longitudinally oriented collagen fibres (Screen 2009).

Future work should incorporate both changes in the material properties and transverse geometry along the length of the tendon. We expect that modifying the width and thickness of the tendon along its length will result in a more variable axial strain profile along the length of the tendon than was observed in Chapter 2. Since the tendon is thinnest along the midportion, we would expect the axial strains to be highest here. This would then feed into differences in the stiffness and permeability changes observed in Chapter 3. The proportions of different tendon constituents such as proteoglycans can vary along the length of the healthy tendon (Cook et al. 2012). Whilst we have included heterogeneity in the material properties to mimic damage, there is also likely to be heterogeneity in the baseline material properties for a healthy tendon. Varying the Young's modulus along the length of tendon would also contribute to variability in the axial strain profile along the length of the tendon.

5.2.3 Investigating the Osmotic Effect of Proteoglycans

In this work we assumed that proteoglycans predominately affect the local mechanical environment by reducing permeability. This assumption has been made by previous authors (Cook et al. 2012) and is supported by experimental evidence showing a reduction in the permeability of cartilage with increasing proteoglycan content (Tavakoli Nia et al. 2015). However, since proteoglycans are negatively charged molecules, they can also attract water molecules and contribute to osmotic swelling of the tendon (Han et al. 2011). For simplicity, due to a lack of fundamental poroelastic models of tendon, and due to an absence of knowledge surrounding the role of proteoglycans on the Young's or aggregate modulus, we did not incorporate this effect in our model. However, since fluid accumulation is known to occur with tendinopathy, this is a key aspect that should be incorporated in future modelling work.

5.2.4 Constitutive Relationships for the Mechanical and Adaptation Models of Tendon

The mechanical model of tendon presented in Chapter 2 and the adaptation model presented in Chapter 3 relied on a series of constitutive equations which related the stress and strain during loading, and changes in material properties in response to the mechanical environment between loading bouts. Future work should consider alternative constitutive equations and seek to elucidate the effect of the constitutive relationships on the mechanical environment occurring with, and on the material property changes occurring due to, loading.

Hooke's law was used to model the relationship between the stress and strain within the solid skeleton of the tendon in Chapter 2. We utilised this linear law as the tendon stress-strain curve is approximately linear (Section 1.4 Figure 1.6) and evidence suggests viscoelastic effects are unimportant with the frequencies of interest investigate in this work (Section 1.4). However, modification of Equation (2.23) to include a strain rate dependent term would allow for the incorporation of viscoelastic effects in future work.

Evidence has suggested that collagen and proteoglycan synthesis and degradation by tendon, or other musculoskeletal, cells in response to a loading bout are time-dependent (Magnusson et al. 2010). In Chapter 3 we prescribed the time-dependency of stiffness changes based on a previous study looking at collagen synthesis in response to a bout of running (Langberg et al. 1999b), and the time-dependency of permeability changes were based on experimental work investigating proteoglycan production after mechanical stimulation of cartilage (Schätti et al. 2013, De Croos et al. 2006). Further clinical and experimental work is needed to determine how the loading frequency, or the magnitude of the local stimulus causing these cellular responses, affects the time-dependency of the type I collagen/stiffness and proteoglycan/permeability changes in tendon. In Chapter 3 we also only modelled collagen and proteoglycan changes indirectly, using changes in the stiffness and permeability as

surrogates. Further experimental work quantifying changes in these constituents and their relationship to material properties would allow us to build on the work in Chapter 3 and incorporate changes in these constituents directly.

5.2.5 Correlating Image Segmentation Results with Severity and Local Material Property Measurements

The imaging segmentation algorithm developed in Chapter 4 was aimed at providing a tool for quantifying disease severity based on changes in texture on ultrasound. However, the dataset used to validate our algorithm consisted of images labelled as tendinopathic or healthy, but no other clinical information was available. As such, the algorithm was only validated by assessing its use in classification. A one-level decision tree, utilising the texture class proportions for each image, was implemented to classify the images. Of the 49 images, 47 (23 of 25 for the test set) were successfully classified using a simple texture class proportion cut-off for each image. These results incentivise future clinical work which captures additional clinical features, such as pain, and can be used to further validate whether the segmentation approach used here correlates with disease severity as well as the presence of disease. In this case, the framework presented in Chapter 4 would remain the same but the decision tree should be modified to predict pain levels rather than binary label of tendinopathic/healthy. The hyperparameters of the algorithm should then be tuned to optimise the pain status classification (Section 4.6.1).

To see how a tendon's material properties may evolve with a series of loading bouts, the adaptation model presented in Chapter 3 requires a two-dimensional map of the current material properties (stiffness and permeability) of the tendon as an initial input. Whilst the machine learning imaging algorithm in Chapter 4 provides a two-dimensional map of tendon damage, it is unclear how local regions of damage predicted by the model correlate with local material property values. Shear-wave elastography has been used to measure the

local stiffness and Young's modulus of tendon (Ooi et al. 2014). Future clinical work should investigate the correlation between output from shear-wave elastrography and the machine learning tool presented in Chapter 4. While shear-wave elastography results could also be used as direct input for the adaptation model, shear-wave elastography is operator dependent and requires specialised ultrasound equipment.

5.3 Concluding Remarks

This thesis builds on the ability of mathematical modelling and machine learning approaches to image analysis to advance our understanding of loading related musculoskeletal injuries. We have provided a framework which integrates experimental and clinical findings and is applicable not only to tendinopathy, but to other loading related musculoskeletal diseases, such as osteoarthritis. Whilst future work is required to build a model that is better representative of the complex tendon geometry, we have provided the mathematical foundations to investigate why different forms of loading have a differential effect on tendon. We have shown how image analysis methods can be used to provide additional insight into the spatial pattern of changes that occur with tendinopathy, and can be paired with a mechanical model to provide mechanistic insight into why damage occurs over certain regions.

Bibliography

Abate, M., V. Salini, and C. Schiavone. 2016. "Achilles tendinopathy in elderly subjects with type II diabetes: the role of sport activities". *Aging clinical and experimental research* 28 (2): 355–358.

Acharya, U., K. Meiburger, J.E.W. Koh, E. Ciaccio, N. Arunkumar, M.H. See, N.A.M. Taib, A. Vijayananthan, K. Rahmat, F. Fadzli, and S.S. Leong. 2019. "A novel algorithm for breast lesion detection using textons and local configuration pattern features with ultrasound imagery". *IEEE Access* 7:22829–22842.

Ahmadzadeh, H., B. Connizzo, B. Freedman, L. Soslowsky, and V. Shenoy. 2013. "Determining the contribution of glycosaminoglycans to tendon mechanical properties with a modified shear-lag model". *Journal of biomechanics* 46 (14): 2497–2503.

AlZubi, S., N. Islam, and M. Abbod. 2011. "Multiresolution analysis using wavelet, ridgelet, and curvelet transforms for medical image segmentation". *International journal of biomedical imaging* 2011.

Alzyadat, T., S. Praet, G. Chetty, R. Goecke, D. Hughes, D. Kumar, M. Welvaert, N. Vlahovich, and G. Waddington. 2020. "Automatic Segmentation of Achilles Tendon Tissues Using Deep Convolutional Neural Network". In *International Workshop on Machine Learning in Medical Imaging*, 444–454. Springer.

Ambartsumyan, I., E. Khattatov, T. Nguyen, and I. Yotov. 2019. "Flow and transport in fractured poroelastic media". *GEM-International Journal on Geomathematics* 10 (1): 11.

Arampatzis, A., K. Karamanidis, and K. Albracht. 2007. "Adaptational responses of the human Achilles tendon by modulation of the applied cyclic strain magnitude". *Journal of experimental biology* 210 (15): 2743–2753.

Arampatzis, A., A. Peper, S. Bierbaum, and K. Albracht. 2010. "Plasticity of human Achilles tendon mechanical and morphological properties in response to cyclic strain". *Journal of biomechanics* 43 (16): 3073–3079.

Archambault, J., M. Elfervig-Wall, M. Tsuzaki, W. Herzog, and A. Banes. 2002. "Rabbit tendon cells produce MMP-3 in response to fluid flow without significant calcium transients". *Journal of biomechanics* 35 (3): 303–309.

Ark, M. van, E. Rio, J. Cook, I. van den Akker-Scheek, J. Gaida, J. Zwerver, and S. Docking. 2018. "Clinical improvements are not explained by changes in tendon structure on UTC following an exercise program for patellar tendinopathy". *American Journal of Physical Medicine* 97 (10): 708–714.

Armstrong, C., W. Lai, and V. Mow. 1984. "An analysis of the unconfined compression of articular cartilage". *Journal of biomechanical engineering* 106 (2): 165–173.

Arnoczky, S., M. Lavagnino, and M. Egerbacher. 2007. "The mechanobiological aetiopathogenesis of tendinopathy: is it the over-stimulation or the under-stimulation of tendon cells?" *International journal of experimental pathology* 88 (4): 217–226.

Arnoczky, S., M. Lavagnino, J. Whallon, and A. Hoonjan. 2002. "In situ cell nucleus deformation in tendons under tensile load; a morphological analysis using confocal laser microscopy". *Journal of orthopaedic research* 20 (1): 29–35.

Arya, S., and K. Kulig. 2010. "Tendinopathy alters mechanical and material properties of the Achilles tendon". *Journal of applied physiology* 108 (3): 670–675.

Ateshian, G., and J. Humphrey. 2012. "Continuum mixture models of biological growth and remodeling: past successes and future opportunities". *Annual review of biomedical engineering* 14:97–111.

Atkinson, T, R Haut, and N Altiero. 1997. "A poroelastic model that predicts some phenomenological responses of ligaments and tendons".

Azmi, R., and N. Norozi. 2011. "A new markov random field segmentation method for breast lesion segmentation in MR images". *Journal of medical signals and sensors* 1 (3): 156.

Bajuri, M., H. Isaksson, P. Eliasson, and M. Thompson. 2016. "A hyperelastic fibre-reinforced continuum model of healing tendons with distributed collagen fibre orientations". *Biomechanics and modeling in mechanobiology* 15 (6): 1457–1466.

Benjamin, M., E. Kaiser, and S. Milz. 2008. "Structure-function relationships in tendons: a review". *Journal of anatomy* 212 (3): 211–228.

Benrabha, J., and F. Meziane. 2017. "Automatic ROI detection and classification of the Achilles tendon ultrasound images". In *Proceedings of the 1st International Conference on Internet of Things and Machine Learning*, 1–7.

Besag, J. 1975. "Statistical analysis of non-lattice data". *Journal of the Royal Statistical Society: Series D (The Statistician)* 24 (3): 179–195.

Beyer, R., M. Kongsgaard, B. Hougs Kjær, T. Øhlenschlæger, M. Kjær, and S. Magnusson. 2015. "Heavy slow resistance versus eccentric training as treatment for Achilles tendinopathy: a randomized controlled trial". *The American journal of sports medicine* 43 (7): 1704–1711.

Bhosle, V., and V. Pawar. 2013. "Texture segmentation: different methods". *International Journal of Soft Computing and Engineering (IJSCE)* 3 (5): 69–74.

Biot, M. 1941. "General theory of three-dimensional consolidation". *Journal of applied physics* 12 (2): 155–164.

– . 1955. "Theory of elasticity and consolidation for a porous anisotropic solid". *Journal of applied physics* 26 (2): 182–185.

Bisseling, R., A. Hof, S. Bredeweg, J. Zwerver, and T. Mulder. 2008. "Are the take-off and landing phase dynamics of the volleyball spike jump related to patellar tendinopathy?" *British journal of sports medicine* 42 (6): 483–489.

Bohm, S., F. Mersmann, and A. Arampatzis. 2015. "Human tendon adaptation in response to mechanical loading: a systematic review and meta-analysis of exercise intervention studies on healthy adults". *Sports medicine-open* 1 (1): 1–18.

Bohm, S., F. Mersmann, M. Tettke, M. Kraft, and A. Arampatzis. 2014. "Human Achilles tendon plasticity in response to cyclic strain: effect of rate and duration". *Journal of Experimental Biology* 217 (22): 4010–4017.

Bontempi, M. 2009. "Probabilistic model of ligaments and tendons: quasistatic linear stretching". *Physical Review E* 79 (3): 030903(R).

Bowen, R. 1982. "Compressible porous media models by use of the theory of mixtures". *International Journal of Engineering Science* 20 (6): 697–735.

Brattain, L., B. Telfer, M. Dhyani, J. Grajo, and A. Samir. 2018. "Machine learning for medical ultrasound: status, methods, and future opportunities". *Abdominal radiology* 43 (4): 786–799.

Burgio, V., M. Civera, M. Rodriguez Reinoso, E. Pizzolante, S. Prezioso, A. Bertuglia, and C. Surace. 2022. "Mechanical Properties of Animal Tendons: A Review and Comparative Study for the Identification of the Most Suitable Human Tendon Surrogates". *Processes* 10 (3): 485.

Burova, I., I. Wall, and R. Shipley. 2019. "Mathematical and computational models for bone tissue engineering in bioreactor systems". *Journal of Tissue Engineering* 10:2041731419827922.

Burssens, A., R. Forsyth, W. Bongaerts, M. Jagodzinski, N. Mahieu, M. Praet, and J. Victor. 2013. "Arguments for an increasing differentiation towards fibrocartilaginous components in midportion Achilles tendinopathy". *Knee Surgery, Sports Traumatology, Arthroscopy* 21 (6): 1459–1467.

Buschmann, M., Y. -J. Kim, M. Wong, E. Frank, E. Hunziker, and A. Grodzinsky. 1999. "Stimulation of aggrecan synthesis in cartilage explants by cyclic Loading is localized to regions of high interstitial fluid flow". *Archives of biochemistry and biophysics* 366 (1): 1–7.

Butler, S., S. Kohles, R. Thielke, C. Chen, and R. Vanderby. 1997. "Interstitial fluid flow in tendons or ligaments: a porous medium finite element simulation". *Medical and Biological Engineering and Computing* 35 (6): 742–746.

Candes, E., L. Demanet, D. Donoho, and L. Ying. 2006. "Fast discrete curvelet transforms". *multiscale modeling & simulation* 5 (3): 861–899.

Cao, J., H. Gao, L. Dou, M. Zhang, and T. Li. 2019. "Modeling flow in anisotropic porous medium with full permeability tensor". In *Journal of Physics: Conference Series*, 012054. 1324. IOP Publishing.

Carcione, J. 2007. *Wave fields in real media: Wave propagation in anisotropic, anelastic, porous and electromagnetic media*. Chap. 2. Elsevier.

Carniel, T., A. Formenton, B. Klahr, J. Vassoler, C. de Mello Roesler, and E. Fancello. 2019. "An experimental and numerical study on the transverse deformations in tensile test of tendons". *Journal of biomechanics* 87:120–126.

Carter, D., and M. Wong. 2003. "Modelling cartilage mechanobiology". *Philosophical Transactions of the Royal Society of London. Series B: Biological Sciences* 358 (1437): 1461–1471.

Celeux, G., F. Forbes, and N. Peyrard. 2003. "EM procedures using mean field-like approximations for Markov model-based image segmentation". *Pattern recognition* 36 (1): 131–144.

Chan, V., and A. Perlas. 2011. *Basics of ultrasound imaging*, 13–19. Springer.

Chatterjee, M., P. Muljadi, and N. Andarawis-Puri. 2021. "The role of the tendon ECM in mechanotransduction: disruption and repair following overuse". *Connective Tissue Research* 63 (1): 28–42.

Chen, C.- T., D. Malkus, and R. Vanderby Jr. 1998. "A fiber matrix model for interstitial fluid flow and permeability in ligaments and tendons". *Biorheology* 35 (2): 103–118.

Chen, H. -C., C. -K. Chen, T. -H. Yang, L. -C. Kuo, I.M. Jou, F. -C. Su, and Y. -N. Sun. 2011. "Model-based segmentation of flexor tendons from magnetic resonance images of finger joints". In *2011 Annual International Conference of the IEEE Engineering in Medicine and Biology Society*, 8009–8012. IEEE.

Chuang, B. -I., Y. -N. Sun, T. -H. Yang, F. -C. Su, L. -C. Kuo, and I. -M. Jou. 2014. "Model-based tendon segmentation from ultrasound images". In *2014 40th Annual Northeast Bioengineering Conference (NEBEC)*, 1–2. IEEE.

Clifford, C., D. Challoumas, L. Paul, G. Syme, and N. Millar. 2020. "Effectiveness of isometric exercise in the management of tendinopathy: a systematic review and meta-analysis of randomised trials". *BMJ open sport & exercise medicine* 6 (1): e000760.

Collinger, J., B. Fullerton, B. Impink, A. Koontz, and M. Boninger. 2010. "Validation of greyscale-based quantitative ultrasound in manual wheelchair users: relationship to established clinical measures of shoulder pathology". *American journal of physical medicine & rehabilitation/Association of Academic Physiatrists* 89 (5): 390.

Comper, W., and R. Williams. 1987. "Hydrodynamics of concentrated proteoglycan solutions." *Journal of Biological Chemistry* 262 (28): 13464–13471.

Cook, J. 2019. "The role of imaging in diagnosing and managing tendinopathy". *Ultrasound in Medicine & Biology* 45:S16–S17.

Cook, J., K. Khan, Z. Kiss, C. Purdam, and L. Griffiths. 2000. "Prospective imaging study of asymptomatic patellar tendinopathy in elite junior basketball players." *Journal of Ultrasound in Medicine* 19 (7): 473–479.

Cook, J., and C. Purdam. 2012. "Is compressive load a factor in the development of tendinopathy?" *British journal of sports medicine* 46 (3): 163–168.

– . 2009. "Is tendon pathology a continuum? A pathology model to explain the clinical presentation of load-induced tendinopathy". *British journal of sports medicine* 43 (6): 409–416.

– . 2014. "The challenge of managing tendinopathy in competing athletes". *British journal of sports medicine* 48 (7): 506–509.

Cook, J., E. Rio, C. Purdam, and S. Docking. 2016. "Revisiting the continuum model of tendon pathology: what is its merit in clinical practice and research?" *British journal of sports medicine* 50 (19): 1187–1191.

Cowin, S. 1999. "Bone poroelasticity". *Journal of biomechanics* 32 (3): 217–238.

De Croos, J., S. Dhaliwal, M. Grynpas, R. Pilliar, and R. Kandel. 2006. "Cyclic compressive mechanical stimulation induces sequential catabolic and anabolic gene changes in chondrocytes resulting in increased extracellular matrix accumulation". *Matrix Biology* 25 (6): 323–331.

De Zee, M., F. Bojsen-Møller, and M. Voigt. 2000. "Dynamic viscoelastic behavior of lower extremity tendons during simulated running". *Journal of Applied Physiology* 89 (4): 1352–1359.

Dean, P., B.and Gettings, S. Dakin, and A. Carr. 2016. "Are inflammatory cells increased in painful human tendinopathy? A systematic review". *British journal of sports medicine* 50 (4): 216–220.

Del Buono, A., F. Oliva, L. Osti, and N. Maffulli. 2013. "Metalloproteases and tendinopathy". *Muscles, ligaments and tendons journal* 3 (1): 51.

Dempster, A., N. Laird, and D. Rubin. 1977. "Maximum likelihood from incomplete data via the EM algorithm". *Journal of the Royal Statistical Society: Series B (Methodological)* 39 (1): 1–22.

Detournay, E., and A. Cheng. 1993. *Fundamentals of poroelasticity*, 113–171. Elsevier.

Docking, S., and J. Cook. 2019a. "How do tendons adapt? Going beyond tissue responses to understand positive adaptation and pathology development: A narrative review". *Journal of musculoskeletal & neuronal interactions* 19 (3): 300.

Docking, S., C.C. Ooi, and D. Connell. 2015. "Tendinopathy: is imaging telling us the entire story?" *Journal of orthopaedic & sports physical therapy* 45 (11): 842–852.

Docking, S., E. Rio, J. Cook, D. Carey, and L. Fortington. 2019b. "Quantification of Achilles and patellar tendon structure on imaging does not enhance ability to predict self-reported symptoms beyond grey-scale ultrasound and previous history". *Journal of science and medicine in sport* 22 (2): 145–150.

Docking, S., S. Rosengarten, and J. Cook. 2016. "Achilles tendon structure improves on UTC imaging over a 5-month pre-season in elite A ustralian football players". *Scandinavian journal of medicine & science in sports* 26 (5): 557–563.

Docking, S., S. Rosengarten, J. Daffy, and J. Cook. 2014. "Treat the donut, not the hole: the pathological Achilles and patellar tendon has sufficient amounts normal tendon structure". *Journal of Science and Medicine in Sport* 18:e2.

Docking, S., T. Samiric, E. Scase, C. Purdam, and J. Cook. 2013. "Relationship between compressive loading and ECM changes in tendons". *Muscles, ligaments and tendons journal* 3 (1): 7.

Drew, B., T. Smith, C. Littlewood, and B. Sturrock. 2014. "Do structural changes (eg, collagen/matrix) explain the response to therapeutic exercises in tendinopathy: a systematic review". *British journal of sports medicine* 48 (12): 966–972.

Eckstein, F., M. Tieschky, S. Faber, K.- H. Englmeier, and M. Reiser. 1999. "Functional analysis of articular cartilage deformation, recovery, and fluid flow following dynamic exercise in vivo". *Anatomy and embryology* 200 (4): 419–424.

Elvin, N., A. Elvin, C. Scheffer, S. Arnoczky, E. Dillon, and P.J. Erasmus. 2009. "A preliminary study of patellar tendon torques during jumping". *Journal of applied biomechanics* 25 (4): 360–368.

Fang, F., and S. Lake. 2016. "Modelling approaches for evaluating multiscale tendon mechanics". *Interface Focus* 6 (1): 20150044.

Farris, D., E. Buckeridge, G. Trewartha, and M. McGuigan. 2012a. "The effects of orthotic heel lifts on Achilles tendon force and strain during running". *Journal of applied biomechanics* 28 (5): 511–519.

Farris, D., G. Trewartha, and M. McGuigan. 2012b. "The effects of a 30-min run on the mechanics of the human Achilles tendon". *European journal of applied physiology* 112 (2): 653–660.

Federico, S., and W. Herzog. 2008. "On the permeability of fibre-reinforced porous materials". *International Journal of Solids and Structures* 45 (7-8): 2160–2172.

Fernández, M., and A. Mavilio. 2002. "Texture analysis of medical images using the wavelet transform". In *AIP Conference Proceedings*, 630:164–168. 1. American Institute of Physics.

Fessel, G., and J. Snedeker. 2011. "Equivalent stiffness after glycosaminoglycan depletion in tendon—an ultra-structural finite element model and corresponding experiments". *Journal of theoretical biology* 268 (1): 77–83.

Finni, T., J. Peltonen, L. Stenroth, and N. Cronin. 2013. "On the hysteresis in the human Achilles tendon". *Journal of Applied Physiology* 114 (4): 515–517.

Firminger, C., and W. Edwards. 2021. "A biomechanical study of clamping technique on patellar tendon surface strain and material properties using digital image correlation". *Journal of the Mechanical Behavior of Biomedical Materials* 113:104156.

Fitzgerald, J.B, M. Jin, and A. Grodzinsky. 2006. "Shear and compression differentially regulate clusters of functionally related temporal transcription patterns in cartilage tissue". *Journal of Biological Chemistry* 281 (34): 24095–24103.

Fong, K., M. Trindade, Z. Wang, R. Nacamuli, H. Pham, T. Fang, H. Song, R. Smith, M. Longaker, and J. Chang. 2005. "Microarray analysis of mechanical shear effects on flexor tendon cells". *Plastic and Reconstructive Surgery* 116 (5): 1393–1404.

Fredberg, U., and L. Bolvig. 2002. "Significance of ultrasonographically detected asymptomatic tendinosis in the patellar and achilles tendons of elite soccer players: a longitudinal study". *The American journal of sports medicine* 30 (4): 488–491.

Freedman, B., A. Rodriguez, R. Leiphart, J. Newton, E. Ban, J. Sarver, R. Mauck, V. Shenoy, and L. Soslowsky. 2018. "Dynamic loading and tendon healing affect multiscale tendon properties and ECM stress transmission". *Scientific reports* 8 (1): 1–13.

Gatt, R., M. Wood, A. Gatt, C. Zarb F.and Formosa, K. Azzopardi, A. Casha, T. Agius, P. Schembri-Wismayer, L. Attard, N Chockalingam, and J Grima. 2015. "Negative Poisson's ratios in tendons: an unexpected mechanical response". *Acta biomaterialia* 24:201–208.

Gay, S., J. Vijanto, J. Raekallio, and R. Penttinen. 1978. "Collagen types in early phases of wound healing in children." *Acta Chirurgica Scandinavica* 144 (4): 205–211.

Gigante, A., M. Marinelli, C. Chillemi, and F. Greco. 2004. "Fibrous cartilage in the rotator cuff: A pathogenetic mechanism of tendon tear?" *Journal of shoulder and elbow surgery* 13 (3): 328–332.

Grad, S., D. Eglin, M. Alini, and M. Stoddart. 2011. "Physical stimulation of chondrogenic cells in vitro: a review". *Clinical Orthopaedics and Related Research®* 469 (10): 2764–2772.

Granger, H., G. Meininger, J. Borders, R. Morff, and A. Goodman. 1984. "Microcirculation of skeletal muscle". *The physiology and pharmacology of the microcirculation* 2:181–265.

Grassi, W., E. Filippucci, A. Farina, and C. Cervini. 2000. "Sonographic imaging of tendons". *Arthritis & Rheumatism: Official Journal of the American College of Rheumatology* 43 (5): 969–976.

Grigg, N., S. Wearing, and J. Smeathers. 2009. "Eccentric calf muscle exercise produces a greater acute reduction in Achilles tendon thickness than concentric exercise". *British journal of sports medicine* 43 (4): 280–283.

Guo, L., J. Vardakis, D. Chou, and Y. Ventikos. 2020. "A multiple-network poroelastic model for biological systems and application to subject-specific modelling of cerebral fluid transport". *International Journal of Engineering Science* 147:103204.

Gupta, H.S., J. Seto, S. Krauss, P. Boesecke, and H. Screen. 2010. "In situ multi-level analysis of viscoelastic deformation mechanisms in tendon collagen". *Journal of structural biology* 169 (2): 183–191.

Gupta, R., I. Elamvazuthi, S. Dass, I. Faye, P. Vasant, J. George, and F. Izza. 2014. "Curvelet based automatic segmentation of supraspinatus tendon from ultrasound image: a focused assistive diagnostic method". *Biomedical engineering online* 13 (1): 1–18.

Han, E.- H., S. Chen, S. Klisch, and R. Sah. 2011. "Contribution of proteoglycan osmotic swelling pressure to the compressive properties of articular cartilage". *Biophysical journal* 101 (4): 916–924.

Han, S., S.J. Gemmell, K.G. Helmer, P. Grigg, J.W. Wellen, A.H. Hoffman, and C.H. Sotak. 2000. "Changes in ADC caused by tensile loading of rabbit achilles tendon: evidence for water transport". *Journal of Magnetic Resonance* 144 (2): 217–227.

Hannafin, J., and S. Arnoczky. 1994. "Effect of cyclic and static tensile loading on water content and solute diffusion in canine flexor tendons: an in vitro study". *Journal of Orthopaedic Research* 12 (3): 350–356.

Haralick, R., K. Shanmugam, and I. Dinstein. 1973. "Textural features for image classification". *IEEE Transactions on systems, man, and cybernetics*, no. 6: 610–621.

Haudenschild, A., A. Hsieh, S. Kapila, and J. Lotz. 2009. "Pressure and distortion regulate human mesenchymal stem cell gene expression". *Annals of biomedical engineering* 37 (3): 492–502.

Hawkins, D., C. Lum, D. Gaydos, and R. Dunning. 2009. "Dynamic creep and pre-conditioning of the Achilles tendon in-vivo". *Journal of biomechanics* 42 (16): 2813–2817.

Hirose, K., S. Kondo, H.- R. Choi, S. Mishima, H. Iwata, and N. Ishiguro. 2004. "Spontaneous healing process of a supraspinatus tendon tear in rabbits". *Archives of orthopaedic and trauma surgery* 124 (6): 374–377.

Hirsch, S. 2018. *A biphasic poroelasticity model for soft tissue*, 71–88. Springer.

Hirschmüller, A., V. Frey, L. Konstantinidis, H. Baur, H.- H. Dickhuth, N.P. Suedkamp, and P. Helwig. 2012. "Prognostic value of Achilles tendon Doppler sonography in asymptomatic runners." *Medicine and science in sports and exercise* 44 (2): 199–205.

Hodgson, R., P. O'Connor, and A. Grainger. 2012. "Tendon and ligament imaging". *The British journal of radiology* 85 (1016): 1157–1172.

Howard, P., U. Kucich, R. Taliwal, and J. Korostoff. 1998. "Mechanical forces alter extracellular matrix synthesis by human periodontal ligament fibroblasts". *Journal of periodontal research* 33 (8): 500–508.

Huang, Y., V. De Bortoli, F. Zhou, and J. Gilles. 2018. "Review of wavelet-based unsupervised texture segmentation, advantage of adaptive wavelets". *IET Image Processing* 12 (9): 1626–1638.

Huisman, A., E.and Lu, R. McCormack, and A. Scott. 2014. "Enhanced collagen type I synthesis by human tenocytes subjected to periodic in vitro mechanical stimulation". *BMC musculoskeletal disorders* 15 (1): 1–8.

Hurschler, C., B. Loitz-Ramage, and R. Vanderby Jr. 1997. "A structurally based stress-stretch relationship for tendon and ligament". 119 (4): 392–399.

Ilea, D., and P. Whelan. 2011. "Image segmentation based on the integration of colour–texture descriptors—A review". *Pattern Recognition* 44 (10-11): 2479–2501.

Jahanifar, M., N. Tajeddin, M. Hasani, B. Shekarchi, and K. Azema. 2020. "Automatic Recognition of the Supraspinatus Tendinopathy from Ultrasound Images using Convolutional Neural Networks". *arXiv preprint arXiv:2011.11777*.

Jain, A., and F. Farrokhnia. 1991. "Unsupervised texture segmentation using Gabor filters". *Pattern recognition* 24 (12): 1167–1186.

Jansen, K., A. Licup, A. Sharma, R. Rens, F. MacKintosh, and G. Koenderink. 2018. "The role of network architecture in collagen mechanics". *Biophysical journal* 114 (11): 2665–2678.

Jaynes, E. 1957. "Information theory and statistical mechanics". *Physical review* 106 (4): 620.

Jones, E., G. Jones, K. Legerlotz, and G. Riley. 2013. "Cyclical strain modulates metalloprotease and matrix gene expression in human tenocytes via activation of TGFβ". *Biochimica et Biophysica Acta (BBA)-Molecular Cell Research* 1833 (12): 2596–2607.

Jonsson, P., and H. Alfredson. 2005. "Superior results with eccentric compared to concentric quadriceps training in patients with jumper's knee: a prospective randomised study". *British journal of sports medicine* 39 (11): 847–850.

Jordan, M., and T. Mitchell. 2015. "Machine learning: Trends, perspectives, and prospects". *Science* 349 (6245): 255–260.

Julesz, B. 1981. "Textons, the elements of texture perception, and their interactions". *Nature* 290 (5802): 91–97.

Jull, G., A. Moore, D. Falla, C. Lewis J.and McCarthy, and M. Sterling. 2015. *Grieve's Modern Musculoskeletal Physiotherapy E-Book*. Churchill Livingstone.

Jung, H., and Y. Oh. 2021. "Towards better explanations of class activation mapping". In *Proceedings of the IEEE/CVF International Conference on Computer Vision*, 1336–1344.

Jurvelin, J., A.M. Säämänen, J. Arokoski, H.J Helminen, I. Kiviranta, and M. Tammi. 1988. "Biomechanical properties of the canine knee articular cartilage as related to matrix proteoglycans and collagen". *Engineering in Medicine* 17 (4): 157–162.

Kafka, V. 2002. "Surface fissures in articular cartilage: new concepts, hypotheses and modeling". *Clinical Biomechanics* 17 (1): 73–80.

Kameo, Y., T. Adachi, and M. Hojo. 2008. "Transient response of fluid pressure in a poroelastic material under uniaxial cyclic loading". *Journal of the Mechanics and Physics of Solids* 56 (5): 1794–1805.

Kameo, Y., Y. Ootao, and M. Ishihara. 2016. "Poroelastic analysis of interstitial fluid flow in a single lamellar trabecula subjected to cyclic loading". *Biomechanics and modeling in mechanobiology* 15 (2): 361–370.

Kannus, P. 2000. "Structure of the tendon connective tissue". *Scandinavian journal of medicine & science in sports* 10 (6): 312–320.

Kapellos, G., T. Alexiou, and A.C Payatakes. 2010. "Theoretical modeling of fluid flow in cellular biological media: An overview". *Mathematical biosciences* 225 (2): 83–93.

Kaya, M., N. Karahan, and B. Yılmaz. 2019. *Tendon Structure and Classification*. IntechOpen.

Khan, K., J. Cook, Z. Kiss, P. Visentini, M. Fehrmann, P. Harcourt, B. Tress, and J. Wark. 1997. "Patellar tendon ultrasonography and jumper's knee in female basketball players: a longitudinal study." *Clinical journal of sport medicine: official journal of the Canadian Academy of Sport Medicine* 7 (3): 199–206.

Khan, K.M., B.B. Forster, J. Robinson, Y. Cheong, L. Louis, L. Maclean, and J.E. Taunton. 2003. "Are ultrasound and magnetic resonance imaging of value in assessment of Achilles tendon disorders? A two year prospective study". *British journal of sports medicine* 37 (2): 149–153.

Kharazi, M., S. Bohm, C. Theodorakis, F. Mersmann, and A. Arampatzis. 2021. "Quantifying mechanical loading and elastic strain energy of the human Achilles tendon during walking and running". *Scientific Reports* 11 (1): 1–13.

Khayyeri, H., A. Gustafsson, A. Heuijerjans, M.K. Matikainen, P. Julkunen, P. Eliasson, P. Aspenberg, and H. Isaksson. 2015. "A fibre-reinforced poroviscoelastic model accurately describes the biomechanical behaviour of the rat achilles tendon". *PloS one* 10 (6): e0126869.

Khayyeri, H., G. Longo, A. Gustafsson, and H. Isaksson. 2016. "Comparison of structural anisotropic soft tissue models for simulating Achilles tendon tensile behaviour". *Journal of the mechanical behavior of biomedical materials* 61:431–443.

Kim, N.- D., L. Booth, V. Amin, J. Lim, and S. Udpa. 1998. "Ultrasonic image processing for tendon injury evaluation". In *Proceedings of the IEEE-SP International Symposium on Time-Frequency and Time-Scale Analysis (Cat. No. 98TH8380)*, 241–244. IEEE.

Kjær, M., H. Langberg, K. Heinemeier, M.L. Bayer, M. Hansen, L. Holm, S. Doessing, M. Kongsgaard, M Krogsgaard, and S. Magnusson. 2009. "From mechanical loading to collagen synthesis, structural changes and function in human tendon". *Scandinavian journal of medicine & science in sports* 19 (4): 500–510.

Korhonen, R., M. Laasanen, J. Töyräs, R. Lappalainen, H. Helminen, and J. Jurvelin. 2003. "Fibril reinforced poroelastic model predicts specifically mechanical behavior of normal, proteoglycan depleted and collagen degraded articular cartilage". *Journal of biomechanics* 36 (9): 1373–1379.

Kubo, K., H. Akima, J. Ushiyama, I. Tabata, H. Fukuoka, H. Kanehisa, and T. Fukunaga. 2004. "Effects of 20 days of bed rest on the viscoelastic properties of tendon structures in lower limb muscles". *British Journal of Sports Medicine* 38 (3): 324–330.

Kubo, K., Y. Kawakami, H. Kanehisa, and T. Fukunaga. 2002. "Measurement of viscoelastic properties of tendon structures in vivo". *Scandinavian journal of medicine & science in sports* 12 (1): 3–8.

Kulig, K., R. Landel, Y. -J. Chang, N. Hannanvash, S.F. Reischl, P. Song, and G.R. Bashford. 2013. "Patellar tendon morphology in volleyball athletes with and without patellar tendinopathy". *Scandinavian journal of medicine & science in sports* 23 (2): e81–e88.

Kumar, C., A. Agarwal, and R. Chillarige. 2012. "Color and texture image segmentation". In *International Workshop on Multi-disciplinary Trends in Artificial Intelligence*, 69–80. Springer.

Kumar, S., A. Fred, and P. Varghese. 2020. "An overview of segmentation algorithms for the analysis of anomalies on medical images". *Journal of Intelligent Systems* 29 (1): 612–625.

Kurihara, T., R. Sasaki, and T. Isaka. 2012. "Mechanical properties of achilles tendon in relation to various sport activities of collegiate athletes". In *ISBS-Conference Proceedings Archive*.

Lalumiere, M., C. Larivière, M. -J. Nadeau, P. Paquette, M. Lamontagne, F. Desmeules, and D. Gagnon. 2020. "Proposing a Minimal Data Set of Musculoskeletal Ultrasound Imaging Biomarkers to Inform Clinical Practice: An Analysis Founded on the Achilles Tendon". *Ultrasound in Medicine & Biology* 46 (9): 2222–2235.

Langberg, H., H. Ellingsgaard, T. Madsen, J. Jansson, S. Magnusson, P. Aagaard, and M. Kjær. 2007. "Eccentric rehabilitation exercise increases peritendinous type I collagen synthesis in humans with Achilles tendinosis". *Scandinavian journal of medicine & science in sports* 17 (1): 61–66.

Langberg, H., D. Skovgaard, S. Asp, and M. Kjaer. 2000. "Time pattern of exercise-induced changes in type I collagen turnover after prolonged endurance exercise in humans". *Calcified tissue international* 67 (1): 41–44.

Langberg, H., D. Skovgaard, M. Karamouzis, J. Bülow, and M. Kjær. 1999a. "Metabolism and inflammatory mediators in the peritendinous space measured by microdialysis during intermittent isometric exercise in humans". *The Journal of physiology* 515 (3): 919–927.

Langberg, H., D. Skovgaard, L. Petersen, J. Bülow, and M. Kjær. 1999b. "Type I collagen synthesis and degradation in peritendinous tissue after exercise determined by microdialysis in humans". *The Journal of physiology* 521 (1): 299–306.

Lavagnino, M., S. Arnoczky, E. Kepich, O. Caballero, and R. Haut. 2008. "A finite element model predicts the mechanotransduction response of tendon cells to cyclic tensile loading". *Biomechanics and modeling in mechanobiology* 7 (5): 405–416.

Lavagnino, M., M. Wall, D. Little, A. Banes, F. Guilak, and S. Arnoczky. 2015. "Tendon mechanobiology: Current knowledge and future research opportunities". *Journal of Orthopaedic Research* 33 (6): 813–822.

Lee, K., S. Ling, and P. Yung. 2019. "Controlled trial to compare the Achilles tendon load during running in flatfeet participants using a customized arch support orthoses vs an orthotic heel lift". *BMC musculoskeletal disorders* 20 (1): 1–12.

Lee, M., M. Trindade, T. Ikenoue, D. Schurman, S. Goodman, and R. Smith. 2002. "Effects of shear stress on nitric oxide and matrix protein gene expression in human osteoarthritic chondrocytes in vitro". *Journal of orthopaedic research* 20 (3): 556–561.

Leung, T., and J. Malik. 2001. "Representing and recognizing the visual appearance of materials using three-dimensional textons". *International journal of computer vision* 43 (1): 29–44.

Li, K., Z. Wu, K. -C. Peng, J. Ernst, and Y. Fu. 2018. "Tell me where to look: Guided attention inference network". In *Proceedings of the IEEE Conference on Computer Vision and Pattern Recognition*, 9215–9223.

Li, X. -Z., S. Williams, and M. Bottema. 2014. "Texture and region dependent breast cancer risk assessment from screening mammograms". *Pattern recognition letters* 36:117–124.

Lichtwark, .G, R. Ker, N. Reeves, S. Magnusson, A. Nordez, A. Arampatzis, M. Vagula, A. Cresswell, C. Maganaris, R. Svensson, and C. Coupe. 2013. "Commentaries on viewpoint: on the hysteresis in the human Achilles tendon". *Journal of Applied Physiology* 114 (4): 518–520.

Loboa, E., T. Wren, G. Beaupré, and D. Carter. 2003. "Mechanobiology of soft skeletal tissue differentiation—a computational approach of a fiber-reinforced poroelastic model based on homogeneous and isotropic simplifications". *Biomechanics and modeling in mechanobiology* 2 (2): 83–96.

Maceri, F., M. Marino, and G. Vairo. 2012. "An insight on multiscale tendon modeling in muscle–tendon integrated behavior". *Biomechanics and Modeling in Mechanobiology* 11 (3): 505–517.

MacMinn, C., E. Dufresne, and J. Wettlaufer. 2016. "Large deformations of a soft porous material". *Physical Review Applied* 5 (4): 044020.

Maffulli, N., R. Regine, M. Angelillo, G. Capasso, and S. Filice. 1987. "Ultrasound diagnosis of Achilles tendon pathology in runners." *British journal of sports medicine* 21 (4): 158–162.

Maffulli, N., P. Sharma, and K. Luscombe. 2004. "Achilles tendinopathy: aetiology and management". *Journal of the Royal Society of Medicine* 97 (10): 472–476.

Maffulli, N., J. Wong, and L. Almekinders. 2003. "Types and epidemiology of tendinopathy". *Clinics in sports medicine* 22 (4): 675–692.

Maganaris, C., P. Chatzistergos, N. Reeves, and M. Narici. 2017. "Quantification of internal stress-strain fields in human tendon: unraveling the mechanisms that underlie regional tendon adaptations and mal-adaptations to mechanical loading and the effectiveness of therapeutic eccentric exercise". *Frontiers in physiology* 8:91.

Maganaris, C., M. Narici, L. Almekinders, and N. Maffulli. 2004. "Biomechanics and pathophysiology of overuse tendon injuries". *Sports medicine* 34 (14): 1005–1017.

Maganaris, C., and J. Paul. 2000. "Hysteresis measurements in intact human tendon". *Journal of biomechanics* 33 (12): 1723–1727.

– . 2002. "Tensile properties of the in vivo human gastrocnemius tendon". *Journal of biomechanics* 35 (12): 1639–1646.

Magnusson, S., H. Langberg, and M. Kjaer. 2010. "The pathogenesis of tendinopathy: balancing the response to loading". *Nature Reviews Rheumatology* 6 (5): 262–268.

Malaviya, P., D. Bultler, G. Boivin, F. Smith, F. Barry, J. Murphy, and K. Vogel. 2000. "An in vivo model for load-modulated remodeling in the rabbit flexor tendon". *Journal of Orthopaedic Research* 18 (1): 116–125.

Malliaras, P., C. Barton, N. Reeves, and H. Langberg. 2013. "Achilles and patellar tendinopathy loading programmes". *Sports medicine* 43 (4): 267–286.

Malliaras, P., J. Cook, C. Purdam, and E. Rio. 2015. "Patellar tendinopathy: clinical diagnosis, load management, and advice for challenging case presentations". *journal of orthopaedic & sports physical therapy* 45 (11): 887–898.

Malliaras, P., and S. O'Neill. 2017. "Potential risk factors leading to tendinopathy". *Apunts. Medicina de l'Esport* 52 (194): 71–77.

Mascaró, A., M. Cos, A. Morral, A. Roig, C. Purdam, and J. Cook. 2018. "Load management in tendinopathy: Clinical progression for Achilles and patellar tendinopathy". *Apunts. Medicina de l'Esport* 53 (197): 19–27.

McGarry, J., J. Klein-Nulend, M. Mullender, and P. Prendergast. 2005. "A comparison of strain and fluid shear stress in stimulating bone cell responses—a computational and experimental study". *The FASEB journal* 19 (3): 1–22.

McKee, C., J. Last, P. Russell, and C. Murphy. 2011. "Indentation versus tensile measurements of Young's modulus for soft biological tissues". *Tissue Engineering Part B: Reviews* 17 (3): 155–164.

Mead, M., J. Gumucio, T. Awan, C. Mendias, and K. Sugg. 2018. "Pathogenesis and management of tendinopathies in sports medicine". *Translational sports medicine* 1 (1): 5–13.

Mehdizadeh, A., B. Gardiner, M. Lavagnino, and D. Smith. 2017. "Predicting tenocyte expression profiles and average molecular concentrations in Achilles tendon ECM from tissue strain and fiber damage". *Biomechanics and modeling in mechanobiology* 16 (4): 1329–1348.

Meiburger, K., U. Acharya, and F. Molinari. 2018. "Automated localization and segmentation techniques for B-mode ultrasound images: A review". *Computers in biology and medicine* 92:210–235.

Merza, E., S. Pearson, G. Lichtwark, M. Ollason, and P. Malliaras. 2021. "Immediate and long-term effects of mechanical loading on Achilles tendon volume: A systematic review and meta-analysis". *Journal of Biomechanics*: 110289.

Metzger, T., S. Schwaner, A. LaNeve, T. Kreipke, and G. Niebur. 2015. "Pressure and shear stress in trabecular bone marrow during whole bone loading". *Journal of biomechanics* 48 (12): 3035–3043.

Miller, B., J. Olesen, M. Hansen, S. Døssing, R. Crameri, R. Welling, H. Langberg, A. Flyvbjerg, M. Kjaer, J. Babraj, K. Smith, and M. Rennie. 2005. "Coordinated collagen and muscle protein synthesis in human patella tendon and quadriceps muscle after exercise". *The Journal of physiology* 567 (3): 1021–1033.

Morgado, P., M. Silveira, and D. Costa. 2013. "Texton-based diagnosis of Alzheimer's disease". In *2013 IEEE International Workshop on Machine Learning for Signal Processing (MLSP)*, 1–6. IEEE.

Mos, M. de, W. Koevoet, H. van Schie, H. Kops N.and Jahr, J. Verhaar, and G. van Osch. 2009. "In vitro model to study chondrogenic differentiation in tendinopathy". *The American journal of sports medicine* 37 (6): 1214–1222.

Mostaço-Guidolin, L., A. Ko, D. Popescu, M. Smith, E. Kohlenberg, M. Shiomi, A. Major, and M. Sowa. 2011. "Evaluation of texture parameters for the quantitative description of multimodal nonlinear optical images from atherosclerotic rabbit arteries". *Physics in Medicine & Biology* 56 (16): 5319.

Mow, V., S. Kuei, W. Lai, and C. Armstrong. 1980. "Biphasic creep and stress relaxation of articular cartilage in compression: theory and experiments". *Journal of biomechanical engineering* 102 (1): 73–84.

Murray, R., C. Zhu, A. Goodship, K. Lakhani, C. Agrawal, and K. Athanasiou. 1999. "Exercise affects the mechanical properties and histological appearance of equine articular cartilage". *Journal of Orthopaedic Research* 17 (5): 725–731.

Murtaugh, B., and J. Ihm. 2013. "Eccentric training for the treatment of tendinopathies". *Current sports medicine reports* 12 (3): 175–182.

Nadeau, A., M. -J.and Desrochers, M. Lamontagne, C. Larivière, and D. Gagnon. 2016. "Quantitative ultrasound imaging of Achilles tendon integrity in symptomatic and asymptomatic individuals: reliability and minimal detectable change". *Journal of foot and ankle research* 9 (1): 1–17.

Newcomb, S. 1886. "A generalized theory of the combination of observations so as to obtain the best result". *American journal of Mathematics* 8 (4): 343–366.

Nielsen, M.J., and M. Karsdal. 2016. *Type III collagen*, 21–30. Elsevier.

Obst, S., L. Heales, B. Schrader, S. Davis, K. Dodd, C. Holzberger, L. Beavis, and R. Barrett. 2018. "Are the mechanical or material properties of the achilles and patellar tendons altered in tendinopathy? A systematic review with meta-analysis". *Sports medicine* 48 (9): 2179–2198.

Oftadeh, R., B. Connizzo, H. Nia, C. Ortiz, and A. Grodzinsky. 2018. "Biological connective tissues exhibit viscoelastic and poroelastic behavior at different frequency regimes: application to tendon and skin biophysics". *Acta biomaterialia* 70:249–259.

Ogden, R. 1997. *Non-linear elastic deformations*. Courier Corporation.

Ooi, C.- C., P. Malliaras, M Schneider, and D. Connell. 2014. ""Soft, hard, or just right?" Applications and limitations of axial-strain sonoelastography and shear-wave elastography in the assessment of tendon injuries". *Skeletal radiology* 43 (1): 1–12.

Oshiro, W., J. Lou, X. Xing, Y. Tu, and P. Manske. 2003. "Flexor tendon healing in the rat: a histologic and gene expression study". *The Journal of hand surgery* 28 (5): 814–823.

Owan, I., D. Burr, C. Turner, J. Qiu, Y. Tu, J. Onyia, and R. Duncan. 1997. "Mechanotransduction in bone: osteoblasts are more responsive to fluid forces than mechanical strain". *American Journal of Physiology-Cell Physiology* 273 (3): C810–C815.

Paavola, M., T. Paakkala, P. Kannus, and M. Järvinen. 1998. "Ultrasonography in the differential diagnosis of Achilles tendon injuries and related disorders: a comparison between pre-operative ultrasonography and surgical findings". *Acta radiologica* 39 (6): 612–619.

Park, B., W. Jang, and S. Yoo. 2016. "Texture analysis of supraspinatus ultrasound image for computer aided diagnostic system". *Healthcare informatics research* 22 (4): 299–304.

Parkinson, J., T. Samiric, M.Z. Ilic, J. Cook, and C.J. Handley. 2011. "Involvement of proteoglycans in tendinopathy". *The Journal of Musculoskeletal and Neuronal Interactions* 11 (2): 86–93.

Pearson, K. 1894. "Contributions to the mathematical theory of evolution". *Philosophical Transactions of the Royal Society of London.* 185:71–110.

Peltonen, J., N. Cronin, L. Stenroth, T. Finni, and J. Avela. 2013. "Viscoelastic properties of the Achilles tendon in vivo". *Springerplus* 2 (1): 1–8.

Petroudi, S., and M. Brady. 2006. "Breast density segmentation using texture". In *International Workshop on Digital Mammography*, 609–615. Springer.

Pountos, I., and P. Giannoudis. 2005. "Biology of mesenchymal stem cells". *Injury* 36 (3): S8–S12.

Rawat, W., and Z. Wang. 2017. "Deep convolutional neural networks for image classification: A comprehensive review". *Neural computation* 29 (9): 2352–2449.

Raz, E., and Y. Lanir. 2009. "Recruitment viscoelasticity of the tendon". *Journal of biomechanical engineering* 131 (11): 111008.

Rees, J., G. Lichtwark, R. Wolman, and A. Wilson. 2008. "The mechanism for efficacy of eccentric loading in Achilles tendon injury; an in vivo study in humans". *Rheumatology* 47 (10): 1493–1497.

Reese, S., S. Maas, and J. Weiss. 2010. "Micromechanical models of helical superstructures in ligament and tendon fibers predict large Poisson's ratios". *Journal of biomechanics* 43 (7): 1394–1400.

Rıos-Dıaz, J., J. Martınez-Payá, A. De-Groot-Ferrando, and M. Del-Baño-Aledo. 2012. "Utility of grey level co-occurrence matrices for the ultrasonographic quantitative study of the textural patterns of patellar ligament". *Adv Med Biol* 51:253–268.

Rodrıguez, J., F. Cacho, J. Bea, and M.l Doblaré. 2006. "A stochastic-structurally based three dimensional finite-strain damage model for fibrous soft tissue". *Journal of the Mechanics and Physics of Solids* 54 (4): 864–886.

Roeder, B., K. Kokini, J. Sturgis, J. Robinson, and S. Voytik-Harbin. 2002. "Tensile mechanical properties of three-dimensional type I collagen extracellular matrices with varied microstructure". *Journal of biomechanical engineering* 124 (2): 214–222.

Rosario, M., and T. Roberts. 2020. "Loading rate has little influence on tendon fascicle mechanics". *Frontiers in physiology* 11:255.

Rowlands, A., M. Stone, and R. Eston. 2007. "Influence of speed and step frequency during walking and running on motion sensor output". *Medicine & Science in Sports & Exercise* 39 (4): 716–727.

Rue, H., and L. Held. 2005. *Gaussian Markov random fields: theory and applications*. Chapman / Hall/CRC.

Ryou, H., K. Sirinukunwattana, A. Aberdeen, G. Grindstaff, B. Stolz, H. Byrne, H. Harrington, N. Sousos, A. Godfrey, C. Harrison, B Psaila, A Mead, G Rees, G Turner, J Rittscher, and D Royston. 2022. "Continuous Indexing of Fibrosis (CIF): Improving the Assessment and Classification of MPN Patients". *medRxiv*.

Safa, B., E. Bloom, A. Lee, M. Santare, and D. Elliott. 2020. "Evaluation of transverse poroelastic mechanics of tendon using osmotic loading and biphasic mixture finite element modeling". *Journal of Biomechanics* 109:109892.

Sawicki, A., and W. Świdziński. 1998. "Elastic moduli of non-cohesive particulate materials". *Powder Technology* 96 (1): 24–32.

Schätti, O., D. Waldvogel, and L. Gallo. 2013. "Mechanobiological response of chondrocytes to a TMJ-specific loading pattern over time". *Osteoarthritis and Cartilage* 21:S209–S210.

Schie, H. van, E. Bakker, A. Jonker, and P. van Weeren. 2003. "Computerized ultrasonographic tissue characterization of equine superficial digital flexor tendons by means of stability quantification of echo patterns in contiguous transverse ultrasonographic images". *American journal of veterinary research* 64 (3): 366–375.

– . 2000. "Ultrasonographic tissue characterization of equine superficial digital flexor tendons by means of gray level statistics". *American journal of veterinary research* 61 (2): 210–219.

Schlesinger, P., H. Blair, D. Beer Stolz, V. Riazanski, E. Ray, I. Tourkova, and D. Nelson. 2020. "Cellular and extracellular matrix of bone, with principles of synthesis and dependency of mineral deposition on cell membrane transport". *American Journal of Physiology-Cell Physiology* 318 (1): C111–C124.

Schmid, C. 2001. "Constructing models for content-based image retrieval". In *Proceedings of the 2001 IEEE Computer Society Conference on Computer Vision and Pattern Recognition. CVPR 2001*, 2:II39–II45. IEEE.

Schneebeli, A., F. Del Grande, G. Vincenzo, C. Cescon, and M. Barbero. 2017. "Test-retest reliability of echo intensity parameters in healthy Achilles tendons using a semi-automatic tracing procedure". *Skeletal radiology* 46 (11): 1553–1558.

Screen, H. 2009. "Hierarchical approaches to understanding tendon mechanics". *Journal of Biomechanical Science and Engineering* 4 (4): 481–499.

Screen, H., J. Shelton, V. Chhaya, M. Kayser, D. Bader, and D. Lee. 2005. "The influence of noncollagenous matrix components on the micromechanical environment of tendon fascicles". *Annals of biomedical engineering* 33 (8): 1090–1099.

Sensini, A., and L. Cristofolini. 2018. "Biofabrication of electrospun scaffolds for the regeneration of tendons and ligaments". *Materials* 11 (10): 1963.

Seynnes, O., J. Bojsen-Møller, K. Albracht, A. Arndt, N. Cronin, T. Finni, and S. Magnusson. 2015. "Ultrasound-based testing of tendon mechanical properties: a critical evaluation". *Journal of Applied Physiology* 118 (2): 133–141.

Sezer, A., and H. Sezer. 2019. "Capsule network-based classification of rotator cuff pathologies from MRI". *Computers & Electrical Engineering* 80:106480.

Sharma, N., and L. Aggarwal. 2010. "Automated medical image segmentation techniques". *Journal of medical physics/Association of Medical Physicists of India* 35 (1): 3.

Shearer, T. 2015. "A new strain energy function for the hyperelastic modelling of ligaments and tendons based on fascicle microstructure". *Journal of biomechanics* 48 (2): 290–297.

Shieh, A., and K. Athanasiou. 2007. "Dynamic compression of single cells". *Osteoarthritis and cartilage* 15 (3): 328–334.

Shim, J., and S. Elder. 2006. "Influence of cyclic hydrostatic pressure on fibrocartilaginous metaplasia of achilles tendon fibroblasts". *Biomechanics and modeling in mechanobiology* 5 (4): 247–252.

Silverman, M., D. Grosof, R. De Valois, and S. Elfar. 1989. "Spatial-frequency organization in primate striate cortex". *Proceedings of the National Academy of Sciences* 86 (2): 711–715.

Steeb, H., and J. Renner. 2019. "Mechanics of poro-elastic media: a review with emphasis on foundational state variables". *Transport in Porous Media* 130 (2): 437–461.

Steward, A., and D. Kelly. 2015. "Mechanical regulation of mesenchymal stem cell differentiation". *Journal of anatomy* 227 (6): 717–731.

Szaro, P., and K. Gataa. 2021. "The correlations between dimensions of the normal tendon and tendinopathy changed Achilles tendon in routine magnetic resonance imaging". *Scientific Reports* 11 (1): 1–11.

Tavakoli Nia, H., L. Han, I. Soltani Bozchalooi, P. Roughley, K. Youcef-Toumi, A. Grodzinsky, and C. Ortiz. 2015. "Aggrecan nanoscale solid–fluid interactions are a primary determinant of cartilage dynamic mechanical properties". *ACS nano* 9 (3): 2614–2625.

Texture classification - filters. https://www.robots.ox.ac.uk/ vgg/research/texclass/filters.html. Accessed: 01-03-2021.

Thomopoulos, S., G. Genin, and L. Galatz. 2010. "The development and morphogenesis of the tendon-to-bone insertion What development can teach us about healing". *Journal of musculoskeletal & neuronal interactions* 10 (1): 35.

Thompson, M., M. Bajuri, H. Khayyeri, and H. Isaksson. 2017. "Mechanobiological modelling of tendons: Review and future opportunities". *Proceedings of the Institution of Mechanical Engineers, Part H: Journal of Engineering in Medicine* 231 (5): 369–377.

Thorpe, C., K. Karunaseelan, J. Ng Chieng Hin, G. Riley, H. Birch, P. Clegg, and H. Screen. 2016a. "Distribution of proteins within different compartments of tendon varies according to tendon type". *Journal of anatomy* 229 (3): 450–458.

Thorpe, C., G. Riley, H. Birch, P. Clegg, and H. Screen. 2014. "Effect of fatigue loading on structure and functional behaviour of fascicles from energy-storing tendons". *Acta biomaterialia* 10 (7): 3217–3224.

Thorpe, C., and H. Screen. 2016b. "Tendon structure and composition". *Metabolic influences on risk for tendon disorders*: 3–10.

Tom, S., J. Parkinson, M. Ilic, J. Cook, J. Feller, and C. Handley. 2009. "Changes in the composition of the extracellular matrix in patellar tendinopathy". *Matrix Biology* 28 (4): 230–236.

Tresoldi, I., F. Oliva, M. Benvenuto, M. Fantini, L. Masuelli, and A. Bei R.oand Modesti. 2013. "Tendon's ultrastructure". *Muscles, ligaments and tendons journal* 3 (1): 2.

Tsai, Y. -H., K. -C. Huang, S. -H. Shen, T. -Y. Yang, T. -J. Huang, and R. Hsu. 2014. "Quantification of sonographic echogenicity by the gray-level histogram in patients with supraspinatus tendinopathy". *Journal of Medical Ultrasonics* 41 (3): 343–349.

Turner, C., J. Rho, Y. Takano, T. Tsui, and G. Pharr. 1999. "The elastic properties of trabecular and cortical bone tissues are similar: results from two microscopic measurement techniques". *Journal of biomechanics* 32 (4): 437–441.

Urdang, L. 1968. *The Random House dictionary of the English language*. New York: Random House.

Van Schie, H., R. -J. de Vos, S. de Jonge, E.M. Bakker, M.P Heijboer, J. Verhaar, J.L. Tol, and H. Weinans. 2010. "Ultrasonographic tissue characterisation of human Achilles tendons: quantification of tendon structure through a novel non-invasive approach". *British journal of sports medicine* 44 (16): 1153–1159.

Varma, M., and A. Zisserman. 2005. "A statistical approach to texture classification from single images". *International journal of computer vision* 62 (1-2): 61–81.

– . 2002. "Classifying images of materials: Achieving viewpoint and illumination independence". In *European Conference on Computer Vision*, 255–271. Springer.

Voleti, P., M. Buckley, and L. Soslowsky. 2012. "Tendon healing: repair and regeneration". *Annual review of biomedical engineering* 14:47–71.

Wang, C., C. Hung, and V. Mow. 2001. "An analysis of the effects of depth-dependent aggregate modulus on articular cartilage stress-relaxation behavior in compression". *Journal of Biomechanics* 34 (1): 75–84.

Wang, D. -L., S. -D. Jiang, and L. -Y. Dai. 2007. "Biologic response of the intervertebral disc to static and dynamic compression in vitro". *Spine* 32 (23): 2521–2528.

Wang, J., Q. Guo, and B. Li. 2012. "Tendon biomechanics and mechanobiology—a minireview of basic concepts and recent advancements". *Journal of Hand Therapy* 25 (2): 133–141.

Wang, Q. 2012. "HMRF-EM-image: implementation of the hidden markov random field model and its expectation-maximization algorithm". *arXiv preprint arXiv:1207.3510*.

Warden, S., Z. Kiss, F. Malara, A. Ooi, J. Cook, and K. Crossley. 2007. "Comparative accuracy of magnetic resonance imaging and ultrasonography in confirming clinically diagnosed patellar tendinopathy". *The American journal of sports medicine* 35 (3): 427–436.

Westh, E., M. Kongsgaard, J. Bojsen-Moller, P. Aagaard, M. Hansen, M. Kjaer, and S. Magnusson. 2008. "Effect of habitual exercise on the structural and mechanical properties of human tendon, in vivo, in men and women". *Scandinavian journal of medicine & science in sports* 18 (1): 23–30.

Wezenbeek, E., N. Mahieu, T.M. Willems, D. Van Tiggelen, M. De Muynck, D. De Clercq, and E. Witvrouw. 2017. "What does normal tendon structure look like? New insights into tissue characterization in the Achilles tendon". *Scandinavian journal of medicine & science in sports* 27 (7): 746–753.

Whittaker, R., R. Booth, R. Dyson, C. Bailey, L. Chini, S. Naire, Sevil Payvandi, Z. Rong, H. Woollard, L. Cummings, and S. Waters. 2009. "Mathematical modelling of fibre-enhanced perfusion inside a tissue-engineering bioreactor". *Journal of theoretical biology* 256 (4): 533–546.

Winkler, G. 2003. *Image analysis, random fields and Markov chain Monte Carlo methods: a mathematical introduction*. Vol. 27. Springer Science & Business Media.

Wittkowske, C., G. Reilly, D. Lacroix, and C. Perrault. 2016. "In vitro bone cell models: impact of fluid shear stress on bone formation". *Frontiers in Bioengineering and Biotechnology* 4:87.

Wren, T., G. Beaupre, and D. Carter. 2000. "Mechanobiology of tendon adaptation to compressive loading through fibrocartilaginous metaplasia". *Journal of rehabilitation research and development* 37 (2): 135–144.

Wren, T., D. Lindsey, G. Beaupré, and D. Carter. 2003. "Effects of creep and cyclic loading on the mechanical properties and failure of human Achilles tendons". *Annals of biomedical engineering* 31 (6): 710–717.

Wu, J., H. Yuan, L. Li, K. Fan, S. Qian, and B. Li. 2018. "Viscoelastic shear lag model to predict the micromechanical behavior of tendon under dynamic tensile loading". *Journal of theoretical biology* 437:202–213.

Wyburd, M., L. Hesse, M. Aliasi, M. Jenkinson, A. Papageorghiou, M. Haak, and A. Namburete. 2021. "Assessment of Regional Cortical Development Through Fissure Based Gestational Age Estimation in 3D Fetal Ultrasound". In *Uncertainty for Safe Utilization of Machine Learning in Medical Imaging, and Perinatal Imaging, Placental and Preterm Image Analysis*, 242–252. Springer.

Wyndow, N., S. Cowan, T. Wrigley, and K. Crossley. 2010. "Neuromotor control of the lower limb in Achilles tendinopathy". *Sports Medicine* 40 (9): 715–727.

Yoo, J.H., S.R. Yi, and J.H. Kim. 2007. "The geometry of patella and patellar tendon measured on knee MRI". *Surgical and radiologic anatomy* 29 (8): 623–628.

Zamparo, O., and W.D. Comper. 1989. "Hydraulic conductivity of chondroitin sulfate proteoglycan solutions". *Archives of biochemistry and biophysics* 274 (1): 259–269.

Zech, J.R., M.A. Badgeley, M. Liu, J.J. Costa A.B .and Titano, and E.K. Oermann. 2018. "Confounding variables can degrade generalization performance of radiological deep learning models". *arXiv preprint arXiv:1807.00431*.

Zhang, L., S. Miramini, D. W Smith, B.S. Gardiner, and A.J. Grodzinsky. 2015. "Time evolution of deformation in a human cartilage under cyclic loading". *Annals of biomedical engineering* 43 (5): 1166–1177.

Zhang, Y., J.M. Brady, and S. Smith. 2000. "Hidden Markov random field model for segmentation of brain MR image". In *Medical Imaging 2000: Image Processing*, 3979:1126–1137. International Society for Optics and Photonics.

Zhou, Z.- H. 2018. "A brief introduction to weakly supervised learning". *National science review* 5 (1): 44–53.

Zhu, S. -C., C. -E. Guo, Y. Wang, and Z. Xu. 2005. "What are textons?" *International Journal of Computer Vision* 62 (1): 121–143.

Zhu, S.- C, Y. Wu, and D. Mumford. 1998. "Filters, random fields and maximum entropy (FRAME): Towards a unified theory for texture modeling". *International Journal of Computer Vision* 27 (2): 107–126.